Mechanistic, Sensitivity, and Uncertainty Studies of the Atmospheric Oxidation of Dimethylsulfide

by

Donald David Lucas

Bachelor of Science in Chemistry, Massachusetts Institute of Technology, 1996

Submitted to the Department of Earth, Atmospheric, and Planetary Sciences
in partial fulfillment of the requirements for the degree of

Doctor of Philosophy in Atmospheric Chemistry

at the

MASSACHUSETTS INSTITUTE OF TECHNOLOGY

June 2003

Signature of Author .....
Department of Earth, Atmospheric, and Planetary Sciences
May 2, 2003

Certified by .....
Ronald G. Prinn
TEPCO Professor of Atmospheric Chemistry
Thesis Supervisor

Accepted by .....
Ronald G. Prinn
Head, Department of Earth, Atmospheric, and Planetary Sciences

Mechanistic, Sensitivity, and Uncertainty Studies of the Atmospheric Oxidation of Dimethylsulfide

by

Donald David Lucas

Submitted to the Department of Earth, Atmospheric, and Planetary Sciences
on May 2, 2003, in partial fulfillment of the
requirements for the degree of
Doctor of Philosophy in Atmospheric Chemistry

Abstract

The global-scale emissions and reactivity of dimethylsulfide (CH_3SCH_3, DMS) make it an integral component in the atmospheric sulfur cycle. DMS is rapidly oxidized in the atmosphere by a complex gas-phase mechanism involving many species and reactions. The resulting oxidized sulfur-bearing products are hygroscopic and interact with aerosols through condensation and secondary aerosol formation. Predictions of the impacts of DMS chemistry on aerosols and climate are inhibited by the poorly understood DMS oxidation mechanism. This thesis diagnoses the gas-phase connections between DMS and its oxidation products by simulating comprehensive DMS chemistry (approximately 50 reactions and 30 species) using three atmospheric models of varying size and complexity.

A diurnally-varying box model of the DMS cycle in the remote marine boundary layer is used to identify important DMS-related parameters and propagate parameter uncertainties to the sulfur-containing species. This analysis shows that the concentrations of DMS and sulfur dioxide (SO_2) are sensitive to relatively few parameters. Moreover, the concentrations of DMS and SO_2 are found to have factor of 2 uncertainties caused primarily (more than 60% of the variance) by uncertainties in DMS emissions and heterogeneous removal, respectively. In contrast, the concentrations of other products, such as sulfuric acid (H_2SO_4) and methanesulfonic acid (CH_3SO_3H, MSA), are found to be sensitive to many parameters and have larger uncertainties (factors of 2 to 7) resulting from multiple uncertain chemical and non-photochemical processes.

The DMS oxidation mechanism is quantitatively assessed using a one-dimensional column model constrained by high-frequency aircraft measurements from the First Aerosol Characterization Experiment (ACE-1). From this analysis, the baseline mechanism predicts DMS and SO_2 concentrations in statistical agreement with the observations, yet it underestimates MSA concentrations by a factor of 10^4 to 10^5. These differences for MSA are statistically very significant and indicative of missing gas-phase reactions in the DMS mechanism. To reconcile these differences, five hypothetical MSA production paths are individually tested which greatly improve the model predictions to within a factor of 2 to 3 of the observations. Overall, the best improvement occurs when MSA is produced from the oxidation of methanesulfinic acid ($CH_3S(O)OH$). Furthermore, the boundary layer model predictions of H_2SO_4 show improvement after an SO_2-independent sulfuric acid production channel is added to the mechanism.

The DMS cycle is simulated in a global three-dimensional chemical transport model using, for the first time, comprehensive DMS oxidation chemistry. Four model cases are considered,

which include two new comprehensive mechanisms and two parameterized schemes of 4 to 5 reactions taken from previous global sulfur models. The mole fractions of DMS, SO_2, H_2SO_4, and MSA are compared between these four cases and with observations from the ACE-1 and PEM-Tropics A campaigns. Among the four cases, the calculated mole fractions of DMS and SO_2 are largely invariant, while those for H_2SO_4 and MSA exhibit order-of-magnitude differences. These results indicate that H_2SO_4 and MSA are sensitive to the details of the mechanism, while DMS and SO_2 are not. The comparisons between the model predictions and observations in the lower troposphere show reasonable agreement for DMS and SO_2 (within a factor of 5), but larger disagreements for H_2SO_4 and MSA (factors of 5 to 30) due to the difficulty in constraining their sources and sinks. The four model cases, however, bound the H_2SO_4 and MSA measurements. Moreover, the comprehensive mechanisms provide a better match to the MSA observations.

Thesis Supervisor: Ronald G. Prinn
Title: TEPCO Professor of Atmospheric Chemistry

Contents

List of Figures

List of Tables

Common Abbreviations

ACE-1 ..... First Aerosol Characterization Experiment

BL ..... Boundary Layer

DIM ..... Direct Integration Method

DMS ..... Dimethylsulfide

DMSO ..... Dimethylsulfoxide

$DMSO_2$ ..... Dimethylsulfone

FL ..... Buffer Layer

FT ..... Free Troposphere

GADS ..... Global Aerosol Data Set

LSODE ..... Livermore Solver for Ordinary Differential Equations

MATCH ..... Model of Atmospheric Chemistry and Transport

MSEA ..... Methanesulfenic acid

MSIA ..... Methanesulfinic acid

MSA ..... Methanesulfonic acid

NCAR ..... National Center for Atmospheric Research

NCEP ..... National Center for Environmental Prediction

ODE ..... Ordinary Differential Equation

ODESSA ..... Ordinary Differential Equation Solver with Sensitivity Analysis

PEM-TA ..... Pacific Exploratory Mission - Tropics A

PCE ..... Polynomial Chaos Expansion

PCM ..... Probabilistic Collocation Method

PDF ..... Probability Density Function

RMBL ..... Remote Marine Boundary Layer

RMSR ..... Root Mean Square Residual

Chapter 1

Introduction

1.1 Motivations

Sulfur compounds have a long, rich history in atmospheric chemistry, ranging from the recognition of sulfur-containing species in air and rain by Robert Boyle more than three centuries ago (Seinfeld and Pandis, 1998, p.1030), to the recent investigations focused on the impacts of naturally and anthropogenically emitted sulfur-based compounds across a wide range of spatial scales. On urban to regional scales, fossil-fuel combustion and industrial activity lead to pronounced atmospheric inputs of sulfur dioxide (SO_2). Through gas- and aqueous-phase chemical reactions, SO_2 is readily converted to acidic sulfate, which is then removed from the atmosphere by wet and dry deposition. Acidic deposition has been found to severely damage terrestrial and aquatic ecosystems, cause structural damage to buildings and materials, and is a potential health hazard (Cowling, 1982; World Health Organization, 2000). More recently, the focus has shifted towards understanding the regional to global scale influences of atmospheric sulfur chemistry on climate (Andreae and Crutzen, 1997). The interest in sulfur-climate interactions originates from work by Twomey (1974) and Charlson et al. (1992), who implicate anthropogenic sulfur compounds as possible climate perturbers, and research by Shaw (1983) and Charlson et al. (1987), who suggest a possible climate-regulating feedback induced by naturally emitted sulfur-containing species.

At the heart of these sulfur-climate interactions are the sulfate aerosols produced from the oxidation of SO_2. Sulfate aerosols directly influence climate by scattering in-coming solar radiation, which leads to an estimated global radiative forcing of -0.2 to -0.8 W m^{-2} (Ramaswamy et al., 2001). Sulfate aerosols also indirectly force climate by altering cloud properties such

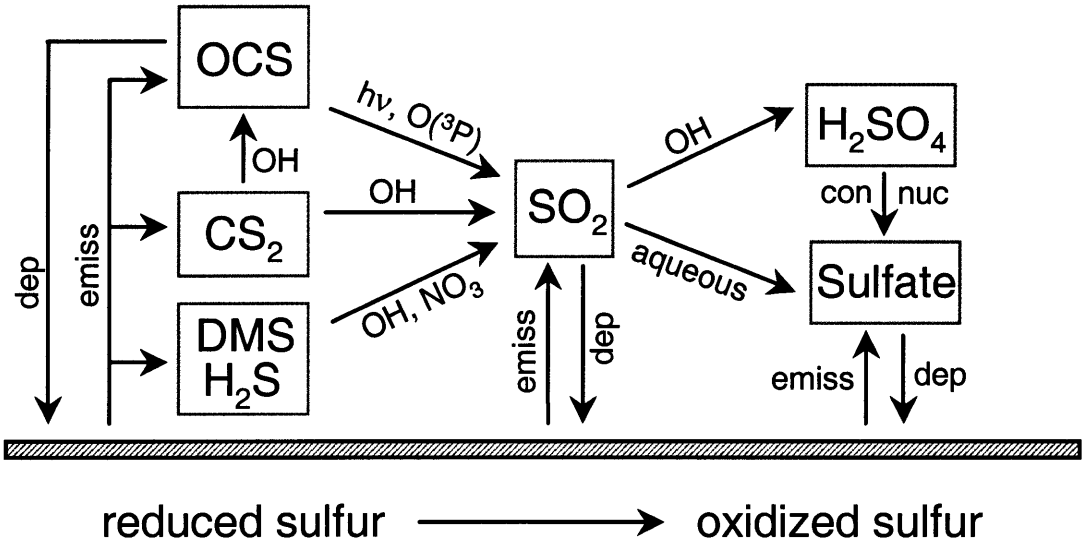

Figure 1-1: Schematic of the atmospheric sulfur cycle. Emissions, deposition, condensation, and nucleation are indicated by *emiss*, *dep*, *con*, and *nuc*, respectively.

as albedo, precipitation efficiency, and lifetime (Ramanathan et al., 2001). The total indirect forcing is separated into the first and second indirect effects, which describe changes in cloud droplet number concentrations and precipitation efficiency, respectively. Current estimates for the global forcing from the first indirect effect for sulfate aerosols range between -0.3 to -1.8 W m^{-2} (Ramaswamy et al., 2001). Estimates for the second indirect effect are sparse, but it is believed to have the same sign and a similar magnitude as the first indirect effect (Ramaswamy et al., 2001). Relative to other climate forcings –such as CO_2, ozone, and mineral dust– the net radiative impact due to sulfate aerosols alone is among the largest and most uncertain of the climatically-important agents (Ramaswamy et al., 2001). Given this intimate connection between the atmospheric sulfur cycle and climate, there is a pressing need to better quantify the mechanisms linking sulfur-containing gases to sulfate aerosols.

1.1.1 Atmospheric Sulfur Cycle

A general schematic of the atmospheric sulfur cycle is shown in Figure 1-1. The cycle is divided into the following three components: (1) surface emissions, (2) chemical and physical transformations, and (3) atmospheric removal. These components are briefly described below. Thorough overviews of the atmospheric sulfur cycle are found in Berresheim et al. (1995)

Table 1.1: Global Sulfur Emissions (Tg S yr^{-1})

Source	DMS	H_2S	CS_2	OCS	SO_2	Sulfate	Total	NH/SH
Fossil-fuel/Industry	*	*	*	*	70	2.2	71-77	68/6
Biomass burning	—	<0.01	<0.01	0.075	2.8	0.1	2.2-3.0	1.4/1.1
Oceans	15-25	<0.3	0.08	0.08	—	40-320	15-25	8.4/11.6
Wetlands	0.003-0.68	0.006-1.1	0.0003-0.06	—	—	—	0.01-2	0.8/0.2
Plants/Soils	0.05-0.16	0.17-0.53	0.02-0.05	—	—	2-4	0.25-0.78	0.3/0.2
Volcanoes	—	0.5-1.5	—	0.01	7-8	2-4	9.3-11.8	7.6/3.0
Anthropogenic							73-80	
Natural							25-40	
Total							98-120	

Adopted from Seinfeld and Pandis (1998, p.59). Fluxes are also shown for the Northern and Southern Hemispheres (NH/SH). Fossil-fuel/Industry has a total reduced sulfur flux of 2.2 (i.e., the sum of the *'s) and the net total is for the mid-1980s. The total oceanic flux excludes sea-salt contribution because sea-salt sulfate is rapidly re-deposited on the surface. The total plants/soil flux excludes soil dust contribution. The two most significant contributions are shown in boxes.

and Seinfeld and Pandis (1998, p.55-66). For detailed budget information consult the recent model-based global studies by Langner and Rodhe (1991), Pham et al. (1995), and Chin et al. (1996).

Emissions

The atmospheric sulfur cycle is initiated by the surface emissions of natural and anthropogenic sulfur compounds. The natural sulfur contributions derive mainly from volcanic activity and the terrestrial and marine biospheres. These natural emissions include the reduced sulfur-containing gases dimethylsulfide (CH_3SCH_3, DMS), hydrogen sulfide (H_2S), carbon disulfide (CS_2), carbonyl sulfide (OCS), as well as volcanic injections of SO_2. With time, the biospheric emissions exhibit strong seasonal cycles, while the volcanic emissions are highly episodic. The anthropogenic emissions are mainly in the form of gaseous SO_2 and arise from a combination of fossil-fuel combustion, industrial activity, and biomass burning. Table 1.1 summarizes the sources of these natural and anthropogenic inputs and lists estimates of their corresponding emissions (Seinfeld and Pandis, 1998). A more recent estimate of 15-33 Tg S yr^{-1} for the global oceanic DMS flux was compiled by Kettle and Andreae (2000), which is consistent with the range given in the table, but with a slightly larger uncertainty. On the basis of the magnitudes

of the emissions in the table, DMS and SO_2 are the dominant sulfur-based sources, so studies aimed at understanding the atmospheric sulfur cycle typically focus on these two species.

Transformations

Once emitted into the atmosphere, the sulfur-based compounds undergo a rich variety of chemical and physical transformations. Chemically, the reduced sulfur-containing species are reactive and susceptible to oxidation by hydroxyl radicals (OH) to form SO_2. DMS is additionally oxidized by nitrate radicals (NO_3), which is an important DMS sink at night. The SO_2 that is either directly emitted or chemically produced undergoes further oxidation in the gas- and aqueous-phases to sulfuric acid (H_2SO_4) and sulfate (SO_4^{2-}), respectively. This tendency to go from reduced forms of sulfur to oxidized forms is noted in Figure 1-1 and is driven by the oxidative nature of our atmosphere. Other chemical processes in the cycle include the photolysis of OCS in the stratosphere, multiphase chemistry between SO_2 and aerosols, and aqueous-phase reactions of the soluble sulfur-bearing species. The physical transformations in the sulfur cycle involve the transfer of sulfur compounds between the gas-, aerosol-, and aqueous-phases. The mass transfer between the gas- and aerosol-phases ultimately occurs through either particle nucleation –which converts gaseous H_2SO_4 into new sulfate aerosol particles– or the condensation and evaporation of semi-volatile sulfur-based vapors to and from existing aerosol particles and cloud droplets.

Removal

The eventual fate of the atmospheric sulfur compounds is their removal by dry and wet deposition. In dry deposition, gaseous and particulate sulfur-containing species are lost through contact with land and ocean surfaces. Gas-phase SO_2 is comparatively more reactive towards the surface than the reduced sulfur compounds, and so dry deposition is an efficient sink primarily for SO_2. For sulfate aerosols, dry deposition depends on the particle size, where the smallest (diameter < 0.005 μm) and largest (diameter > 1 μm) sulfate particles are most effectively depleted at the surface. The most significant atmospheric sink for the highly oxidized sulfur-based species, however, occurs through wet deposition. Wet deposition is efficient because the oxidized sulfur-containing products and sulfate aerosols are extremely soluble and are readily taken up by clouds and removed by precipitation. To a large extent, therefore, wet deposition controls the atmospheric lifetime of many species in the atmospheric sulfur cycle.

1.1.2 Role of Dimethylsulfide

DMS plays a prominent role in the atmospheric sulfur cycle because it is the largest natural source of sulfur globally (12-25% of the net sulfur in Table 1.1), the largest single source in the Southern Hemisphere, and its cycling may influence climate on regional to global scales. DMS first came to light as an important component in the sulfur cycle with its discovery in oceanic waters by Lovelock et al. (1972). In the ocean, DMS is produced biologically by phytoplankton (Keller et al., 1989), where it is postulated to offer cellular protection as an antioxidant (Sundra et al., 2002). Due to its relatively low aqueous solubility (Sander, 1997), surface waters are usually supersaturated in DMS, resulting in a net ocean-to-atmosphere flux.

Once emitted to the atmosphere, DMS undergoes a complex series of oxidation reactions primarily by HO_x, O_3, and NO_x as discussed in Chapter 2. The gas-phase products of these reactions include, but are not limited to, SO_2, H_2SO_4, dimethylsulfoxide ($CH_3S(O)CH_3$, DMSO), dimethylsulfone ($CH_3S(O)_2CH_3$, $DMSO_2$) and methanesulfonic acid (CH_3SO_3H, MSA). Because these oxidized sulfur-based products are extremely hygroscopic, they condense on existing aerosols or form new particles through particle nucleation. The freshly nucleated particles are condensation nuclei (CN) that, through coagulation and additional condensation, grow into cloud condensation nuclei (CCN). Under typical supersaturations in the atmosphere (~0.1-1%), CCN are activated into cloud droplets. The atmospheric pathways linking DMS to CN and CCN are illustrated in Figure 1-2. These pathways are described in numerous studies, a few examples of which include Raes and Van Dingenen (1992), Pandis et al. (1994), and Russell et al. (1994).

Because the phytoplankton production of DMS depends on climatic variables –such as temperature and sunlight– which are, in turn, affected by the CCN produced from DMS, Charlson et al. (1987) first suggested that DMS plays a central role in a self-regulating climate feedback loop. To illustrate the negative feedback, assume that temperature increases by a given amount. For this temperature increase, the biological production of DMS by phytoplankton is presumed to be more active, which leads to larger atmospheric concentrations of DMS. Higher concentrations of atmospheric DMS implies increased amounts of sulfate aerosols, which scatter more radiation and cool the system back towards its initial state. In this way, the climate is stabilized and self-regulated. Though simple to state in words, the multiple components involved in this feedback loop have been difficult to quantify. A decade and a half of DMS-related research has taken place since the Charlson et al. (1987) paper, yet the magnitudes and signs of many of the processes are still highly uncertain (Andreae and Crutzen, 1997). Processes

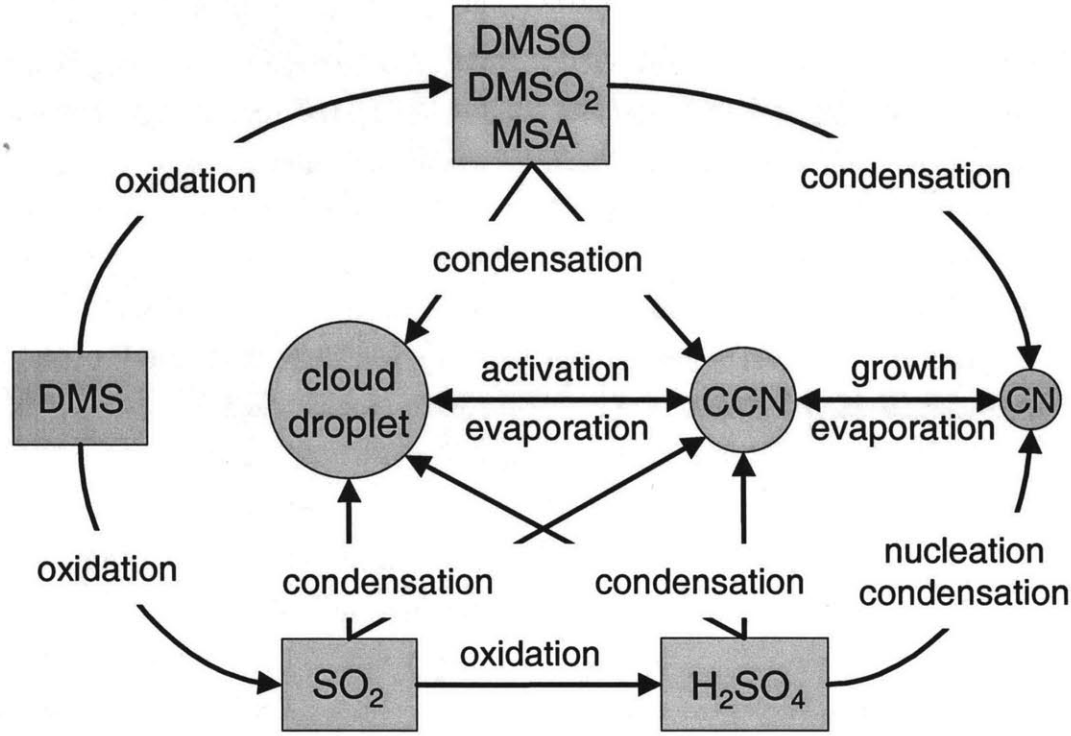

Figure 1-2: Pathways linking DMS to aerosols and cloud droplets in the atmospheric sulfur cycle. Rectangles and circles represent gas-phase and aerosol-/cloud-phase species, respectively.

fraught with large uncertainties include the microphysical connections between aerosols and clouds, the response of phytoplankton to environmental stresses, and the non-linear production of gas-phase SO_2, MSA, and H_2SO_4 from atmospheric DMS. Quantifying this last process –the photochemical oxidation of DMS to SO_2, MSA, and H_2SO_4– is the major objective in this thesis.

As a point of emphasis and clarification, the rectangles in Figure 1-2 represent sulfur-containing species in the *gas*-phase, as opposed to the *aerosol-* and *aqueous*-phase species present in the CN, CCN, and cloud droplets illustrated by the circles. Scattered throughout the DMS-related literature, however, are references associating gas-phase H_2SO_4 to non-sea-salt sulfate (nss-SO_4^{2-}) and gas-phase MSA to the methanesulfonate anion ($CH_3SO_3^-$, MS^-). To cite a recent example, Capaldo and Pandis (1997) modeled the gas-phase concentration of MSA, which they then compared to observations of MS^-. These associations persevered in the literature because H_2SO_4 and MSA are extremely soluble, and because, until recently,

only measurements of SO_4^{2-} and MS^- were available. Also, previous studies centered on SO_4^{2-} rather than H_2SO_4 because sulfate aerosols interact with climate. Distinguishing the gas-phase species from their aerosol- and aqueous-based counterparts is highly important and not merely an issue of semantics. For instance, gas-phase H_2SO_4 has the potential to nucleate into new aerosol particles (Viisanen et al., 1997; Kulmala et al., 1998), which makes it critical to know the H_2SO_4 concentration separately from SO_4^{2-}. Furthermore, MS^- can be formed in two independent ways, (1) through aqueous-phase chemistry (Bardouki et al., 2002), and (2) the condensation of MSA followed by acid dissociation. Therefore, the gas-phase concentration of MSA is not necessarily a good measure of MS^- in the aqueous-phase. Because the gas-phase DMS oxidation mechanism is the focus of this thesis, all of the DMS-related species are hereafter considered to be in the gas-phase unless otherwise noted.

1.2 Overview and Objectives

This thesis thematically centers around the gas-phase oxidation of DMS, which connects emissions to aerosols in the atmospheric DMS cycle. Because DMS is emitted primarily from oceans, DMS oxidation is restricted to the *remote marine atmosphere* throughout this thesis. This restriction serves two useful purposes. First, this imparts important limiting conditions on the oxidation chemistry. In particular, NO_x levels are lower in the remote marine environment than in urban settings, which leads to a drastic reduction in the required number of DMS oxidation reactions. Second, a thorough understanding of the marine oxidation of DMS is useful for characterizing the natural background sulfur cycle because the natural sulfur cycle is dominated by DMS emissions. By establishing a baseline for the natural background sulfur cycle, therefore, any anthropogenic perturbations to the total sulfur cycle are more easily discerned and analyzed.

1.2.1 Active Questions

There are numerous active questions surrounding the atmospheric DMS cycle. Rather than attempting to answer all of these questions, this thesis addresses the subset of questions related to the sources and sinks of the gas-phase DMS-related species, which are displayed by the arrows going to and from the rectangles in Figure 1-2. Certain non-gas-phase phenomena, such as the effects of the uptake of soluble sulfur-containing gases on the growth of aerosols, are not covered. Though slightly prohibitive, the spectrum of remaining issues is still very large, as

illustrated by the following set of questions that are actively pursued in this dissertation.

Q1. The cycling of DMS in the remote marine atmosphere involves many simultaneous photochemical and non-photochemical processes. For instance, SO_2 is affected by a complex combination of chemistry, transport, dry deposition, and other heterogeneous processes. Which of these chemical and physical processes, therefore, are most important in regulating the gas-phase concentrations of the DMS-related species? Further, once the most important processes are identified, can the number of parameters required to simulate the DMS cycle be reduced by eliminating the non-important parameters?

Q2. The two most commonly used sea-to-air transfer parameterizations yield surface fluxes that differ from each other by a factor of two (Liss and Merlivat, 1986; Wanninkhof, 1992). Because DMS is produced in ocean surface waters, the resulting DMS emissions are also uncertain by a factor of two. Adding to this uncertainty, the DMS oxidation mechanism contains many reactions with highly indeterminate rate constants. Therefore, are the uncertainties in the DMS-related species primarily due to uncertainties in emissions or chemistry, or some other process? Furthermore, can the specific processes and reactions that contribute to these DMS-related uncertainties be identified?

Q3. DMS and SO_2 have long been measured in the remote marine atmosphere because of their relatively large abundances and lifetimes ($\sim 10^9$ molecules cm^{-3}, 3-5 days). These measurements, however, do not peer deep enough into the DMS oxidation mechanism to assess key branching ratios. Recent advancements in instrumentation now allow for high-frequency, atmospheric measurements of gas-phase H_2SO_4 and MSA aboard aircraft (Eisele and Tanner, 1993). When combined with observations of DMS and SO_2, can these new gas-phase measurements provide a deeper insight into the DMS oxidation mechanism? More specifically, can they be used to elucidate the complex branching within the DMS mechanism? Furthermore, what sort of modeling framework is most appropriate for simulating these new measurements?

Q4. DMS is photochemically destroyed by the OH radical, so, at the very least, models of DMS chemistry require knowledge of the oxidative state of the atmosphere as a constraint. Besides photochemistry, the DMS-related species are also largely affected by non-photochemical processes such as heterogeneous removal and turbulent mixing. Gas-phase H_2SO_4, for example, is highly soluble and readily condenses on aerosols. This means that ambient aerosol distributions are required to constrain H_2SO_4. This leads

to the question, what photochemical and non-photochemical observations are required to constrain models of the DMS cycle in the remote marine environment?

Q5. Temperature affects the DMS cycle in profound ways. Perhaps the largest influence is through the initial attack of OH on DMS, which occurs through two channels with opposite temperature-dependencies. One channel leads to SO_2 and H_2SO_4; the other yields DMSO and $DMSO_2$. Consequently, the ratios of important sulfur-containing compounds may vary as a function of temperature. One related ratio involves the anions MS^- and nss-SO_4^{2-}, which are measured in ice cores as a proxy for the biogenic sulfur cycle in ancient climates (Whung et al., 1994; Saltzman et al., 1997; Legrand et al., 1997). Thus, how do the products of DMS oxidation vary with temperature? Are these temperature variations attributable to a few, or many, chemical reactions? As related to Q2, do the uncertainties of the DMS-related species also vary with temperature?

Q6. Due to limited computational resources, previous model-based studies of the global sulfur cycle used highly-parameterized mechanisms for DMS oxidation. These simplified mechanisms represented multi-step pathways using single reactions. Some of these studies even fixed the yields at important branching points. In one recent example, only 5 gas-phase reactions connected DMS to DMSO, MSA, SO_2, and sulfate (Pham et al., 1995). An obvious question is, how well do these parameterized DMS mechanisms perform relative to more comprehensive schemes? Further, do the parameterized and comprehensive mechanisms agree at some locations, but not others (e.g., the boundary layer versus the free troposphere)?

Q7. Given the connection between sulfate aerosols and climate, global model-based studies of the sulfur cycle attempt to calculate the amount of sulfate aerosols formed from oceanic DMS emissions. As mentioned in Q6, the pathways leading to sulfate aerosols represented in global models are usually parameterized. In fact, most of these models do not even resolve gas-phase H_2SO_4. Instead, they assume that H_2SO_4 is instantly converted to sulfate aerosols. These studies, therefore, miss out on the dynamics of aerosol nucleation. Therefore, as an addendum to Q6, what levels of H_2SO_4 are required for new particle production through binary nucleation? Given the low temperatures and high concentrations of H_2O and H_2SO_4 required for nucleation, which regions of the remote marine atmosphere support the largest nucleation rates? Lastly, how sensitive are these nucleation rates to the type of DMS oxidation mechanism (parameterized versus comprehensive)?

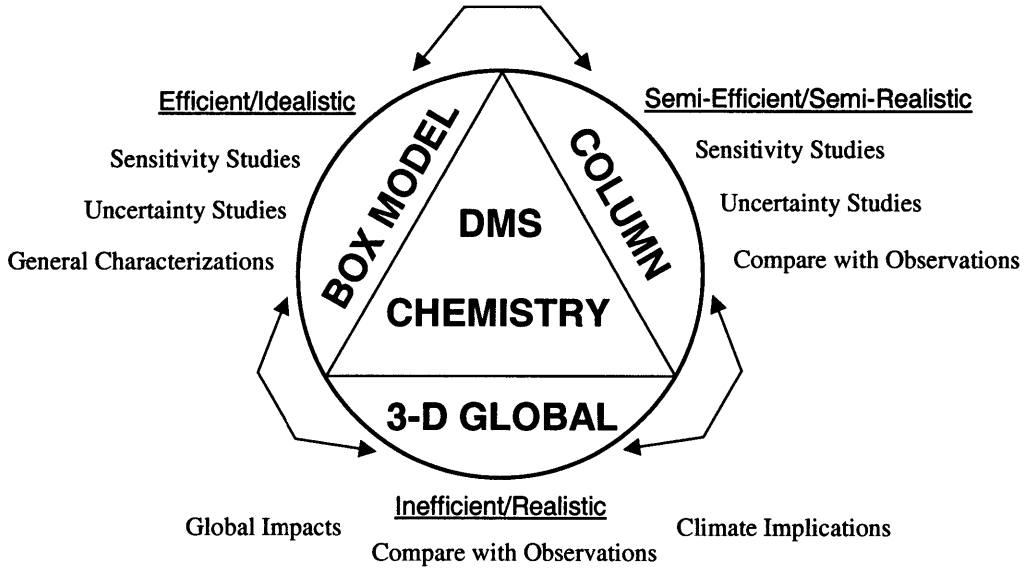

Figure 1-3: The modeling hierarchy used to examine DMS oxidation chemistry. The focus of this thesis is on DMS chemistry, which lies at the center of the diagram. The three separate models –and their advantages, disadvantages, and uses– are shown surrounding the DMS chemistry. The flow of information between the various models is depicted by the arrows.

1.2.2 Modeling Hierarchy

The aforementioned questions cover a wide range of temporal and spatial scales, and thus require model-based approaches of varying size and complexity. Hence, this dissertation uses a hierarchy of three different models in an attempt to answer these DMS-related questions. These three models are depicted schematically in Figure 1-3. As noted in the figure, the lower dimensional models are numerically efficient, which makes them ideal for exploring the sensitivities and uncertainties of DMS chemistry. The higher dimensional models, on the other hand, are more realistic, may be used to compare with observations, and sample a larger range of atmospheric conditions. These three models are not independent from one another, however, as portrayed by the connecting arrows in the figure. That is, the sensitivity and uncertainty information gained from the box and column models can be used to identify and constrain important factors in the global study. Further, the global model results can be used to choose optimal settings for the box model. Although the DMS-related information flows between the three models, this thesis describes each model using separate, stand-alone chapters. This structure leads to some repetition and overlap, but allows for self-contained chapters with minimal reliance on

the other chapters. The three models are briefly introduced below as they relate to questions Q1-Q7.

Remote Marine Boundary Layer Box Model

A box model of the DMS cycle in remote marine boundary layer (RMBL) is discussed in Chapter 3. This model uses a comprehensive DMS oxidation mechanism and has representations for DMS emissions, heterogeneous removal, and mixing into and out of the RMBL. The general model conditions are based on a set of observations made during a recent measurement campaign in the remote Pacific. Important oxidizing species such as OH and O_3 were also measured during this campaign. The observed time-series of these oxidants define a set of forcing-functions used to drive the diurnal variations in the DMS photochemistry. Because this model is numerically very efficient, it can be integrated thousands of times for different sets of conditions and model parameters. For these reasons, this model well-suited for characterizing the sensitivities and uncertainties of the sulfur-based species as addressed by questions Q1 and Q2. Additionally, the response of the model to temperature changes, as noted in question Q5, is easily handled. Because the box model is highly idealized, however, it is ill-suited for comparisons with real atmospheric observations as mentioned in questions Q3 and Q4.

Observationally-Constrained Column Model

A one-dimensional column model of DMS chemistry and mixing is detailed in Chapter 4. As with the box model, this model uses a comprehensive DMS oxidation mechanism. The column model also includes gas-to-aerosol transfer through condensation on background aerosols and dry deposition at the ocean surface. The column model vertically resolves the marine atmosphere into three dynamic layers (boundary layer, buffer layer, and free troposphere) and explicitly calculates the mixing into and out of these layers. Most importantly, many model inputs are constrained using high-frequency observations made aboard an aircraft flight during a recent measurement campaign. These aircraft observations constrain the meteorology, oxidation chemistry, and ambient aerosols in the column model. Aircraft soundings of DMS also constrain the surface flux of DMS and vertical mixing in the model. As related to the model outputs, concurrent observations of SO_2, MSA, and H_2SO_4 in the gas-phase were made by the aircraft. The highly-constrained nature of the column model provides an excellent platform for scrutinizing the gas-phase kinetics of DMS oxidation because all of the major photochemical and non-photochemical sources and sinks are constrained, accept for the DMS mechanism.

This observationally-constrained column model, therefore, is used to directly address questions Q3 and Q4. This column model is also fairly computationally efficient, and so it is useful for assessing the uncertainties referred to in question Q2. Note, question Q1 is partially addressed through a budget analysis of the important DMS-related species.

Three-Dimensional Global Model

A three-dimensional global chemical transport model is described in Chapter 5. This model is driven by offline meteorological fields, rather than calculating these variables online. This frees up valuable computational resources that are used for computing expensive photochemical-related processes. As such, a comprehensive version of the DMS oxidation mechanism is utilized in this study. Other important DMS-related processes included in the model are: (1) seasonally-varying sea-surface DMS concentrations based on climatology, (2) an explicit formulation for the loss of sulfur-bearing compounds on climatologically-derived global aerosol distributions, (3) the scavenging of soluble oxidized sulfur-containing species in clouds, and (4) the dynamic calculation of dry deposition for SO_2 over the oceans using a resistance-based model. For simplicity, however, offline oxidation fields (e.g., HO_x and NO_x) taken from another study are used to drive the DMS chemistry. The main outputs of this model are the gas-phase concentrations of the DMS-related species –including H_2SO_4 and MSA. Note that aerosol concentrations of SO_4^{2-} and MS^- are not tracked in this model. Because this model uses a comprehensive DMS mechanism, question Q6 is addressed directly by replacing the full mechanism with parameterized versions. Moreover, the model predictions of gas-phase H_2SO_4 allow for an assessment of the nucleation rates of sulfate aerosols, as noted in question Q7. Pertaining to question Q3, the offline meteorological fields driving the model are based on observations, which suggests that realistic comparisons can be made between modeled and measured DMS-related species. There are many factors, however, that limit these comparisons. These include poor knowledge of the DMS surface flux, short-lived species, the sparsity of observations in space and time, and coarse model resolution. Tentative model-observation comparisons are done, but not to ascertain mechanistic information as noted in question Q3.

1.3 Previous Studies Using Comprehensive DMS Mechanisms

The core of this thesis is to use modeling-based approaches to study the atmospheric pathways in the oxidation of DMS. While numerous published studies have addressed important issues

related to atmospheric DMS oxidation, most of these studies employed parameterized DMS mechanisms (for example, see Davis et al. (1999) and Shon et al. (2001)). Falling into the realm of studies using parameterized mechanisms are all of the global-scale models with DMS chemistry (for example, see Pham et al. (1995) and Barth et al. (2000)). The studies that did use complex DMS mechanisms are summarized here in chronological order. This summary gives a sense which DMS-related questions have been addressed, and which questions are still open.

Using an extensive compilation of available kinetic and thermochemical data related to organosulfur compounds, Yin et al. (1990b) assembled a comprehensive mechanism for the oxidation of DMS (~150 reactions and ~50 species). In a companion paper, Yin et al. (1990a) tested their mechanism through a series of smog chamber experiments. These experiments monitored the evolution of gas-phase DMS and SO_2 over a four-hour period and for a range of high NO_x conditions. They also measured the average aerosol-phase concentrations of MS^- and SO_4^{2-}. Using their mechanism, Yin et al. (1990a) simulated successfully the decay of DMS and increase in SO_2 with time. Their mechanism, however, consistently overestimated the yields of sulfate and methanesulfonate. Their overestimation could have resulted from not taking wall losses into account for these species or some other experimental procedure. At odds with these results are recent studies indicating that the same mechanism actually underestimates MSA in the remote marine atmosphere. This disagreement may be due to differences between DMS chemistry in polluted and non-polluted conditions (i.e., the high NO_x chamber versus the low NO_x marine atmosphere). More likely, however, are missing MSA production reactions in the original Yin et al. (1990b) mechanism. Nevertheless, the Yin et al. (1990b) mechanism has solidified our understanding of DMS oxidation chemistry and serves as a strong foundation for building up future knowledge of DMS chemistry.

Koga and Tanaka (1993) constructed a moderately complex model of DMS oxidation chemistry in the surface mixing layer. They applied this model to the variations in temperature, photolysis, and surface DMS flux typically encountered between 60°S and 60°N. Their chemical mechanism included reactions related to DMS oxidation (40 reactions and 23 sulfur-containing species taken from Yin et al. (1990b)) and the production of important oxidizing species (12 photolytic and 34 chemical reactions relevant to HO_x-NO_x-CH_4 chemistry). Other processes included the dry deposition of SO_2, heterogeneous removal of DMSO, $DMSO_2$, MSA, and H_2SO_4, and the aqueous-phase production of non-sea-salt sulfate from condensed DMSO, $DMSO_2$, MSA, and SO_2. Numerous simplifications were made in their model, including fixed values for

important parameters (e.g., the surface layer height, condensation rates, and the heterogeneous conversion of SO_2 to sulfate). Perhaps the most constraining simplification is the lack of mixing into and out of the surface layer. In spite of these deficiencies, Koga and Tanaka recognized of the extreme influence of temperature on the distribution of oxidized sulfur-bearing products. In particular, they suggested that the temperature-dependent reactions between DMS and OH may explain fully the latitudinal trends in the ratio of nss-SO_4^{2-} to MS^-. The basis of their premise is that MSA is produced primarily through a DMS+OH addition channel that has a negative temperature-dependence (i.e., increases with falling temperature). Because the Yin et al. (1990b) mechanism does not include such pathways, Koga and Tanaka (1993) postulated the existence of two new MSA production routes. Their conclusions are re-assessed in this thesis in light of new DMS mechanistic details.

As an extension of the previous studies, Hertel et al. (1994) utilized a fairly sophisticated one-dimensional Lagrangian trajectory model to reproduce the concentrations of observed DMS-related species arriving at a coastal location in France. Their model explicitly solved for vertical mixing, and included detailed representations of wet and dry deposition. On the chemistry side, they used a large mechanism (~200 reactions and ~80 species) to calculate important background photochemical species (e.g., O_3, NO_x, and RO_x) and DMS-related species (58 sulfur-based reactions, 26 sulfur-containing species). Despite the large number of sulfur-based reactions, their representation of DMS chemistry was highly parameterized and laden with mechanistic inaccuracies. As one example, Hertel et al. (1994) assumed that DMS reacts with OH through an addition channel with a positive temperature dependence. This assumption stands in contrast to laboratory measurements (Hynes et al., 1986; Barone et al., 1996; Turnipseed et al., 1996) and other modeling studies that show a negative temperature dependence for this reaction. As another example, Hertel et al. (1994) eliminated many radical species, including one that may play a role in the branching between SO_2, H_2SO_4, and MSA. Further, they simplified the DMS mechanism by fixing the yields of MSA (83%) and H_2SO_4 (17%) produced from eight different reactions. Their analysis was also complicated by the fact that the coastal location was influenced by continental air masses. This polluted air was rich in anthropogenic SO_2, which greatly perturbed the chemistry and obscured their calculated concentrations of DMS-based end products. Collectively, their simplifications caused large discrepancies between the modeled and observed concentrations. These discrepancies are as large as an order of magnitude for DMS and SO_2, which brings into question their reasonable agreement for MS^-.

Saltelli and Hjorth (1995) developed a moderately complex gas-phase DMS mechanism

comprised of 37 sulfur-based reactions and 18 sulfur-containing species. They also assigned uncertainty ranges for each of the reaction rate constants, which allowed them to carry out quantitative analyses of the sensitivities and uncertainties of the DMS-related species to important kinetic parameters. There are two important points regarding the Saltelli and Hjorth (1995) mechanism. First, they removed DMSO as intermediate species, which eliminated any possible branching involving this species. Second, they used anomalous values for the rate constants associated with reactions producing SO_2 and MSA, with the net effect of enhancing and degrading the production rates of MSA and SO_2, respectively. These adjustments compensated for the underestimation of MSA inherent in the Yin et al. (1990b) scheme. Using their mechanism, Saltelli and Hjorth (1995) performed simulations for polluted and non-polluted conditions and focused on the following three different model outputs: (1) the ratio of MSA to SO_2+H_2SO_4, (2) the formation paths to SO_2 and H_2SO_4, and (3) the role of sulfur-containing peroxynitrate species. Saltelli and Hjorth (1995) found that, for their specific mechanism structure, reactions involving methylsulfoxyl radicals played critical roles in the production of SO_2, H_2SO_4, and MSA. Furthermore, they dismissed a potentially important pathway suggested by Bandy et al. (1992) that forms H_2SO_4 from DMS in the absence of SO_2. Regarding the formation of sulfur-bearing peroxynitrates, they concluded that they are formed in small quantities at 298 K, but may be more important at lower temperatures and could be involved in heterogeneous reactions. In spite of their thorough statistical analysis, certain model limitations prevent their results from having widespread applicability, especially in the interpretation of atmospheric DMS-related data. In particular, the influence of temperature on DMS oxidation was ignored. Other neglected processes included diurnal variability, vertical mixing, and heterogeneous removal through dry deposition and condensation.

Because the majority of DMS modeling studies use parameterized oxidation mechanisms, Capaldo and Pandis (1997) sought to quantify the differences between these condensed schemes versus more comprehensive versions. Specifically, they tested three comprehensive (Yin et al., 1990b; Koga and Tanaka, 1993; Hertel et al., 1993) and two parameterized mechanisms (Pham et al., 1995; Benkovitz et al., 1994) using a box model representation of the marine boundary layer. Besides gas-phase chemistry, they included routines for wet and dry deposition, entrainment into the boundary layer, and the heterogeneous conversion of SO_2 to nss-SO_4^{2-} in cloud-droplets and sea-salt aerosols. Note that, as in many other reports, Capaldo and Pandis (1997) equated gas-phase MSA to MS^-, and thus did not include the chemical production of MS^- in clouds and aerosols. Capaldo and Pandis (1997) subjected these mechanisms to a

range of conditions at six surface locations between 40°S and 35°N. The five mechanisms had good agreement in terms of gas-phase DMS at the six locations because all of the schemes used similar initial oxidation steps. More surprisingly, four of the five mechanisms gave comparable results for SO_2 and nss-SO_4^{2-}, where the outlying mechanism was from Hertel et al. (1994). For MS^-, however, the mechanisms had significant disagreements, some of which were as large as two orders of magnitude. They found that the Hertel et al. (1994) mechanism consistently produced the most MS^-, while the Yin et al. (1990b) scheme produced the least. In spite of these large differences, there were no discernible biases towards the parameterized and comprehensive DMS mechanisms. When compared to measurements of sulfur-containing species, Capaldo and Pandis found that not a single mechanism reproduced the observations at all of the locations. This study, therefore, reinforces the fact that the gas-phase production routes of MSA require further scrutiny. Finally, Capaldo and Pandis (1997) asserted that the parameterized and comprehensive DMS mechanisms are comparable. This, however, follows only for the conditions in the marine boundary layer to which their model was confined. Above the marine boundary layer the effects of temperature- and pressure-dependent chemistry are more pronounced, and so the differences between the parameterized and comprehensive mechanisms are likely to be larger.

Campolongo et al. (1999) recognized both the power of the statistical techniques and the model and mechanism deficiencies in the study by Saltelli and Hjorth (1995). By correcting these deficiencies and using Monte Carlo methods, Campolongo et al. (1999) greatly expanded on the work of Saltelli and Hjorth (1995). The specific improvements implemented by Campolongo et al. (1999) included the addition of multiphase processes (i.e., gas-aerosol partitioning and aqueous chemistry) and wet and dry deposition. Mechanistic improvements consisted of the introduction of DMSO as an intermediate species and the update of the rate constant for the dissociation of CH_3SO_2, which is a critical SO_2 precursor. In spite of these vast improvements, the model still did not account for SO_2 processing on sea-salt aerosols, and the gas-phase mechanism still used anomalous values for MSA-related rate constants to enhance its production. In a fashion similar to previous studies, Campolongo et al. (1999) subjected their model to latitudinal variations (55°S to 55°N) in meteorological and oxidizing conditions. They investigated the variations in the ratio of MS^- to nss-SO_4^{2-} as a function of latitude, both with and without multiphase chemistry. When compared to observed values for this ratio, they found that only the model version containing multiphase chemical pathways agreed statistically with the observations. Campolongo et al. (1999) also concluded that new pathways producing

MS^- must exist, and they endorsed an aqueous-phase path as being the best candidate, though they did not rule out pathways that enhance gas-phase MSA.

Chapter 2

DMS Oxidation Chemistry in the Remote Atmosphere

The mechanism for the gas-phase oxidation of dimethylsulfide (CH_3SCH_3, DMS) in the remote marine atmosphere is summarized in this chapter. To avoid repetition with previous reviews, only the key sulfur-containing species and reactions are highlighted here. As will be shown shortly, an immense insight into DMS oxidation chemistry is gained by concentrating on the general trends and aspects, rather than the specific details. Consult the exhaustive review by Yin et al. (1990b) for the detailed kinetics of individual DMS-related reactions. Additional overviews of DMS chemistry are also found in Turnipseed and Ravishankara (1993), Berresheim et al. (1995), and Urbanski and Wine (1999). Because the focus is on DMS chemistry in the remote marine atmosphere, the discussion in this chapter is centered around the relevant oxidizing conditions for that environment (e.g., low concentrations of NO_x). Refer to Yin et al. (1990b) for the chemistry of DMS in a polluted atmosphere.

A diagram of the mechanism for the oxidation of DMS in the remote marine atmosphere is shown in Figure 2-1. The complexity in the mechanism is apparent from the outset. DMS can initially react with hydroxyl radicals through two separate channels called the *H-abstraction* and *OH-addition* branches. As shown in the darker shaded region in Figure 2-1, dimethylsulfoxide ($CH_3S(O)CH_3$, DMSO), dimethylsulfone ($CH_3S(O)_2CH_3$, $DMSO_2$), methanesulfenic acid (CH_3SOH, MSEA), and methanesulfinic acid ($CH_3S(O)OH$, MSIA) are produced solely along the OH-addition branch. SO_2 and sulfuric acid (H_2SO_4), on the other hand, are produced primarily through the H-abstraction branch shown in the lighter shaded region. Another major end-product is methanesulfonic acid (CH_3SO_3H, MSA), which is intermediate to the OH-

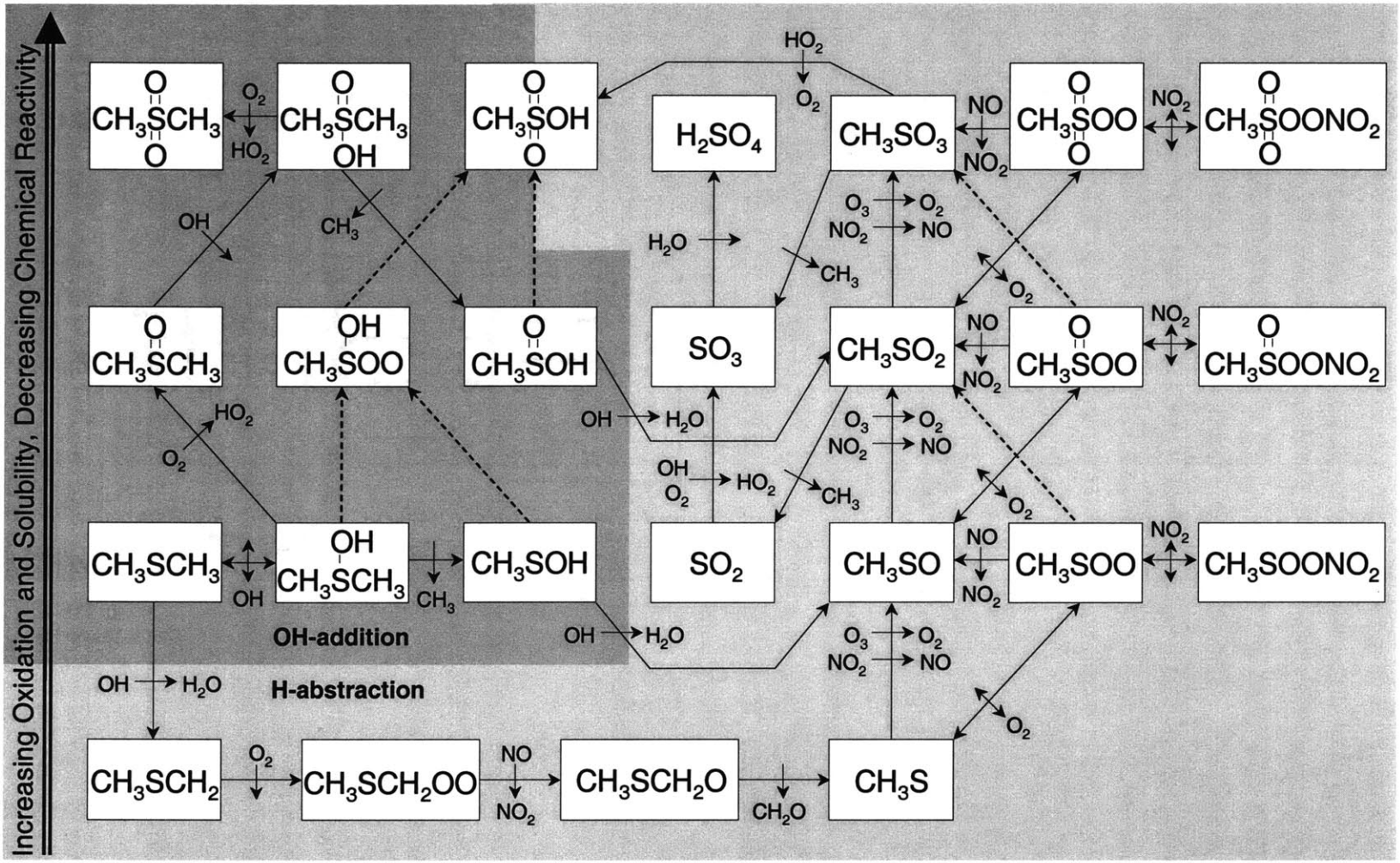

Figure 2-1: The DMS oxidation mechanism in the remote marine atmosphere. The diagram is organized so that species within a column tend to have similar molecular structures. Also, the general trends in oxidation state, chemical reactivity, and solubility are shown on the left. The dark and light gray regions denote the DMS+OH addition and abstraction branches, respectively. Speculative pathways that are tested in this thesis are denoted by dashed arrows.

addition and H-abstraction branches because the highly uncertain production of MSA likely involves a combination of the two pathways.

To complicate matters, the OH-addition and H-abstraction branches are not completely independent. MSEA and MSIA are products along the OH-addition branch, but can react with OH to form precursors to SO_2 and H_2SO_4. Further, many of the branching points in the DMS mechanism –including the initial branching at DMS+OH– are extremely sensitive to temperature and pressure. Moreover, many of the sulfur-based species are susceptible to removal by condensation on ambient aerosols and other heterogeneous processes. Taken together, these overlapping factors complicate the attempts to decipher the DMS oxidation chemistry.

There are, however, certain underlying features that simplify the analysis of DMS oxidation chemistry. Figure 2-1 is organized logically to highlight some of these features. Specifically, species that have similar molecular structures are aligned vertically in the diagram. As an example, DMS, DMSO, and $DMSO_2$ are all contained in the same column (i.e., the left-hand column in Figure 2-1). Organizing the diagram is this manner has two main advantages. First, the species within a column tend to undergo similar types of reactions. To illustrate, DMS and DMSO both react with OH through an addition channel, while MSEA and MSIA both react with OH through an abstraction channel. This allows for the classification of characteristic reactions and the identification of critical branching points. The second advantage pertains to important chemical and physical trends within a given group of species. That is, the sulfur-based species increase in oxidation going from the bottom of a given column to the top. In other words, $DMSO_2$ is more oxidized than DMSO, which is more oxidized than DMS. The change in the oxidation state has important consequences for the chemical reactivities and solubilities.

The logical structure of Figure 2-1, therefore, reflects the most important general aspects of DMS oxidation chemistry and serves to guide the rest of the discussion in this chapter. The general aspects touched on include (a) trends in the reactivities and solubilities of the sulfur-based species as related to their structures and degree of oxidation, (b) classification of the reactions into five characteristic reaction types, and (c) a break-down of the branching at the three most important sets of branching points in the mechanism.

2.1 Species, Structures, and Properties

The important sulfur-containing species involved in the atmospheric DMS cycle are shown in Table 2.1. The valence structures around the central sulfur atoms are also displayed, as are some relevant chemical and physical properties and typical atmospheric concentrations.

Table 2.1: Important Gas-Phase DMS-Related Species and Their Properties

Name	Symbol	Formula	Structure	Ox # [a]	Solubility [b]	Lifetime [c]	Concen [d]	ΔH_f [e]
dimethylsulfide	DMS	CH_3SCH_3	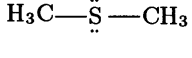	−2	5×10^{-1}	days (c)	10^9	−35.9
dimethylsulfoxide	DMSO	$CH_3S(O)CH_3$	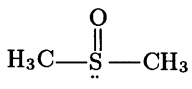	0	$> 5 \times 10^4$	hrs (c+a)	10^7	−145.4
dimethylsulfone	$DMSO_2$	$CH_3S(O)_2CH_3$	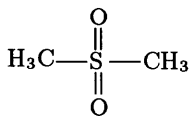	+2	$> 5 \times 10^4$	hrs (a)	10^6	−365.6
methanesulfenic acid	MSEA	CH_3SOH	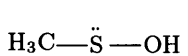	0	?	? hrs (c)	?	−139.4
methanesulfinic acid	MSIA	$CH_3S(O)OH$	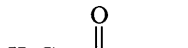	+2	?	? hrs-days (c+a+s)	?	−318.2
methanesulfonic acid	MSA	CH_3SO_3H	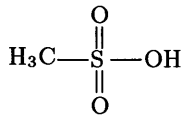	+4	$\sim 10^{12}$	hrs (a)	10^4-10^7	−547.6
sulfur dioxide	—	SO_2	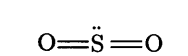	+4	1.4	days (c+a+s)	10^9	−285.9
sulfuric acid	—	H_2SO_4	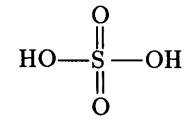	+6	∞	mins-hrs (a)	10^4-10^7	−711.0

[a] Oxidation numbers are given for the central sulfur atom.
[b] Solubilities are given in terms of Henry's law coefficients (M atm^{-1}) at 298 K from Sander (1997).
[c] Approximate atmospheric lifetimes based on the dominant removal process(es) (c = chemistry, a = aerosols, and s = surface). Question marks denote highly uncertain lifetimes.
[d] Typical concentrations (molecules cm^{-3}) in the marine boundary layer. MSEA and MSIA have not been observed in the atmosphere.
[e] Calculated enthalpies of formation (kJ mole^{-1}) at 298 K from Wang and Zhang (2002a).

To understand the variety of structures and properties, first note that neutral sulfur atoms are isoelectronic with neutral oxygen atoms (i.e., they have the same number of outershell electrons). Thus, swapping sulfur atoms for the oxygen atoms in common oxygenated hydrocarbons yields a plausible set of sulfur-containing compounds. As an example, DMS is the sulfur-based analog to dimethylether (CH_3OCH_3). Other examples are illustrated below:

oxygen-containing			sulfur-containing	
alcohol	R–O–H	$\Longleftrightarrow$	thiol	R–S–H
ether	R–O–R′	$\Longleftrightarrow$	sulfide	R–S–R′
peroxide	R–O–O–R′	$\Longleftrightarrow$	disulfide	R–S–S–R′
ketone	R–C(O)–R′	$\Longleftrightarrow$	thioketone	R–C(S)–R′
carboxylic acid	R–C(O)–OH	$\Longleftrightarrow$	dithiocarboxylic acid	R–C(S)–SH

Unlike oxygen atoms, however, sulfur atoms have empty, low-lying $3d$-orbitals. Sulfur atoms use these unfilled orbitals to engage in p-d bonding in a manner similar to π-bonding between p-orbitals. This enables sulfur atoms to expand their valence electron octets, thereby resulting in an enormous extension to the range of feasible structures, oxidation numbers, and properties as compared to the oxygenated hydrocarbons. As illustrated in Table 2.1, $DMSO_2$, MSA, and H_2SO_4 are three common examples of sulfur-based species with expanded valence counts.

Because sulfur atoms can extend their valence structures, their oxidation numbers have a wider range of values than oxygen atoms in oxygenated hydrocarbons. Referring to Table 2.1, these sulfur-based oxidation numbers range from -2 for DMS to $+6$ for H_2SO_4. By comparison, oxygen-containing compounds exhibit an oxidation state of mainly -2, or -1 in peroxides. This wide range of sulfur-based oxidation numbers coincides with important trends in the physical and chemical properties of the DMS-related species.

One trend is associated with chemical reactivity, where the species with lower oxidation numbers are more susceptible to photochemical oxidation than the species with higher oxidation numbers. For example, DMS is the most reduced form of sulfur in the DMS cycle and it is rapidly oxidized by OH radicals during the day and NO_3 radicals at night. H_2SO_4, on the other hand, is highly oxidized and does not undergo additional chemical oxidation. As another example, MSEA has a lower oxidation number and higher chemical reactivity than MSIA and MSA. This trend in reactivity occurs for two reasons, depending upon the type of reaction. Addition-type reactions can only occur to sulfur atoms with unsaturated valences, and so DMS is more likely to react than $DMSO_2$ by way of addition. Second, sulfur atoms with higher oxidation numbers are less able to stabilize, through resonance, the excess electron

density resulting from abstraction-type reactions. Considering the scission of O–H bonds in $CH_3S(O)_xO$–H, for instance, the sulfur atom in MSEA accommodates the unpaired electron more easily than the sulfur atom in MSA. This is nicely reflected in the calculated O–H bond strengths of 299, 340, and 471 kJ mole^{-1} for MSEA, MSIA, and MSA, respectively (Wang and Zhang, 2002a).

The wide range of sulfur-based oxidation numbers also has a connection to the solubility properties of the DMS-related species. Solubilities play a role in the uptake of oxidized sulfur-containing compounds into cloud droplets and on aerosols, which are dominant sinks for many of the species. As shown in Table 2.1, species with larger oxidation numbers also have higher Henry's law coefficients. To understand this solubility trend, it is useful to consider the polarities of the compounds because polar molecules are more soluble in aqueous solutions than non-polar molecules. Carbon, sulfur, and oxygen atoms have electronegativities of 2.55, 2.58, and 3.44, respectively, on Pauling's electronegativity scale. This implies that S–C bonds are largely non-polar, while S–O bonds are highly polarized. As a result, DMS is only moderately soluble because it is comprised of S–C bonds. MSA and H_2SO_4, on the other hand, have multiple S–O bonds, so they are highly polarized and immensely soluble. On a related note, the highly oxidized species H_2SO_4 also has an extremely low vapor pressure, which allows it to nucleate with water vapor to form new aerosols under certain atmospheric conditions.[1]

The chemical reactivities and efficiency of heterogeneous removal dictate the atmospheric lifetimes of the gas-phase sulfur-based species. The reduced or mildly oxidized species DMS and MSEA have significant photochemical sinks and negligible heterogeneous losses. These species are mainly controlled by their reaction with OH, resulting in lifetimes of hours (for MSEA) to days (for DMS). At the high oxidation limit are the species $DMSO_2$, MSA, and H_2SO_4, which have large heterogeneous removal sinks and virtually no photochemical losses. These species have atmospheric lifetimes of minutes to hours, which is essentially due to their uptake by aerosols and cloud droplets. Between these two limits, the intermediate species DMSO, MSIA, and SO_2 depend on a combination of photochemical loss and heterogeneous removal, which leads to lifetimes in the range of hours to days.

Finally, it is useful to point out the structural similarities and differences between the species in Table 2.1. Referring to their structures, DMS, DMSO, and $DMSO_2$ are similar and form a group called $DMSO_x$. Additionally, MSEA, MSIA, and MSA are similar and form a group called $CH_3S(O)_xOH$. These two groups differ from each other only by the attachments

[1]The vapor pressure for H_2SO_4 over ammonium sulfate at 298 K is $\sim 5\times10^{-11}$ Pa (Marti et al., 1997).

to the central sulfur atom. The $DMSO_x$ species contain two methyl substituents ($-CH_3$), while the $CH_3S(O)_xOH$ species have one hydroxyl (–OH) and one methyl. Though this difference may seem small, it greatly affects their chemical reactivities, as addressed in the next section. Another group of species worth mentioning, but not displayed in Table 2.1, are the methyl sulfoxyl radicals. These species are denoted by $CH_3S(O)_x$ for $x = 1 - 3$, and are similar to MSEA, MSIA, and MSA, but with the hydroxyl hydrogens removed. As shown in Figure 2-1, the methyl sulfoxyl radicals are important intermediates along the H-abstraction branch.

2.2 Characteristic Reactions

The DMS oxidation mechanism in Figure 2-1 displays a dizzying array of chemical reactions. By classifying these reactions according to their general characteristics, however, a simplified picture of DMS oxidation emerges. This classification is based on the premise that species with similar structures undergo similar chemical transformations. For example, DMS and DMSO both belong to the $DMSO_x$-group and both react by way of OH addition. The reactions are classified into the following five categories: abstraction, addition, oxidation, dissociation, and isomerization.

Classifying the reactions in the mechanism in this manner has two important uses. First, instead of memorizing the numerous reactions in the scheme, it can be navigated just by knowing the general types of reactions that occur for a particular species. Second, if any deficiencies in the oxidation scheme are found, they may be filled in by using analogous reactions as a first guess. For instance, reactions that are important for MSEA may also apply for MSIA. The procedure of using analogous reactions is implemented in Chapter 4 to predict missing MSA production routes.

During the following discussion it is also important to keep in mind that many of the rates of the DMS oxidation reactions have not been directly measured in the laboratory. They are, instead, mainly inferred from thermochemical and kinetic arguments and observed end-products.[2] The large gaps in the kinetic information are due, primarily, to the fleeting nature of the intermediates. Quantum chemical computations are beginning to fill in some of these gaps (Kukui et al., 2000; Wang and Zhang, 2001, 2002b), but there is still a long way to go. Of the DMS oxidation reactions shown in Figure 2-1, less than half have rate constants based on

[2]Many reaction rates were estimated by Yin et al. (1990b) using bond strengths and analogous reactions. Also, Urbanski et al. (1998) detected CH_3 radicals as end products from the reaction between DMSO and OH, which suggests the formation of MSIA.

Table 2.2: DMS Oxidation Reactions With Measured Rate Constants

Reaction	Rate Constant	Reference
$CH_3SCH_3 + OH \rightarrow CH_3SCH_2 + H_2O$	$1.2 \times 10^{-11} \exp(-260/T)$	DeMore et al. (1997)
$CH_3SCH_3 + NO_3 \rightarrow CH_3SCH_2 + HNO_3$	$1.9 \times 10^{-13} \exp(500/T)$	DeMore et al. (1997)
$CH_3SCH_3 + OH \rightarrow CH_3S(OH)CH_3$	k_f	Atkinson et al. (1997)
$CH_3S(OH)CH_3 \rightarrow CH_3SCH_3 + OH$	k_r	Barone et al. (1996)
$CH_3S(OH)CH_3 + O_2 \rightarrow CH_3S(O)CH_3 + HO_2$	5×10^{-13}	Turnipseed et al. (1996)
$CH_3S(O)CH_3 + OH \rightarrow CH_3S(O)(OH)CH_3$	$6.3 \times 10^{-12} \exp(800/T)$	Hynes and Wine (1996)
$CH_3S(O)(OH)CH_3 \rightarrow CH_3S(O)OH + CH_3$	2×10^{6}	Urbanski et al. (1998)
$CH_3SCH_2 + O_2 \rightarrow CH_3SCH_2OO$	5.7×10^{-12}	DeMore et al. (1997)
$CH_3SCH_2OO + NO \rightarrow CH_3SCH_2O + NO_2$	$7.9 \times 10^{-12} \exp(128/T)$	Turnipseed et al. (1996)
$CH_3SCH_2O \rightarrow CH_3S + CH_2O$	3.3×10^{4}	Turnipseed et al. (1996)
$CH_3S + NO_2 \rightarrow CH_3SO + NO$	$2.1 \times 10^{-11} \exp(320/T)$	DeMore et al. (1997)
$CH_3S + O_3 \rightarrow CH_3SO + O_2$	$2.0 \times 10^{-12} \exp(290/T)$	DeMore et al. (1997)
$CH_3S + O_2 \rightarrow CH_3SOO$	$1.4 \times 10^{-16} \exp(1550/T)$	Atkinson et al. (1997)
$CH_3SOO \rightarrow CH_3S + O_2$	$1.5 \times 10^{11} \exp(-3910/T)$	Atkinson et al. (1997)
$CH_3SOO + NO \rightarrow CH_3SO + NO_2$	1.1×10^{-11}	DeMore et al. (1997)
$CH_3SOO + NO_2 \rightarrow CH_3SOONO_2$	2.2×10^{-11}	Atkinson et al. (1997)
$CH_3SO + NO_2 \rightarrow CH_3SO_2 + NO$	1.2×10^{-11}	DeMore et al. (1997)
$CH_3SO + O_3 \rightarrow CH_3SO_2 + O_2$	6.0×10^{-13}	DeMore et al. (1997)
$CH_3SO_2 + NO_2 \rightarrow CH_3SO_3 + NO$	2.2×10^{-12}	Ray et al. (1996)
$CH_3SO_2 \rightarrow CH_3 + SO_2$	$k_{CH_3SO_2}$	Kukui et al. (2000)
$SO_2 + OH \rightarrow HOSO_2$	k_{SO_2+OH}	DeMore et al. (1997)
$HOSO_2 + O_2 \rightarrow SO_3 + HO_2$	$1.3 \times 10^{-12} \exp(-330/T)$	DeMore et al. (1997)
$SO_3 + H_2O \rightarrow H_2SO_4$	$k_{SO_3+H_2O}$	Lovejoy et al. (1996)

First- and second-order rate constants have units of s^{-1} and cm^3 molecule^{-1} s^{-1}, respectively, and temperature has units of K. Refer to the cited references and Table 4.1 in Chapter 4 for further information.

measurements. The reactions with known rate constants are shown in Table 2.2. The values for the remaining, non-measured rate constants are cited as they are used throughout this thesis, where they are mainly taken from previous references, though some are also estimated here.

2.2.1 Abstraction

Reactions that abstract hydrogen are an integral part of the DMS oxidation mechanism. In fact, the initial abstraction of hydrogen from CH_3SCH_3 by OH is one of the most important reactions in the whole oxidation sequence. H-atom abstractions are not the dominant reactions, however,

because the potential for sulfur atoms to expand their valence structures allows addition-type reactions to effectively compete with abstraction.

Two classes of H-atom abstraction reactions occur in the DMS mechanism. The first class involves the abstraction of hydrogen from methyl substituents ($-CH_3$). The only significant reactions of this type occur for CH_3SCH_3, where the methyl-based hydrogen is abstracted primarily by OH radicals during the day and by NO_3 radicals at night, as shown by:

$$CH_3SCH_3 + OH \rightarrow CH_3SCH_2 + H_2O \quad (2.1)$$

$$CH_3SCH_3 + NO_3 \rightarrow CH_3SCH_2 + HNO_3 \quad (2.2)$$

These reactions initiate the oxidation of DMS along the so-called *H-abstraction path* that eventually leads to SO_2 and H_2SO_4. This abstraction pathway is thoroughly described in the following section on important mechanism branches.

The second class of abstraction involves the removal of hydrogen from hydroxyl substituents ($-OH$). By far, this class of reactions is the predominant form of H-atom abstraction throughout the DMS scheme. The two most common examples of this type of abstraction are

$$CH_3S(O)_x(OH)CH_3 + O_2 \rightarrow CH_3S(O)_{x+1}CH_3 + HO_2 \quad (2.3)$$

$$CH_3S(O)_xOH + OH \rightarrow CH_3S(O)_xO + H_2O \quad (2.4)$$

where $x = 0$ and 1 in both cases. Reaction 2.3 involves the abstraction of hydrogen from the $DMSO_x$-related species by O_2, while reaction 2.4 illustrates the hydrogen-donating nature of the methane sulfur-based acids. Regarding reaction 2.4, the hydrogen is abstracted from $-OH$, not $-CH_3$, because the central sulfur atom readily accepts the excess electron density from the oxygen atom. This acts to stabilize the resulting radical through delocalization, which, in effect, makes the O–H bond weaker than the C–H bond. Another extremely important example of reaction 2.3 occurs through the oxidation of SO_2 to SO_3, which contributes to new particle production in the atmosphere. A reaction similar to reaction 2.3 is also postulated to play a role in oxidizing MSIA to MSA, as described in Chapter 4.

2.2.2 Addition

Addition reactions in the DMS mechanism fall into two broad categories, depending upon where the addition takes place. The first type involves electrophilic addition to the electron-rich sulfur centers, which results from the unique valence properties of sulfur atoms. Two

different electrophiles add to the sulfur centers. Hydroxyl radicals add to electroneutral sulfur-bearing molecules such as DMS and DMSO, while molecular oxygen adds to the methyl sulfoxyl radicals $CH_3S(O)_x$. These two additions are shown by

$$CH_3S(O)_xCH_3 + OH \rightleftharpoons CH_3S(O)_x(OH)CH_3 \quad (2.5)$$

$$CH_3S(O)_x + O_2 \rightleftharpoons CH_3S(O)_xOO \quad (2.6)$$

where $x = 0$ and 1 in reaction 2.5, and $x = 0 - 2$ in reaction 2.6. Both additions are shown as reversible reactions because the addition adducts are unstable and quickly fall apart unless they are collisionally-stabilized or rapidly undergo further reaction. The addition adducts produced in reaction 2.5 serve as a branching point between the formation of $DMSO_x$ and $CH_3S(O)_xOH$. Moreover, the OH-addition in reaction 2.5 is also known to occur for SO_2 and possibly MSIA. Case $x = 1$ in reaction 2.6 is important because it may enhance the production of H_2SO_4 through a channel not involving SO_2.

The second type of addition involves reactions similar to the reactions that form peroxy and nitrate radicals in the atmospheric chemistry of hydrocarbons. These are shown by

$$CH_3SCH_2 + O_2 \rightarrow CH_3SCH_2OO \quad (2.7)$$

$$CH_3S(O)_xOO + NO_2 \rightleftharpoons CH_3S(O)_xOONO_2 \quad (2.8)$$

where $x = 0 - 2$ in reaction 2.8. The peroxy radical produced in reaction 2.7 is similar to the alkyl peroxy radicals (RO_2) formed during the oxidation of hydrocarbons. It is, however, the only alkyl-type peroxy radical in the mechanism, because CH_3SCH_3 is the only species that undergoes efficient methyl-based H-abstraction. The sulfur-containing peroxynitrates produced from reaction 2.8 are similar to peroxyacetyl nitrate ($CH_3C(O)OONO_2$, PAN) formed during the oxidation of acetaldehyde in the presence of NO_2. As with PAN, the sulfur-bearing peroxynitrates are stable and amenable to long-distance transport. Given the typically low mixing ratios of NO_2 in the remote atmosphere, however, the influence of the sulfur peroxynitrates in the DMS oxidation cycle is yet to be demonstrated.

2.2.3 Oxidation

There are two primary modes of oxidation operating in the DMS mechanism, where oxidation is defined by adding an oxygen atom to the sulfur compounds. Both modes increase the oxidation number on the central sulfur atom by 2, but one method is direct, while the other is indirect.

The direct oxidation involves the reaction between the methyl sulfoxyl radicals $CH_3S(O)_x$ and an oxidizing species. This reaction is shown below for O_3 and NO_2.

$$CH_3S(O)_x + \begin{bmatrix} O_3 \\ NO_2 \end{bmatrix} \rightarrow CH_3S(O)_{x+1} + \begin{bmatrix} O_2 \\ NO \end{bmatrix} \tag{2.9}$$

Other species such as RO_2 or NO_3 can also oxidize $CH_3S(O)_x$, but O_3 and NO_2 are the most efficient oxidants considering their concentrations and the reaction rate constants. Reaction 2.9 plays an important role in the branching between the production of SO_2, H_2SO_4 and MSA, as discussed in a later section.

The indirect oxidation method involves a sequence of two reactions that, when added together, have the net result of attaching an oxygen atom to the sulfur atom. Two such indirect schemes occur in the mechanism, as shown below.

$$-S(O)_x- + OH \rightarrow -S(O)_x(OH)- \xrightarrow{O_2} -S(O)_{x+1}- + HO_2 \tag{2.10}$$

$$CH_3S(O)_x + O_2 \rightleftharpoons CH_3S(O)_xOO \xrightarrow{NO} CH_3S(O)_{x+1} + NO_2 \tag{2.11}$$

Scheme 2.10 oxidizes sulfur through a combination of OH-addition and H-abstraction (reactions 2.5 + 2.3). This very important scheme oxidizes DMS to DMSO, DMSO to $DMSO_2$, and SO_2 to SO_3. This scheme is also postulated to play a role in oxidizing MSIA to MSA (see Chapter 4). Scheme 2.11 is a two-step oxidation process that first involves the formation of the sulfoxylperoxy radicals through addition reaction 2.6, which is followed by the removal of an oxygen atom by NO. Scheme 2.11 provides an alternate path (i.e., in lieu of scheme 2.9) for oxidizing the methyl sulfoxyl radicals.

It is interesting to note that, considering the large reservoir of O_2 in the atmosphere, reactions 2.9 and 2.11 together form a 'catalytic cycle' whereby two $CH_3S(O)_x$ radicals are oxidized and NO_x is conserved. This cycle is summarized below:

$$\begin{aligned} CH_3S(O)_x + NO_2 &\rightarrow CH_3S(O)_{x+1} + NO \\ CH_3S(O)_x &\xrightarrow{O_2} CH_3S(O)_xOO \\ \underline{CH_3S(O)_xOO + NO &\rightarrow CH_3S(O)_{x+1} + NO_2} \\ \text{net: } 2\ CH_3S(O)_x &\xrightarrow{O_2} 2\ CH_3S(O)_{x+1} \end{aligned} \tag{2.12}$$

As cycle 2.12 implies, even the low levels of NO_x typical in the remote marine atmosphere may be effective oxidants in the DMS cycle. Furthermore, the $x = 2$ case may influence the

branching between SO_2, H_2SO_4, and MSA.

2.2.4 Dissociation

There are only a few dissociation reactions in the mechanism, but they impact the branching at two key areas. These dissociation reactions are summarized by

$$CH_3S(O)_x(OH)CH_3 \rightarrow CH_3S(O)_xOH + CH_3 \quad (2.13)$$

$$CH_3S(O)_x \rightarrow CH_3 + SO_x \quad (2.14)$$

where $x = 0$ and 1 in reaction 2.13, and $x = 2$ and 3 in reaction 2.14. In both cases, the reactant is severed at the S–C bond, thus liberating a sulfur-bearing species and a methyl radical. Reaction 2.13 produces MSEA and MSIA, and competes with the production of DMSO and $DMSO_2$ through reaction 2.3. Reaction 2.13, therefore, provides a means of cross-over from the OH-addition path to the H-abstraction path as shown in Figure 2-1. Recent quantum chemical calculations suggest that the dissociation barriers are large and small for $x = 0$ and 1, respectively, in reaction 2.13 (Wang and Zhang, 2001, 2002b). In reaction 2.14, the dissociation of CH_3SO_x leads to SO_x, and competes with the oxidation of CH_3SO_x in reactions 2.9 and 2.11. Hence, reaction 2.14 creates a branching between MSA production and SO_2 and H_2SO_4 production. It is also important to point out that $x = 2$ in reaction 2.14 provides the only known, efficient production route of SO_2 from DMS, so extensive effort has gone into elucidating the rate of this dissociation.

2.2.5 Isomerization

The following isomerization reactions are speculative, but they may potentially impact DMS chemistry in a profound way.

$$CH_3S(O)_xOO \rightarrow CH_3S(O)_{x+2} \quad (2.15)$$

$$CH_3S(OH)OO \rightarrow CH_3SO_3H \quad (2.16)$$

Note that $x = 0$ and 1 in reaction 2.15. These isomerizations start from sulfur-centered peroxy-type radicals that have unpaired electrons on the outer oxygen atom. The sulfur atom in the reactant in 2.16 also has an unpaired electron. The rearrangements and unpaired electrons for these isomerizations are illustrated in Figure 2-2. These isomerizations are thermodynamically

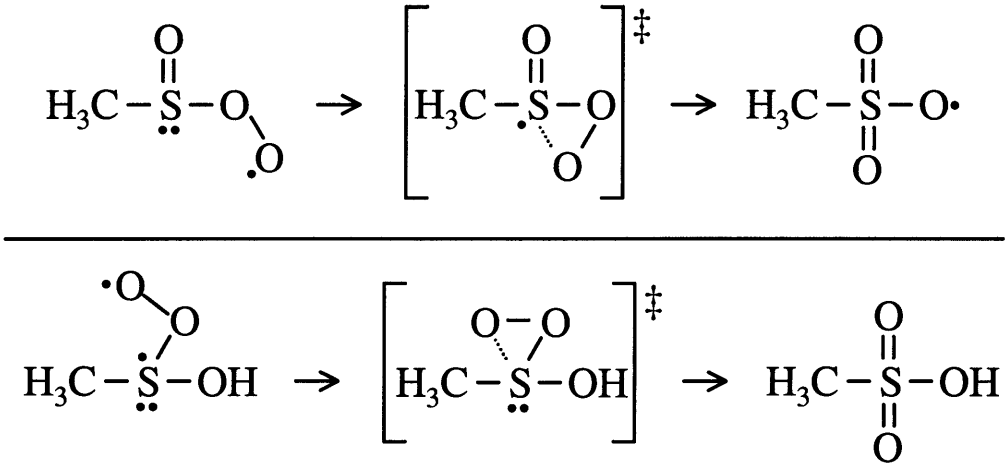

Figure 2-2: Examples of the rearrangements occuring in isomerization reactions 2.15 (upper) and 2.16 (lower). The unpaired electrons are explicitly shown and the transition states are denoted by the square brackets with ‡.

favored due to stability of the products relative to the reactants.[3] Kinetically, however, they have large activation energies associated with the three-member rings. To compensate for the large barriers, the reactants in 2.15 are likely present in sufficiently large concentrations because they are formed through O_2 addition. Note that the rate of the $x = 0$ case in reaction 2.15 has been measured in the aqueous-phase (Zhang et al., 1994), and an upper-limit has been set for the gas-phase (Turnipseed et al., 1993). Reaction 2.16 is invoked as an intermediate step in a reaction first suggested by Hatakeyama and Akimoto (1983) that forms MSA directly from MSEA and O_2 in one step. Regarding their impacts, both isomerizations affect the production of MSA, while reaction 2.15 may also allow for significant production of H_2SO_4 through a channel that bypasses SO_2.

2.3 Important Mechanism Branches

One of the most important questions surrounding the atmospheric chemistry of DMS relates to the final distribution of oxidized sulfur-based products under various atmospheric conditions. Confounding this problem are the many branches in the DMS mechanism, as shown in Figure

[3]For example, the $x = 0$ case in reaction 2.15 has an enthalpy change of -314 kJ mol^{-1} at 298 K (DeMore et al., 1997).

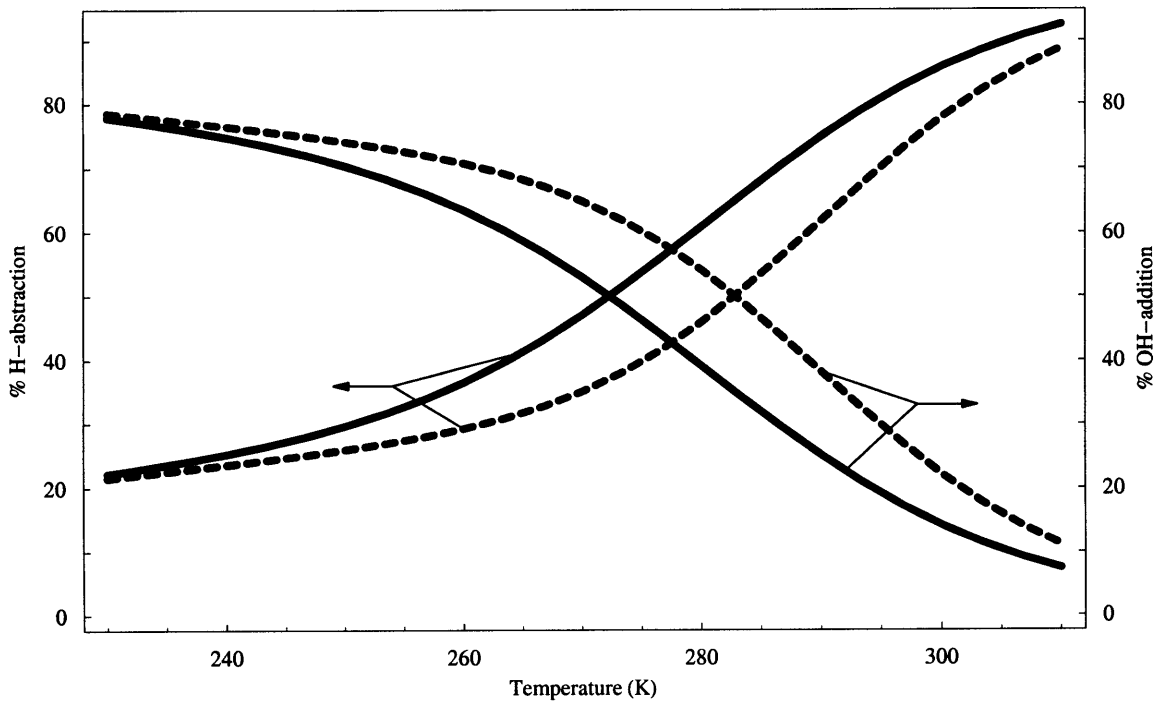

Figure 2-3: The temperature dependence of the branching for the oxidation of DMS by OH. The figure shows the percentage of the net rate through the H-abstraction and OH-addition channels. The solid lines include the reverse OH-addition reaction, the dashed lines do not. The branching ratio is independent of the concentrations of DMS and OH, and dependent only on temperature and pressure (fixed at 1013.25 hPa). The calculations assume the DMS-OH adduct is in steady-state, balanced between production from DMS+OH and destruction from dissociation and reaction with O_2.

2-1, and the large temperature-dependencies at many of the branching points. In spite of these complexities, the general partitioning between $DMSO_x$, $CH_3S(O)_xOH$, and SO_2 and H_2SO_4 can be understood in terms of three different sets of branching points. These three sets of branching points are discussed below, along with the known effects of temperature and pressure at these points.

2.3.1 DMS+OH: H-Abstraction Versus OH-Addition

The initial reaction between DMS and OH is one of the most important branching points in the DMS mechanism. At this point, the reaction can proceed through either a hydrogen abstraction path (reaction 2.1) or the reversible addition of OH to the sulfur atom ($x = 0$ in reaction 2.5).

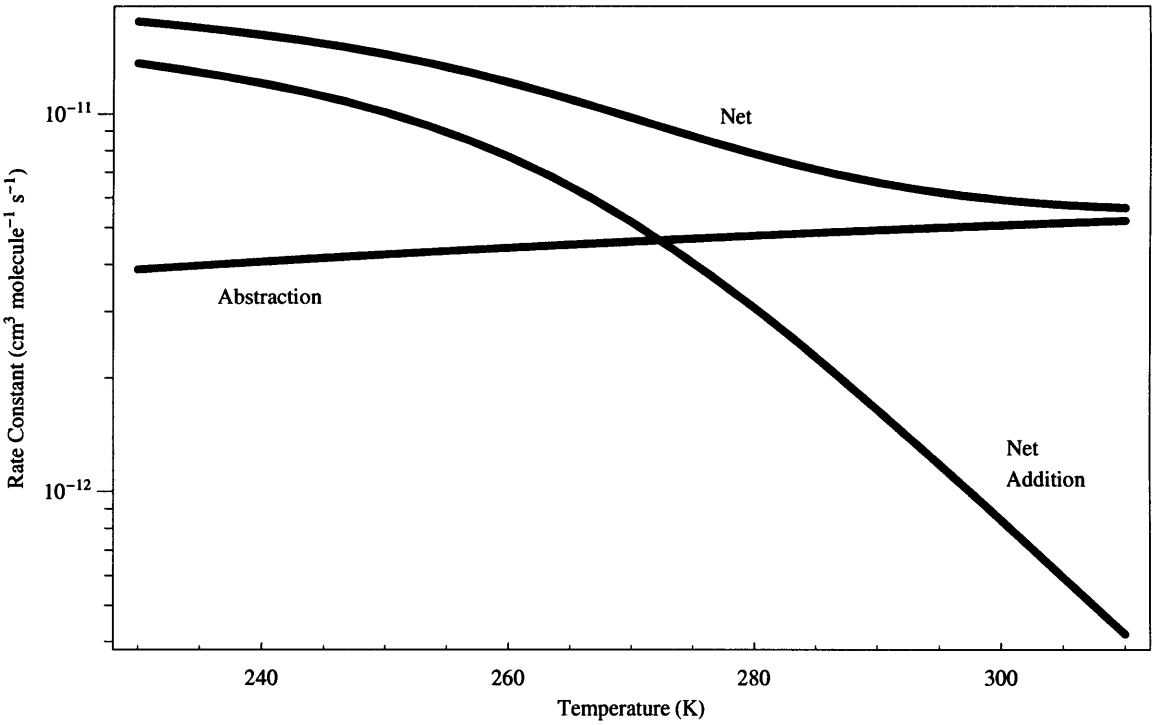

Figure 2-4: The temperature dependence of the rate constants for the oxidation of DMS by OH. The figure shows the abstraction, net addition, and net rate constants. The net addition rate constant accounts for the reverse DMS+OH addition reaction as was done for Figure 2-3.

This branching point is summarized below.

$$CH_3SCH_3 + OH \begin{cases} \rightarrow & CH_3SCH_2 + H_2O & \text{H-abstraction} \\ \rightleftharpoons & CH_3S(OH)CH_3 & \text{OH-addition} \end{cases} \quad (2.17)$$

The H-abstraction and OH-addition channels are also know as the O_2-independent and O_2-dependent channels, respectively, because the adduct formed through OH-addition requires the presence of O_2 for collisional stabilization and further reaction. Otherwise, the DMS-OH adduct quickly dissociates and reforms DMS and OH. This branching point is crucial because the final product yields depend, to a large degree, on the partitioning between the OH-addition and H-abstraction pathways. Recall that $DMSO_x$, MSEA, and MSIA are the major products along the OH-addition path, while SO_2 and H_2SO_4 are primarily formed through the OH-abstraction path. MSA, on the other hand, is believed to be formed from a combination of the H-abstraction and OH-addition paths.

The branching between H-abstraction and OH-addition is also highly temperature dependent. The H-abstraction reaction has a positive activation energy, and hence a rate constant that increases with temperature. The OH-addition reaction, however, has a negative activation energy due to the thermally unstable DMS-OH adduct. The rate constant for OH-addition, therefore, decreases with increasing temperature. Figure 2-3 illustrates this effect, whereby the OH-addition path is favored at low temperatures and the H-abstraction path is dominant at high temperatures. The difference between the solid and dashed lines in Figure 2-3 also shows the influence of the reverse OH-addition path, which can affect the rates by more than 10%. Including the reverse OH-addition path, the rates through the two branches are equal at approximately 272 K.

On the basis of the previous discussion, the yields of SO_2 and H_2SO_4 are expected to increase with temperature because they are formed through the H-abstraction branch. Moreover, the yields of DMSO, $DMSO_2$, MSEA, and MSIA are expected decrease with temperature because they are formed through OH-addition. These two trends do not imply that the rate of DMS oxidation is greater at higher temperatures because the net oxidation rate depends on the sum of the H-abstraction and OH-addition rates, which have temperature dependencies that are not offsetting. As clearly shown in Figure 2-4, the net rate constant for DMS oxidation actually falls with temperature because the negative temperature dependence of OH-addition is stronger than the positive temperature dependence of H-abstraction. This means that, for equal DMS fluxes and OH concentrations, warmer/tropical regions should have higher levels of DMS than cooler/temperate regions.

2.3.2 $CH_3S(O)_x(OH)CH_3$: H-Abstraction Versus Dissociation

Before dissociating back into reactants, the addition adduct $CH_3S(O)_x(OH)CH_3$ formed from reaction 2.5 can further react to form two different products. $DMSO_{x+1}$ is formed if the addition adduct reacts by way of H-abstraction (reaction 2.3); $CH_3S(O)_xOH$ is formed if the adduct undergoes a methyl dissociation (reaction 2.13). The $CH_3S(O)_x(OH)CH_3$ adducts, therefore, serve as points for branching between DMSO versus MSEA and $DMSO_2$ versus MSIA. This branching is summarized below, where $x = 0$ and 1.

$$CH_3S(O)_x(OH)CH_3 \begin{cases} \xrightarrow{O_2} & CH_3S(O)_{x+1}CH_3 + HO_2 & \text{DMSO and } DMSO_2 \\ \rightarrow & CH_3S(O)_xOH + CH_3 & \text{MSEA and MSIA} \end{cases} \quad (2.18)$$

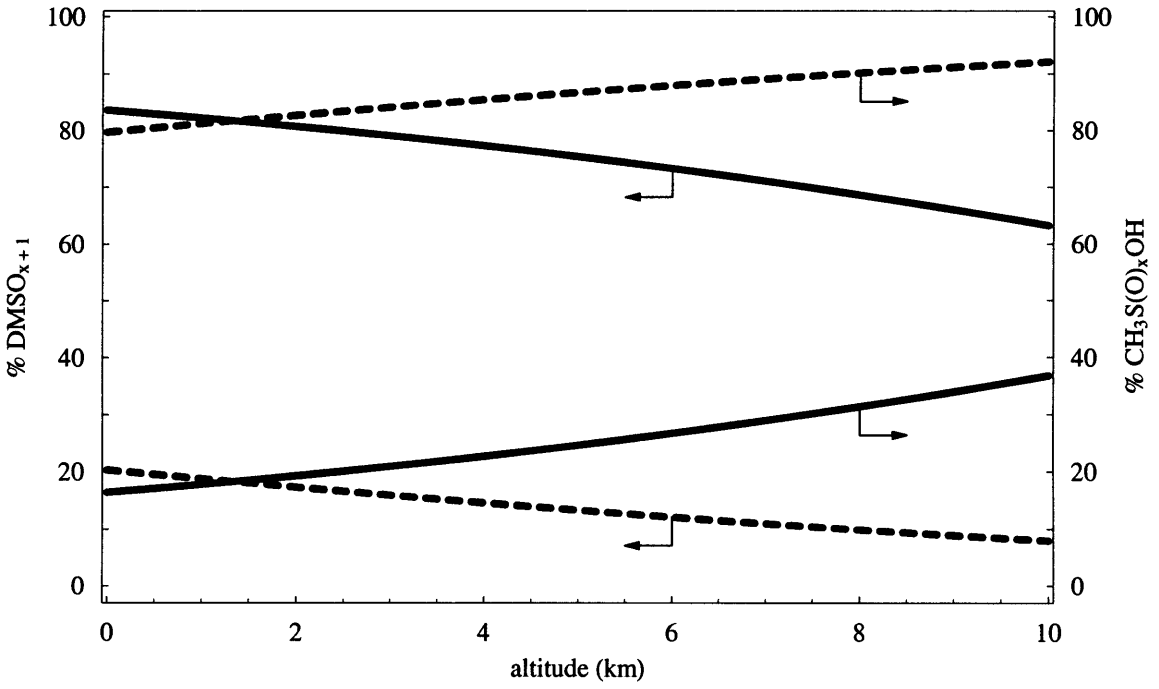

Figure 2-5: The pressure dependence of the branching between the production of $DMSO_{x+1}$ versus $CH_3S(O)_xOH$. The small arrows point to the respective scale and the solid and dashed lines are for the $x = 0$ and 1 cases, respectively. The branching ratio is independent of the concentrations of $DMSO_{x+1}$ and $CH_3S(O)_xOH$, and dependent only on pressure. These calculations use the pressure profile from the U.S. Standard Atmosphere. Refer to Table 4.1 in Chapter 4 for the rate constants used to calculate the branching.

These branching points important because $DMSO_x$ and $CH_3S(O)_xOH$ have unique interactions with aerosols. They are also important because of the reactivity of $CH_3S(O)_xOH$. As previously discussed, the methyl sulfur-based acids easily lose their hydroxyl hydrogen through reaction 2.4, thereby producing the methyl sulfoxyl radicals $CH_3S(O)_x$ that play an important role in SO_2 and H_2SO_4 production. Branch 2.18, therefore, provides a means of cross-over from OH-addition to H-abstraction.

The dissociation portion in branch 2.18 is most likely temperature dependent, having a higher rate constant at higher temperatures. The temperature dependencies of these pathways, however, are not presently known, though an initial quantum mechanical estimate for the dissociation barrier leading to MSIA is 17 kJ $mole^{-1}$ at 0 K (Wang and Zhang, 2002b). In spite of the unknown temperature dependencies, the reaction with molecular oxygen in reaction 2.18

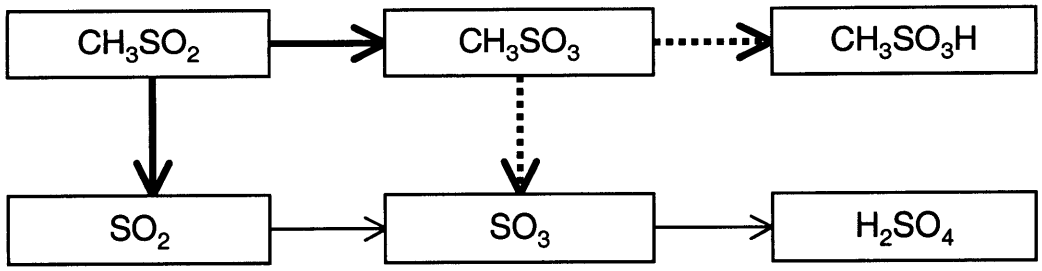

Figure 2-6: Branching of the CH_3SO_x radicals. The thick solid and dashed arrows display the branching for CH_3SO_2 and CH_3SO_3, respectively. The thin solid arrows show the paths leading from SO_2 to H_2SO_4.

does impart a known pressure dependency, which is examined in Figure 2-5. As expected, the relative rates of DMSO and $DMSO_2$ production are largest at the lowest altitudes (i.e., the highest O_2 concentrations). Another important feature is that DMSO is more abundant than MSEA, while $DMSO_2$ is only a minor product relative to MSIA. Furthermore, $DMSO_2$ and MSIA are more dependent on pressure than DMSO and MSEA. Both of these features are due to the smaller rate constant for methyl dissociation from $CH_3S(OH)CH_3$ than from $CH_3S(O)(OH)CH_3$. Though these branching results hinge on the estimated values for two of the four rate constants involved in the calculations, the preponderance of DMSO and MSIA over MSEA and $DMSO_2$ is substantiated in recent calculations (Wang and Zhang, 2001, 2002b).

2.3.3 CH_3SO_x: Oxidation Versus Dissociation

Another critical set of branching points occurs at the methyl sulfoxyl radicals CH_3SO_x. These radicals either dissociate into CH_3 and SO_x, or are oxidized to CH_3SO_{x+1}. The branching points are summarized below and shown schematically in Figure 2-6.

$$CH_3SO_x \begin{cases} \rightarrow & CH_3SO_{x+1} & \text{MSA} \\ \rightarrow & CH_3 + SO_x & SO_2 \text{ and } H_2SO_4 \end{cases} \tag{2.19}$$

Branch 2.19 impacts the formation of SO_2, H_2SO_4, and MSA because the dissociation path leads to SO_2 and H_2SO_4, while the oxidation path leads to MSA.

The CH_3SO_2 radical in branch 2.19 is especially important because the dissociation portion is the only efficient SO_2 production pathway known in the DMS mechanism. CH_3SO_2 dissoci-

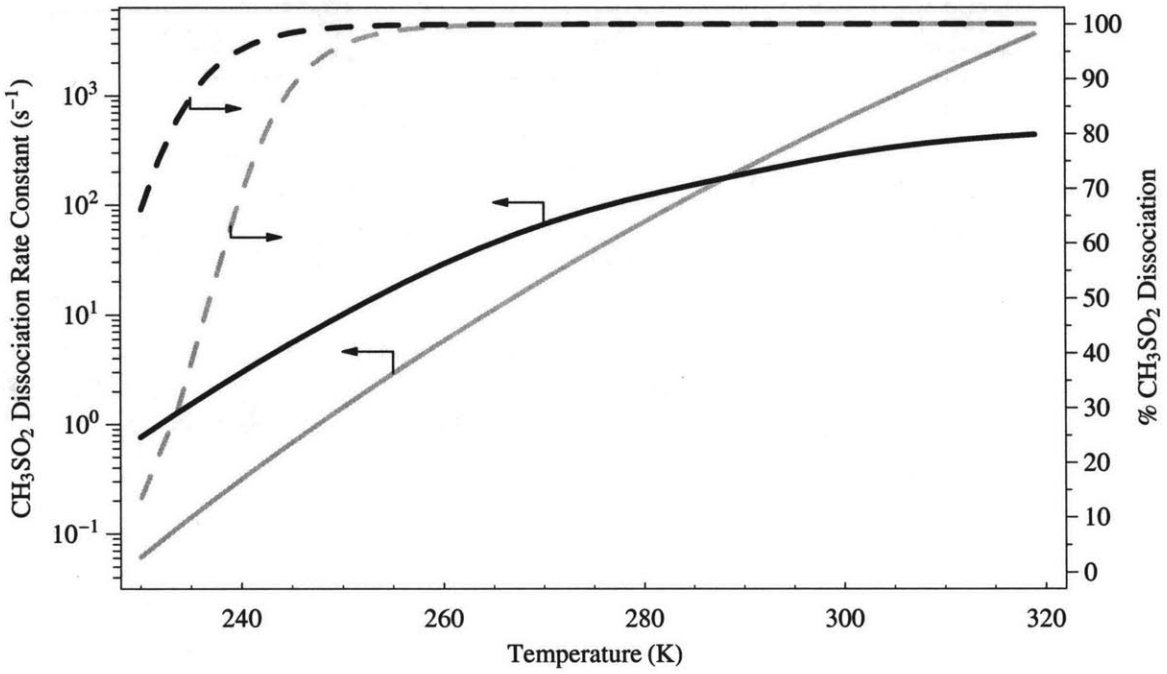

Figure 2-7: CH_3SO_2 dissociation rate constant and branching yield as a function of temperature. The solid and dashed lines correspond to the rate constant (left axis) and relative yield of dissociation (right axis), respectively. The black and gray curves use the dissociation rate constants of Kukui et al. (2000) and Ray et al. (1996), respectively. The relative yield of dissociation accounts for the loss of CH_3SO_2 with NO_2, O_3, and O_2 (reversible) at a fixed pressure of 1013.25 hPa and for typical concentrations for the remote marine boundary layer.

ation is believed to be highly sensitive to temperature, with a dissociation rate constant that increases dramatically with temperature. This temperature dependence has been suggested as a possible explanation for the observed trends of the ratio of nss-SO_4^{2-} to MS^- (see Q5 in Chapter 1) because lower and higher temperatures favor MSA and H_2SO_4, respectively.

Given the importance of the branching at CH_3SO_2, many studies have sought to determine the various rate constants at this branching point. Two recent evaluations of the CH_3SO_2 dissociation rate constant are shown in Figure 2-7 as a function of temperature. Notice that these two evaluations are similar near 300 K where the measurements were made, but rapidly diverge away from this temperature. The evaluation from Ray et al. (1996) does not include pressure effects and has an extremely large temperature-dependence based on a relatively old estimate for the activation energy. Kukui et al. (2000) re-evaluated the temperature and pres-

sure dependence using modern quantum chemical calculations, which yielded good agreement with their lab-based measurements. The Kukui et al. (2000) estimate, thus, is an improvement over the Ray et al. (1996) value.

In spite of the large difference between the two CH_3SO_2 dissociation rate constants, the branching through the dissociation channel using either of the rate constants dominates all of the other CH_3SO_2 loss channels (i.e., the reactions with O_3, NO_2, and O_2). This is shown in Figure 2-7 as the percentage of the net loss rate through the dissociation channel for typical atmospheric conditions. Above temperatures of 250 K, the dissociation channel accounts for practically all of the loss of CH_3SO_2. This implies that, for typical tropospheric conditions, a large majority of the DMS oxidized by H-abstraction winds up as SO_2. This also implies that very little MSA is formed through the H-abstraction channel because CH_3SO_3 dissociation also presumably dominates CH_3SO_3 oxidation.

The CH_3SO_3 radical in branch 2.19 is also important to characterize because it can lead to H_2SO_4 through a pathway not involving SO_2 (see Figure 2-6). In this path, CH_3SO_2 is first oxidized to CH_3SO_3, which then dissociates into SO_3. Thereafter, the SO_3 reacts rapidly with H_2O to form gas-phase H_2SO_4. The potential importance of the CH_3SO_3-SO_3-H_2SO_4 pathway was initially suggested by Bandy et al. (1992) and is still under debate (Saltelli and Hjorth, 1995; Lucas and Prinn, 2002). According to the discussion in the previous paragraph, this pathway appears to be ineffective because the formation of CH_3SO_3 from CH_3SO_2 is a minor channel. There is, however, another possibility. CH_3SO_3 may also be formed through the isomerization of $CH_3S(O)OO$ (reaction 2.15), which bypasses CH_3SO_2 altogether. Either way, if CH_3SO_3 is efficiently produced, then the CH_3SO_3-SO_3-H_2SO_4 pathway has two important consequences. First, SO_2 has an atmospheric lifetime on the order of days (see Table 2.1), which means that atmospheric transport of SO_2 affects the nucleation of H_2SO_4-based aerosols. The precursors of CH_3SO_3, on the other hand, react rather rapidly and are not significantly transported. This means that fresh H_2SO_4-based particles produced through CH_3SO_3 will have a signature more related to DMS. Second, SO_2 is removed by aerosols and cloud droplets, while DMS is not. So, an air parcel heavily laden with DMS and ambient aerosols will suppress nucleation through the SO_2-H_2SO_4 branch, but can still serve as a source of freshly nucleated particles through the CH_3SO_3-SO_3-H_2SO_4 path. The potential importance of the CH_3SO_3-SO_3-H_2SO_4 pathway is ascertained in Chapter 4.

Chapter 3

Sensitivities and Uncertainties in the Remote Marine Boundary Layer

3.1 Introduction

Dimethylsulfide (CH_3SCH_3, DMS) is biologically produced in ocean surface waters as a metabolic by-product from various phytoplankton species (Keller et al., 1989). This oceanic source creates large DMS concentrations in sea surface waters relative to those in the atmosphere over much of the globe (Bates et al., 1992; Kettle et al., 1999). This concentration gradient, in turn, induces significant sea-to-air fluxes of DMS, and serves as the largest source of natural sulfur into the global atmosphere (Bates et al., 1992; Spiro et al., 1992). In the atmosphere, DMS is photochemically oxidized to a multitude of sulfur-containing species, some of which have an affinity for creating new aerosols or interacting with existing particles. This connection between phytoplankton production of DMS and oxidized sulfur-aerosol interactions forms part of a proposed feedback whereby DMS may influence climate and radiation on a planetary scale (Shaw, 1983; Charlson et al., 1987).

The proposed DMS-climate link has sparked much research into the individual processes ranging from DMS emissions to the formation of new particles and cloud condensation nuclei (Restelli and Angeletti, 1993; Andreae and Crutzen, 1997). In spite of these extensive research efforts, many large sources of uncertainty still remain. For instance, the two most widely used sea-air flux parameterizations result in DMS fluxes that differ by a factor of two (Liss and Merlivat, 1986; Wanninkhof, 1992). As another example, the nucleation rates of new sulfate aerosols calculated in two recent studies differ by an order of magnitude (Kulmala et al., 1998;

Verheggen and Mozurkewich, 2002). Such large ranges in estimated DMS fluxes and nucleation rates results naturally in wide ranges of estimated concentrations of DMS oxidation products, fine particle concentrations, and other aerosol-related effects.

Another significant source of uncertainty comes from the gas-phase DMS oxidation mechanism, which connects sea-air fluxes to aerosols in the DMS-climate cycle. The DMS mechanism is highly complex and involves many species, competing reactions, and multiple branch points (Yin et al., 1990b; Turnipseed and Ravishankara, 1993; Urbanski and Wine, 1999; Lucas and Prinn, 2002). Besides DMS, other important gas-phase DMS-related species include dimethylsulfone (DMSO, $CH_3S(O)CH_3$), dimethylsulfoxide ($DMSO_2$, $CH_3S(O)_2CH_3$), sulfur dioxide (SO_2), sulfuric acid (H_2SO_4), and methanesulfenic (MSEA, CH_3SOH), methanesulfinic (MSIA, $CH_3S(O)OH$), and methanesulfonic (MSA, CH_3SO_3H) acids. Because of the plethora of DMS-related species and reactions, the rather large uncertainty in the DMS oxidation mechanism is based on the fact that only a small number of the rate constants have actually been measured in the laboratory. These measured rate constants are for reactions at the beginning of the oxidation sequence and a few reactions towards the middle and end of the scheme. All of the remaining rate constants are estimated and highly uncertain (Yin et al., 1990b; Lucas and Prinn, 2002). In light of this uncertainty, the purpose of this chapter is to quantify and characterize the effects of these uncertain reactions –and other important uncertain processes– on predictions of the aforementioned sulfur-based species. To accomplish this goal, an extensive parametric sensitivity and uncertainty analysis is carried out on a diurnally-varying model of DMS chemistry in the remote marine boundary layer (RMBL) using a comprehensive DMS oxidation mechanism.

Sensitivity and uncertainty methods provide a wealth of information about chemical kinetic systems. These methods are used to determine key kinetic parameters, calculate concentration uncertainties and identify the sources of these uncertainties, eliminate redundant species and pathways in large mechanisms, estimate unknown rate constants, and as an aid in the design of future experiments (Turányi, 1990). Given these many uses, a large number of sensitivity and uncertainty studies have addressed various atmospheric chemistry systems. For example, Thompson and Stewart (1991) used Monte Carlo to study of the effects of uncertain rate constants on the concentrations of tropospheric constituents, while Gao et al. (1995) performed a first-order sensitivity and uncertainty analysis on a regional acid deposition model. As pointed out by Saltelli (1999), however, the most commonly used sensitivity and uncertainty techniques –including the methods used in the above two referenced studies– do not account for non-linear

chemistry or interactions between various model processes.

Because the DMS oxidation cycle in the RMBL is complex and non-linear, the sensitivity and uncertainty analysis in this chapter uses the *probabilistic collocation method* (PCM) (Tatang et al., 1997) to explicitly account for any non-linearities. PCM has been applied to analyses of highly non-linear models of direct and indirect aerosol radiative forcing (Pan et al., 1997, 1998), and has been used to create parameterizations of non-linear chemical processing in an urban-scale model (Calbó et al., 1998; Mayer et al., 2000). In addition, a standard *direct integration method* (DIM) is used to analyze the linear sensitivities and uncertainties (Dickinson and Gelinas, 1976; Dunker, 1984; Leis and Kramer, 1988b). Using these two independent methods (DIM and PCM) provides confidence in the sensitivity and uncertainty assessments and indicates the degree of non-linearity inherent in the cycling of DMS in the RMBL.

Few sensitivity and uncertainty studies have been carried out on models utilizing comprehensive DMS mechanisms. In one study, Capaldo and Pandis (1997) calculated the sensitivities of DMS-related concentrations to five different chemical mechanisms (3 comprehensive, 2 parameterized) in a marine boundary layer box model. Although the Capaldo and Pandis (1997) study is useful for characterizing structural uncertainties, Saltelli (1999) pointed out that they used a technique that did not capture parameter interactions and other non-linearities. Capaldo and Pandis (1997) also did not consider sensitivities to rate constants and the propagation of rate constant uncertainties to the DMS-related concentrations, which are two primary goals of the current study.

In another study, Saltelli and Hjorth (1995) used Monte Carlo sampling and regression analysis to calculate the sensitivities and uncertainties of ratios of important end products from a DMS mechanism of moderate complexity (37 reactions, 18 sulfur-based species) to the kinetic parameters. For reference, an aqueous chemistry extension of their gas-phase mechanism has appeared in subsequent reports (Campolongo et al., 1999; Saltelli, 1999). The regression technique used by Saltelli and Hjorth (1995) captured a certain degree of the system non-linearity because the parameter uncertainty spaces were fully explored. However, they used linear ranked regressions that accounted for less than 85% of the original model's variance, so their regression-based sensitivities may have missed some non-linear interactions. Saltelli and Hjorth (1995) also calculated variance contributions using an alternate method explicitly accounting for non-linearities. They found a qualitative agreement on the key parameters using the two independent methods.

The Saltelli and Hjorth (1995) study was important and methodological. Their results have

a limited value, however, because they used a DMS oxidation mechanism with a deficiency regarding MSA production. In particular, their mechanism arbitrarily increased MSA production by using an excessively large range to describe the first-order formation of MSA from CH_3SO_3. Hence, their model results involving MSA were highly sensitive to this reaction. A recent study suggests that MSA also has a large production channel from the DMS+OH addition branch (Lucas and Prinn, 2002), which was not present in their model. Moreover, their mechanism did not include the recently proposed isomerization of $CH_3S(O)OO$ to CH_3SO_3, which has been found to possibly be important in H_2SO_4 production (Lucas and Prinn, 2002). In addition to these mechanistic issues, the Saltelli and Hjorth (1995) results do not easily aid in the interpretation of surface observations of DMS-related species because their analysis did not include non-chemical processes known to play a large role in DMS cycling in the RMBL, namely oceanic emissions, heterogeneous removal, and mixing into/out of the RMBL. Finally, their model did not include diurnally-varying DMS chemistry, which is required to distinguish the differences between the sensitivities and uncertainties when the photochemistry is active and in-active (i.e., during noon and in the evening).

Given the large uncertainties associated with DMS oxidation chemistry, the incomplete nature of the few previous sensitivity and uncertainty studies using comprehensive DMS mechanisms, and the updated version of the DMS mechanism (Lucas and Prinn, 2002), the sensitivities and uncertainties of the DMS system are re-analyzed in this chapter. A diurnally-forced box model is used because it provides an efficient framework for analyzing the sensitivities to, and uncertainties from, the large number of parameters involved in the formation and loss of the oxidized DMS-products in the RMBL. The parametric sensitivities and uncertainties are the focus here because the external conditions (e.g., temperature and pressure) are typically much better known than the DMS-related parameters. However, because of the extreme influence of temperature on branching in the DMS oxidation mechanism, the uncertainties of the DMS-related species are also examined across a wide temperature range.

3.2 Model of DMS Chemistry in the RMBL

3.2.1 Model Description and Processes

The major processes represented in the model of DMS chemistry in the RMBL are illustrated in Figure 3-1. These processes include an oceanic source of DMS, gas-phase oxidation using a comprehensive DMS mechanism, parameterized heterogeneous removal by dry deposition

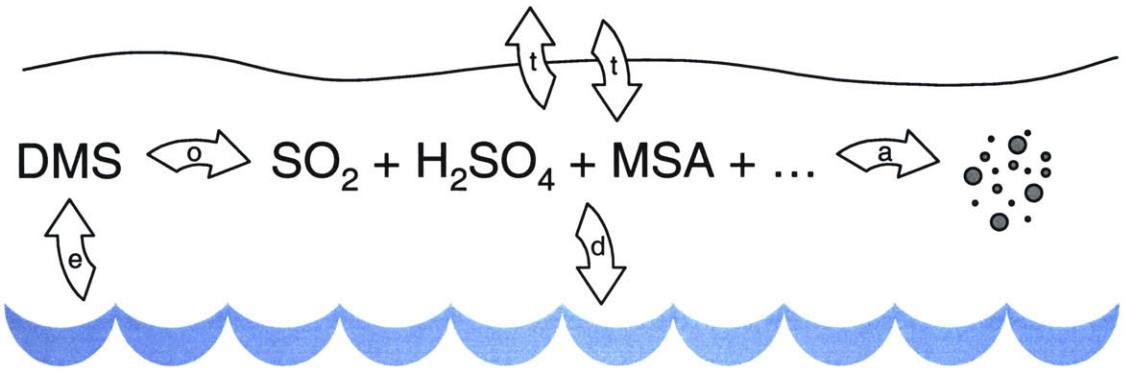

Figure 3-1: Major processes represented in the remote marine boundary layer model of DMS chemistry. The individual processes are labeled as follows: e = emissions of DMS from the ocean; o = oxidiation in the gas-phase; d = dry deposition; a = loss to background aerosols; and t = transport into and out of the remote marine boundary layer.

and scavenging by aerosols, and parameterized transport into and out of the remote marine boundary layer. Mathematically, the DMS chemistry model is described by a coupled set of ordinary differential equations (ODEs). Each ODE takes the general form

$$\frac{dn_i}{dt} = f_i(n, p_c) - p_{h,i}\, n_i + p_t(\bar{n}_i - n_i) + p_{s,i}, \tag{3.1}$$

where n_i and $\bar{n}_i$ are the number concentrations of sulfur-based species i in the RMBL and free troposphere, respectively, f is the net chemical production, and the p's are the various model parameters. Specifically, p_c represents the set of chemical reaction rate constants used in the net chemical production function, p_h defines the first-order heterogeneous removal, p_t is associated with the parameterized vertical transport, and p_s is the emission-related source in the RMBL. The DMS chemistry model solves for the time-dependent concentrations of 25 sulfur-based species using 56 uncertain parameters. These 56 parameters are comprised of 47 chemical reaction rate constants, 7 heterogeneous removal terms, a vertical mixing coefficient, and DMS emissions. The model processes and parameters are listed in Table 3.1 and are described in more detail below.

The DMS model described by equation 3.1 is structurally simple, and similar DMS chemistry models have been used to estimate unknown parameters –such as DMS surface fluxes or heterogeneous removal– and for comparisons with field observations (Davis et al., 1999; Chen

et al., 2000; Shon et al., 2001). However, given the structural simplicity of the model, it is important to point out its major limitations. First, vertical mixing is time-dependent only in the sense that the RMBL concentrations vary with time. Time-dependent changes in the RMBL height and atmospheric stability are not represented because p_t and $\bar{n}_i$ are held constant. Also, aqueous- and cloud-phase processes are not represented in the model, so it is only representative of the clear-sky RMBL. This, however, allows the focus to be drawn on the gas-phase oxidation of DMS, for which the uncertainties are still very large. Despite the simplified DMS chemistry model, it captures the key elements affecting the gas-phase sulfur-based species in the RMBL –from oceanic DMS emissions to scavenging by aerosols– in a computationally very efficient manner. This numerical efficiency, in turn, allows for a thorough investigation of the time-dependent sensitivities and uncertainties that would not be practical in models of greater complexity. An vertically extended version of this model, which is used for comparing predictions with field measurements, is described in Chapter 4.

Finally, due to the often large uncertainties and for other reasons explained in the following sections, the sensitivity and uncertainty analysis is more appropriately carried out in logarithmic space. Thus, log-scaled concentrations and parameters are used throughout this chapter. Log-scaled quantities are denoted by

$$\eta = \log n \quad \text{and} \quad \varrho = \log p, \tag{3.2}$$

where η and ϱ are log-scaled concentrations (n) and parameters (p), respectively. Hereafter, the terms concentrations and parameters are used inter-changeably with logarithmic concentrations and parameters, though the specific context is apparent using the above notation.

Table 3.1: Processes and Parameters in the DMS Chemistry RMBL Model

	Process	Parameter	Uncertainty	Refs
	Gas-Phase DMS Chemistry			
1	$CH_3SCH_3 + OH \rightarrow CH_3SCH_2 + H_2O$	$1.2 \times 10^{-11} \exp(-260/T)$	(1.15, 100)	[1,1]
2	$CH_3SCH_3 + NO_3 \rightarrow CH_3SCH_2 + HNO_3$	$1.9 \times 10^{-13} \exp(500/T)$	(1.2, 200)	[1,1]
3	$CH_3SCH_3 + OH \rightarrow CH_3S(OH)CH_3$	k_f	(2.0, 0)	[2,2]
4	$CH_3S(OH)CH_3 \rightarrow CH_3SCH_3 + OH$	k_r	(2.5, 0)	[3,e]
5	$CH_3S(OH)CH_3 + O_2 \rightarrow CH_3S(O)CH_3 + HO_2$	5×10^{-13}	(1.34, 0)	[4,3]
6	$CH_3S(OH)CH_3 \rightarrow CH_3SOH + CH_3$	5×10^{5}	(2.5, 0)	[5,e]
7	$CH_3S(O)CH_3 + OH \rightarrow CH_3S(O)(OH)CH_3$	$6.3 \times 10^{-12} \exp(800/T)$	(1.3, 0)	[6,6]
8	$CH_3S(O)(OH)CH_3 + O_2 \rightarrow CH_3S(O)_2CH_3 + HO_2$	1×10^{-13}	(2.5, 0)	[e,e]

continued on next page

continued from previous page

	Process	Parameter	Uncertainty	Refs
9	$CH_3S(O)(OH)CH_3 \rightarrow CH_3S(O)OH + CH_3$	2×10^{6}	(2.5, 0)	[7,*e*]
10	$CH_3S(O)OH + OH \rightarrow CH_3SO_2 + H_2O$	1×10^{-12}	(2.5, 0)	[*e*,*e*]
11	$CH_3SCH_2 + O_2 \rightarrow CH_3SCH_2OO$	5.7×10^{-12}	(1.07, 0)	[1,1]
12	$CH_3SCH_2OO + NO \rightarrow CH_3SCH_2O + NO_2$	$7.9 \times 10^{-12} \exp(128/T)$	(2.5, 0)	[4,*e*]
13	$CH_3SCH_2O \rightarrow CH_3S + CH_2O$	3.3×10^{4}	(2.5, 0)	[4,*e*]
14	$CH_3SOH + OH \rightarrow CH_3SO + H_2O$	5×10^{-11}	(2.5, 0)	[*e*,*e*]
15	$CH_3S + NO_2 \rightarrow CH_3SO + NO$	$2.1 \times 10^{-11} \exp(320/T)$	(1.15, 100)	[1,1]
16	$CH_3S + O_3 \rightarrow CH_3SO + O_2$	$2.0 \times 10^{-12} \exp(290/T)$	(1.15, 100)	[1,1]
17	$CH_3S + O_2 \rightarrow CH_3SOO$	$1.4 \times 10^{-16} \exp(1550/T)$	(2.0, 0)	[2,2]
18	$CH_3SOO \rightarrow CH_3S + O_2$	$1.5 \times 10^{11} \exp(-3910/T)$	(2.0, 0)	[2,2]
19	$CH_3SOO + NO \rightarrow CH_3SO + NO_2$	1.1×10^{-11}	(2.0, 100)	[1,1]
20	$CH_3SOO + NO_2 \rightarrow CH_3SOONO_2$	2.2×10^{-11}	(2.0, 100)	[2,1]
21	$CH_3SOONO_2 \rightarrow CH_3SOO + NO_2$	4×10^{-3}	(2.5, 0)	[*e*,*e*]
22	$CH_3SO + NO_2 \rightarrow CH_3SO_2 + NO$	1.2×10^{-11}	(1.4, 0)	[1,1]
23	$CH_3SO + O_3 \rightarrow CH_3SO_2 + O_2$	6.0×10^{-13}	(1.5, 0)	[1,1]
24	$CH_3SO + O_2 \rightarrow CH_3S(O)OO$	$3.6 \times 10^{-16} \exp(1550/T)$	(2.5, 0)	[*e*,*e*]
25	$CH_3S(O)OO \rightarrow CH_3SO + O_2$	$3.9 \times 10^{11} \exp(-3910/T)$	(2.5, 0)	[*e*,*e*]
26	$CH_3S(O)OO + NO \rightarrow CH_3SO_2 + NO_2$	8×10^{-12}	(2.5, 0)	[5,*e*]
27	$CH_3S(O)OO + NO_2 \rightarrow CH_3S(O)OONO_2$	1×10^{-12}	(2.5, 0)	[5,*e*]
28	$CH_3S(O)OONO_2 \rightarrow CH_3S(O)OO + NO_2$	4.2×10^{-3}	(2.5, 0)	[5,*e*]
29	$CH_3SO_2 + NO_2 \rightarrow CH_3SO_3 + NO$	2.2×10^{-12}	(1.5, 0)	[8,8]
30	$CH_3SO_2 + O_3 \rightarrow CH_3SO_3 + O_2$	5×10^{-15}	(2.5, 0)	[5,*e*]
31	$CH_3SO_2 + OH \rightarrow CH_3SO_3H$	5×10^{-11}	(2.5, 0)	[5,*e*]
32	$CH_3SO_2 + O_2 \rightarrow CH_3S(O)_2OO$	$1.2 \times 10^{-16} \exp(1550/T)$	(2.5, 0)	[*e*,*e*]
33	$CH_3S(O)_2OO \rightarrow CH_3SO_2 + O_2$	$1.3 \times 10^{11} \exp(-3910/T)$	(2.5, 0)	[*e*,*e*]
34	$CH_3S(O)_2OO + NO \rightarrow CH_3SO_3 + NO_2$	1×10^{-11}	(2.5, 0)	[5,*e*]
35	$CH_3S(O)_2OO + CH_3O_2 \rightarrow CH_3SO_3 + CH_2O + HO_2$	5.5×10^{-12}	(2.5, 0)	[5,*e*]
36	$CH_3S(O)_2OO + NO_2 \rightarrow CH_3S(O)_2OONO_2$	1×10^{-12}	(2.5, 0)	[5,*e*]
37	$CH_3S(O)_2OONO_2 \rightarrow CH_3S(O)_2OO + NO_2$	4.2×10^{-3}	(2.5, 0)	[5,*e*]
38	$CH_3SO_2 \rightarrow CH_3 + SO_2$	$k_{CH_3SO_2}$	(2.5, 0)	[9,*e*]
39	$CH_3SO_3 \rightarrow CH_3 + SO_3$	1.6×10^{-1}	(2.5, 0)	[5,*e*]
40	$CH_3SO_3 + HO_2 \rightarrow CH_3SO_3H + O_2$	5×10^{-11}	(2.5, 0)	[5,*e*]
41	$SO_2 + OH \rightarrow HOSO_2$	k_{SO_2+OH}	$\sqrt{k^+/k^-}$	[1,1]
42	$HOSO_2 + O_2 \rightarrow SO_3 + HO_2$	$1.3 \times 10^{-12} \exp(-330/T)$	(1.2, 200)	[1,1]
43	$SO_3 + H_2O \rightarrow H_2SO_4$	$k_{SO_3+H_2O}$	(2.0, 110)	[10,10]
44	$CH_3SOO \rightarrow CH_3SO_2$	1×10^{0}	(2.5, 0)	[*e*,*e*]
45	$CH_3S(O)OO \rightarrow CH_3SO_3$	8×10^{-2}	(2.5, 0)	[*e*,*e*]
46	$CH_3S(O)OH \rightarrow CH_3SO_3H$	1×10^{-6}	(2.5, 0)	[*e*,*e*]
47	$CH_3SOH \rightarrow CH_3SO_3H$	5×10^{-5}	(2.5, 0)	[*e*,*e*]

continued on next page

continued from previous page

	Process	Parameter	Uncertainty	Refs
		Non-Gas-Phase Processes		
48	$CH_3S(O)CH_3$ → heterogeneous loss	2×10^{-4} s^{-1}	(2.2, 0)	[e,e]
49	$CH_3S(O)_2CH_3$ → heterogeneous loss	2×10^{-4} s^{-1}	(2.2, 0)	[e,e]
50	CH_3SOH → heterogeneous loss	5×10^{-5} s^{-1}	(2.5, 0)	[e,e]
51	CH_3SO_2H → heterogeneous loss	5×10^{-5} s^{-1}	(2.5, 0)	[e,e]
52	CH_3SO_3H → heterogeneous loss	2×10^{-4} s^{-1}	(2.2, 0)	[e,e]
53	SO_2 → heterogeneous loss	5×10^{-5} s^{-1}	(2.5, 0)	[e,e]
54	H_2SO_4 → heterogeneous loss	1×10^{-3} s^{-1}	(1.8, 0)	[e,e]
55	DMS surface flux	5×10^{9} molecules cm^{-2} s^{-1}	(2.5, 0)	[e,e]
56	RMBL mixing coefficient	5×10^{4} cm^2 s^{-1}	(1.5, 0)	[e,e]

First- and second-order reaction rate constants have units of s^{-1} and cm^3 molecule^{-1} s^{-1}, temperature has units of degrees K, and concentrations are in units of molecules cm^{-3}. Uncertainty factors are specified using (ϕ_{298}, ϵ), where ϕ_{298} and ϵ are given in equation 3.5. The forward addition of OH to DMS is given by $k_f = (1.7 \times 10^{-42}[O_2]\exp(7810/T))/(1 + 5.5 \times 10^{-31}[O_2]\exp(7460/T))$. The reverse reaction is calculated using $k_r = k_f/K_{eq}$, where K_{eq} is the temperature dependent equilibrium constant given by $K_{eq} = 8.3 \times 10^{-29} T \exp(5136/T)$ cm^3 molecule^{-1}. The *ab initio* rate constant for CH_3SO_2 dissociation in Kukui et al. (2000) is used in the model. The effective second-order rate constant reported in DeMore et al. (1997) is used for the SO_2+OH association reaction. The reaction rate between SO_3 and H_2O is second-order in water vapor, which is specified using the following equivalent second-order rate constant $k_{SO_3+H_2O} = 2.26 \times 10^{-43} T \exp(6544/T)[H_2O]$. The first and second entries in the references column are for the rate constant and uncertainty factor, respectively. 1=DeMore et al. (1997), 2=Atkinson et al. (1997), 3=Barone et al. (1996), 4=Turnipseed et al. (1996), 5=Yin et al. (1990b), 6=Hynes and Wine (1996), 7=Urbanski et al. (1998), 8=Ray et al. (1996), 9=Kukui et al. (2000), 10=Lovejoy et al. (1996), *e*=estimated here.

Gas-Phase DMS Chemistry

The net chemical production is calculated using a comprehensive DMS oxidation mechanism containing 47 chemical reactions and 25 sulfur-containing species. This mechanism omits several reactions in the Yin et al. (1990b) scheme which are unimportant under the RMBL conditions, and has incorporated many new features as discussed in the previous chapter and in Lucas and Prinn (2002). A brief review of this DMS mechanism is given here.

The DMS oxidation scheme is initialized by reactions with OH and NO_3, where the former occurs through two independent branches and the latter is potentially important at night. The initial oxidation by halogens (for example, bromine oxide) is also postulated to be important under certain conditions (von Glasow et al., 2002), but these reactions are neglected here due to poorly constrained reactive halogen concentrations in the remote marine atmosphere. Overall, the oxidation by OH dominates the net photochemical loss of DMS in the RMBL because of the relatively abundant amount of OH and large OH-related rate constants. As previously mentioned, the OH-initiated oxidation of DMS proceeds through two channels, abstraction and addition. The H-abstraction branch is favored at higher temperatures and primarily leads to

SO_2 and H_2SO_4. The OH-addition branch has a negative temperature-dependency (that is, it increases with decreasing temperature) and leads to DMSO, $DMSO_2$, MSEA, and MSIA. The production of MSA is highly uncertain and is believed to form through both the H-abstraction and OH-addition channels. In this model, MSA production through the H-abstraction branch is explicitly accounted for through reactions with CH_3SO_3. MSA production through the OH-addition branch, however, is parameterized using first-order conversions from MSEA and MSIA with assumed rate constants taken from Lucas and Prinn (2002). Other important features in this mechanism include the isomerization of $CH_3S(O)_xOO$ to $CH_3S(O)_{x+2}$ and the temperature-dependent addition of O_2 to $CH_3S(O)_x$.

Finally, the model is designed for the remote marine atmosphere where NO_x levels are relatively low. This leaves HO_x and O_3 as the main drivers of the DMS oxidation scheme. These conditions simplify the DMS oxidation chemistry in two important ways. First, many DMS-related reactions are not competitive under these conditions –such as self-reactions of sulfur-containing radicals– and so the full mechanism compiled by Yin et al. (1990b) is reduced down to the more manageable size shown in Table 3.1. Second, simultaneous measurements of O_3 and important HO_x-related species in the RMBL were made during Flight 24 of the First Aerosol Characterization Experiment (ACE-1). These measured values are used to drive the model rather than including the HO_x-NO_x-O_x-CH_4 cycles in the photochemical mechanism. This enables a specific focus on uncertainties in the sulfur compound chemistry.

Heterogeneous Removal

Heterogeneous removal is formally estimated using $p_h = p_a + p_d$, where p_a and p_d are frequencies for the loss of gas-phase sulfur-based species on to aerosols and at the ocean surface through scavenging and dry deposition, respectively. For most of the products of DMS oxidation, loss to aerosols is typically much larger than loss by dry deposition, and so $p_h \approx p_a$. For SO_2, however, losses on aerosols and the ocean surface are both important, so p_h depends on a combination of p_a and p_d. The aerosol portions of the heterogeneous removal parameters are based on observations of aerosol number distributions during Flight 24 of ACE-1 (see Chapter 4, Figures 4-2 and 4-7). The surface removal portions are based on typical dry deposition velocities for a stable marine boundary layer (see Chapter 4, Table 4.2). The heterogeneous removal frequency for SO_2, which accounts for loss to sea-salt aerosols and dry deposition, was empirically derived for the Flight 24 conditions (see Chapter 4, Section 4.2.4). The combined aerosol and surface loss terms yield the specific heterogeneous removal frequencies listed in Table 3.1.

RMBL Mixing

Vertical transport in equation 3.1 is parameterized as the product of p_t and the difference between the concentrations in the RMBL (n) and the overlying free troposphere ($\overline{n}$). This parameterization yields obviously a source in the RMBL when $\overline{n} > n$ and sink when $\overline{n} < n$. The first-order transport coefficient is based on the scaling $\partial_z K_z \partial_z n \sim p_t \Delta n \Rightarrow p_t \sim K_z/(\Delta z)^2$, in which K_z and Δz represent the vertical eddy-diffusion coefficient and vertical mixing depth, respectively. This parameterized transport is applied to all of the important relatively long-lived DMS-related species, but not to the fast-reacting sulfur-based radicals. The specific value of $p_t = 2 \times 10^{-5}$ s^{-1} used in equation 3.1 is derived from observationally-based RMBL estimates of $K_z \approx 5 \times 10^4$ cm^2 s^{-1} and $\Delta z \approx 500$ m during Flight 24 of ACE-1. These estimates, which are extensively discussed in Chapter 4 and in Lucas and Prinn (2002), are typical values for a stable, clear-sky boundary layer in the remote marine atmosphere.

The RMBL mixing scheme also requires the specification of the concentrations of relatively long-lived DMS-related species in the free troposphere. For simplicity and consistency, the free tropospheric concentrations are assumed to be fixed in time and are based on the daily average 'buffer layer' concentrations calculated in Lucas and Prinn (2002). The specific values of $\bar{n}$ used here are listed in Table 3.2. Finally, regarding the assumption of the time-independent p_t, including time variations for K_z and Δz would not likely change the net value of p_t by large amounts because periods of efficient (inefficient) mixing are typically associated with thick (shallow) mixed layer depths.

DMS Emissions

Oceanic DMS emissions are the only known significant sulfur-containing emissions in the remote marine atmosphere. DMS emissions are usually parameterized using the surface wind speed and the difference between the sea-surface and atmospheric concentrations of DMS. For the sake of simplicity, however, a constant sea-to-air flux of 5×10^9 molecules cm^{-2} s^{-1} is assumed for DMS. This flux is based on a previous estimate for Flight 24 during ACE-1 (Lucas and Prinn, 2002), and is consistent with other estimates for this period (Bates et al., 1998b; Mari et al., 1999; Shon et al., 2001). Dividing this flux by the assumed mixed layer depth (Δz) gives the DMS emission source parameter (p_s) used in equation 3.1.

3.2.2 Model Conditions and Forcing Functions

The conditions measured in the boundary layer during Flight 24 of ACE-1 (Bates et al., 1998a) are used to set the model conditions for the sensitivity and uncertainty analysis. A detailed description of these conditions is given in the next chapter and in Lucas and Prinn (2002), so only a brief summary is provided here. The Flight 24 observations were made under clear-sky conditions over the Pacific Ocean near Tasmania. Five-day back trajectories over the measurement region indicated that the surface air masses were of a remote marine origin on that time scale. The region was also characterized by relatively large sea-surface DMS concentrations (De Bruyn et al., 1998), which provided an ample source of atmospheric DMS. Measurements of important oxidizing species (H_2O_2, CH_3OOH, O_3, and OH) were also made, which allows the model to be driven directly by these observations. Combined, these various factors created an optimal setting for observing and analyzing the gas-phase cycling of DMS in the RMBL. The relevant ACE-1 Flight 24 measurements used in the DMS chemistry model were averaged in the boundary layer and are shown in Table 3.2. Measurements that did not vary with time are 'fixed' as noted in the table, while the time-varying measurements are described below.

The Flight 24 measurements resolved the time variations of OH, H_2O_2, and CH_3OOH in the RMBL. These observations were fit to a set of time-dependent 'forcing functions' that drive the diurnal variations in the DMS chemistry model. These forcing functions are expressed by

$$\Phi(a,b,c) = \begin{cases} a \sin\left[\frac{\pi}{15.2}(t-4.4)+c\right]+b & 4.4 \le t \le 19.6 \\ b & \text{other } t \end{cases} \tag{3.3}$$

where t is the local time of day (in hours from midnight), a is the amplitude of the diurnal cycle, b is the nighttime background value, and c is the phase of the diurnal cycle. The values of a and b are based on the fits to the Flight 24 observations. Regarding the phase, setting $c = 0$ gives a diurnal peak at noon, while setting $c = \pi$ gives a diurnal minimum at noon. The values of 4.4 and 15.2 are the local sunrise (in hours) and number of daylight hours, respectively, as defined by the day of year and location of the Flight 24 measurements. The forcing functions for OH, H_2O_2, and CH_3OOH are shown in Table 3.2. These forcing functions also provide diurnal variations to HO_2, CH_3O_2, and NO_2, which are prescribed using the diagnostic expressions in Table 3.2.[1] Because NO_3 was not measured or is not diagnosed, its diurnal cycle is assumed so that the sensitivity of DMS to the nighttime oxidation by NO_3 can be ascertained. The diurnal

[1]See Table 4.3 and Section 4.3.5 in Chapter 4 for a detailed discussion of the diagnostic expressions for HO_2, CH_3O_2, and NO_2.

Table 3.2: Background Conditions Used in the DMS Chemistry RMBL Model

Condition	Value	Time-Dependence
ACE-1		
mixed layer depth	500 m	fixed
temperature	290 K	fixed
pressure	990 hPa	fixed
relative humidity	75%	fixed
O_3	20 ppb	fixed
OH	$10^{\Phi(1.7,4.8,0.0)}$ molecules cm^{-3}	varies
H_2O_2	$\Phi(0.40, 0.0068, 0.0)$ ppb	varies
CH_3OOH	$\Phi(0.20, 0.0034, 0.0)$ ppb	varies
Estimated		
NO	1 ppt	fixed
NO_3	$10^{\Phi(2.0,5.5,\pi)}$ molecules cm^{-3}	varies
Diagnosed (See Table 4.3 and Section 4.3.5 in Chapter 4)		
HO_2	$\sqrt{[H_2O_2](k_2[OH] + J_3)/k_1}$	varies
CH_3O_2	$[CH_3OOH](J_5 + k_6[OH] + k_7)/(k_4[HO_2])$	varies
NO_2	$[NO](k_9[O_3] + k_{10}[HO_2] + k_{11}[CH_3O_2])/J_8$	varies
Free Tropospheric Concentrations (molecules cm^{-3})		
DMS	$10^{8.6}$	fixed
DMSO	$10^{6.8}$	fixed
$DMSO_2$	$10^{6.4}$	fixed
MSEA	$10^{6.6}$	fixed
MSIA	$10^{8.3}$	fixed
MSA	$10^{6.4}$	fixed
SO_2	$10^{9.1}$	fixed
H_2SO_4	$10^{6.6}$	fixed

cycles of these oxidation-related species are shown in Figure 3-2.

3.2.3 Parameter Uncertainties

The uncertainties of the model parameters are also listed in Table 3.1. For this study, the uncertain parameters are assumed to be lognormally distributed, where the logarithm of each parameter follows a normal probability distribution function (PDF). As shown in Table 3.1, the parameter uncertainties are expressed using multiplicative factors. These relationships are given by

$$\overbrace{\bar{p} \times \phi \text{ and } \bar{p} \times 1/\phi}^{\text{normal}} \quad \Leftrightarrow \quad \overbrace{\log \bar{p} \pm \log \phi = \bar{\varrho} \pm \sigma}^{\text{lognormal}}, \tag{3.4}$$

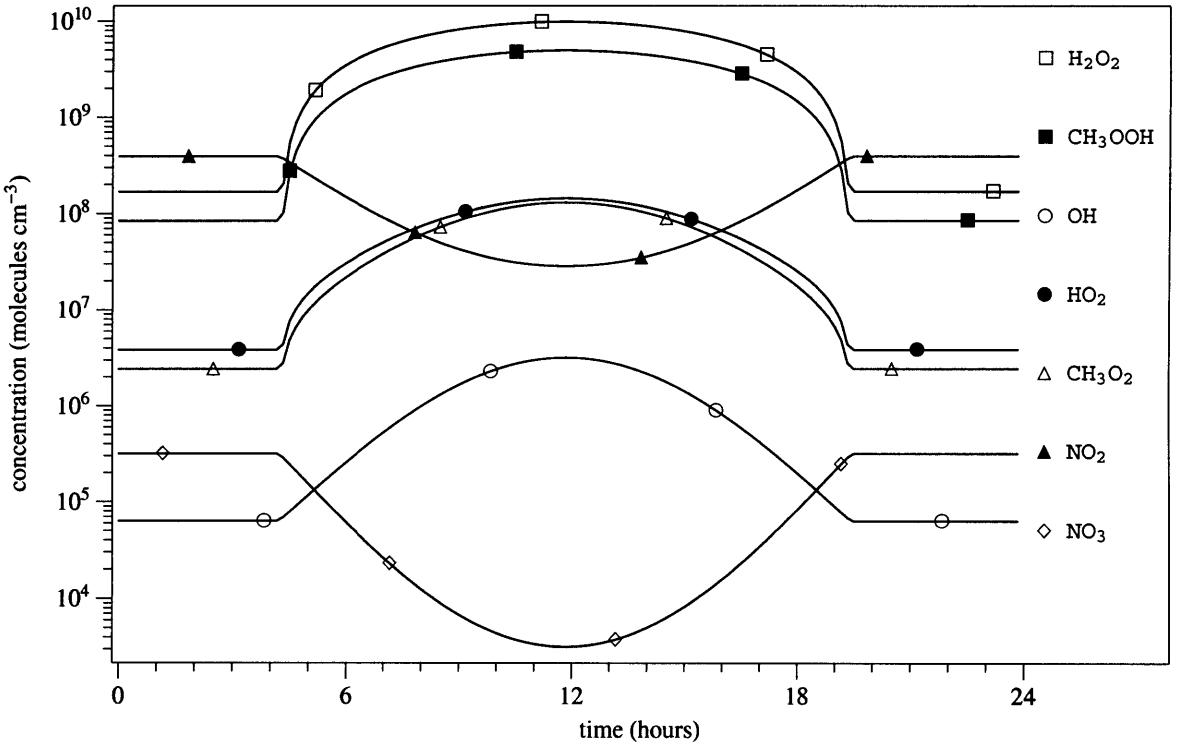

Figure 3-2: Profiles of the number concentrations (molecules cm^{-3}) of the diurnally-varying background species driving the oxidation of DMS. The cycles for OH, H_2O_2, and CH_3OOH are based on fits to the ACE-1 Flight 24 data. The cycles for HO_2, CH_3O_2, and NO_2 use the diagnostic expressions in Table 3.2. The cycle for NO_3 is estimated.

where $\bar{p}$ and $\bar{\varrho}$ are the mean values of the model parameters in normal and lognormal space, respectively, while σ and ϕ are the uncertainties specified as standard deviations and multiplicative factors, respectively. Lognormal parameter PDFs are used is this study for three reasons. First, parameters sampled from lognormal PDFs are positive definite, which prevents non-physical negative values from entering into the model. Second, many of the parameter values are taken from DeMore et al. (1997) and Atkinson et al. (1997), who specify uncertainties using multiplicative factors. Third, lognormal parameter uncertainties simplify the application of normalized sensitivities to estimates of concentration uncertainties.

All of the parameters in Table 3.1, except the rate constant for the reaction between SO_2 and OH, have uncertainty factors specified using

$$\phi(T) = \phi_{298} \exp\left(\varepsilon \left| \frac{1}{T} - \frac{1}{298} \right| \right), \tag{3.5}$$

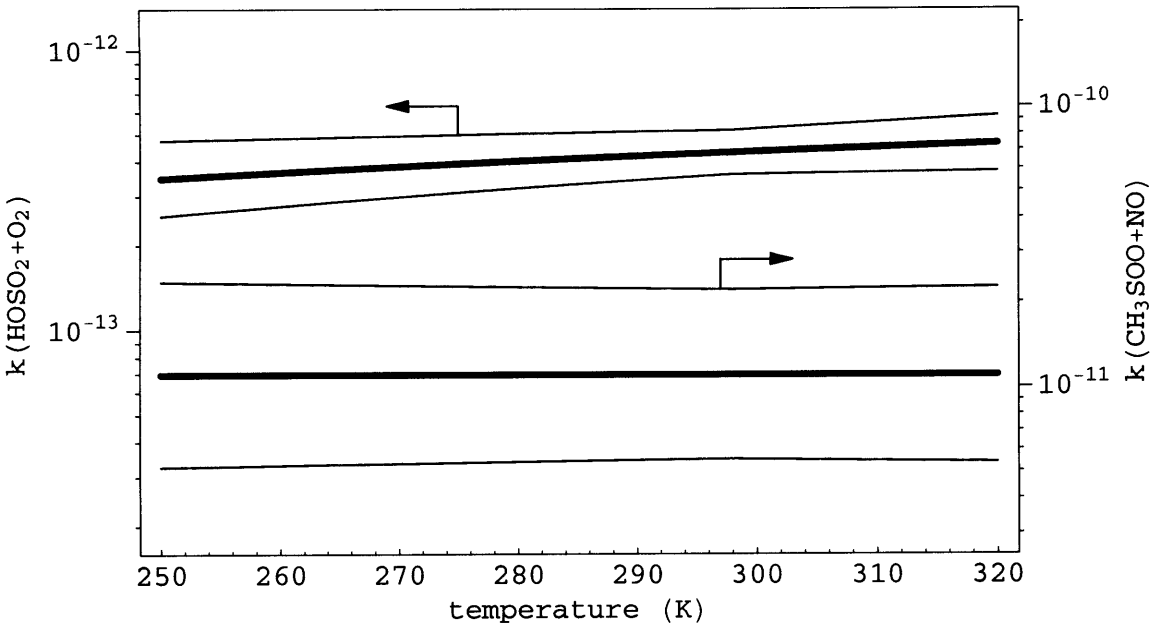

Figure 3-3: The rate constants and uncertainties for the $HOSO_2$+O_2 and CH_3SOO+NO reactions as a function of temperture. The mean values and 1-σ deviations are the thick and thin lines, respectively. The arrows point to the respective vertical scale and the rate constant units are cm^3 $molecules^{-1}$ s^{-1}.

where ϕ_{298} is the uncertainty factor at 298 K and ε is used to the extrapolate the uncertainty factor to temperatures away from 298 K. Equation 3.5 is based on the expressions given by DeMore et al. (1997) and Atkinson et al. (1997). All of the estimated and many of the measured rate constants in Table 3.1 have $\varepsilon = 0$, which simply means that the associated uncertainty factor is not temperature-dependent. Uncertainty factors with $\varepsilon \neq 0$ correspond to measured rate constants with ϕ's that are smallest at room temperature. This behavior is based on the fact that laboratory measurements of rate constants are primarily made at room temperature because measurements at other temperatures are more difficult to carry out (DeMore et al., 1997). Two examples of DMS-related rate constants and their uncertainties as a function of temperature are shown in Figure 3-3.

For the SO_2+OH reaction, DeMore et al. (1997) list 4 separate sources of uncertainty that effect the overall rate constant. By calculating the rate constant for all 16 combinations of these

4 uncertainties, the overall uncertainty factor for this reaction is estimated as

$$\log \phi \approx \frac{1}{2}\left(\log p^{+} - \log p^{-}\right) \quad \Rightarrow \quad \phi \approx \sqrt{\frac{p^{+}}{p^{-}}}, \tag{3.6}$$

where p^{+} and p^{-} are the maximum and minimum values, respectively.

As a final note, the referenced uncertainty factors in Table 3.1 are either derived from DeMore et al. (1997) and Atkinson et al. (1997) or have been set using uncertainty information in the given reference. Most of the processes, however, have deliberately large uncertainty factors that are adopted here for our calculations. The uncertainty factory for the RMBL mixing coefficient is based on a previous estimate of the uncertainty for this process (see Chapter 4, Table 4.2). For the remaining processes, uncertainty factors of 2.5 are generously assigned. This provides sufficiently large ranges for the parameters related to photochemistry, heterogeneous removal, and DMS emissions. In fact, a factor of two uncertainty is generally prescribed for DMS emissions, which is smaller than the factor of 2.5 assumed in this study.

3.3 Numerical Methods

Two different computational methods are used in the sensitivity and uncertainty analysis of the DMS chemistry model. The first approach directly integrates the concentration and concentration sensitivity differential equations (i.e., adjoints computed simultaneously). This version is referred to as the *direct integration method* (DIM). The second approach uses a set of polynomial expansions that numerically approximate the solutions of the concentration ODEs. These polynomials are generated using the *probabilistic collocation method* (PCM). These two methods, their advantages and disadvantages, and their applications to the sensitivity and uncertainty analysis are described in detail below.

3.3.1 Direct Integration Method

The direct integration method (Dickinson and Gelinas, 1976; Turányi, 1990) directly integrates the system of sulfur-based concentration ODEs formed from equation 3.1 and the system of first-order local sensitivity ODEs described in the following section (Section 3.4.1). Because the ODEs for the DMS chemistry model are stiff, a modified version of DIM is used to solve the equations. This version is the *Ordinary Differential Equation Solver with Explicit Sensitivity Analysis* (ODESSA) from Leis and Kramer (1988a,b). ODESSA is adopted as the stiff ODE

solver because it has a number of features that are attractive for the sensitivity analysis as described below. Refer to Leis and Kramer (1988a,b) for more details related to ODESSA.

Utilizing the decoupled direct algorithm presented by Dunker (1984), ODESSA first integrates the concentration ODEs over a given time interval using the GEAR-based LSODE package (Hindmarsh and Radhakrishnan, 1993). Using this concentration information, ODESSA then solves the sensitivity ODEs for the same step-size and integration order. In this way, the two systems of ODEs are decoupled, resulting in efficient numerical solutions for the concentrations and concentration sensitivities. Note that the adaptable step-size and integration order are determined by both the concentrations and sensitivities. ODESSA is numerically reliable because the LSODE package, upon which it is based, has been extensively used to benchmark the numerical solutions of atmospheric chemical systems. In addition, ODESSA offers the same user-interface employed by LSODE, which allows for an explicit sensitivity analysis with only minor additional user-input.

Because there are no constraints dictating the output times for integrating the ODEs, the main advantage to DIM is that it provides near-continuous solutions of the concentrations and sensitivities with time. The major disadvantage is that, due to computational demands, DIM is limited practically to a first-order local sensitivity analysis. However, these DIM-based first-order sensitivities can serve as a basis for extrapolating concentration uncertainties.

3.3.2 Probabilistic Collocation Method

The solutions of the concentration ODEs are also estimated using the probabilistic collocation method. PCM is described in more detail in the reports of Tatang et al. (1997) and Pan et al. (1997, 1998). However, a brief summary of PCM is given here. PCM estimates the outputs of a model in terms of orthogonal polynomial expansions of the model inputs. When the model inputs are cast as random variables, where each input parameter is defined by a PDF, each model output expansion becomes a polynomial chaos expansion (PCE) fit to the model output surface and weighting the high probability regions of the model inputs. The coefficients of the PCEs are determined from multiple model runs at special (collocation) values of the input parameters.

Applying PCM to the DMS Chemistry Model

In using PCM on the DMS chemistry model, the inputs are the model parameters listed in Table 3.1 and the outputs are the logarithmic sulfur-based concentrations from equation 3.1.

Considering the order of approximation, the DMS model has 56 uncertain inputs and the concentrations are most likely non-linear. So, there exists a trade-off between having higher-order expansions to capture the non-linearities, and lower-order expansions to maintain a reasonable number of coefficients in the PCEs. To illustrate, a full third-order expansion for 56 inputs has 32,509 coefficients, while a full second-order expansion has only 1,653 coefficients.[2] As a compromise, the PCEs used here include homogeneous (pure) terms up to cubic order and all possible second-order heterogeneous (cross) terms, resulting in expansions with 1,709 coefficients.

Separate PCEs are generated for the most important DMS-related species (DMS, DMSO, $DMSO_2$, MSEA, MSIA, MSA, SO_2, and H_2SO_4). Each PCE is mathematically specified by the following expression for $M = 56$ parameters

$$\hat{\eta} = \alpha_0 + \overbrace{\sum_{j=1}^{3}\sum_{k=1}^{M} \alpha_{j,k}\, g_{j,k}(\xi_k)}^{\text{j}^{\text{th}}\text{ order pure terms}} + \overbrace{\sum_{k=1}^{M-1}\sum_{\ell=k+1}^{M} \beta_{k,\ell}\, g_{1,k}(\xi_k)\, g_{1,\ell}(\xi_\ell)}^{\text{2}^{\text{nd}}\text{ order cross terms}}, \tag{3.7}$$

where $\hat{\eta}$ is the PCE representation of the logarithmic concentration (i.e., $\hat{\eta} \approx \eta$), α_0 is the zeroth-order coefficient of the expansion, $\alpha_{j,k}$ is the j-th order coefficient of the k-th parameter, $\beta_{k,\ell}$ is the coefficient of the second-order cross term between input parameters k and ℓ, and $g_{j,k}(\xi_k)$ is the j-th order orthogonal polynomial for input parameter ξ_k. The summation indices on the second term ensure that all possible combinations of the cross terms are included. The coefficients in equation 3.7 are computed from 1,709 runs of the DMS chemistry model using DIM at the set of input parameter collocation points. After that, equation 3.7 is used to simulate the original model in a computationally extremely efficient way.

Logarithmic concentrations are used in equation 3.7 for two reasons. First, the solutions to chemical ODEs involve exponential functions, so casting the PCEs in terms of logarithms of concentrations removes much of the exponential behavior of the solutions and allows for better fits using lower-order polynomials. Second, as dictated by the multiplicative central limit theorem, lognormally distributed random variables naturally result from products of random variables, which are represented by the higher-order and cross terms in equation 3.7.

Note that equation 3.7 is independent of time because the PCEs represent the concentrations

[2]The total number of terms in a PCE equals $1 + m \times n_p + \sum_{n=1}^{n_c} C_{m,n}$, where m is the number of parameters, n_p is the order of the pure terms, n_c is the order of the cross terms, and $C_{m,n}$ defines the number of cross terms of order n given by $C_{m,n} = \frac{(n+m-1)!-m!\,n!}{n!\,(m-1)!}$.

at instantaneous values of time. Equation 3.7 could be re-formulated to include time, however, by treating time as an input random variable defined by an equal probability PDF. But because the diurnal variations of many of the DMS-related concentrations are very large, the PCEs with time would require higher-order terms than those contained in equation 3.7. In addition, a parametric analysis is the focus here, and so the influence of 'time uncertainties' is not relevant. Therefore, time-dependence is excluded in equation 3.7. In this regard, DIM has an advantage over PCM because the DIM-based solutions are nearly continuous in time.

Polynomial Chaos Expansions in ξ-Space

The orthogonal polynomials $g_{j,k}(\xi_k)$ in equation 3.7 are defined in terms of *standard* normal random variables (ξ_k), which are random variables that have normal distributions with a mean of zero and standard deviation of one. The transformation between the random variables representing the model parameters and the standard normal random variables is given by

$$\log p = \varrho = \bar{\varrho} + \sigma\,\xi \quad \Leftrightarrow \quad \xi = \frac{\varrho - \bar{\varrho}}{\sigma}, \tag{3.8}$$

where ϱ is the normal random variable representing the log-scaled model parameter p, $\bar{\varrho}$ and σ are the mean value and standard deviation of ϱ, and ξ is the standard normal random variable. Transforming ϱ to ξ yields a single set of orthogonal polynomials that is used for all of the model parameters. The first five orthogonal polynomials for ξ, along with some properties of these polynomials, are shown in Table 3.3. In addition, ξ can be interpreted as a parameter that defines the number of standard deviations ϱ lies from its mean value, where $\xi = 0$ is at the parameter mean and $|\xi| = 1$ is one standard deviation from the mean. This interpretation allows for the analysis of complex system behavior in a compact way and is used in the sections describing probabilistic variations in concentrations and concentration sensitivities.

3.4 Sensitivity Analysis

The parametric sensitivity analysis is concerned with the changes to the sulfur-based concentrations when changes are made to the parameters in the DMS chemistry model. Because the parameters are uncertain, both *local* and *probabilistic local* sensitivities are analyzed. Local concentration sensitivities represent the changes to the sulfur-based concentrations for infinitesimal changes about the *mean values* of the model parameters (i.e., for $\varrho = \bar{\varrho}$). First-order local

Table 3.3: Orthogonal Polynomials and Polynomial Properties For ξ

Order	Polynomial	$\partial g_j/\partial\xi$	$E[g_j]$	$E[g_j^2]$	$E[g_j^3]$	$E[g_j^4]$
0	$g_0 = 1$	0	1	1	1	1
1	$g_1 = \xi$	$1\ g_0$	0	1	0	3
2	$g_2 = \xi^2 - 1$	$2\ g_1$	0	2	8	60
3	$g_3 = \xi^3 - 3\ \xi$	$3\ g_2$	0	6	0	3348
4	$g_4 = \xi^4 - 6\ \xi^2 + 3$	$4\ g_3$	0	24	1728	368064

$E[g_j^q]$ denotes an expected value defined by $E[g_j^q] = \frac{1}{\sqrt{2\pi}} \int_{-\infty}^{\infty} \exp\left(\frac{-\xi^2}{2}\right) g_j^q(\xi)\ d\xi$.

sensitivities are calculated as a function of time using DIM and at specific instances in time using PCM. Probabilistic local sensitivities, on the other hand, are defined as the changes to the sulfur-based concentrations for infinitesimal changes about *any values* of the model parameters from the parameter PDFs (i.e., for $\varrho = \bar{\varrho} + \sigma\,\xi$). Although DIM can be used to calculate probabilistic local sensitivities, PCM is a more powerful tool for assessing them. With little additional effort, PCM also provides higher-order sensitivities that are useful for gauging parameter interactions and non-linearities.

3.4.1 Time-Dependent Local Sensitivities

First-order local concentration sensitivities are expressed by the following set of partial derivatives

$$z_{ij} = \frac{\partial n_i}{\partial p_j}, \tag{3.9}$$

where z_{ij} defines the sensitivity coefficient of the concentration of n_i to model parameter p_j. There are $N \times M$ concentration sensitivity coefficients for the N species and M parameters in the DMS chemistry model. These sensitivity coefficients are *local* because they consider only infinitesimal changes to the model parameters; they are *first-order* because they account for changes only one parameter at a time.

Taking the derivative of equation 3.1 with respect to parameter p_j and applying the chain

rule leads to the following time-dependent system of concentration sensitivity ODEs

$$\frac{dz_{ij}}{dt} = \frac{\partial \dot{n}_i}{\partial p_j} + \sum_{k=1}^{N} \left(\frac{\partial \dot{n}_i}{\partial n_k} z_{kj} \right), \tag{3.10}$$

where $\dot{n}$ is the right hand side of equation 3.1. Together, equations 3.1 and 3.10 form a coupled system of $N \times (1 + M)$ ODEs for sulfur-based concentrations and concentration sensitivities, which leads to 1,425 equations for the DMS chemistry model ($N = 25$, $M = 56$). These equations are solved simultaneously using DIM. Note, information about the parameter uncertainties is not contained in equation 3.10.

Because the parameters in Table 3.1 have different units, the first-order sensitivity coefficients in equation 3.9 consequently have different units.[3] In order to make direct comparisons between the sensitivity coefficients, they are *normalized* by

$$\frac{\partial \eta_i}{\partial \varrho_j} = \frac{\partial \log n_i}{\partial \log p_j} = \frac{p_j}{n_i} z_{ij}, \tag{3.11}$$

which uses the log-scaled concentrations and parameters. By definition, the normalized sensitivities are unitless and describe the fractional changes of the concentrations for fractional changes to the parameters. Also note, multiplying equation 3.11 by the standard deviation of ϱ_j gives an estimate of the uncertainty in η_i due to the uncertainty in ϱ_j. Thus, these DIM-based sensitivity coefficients are used in section 3.5 to calculate uncertainties in concentrations.

Higher-order sensitivities can also be obtained by further differentiation of equation 3.10 with respect to the model parameters. However, solving for the concentrations and the first- and second-order sensitivity coefficients requires the solution of a coupled system of $N \times (1 + M) \times (1 + M/2)$ equations for N species and M parameters. In the DMS chemistry model this yields a system of 41,325 coupled ODEs. For this reason, higher-order DIM-based sensitivities are not calculated here and are not typically analyzed in models of atmospheric chemistry containing many species and reactions.

3.4.2 Probabilistic and Higher-Order Local Sensitivities

In contrast to *local* sensitivities that are evaluated only at the mean values of the parameters, *probabilistic local* concentration sensitivities cover a relatively large range of parameter values

[3] For instance, concentration sensitivities to first- and second-order parameters have units of molecules cm^{-3} s^{-1} and s^{-1}, respectively.

in the uncertainty space of the parameters. More specifically, this large range is defined in a statistical sense as being parameters sampled from the parameter PDFs prescribed in Section 3.2.3. Probabilistic local sensitivities are important for models of atmospheric chemistry because many of the parameters are highly uncertain and the models are typically nonlinear. In fact, these large uncertainties lead to sensitivities that can vary in magnitude and relative importance to the output concentrations across the parameter uncertainty space.

In theory DIM can calculate probabilistic local sensitivities by repeatedly solving equations 3.1 and 3.10 in a Monte Carlo fashion for sets of randomly sampled parameters from the parameter PDFs. This is not practical, however, given the 10^3 ODEs that need to be solved hundreds to thousands of times. PCM, on the other hand, is an efficient and powerful, albeit approximate, tool for investigating probabilistic local sensitivities as illustrated below.

The first-order PCM-based sensitivity coefficients are obtained by taking the partial derivative of equation 3.7 with respect to input parameter ϱ_q and using the properties of the derivatives of orthogonal polynomials ($\partial g_{j,q}/\partial \varrho_q = j\,\sigma_q^{-1} g_{j-1,q}$) listed in Table 3.3. This leads to

$$\frac{\partial \hat{\eta}}{\partial \varrho_q} = \frac{1}{\sigma_q}\left(\sum_{j=1}^{3} j\,\alpha_{j,q}\,g_{j-1,q}(\xi_q) + \sum_{\substack{k=1 \\ k\neq q}}^{M} \beta_{k,q} g_{1,k}(\xi_k)\right), \tag{3.12}$$

where σ_q equals the standard deviation of ϱ_q. Expression 3.12 clearly shows the probabilistic nature of the concentration sensitivities because the right hand side is a polynomial in the M-dimensional probabilistic space of all ξ. Equation 3.12 also shows that the sensitivity of $\hat{\eta}$ to parameter ϱ_q is coupled to the other parameters through the $\beta_{k,q}$ coefficients, and non-linearly depends on itself through the $\alpha_{3,q}$ coefficients.

Equation 3.12 provides a means for examining local sensitivities at specific parameter values by fixing the values of ξ. For instance, setting $\xi = 0$ for all of the parameters in the above equation equals the local sensitivities at the parameter means. This yields

$$\left(\frac{\partial \hat{\eta}}{\partial \varrho_q}\right)_{\xi=0} = \frac{\alpha_{1,q} - 3\,\alpha_{3,q}}{\sigma_q}, \tag{3.13}$$

which is a simple combination of the first- ($\alpha_{1,q}$) and third-order ($\alpha_{3,q}$) PCE coefficients weighted by the standard deviation of the parameter. Equation 3.13 serves as the basis for comparison with the DIM-based local sensitivities. Likewise, setting $\xi = \pm 1$ in equation 3.12, which equals

the sensitivities for the parameters at $\bar{\varrho} \pm \sigma$, gives

$$\left(\frac{\partial \hat{\eta}}{\partial \varrho_q}\right)_{\xi=\pm 1} = \frac{1}{\sigma_q}\left(\alpha_{1,q} \pm 2\,\alpha_{2,q}\right) \pm \frac{1}{\sigma_q}\sum_{\substack{k=1 \\ k\neq q}}^{M} \beta_{k,q}. \tag{3.14}$$

The sensitivities now include second-order ($\alpha_{2,q}$) and cross term ($\beta_{k,q}$) coefficients. The difference between equations 3.13 and 3.14 indicates that the sensitivities may significantly change as ξ is varied if the magnitudes of the PCE coefficients are relatively large. Thus, the designation of the most influential parameters affecting the concentrations may also change as ξ is varied. This analysis is carried out in Section 3.6.2, where the sensitivities from equation 3.12 are displayed as ξ is varied over the range $|\xi| \leq 1$.

Another powerful advantage to using PCM instead of DIM is the ability to easily generate higher-order sensitivities by further differentiating equation 3.12. Taking the second- and third-order derivatives yields the following second- and third-order sensitivity coefficients

$$\frac{\partial^2 \hat{\eta}}{\partial \varrho_q \partial \varrho_r} = \begin{cases} \left(2\,\alpha_{2,q} + 6\,\alpha_{3,q} g_{1,q}(\xi_q)\right)/\sigma_q^2 & \text{for } q = r \\ \beta_{q,r}/\left(\sigma_q \sigma_r\right) & \text{for } q \neq r \end{cases} \quad \text{and} \quad \frac{\partial^3 \hat{\eta}}{\partial \varrho_q^3} = \frac{6\,\alpha_{3,q}}{\sigma_q^3}, \tag{3.15}$$

where only the homogeneous second-order sensitivities ($q = r$) are functions of ξ. These higher-order sensitivities are generally smaller than the first-order sensitivities, but they can provide insight into couplings between model processes and other non-linearities. The largest second- and third-order sensitivities are discussed and displayed later in Section 3.6.2.

3.5 Uncertainty Analysis

The sensitivity analysis identifies the key parameters that influence the sulfur-based concentrations, but it does not convey information about which parameters are most critical in trying to reduce the overall concentration uncertainties. To accomplish this, the techniques of uncertainty analysis are used, which characterize and quantify the probability density functions of the sulfur-based species resulting from uncertainties in the model parameters.

The uncertainty analysis in this chapter has the following three different components: (1) generate the PDFs of the DMS-related species and compute the first three moments of these PDFs, (2) determine the contributions of individual parameters and parameter pairs to the overall concentration uncertainties, and (3) analyze the variations of the net concentration uncertainties over a wide temperature range.

3.5.1 Probability Density Functions

Two different sets of concentration PDFs are explicitly generated for the DMS-related species using randomly sampled parameters from the parameter PDFs. The first set of PDFs is labeled DIM-M and comes from solving equation 3.1 for concentrations multiple times using a Monte Carlo method. The second set comes from the Monte Carlo evaluation of the PCM polynomial approximations in equation 3.7. These two sets of concentration PDFs are qualitatively discussed and compared later in Section 3.6.3.

Quantitatively, the first three moments of the concentration PDFs are also calculated. The moments are related to expected values of the distributions, where the expected value of a variable x with a PDF $f(x)$ is given by $E[x] = \int x\, f(x)\, dx$. In terms of expected values, the first three moments of the concentration PDFs are

$$\langle \eta \rangle = E[\eta], \quad \sigma_\eta^2 = E[(\eta - \langle \eta \rangle)^2], \text{ and } \gamma_\eta = \frac{E[(\eta - \langle \eta \rangle)^3]}{\sigma_\eta^3}, \tag{3.16}$$

where η is the log-scaled concentration, $\langle \eta \rangle$ is the mean value, σ_η^2 is the variance, and γ_η is the skewness. The mean value sets the magnitude of each concentration PDF, while the variance and skewness are related to the PDF shapes.

The moments of the concentration PDF are computed using three different techniques. The first technique (DIM-S) uses the DIM-based local sensitivity coefficients from a single model run of equations 3.1 and 3.10 at the parameter means to estimate statistical information related to the output concentration distributions. The second technique derives the moments using standard statistical expressions directly on the Monte Carlo generated PDFs from DIM-M. The third technique estimates the moments using PCM by taking expected values of equation 3.7. The specific expressions used to calculate the moments of the concentration PDFs using these three techniques follow.

First Moment - Mean Value

DIM-S The DIM-S estimates of the mean values of the DMS-related species are given by the following expression, which is valid for independent, uncorrelated model parameters:

$$\langle \eta \rangle = \eta(\bar{\varrho}) + \frac{1}{2} \sum_{j=1}^{M} \frac{\partial^2 \eta}{\partial \varrho_j^2} \sigma_j^2 \approx \eta(\bar{\varrho}). \tag{3.17}$$

In this expression $\eta(\bar{\varrho})$ is the value of η obtained from running the model at the parameter means and σ_j is the standard deviation of ϱ_j (Turányi, 1990). The above expression is truncated after the first term because second-order sensitivities are not calculated using DIM. This expression shows that the concentration means are not equal to the model evaluated at the parameter means (that is, $\langle\eta\rangle \neq \eta(\bar{\varrho})$) because of the presence of the second term. In most cases the second term is relatively small, but for strongly non-linear models this approximation may not be valid.

DIM-M The first moments of the Monte Carlo generated DIM-M concentration PDFs are directly calculated using the standard expression for the arithmetic mean

$$\langle\eta\rangle = \frac{1}{S}\sum_{j=1}^{S}\eta_j, \tag{3.18}$$

where S is the Monte Carlo sample size. A sample size of $S = 10^4$ is used for all of the estimates of the moments of the DIM-M PDFs.

PCM Instead of computing the moments from the PCM-generated PDFs, which are functions of the Monte Carlo sample size, *exact* PCM moments are obtained by directly taking the expected values of the terms in the PCEs (that is, by taking the expected value of equation 3.7). This procedure is simplified by noting that the expected value of a sum of polynomials of random variables equals the sum of the expected values, $E[g_{j_1,k}+g_{j_2,\ell}] = E[g_{j_1,k}] + E[g_{j_2,\ell}]$, where j_1 and k may or may not equal j_2 and ℓ, respectively. Moreover, because the model parameters are independent, the expected value of a product of polynomials of different random variables equals the product of the expected values, $E\left[g_{j_1,k}\, g_{j_2,\ell}\right] = E\left[g_{j_1,k}\right] \times E\left[g_{j_2,\ell}\right]$, where j_1 may or may not equal j_2 and $k \neq \ell$. Using these properties, and the additional property $E[g_{j,k}] = 0$ for $j > 0$ (see Table 3.3), the expected value of equation 3.7 gives the first moment simply as

$$\langle\hat{\eta}\rangle = \alpha_0, \tag{3.19}$$

which states that the mean value of each PCE equals its zeroth-order coefficient. It is also worth noting that the PCEs can be used to examine the concentrations at the parameter means by

inserting $\xi = 0$ into equation 3.7. This yields

$$\hat{\eta}_{\xi=0} = \alpha_0 - \sum_{k=1}^{M} \alpha_{2,k}, \tag{3.20}$$

which also shows that there is a difference between the true concentration means (α_0) and the concentrations at the parameter means ($\hat{\eta}_{\xi=0}$). This difference can be large for highly non-linear models in a manner similar to the neglected higher-order terms in the estimate of $\langle\eta\rangle$ using DIM-S.

Second Moment - Variance

PDF widths are related to the second moment, or variance, which depends on the amount of uncertainty that the uncertain parameters contribute to the concentrations.

DIM-S The estimate of the variance using DIM-S is given by

$$\sigma_\eta^2 = \sum_{j=1}^{M} \left(\frac{\partial\eta}{\partial\varrho_j}\right)^2 \sigma_j^2 + \sum_{j=1}^{M} \frac{\partial\eta}{\partial\varrho_j}\frac{\partial^2\eta}{\partial\varrho_j^2} E[(\varrho_j - \bar{\varrho}_j)^3] \approx \sum_{j=1}^{M} \left(\frac{\partial\eta}{\partial\varrho_j}\right)^2 \sigma_j^2, \tag{3.21}$$

which is a function of the first- and second-order local sensitivities and the second and third central moments of ϱ_j (Turányi, 1990). As with the DIM-S estimate of the mean, this expression is truncated after the first term for three reasons: (1) the second term is usually much smaller than the first, (2) ODESSA does not calculate second-order sensitivities, and (3) the third moments of the parameters are not known. The truncated expression allows for estimates of the concentration uncertainties using only the first-order local sensitivities and parameter uncertainties.

DIM-M The variances from the Monte Carlo generated DIM-M concentration PDFs are directly calculated using the standard expression

$$\sigma_\eta^2 = \frac{1}{S}\sum_{j=1}^{S} \left(\eta_j - \langle\eta\rangle\right)^2, \tag{3.22}$$

which, again, is a function of the Monte Carlo sample size (S).

PCM Calculating the PCM-based variance requires taking the expected values of the various terms in the expansion of $(\hat{\eta} - \alpha_0)^2$, which is slightly more complicated than the calculation of the mean $\langle\hat{\eta}\rangle$. The expansion results in three different types of products of orthogonal polynomials. The first type involves expected values of products between the pure terms, $E\left[\alpha_{j_1,k}\, g_{j_1,k}\, \alpha_{j_2,\ell}\, g_{j_2,\ell}\right]$. It is easy to show that these expected values equal zero unless $j_1 = j_2$ and $k = \ell$, and thus only the squares of the pure terms contribute. Next, products between the pure and cross terms have to be considered, $E\left[\alpha_{j_1,k}\, g_{j_1,k}\, \beta_{\ell,m}\, g_{1,\ell}\, g_{1,m}\right]$. These expected values always equal zero because $\ell \neq m$. Finally, products between the cross terms give $E\left[\beta_{k,\ell}\, g_{1,k}\, g_{1,\ell}\, \beta_{m,n}\, g_{1,m}\, g_{1,n}\right]$, which trivially equals zero unless $k = m$ and $\ell = n$. Putting these together, and using the expected values from Table 3.3, the PCM-based variance is

$$\sigma^2_{\hat{\eta}} = \sum_{j=1}^{M} \left(\alpha^2_{1,j} + 2\,\alpha^2_{2,j} + 6\,\alpha^2_{3,j}\right) + \sum_{j=1}^{M-1} \sum_{k=j+1}^{M} \beta^2_{j,k}, \tag{3.23}$$

which is a simple combination of the squares of the PCE coefficients. Note that the summations in equations 3.21 and 3.23 are over parameters, which provides the methodology for analyzing parameter variance contributions discussed later.

Third Moment - Skewness

The degree of distribution asymmetry is quantified by the skewness, where values close to zero indicate nearly symmetric PDFs, large positive values indicate significant tails to the right of the mean, and large negative values indicate significant tails to the left.

DIM-M The skewness of each concentration PDF is estimated directly from the Monte Carlo generated DIM-M PDFs using the standard expression

$$\gamma_\eta = \frac{1}{S\,\sigma^3_\eta} \sum_{j=1}^{S} \left(\eta_j - \langle\eta\rangle\right)^3, \tag{3.24}$$

where S is the Monte Carlo sample size.

PCM The PCM-based skewness is obtained by taking the expected values of the terms in the expansion of $(\hat{\eta} - \alpha_0)^3$. The various PCE coefficient combinations are determined by considering all of the possible products of orthogonal polynomials as was done for the PCM-based variance. However, given the large number of products and terms in the expansion, the

details of the derivation are not given here. Rather, the resulting expression for the PCM-based skewness is quoted below:

$$\gamma_{\hat{\eta}} = \frac{1}{\sigma_{\hat{\eta}}^3}\left\{\sum_{j=1}^{M}\left(8\,\alpha_{2,j}^3 + 6\,\alpha_{1,j}^2\alpha_{2,j} + 36\,\alpha_{1,j}\alpha_{2,j}\alpha_{3,j} + 108\,\alpha_{2,j}\alpha_{3,j}^2\right) + \cdots \right. \tag{3.25}$$
$$\left. \cdots + 6\sum_{j=1}^{M-1}\sum_{k=j+1}^{M}\left[\beta_{j,k}\alpha_{1,j}\alpha_{1,k} + \beta_{j,k}^2\left(\alpha_{2,j} + \alpha_{2,k}\right)\right] + 6\sum_{j=1}^{M-2}\sum_{k=j+1}^{M-1}\sum_{\ell=k+1}^{M}\beta_{j,k}\beta_{j,\ell}\beta_{k,\ell}\right\}.$$

The numerical coefficients in this expression are combinations of the multinomial coefficients in the expansion $(3!/p_1!\ p_2!\ p_3!$, where the p_i's, are the respective powers of the coefficients in the given term), the expected values from Table 3.3, and the expected values for products of orthogonal polynomials of the same variable and different order (i.e., $E[g_1^2\,g_2] = 2$, $E[g_1\,g_2\,g_3] = 6$, and $E[g_2\,g_3^2] = 36$). As with the PCM-based variance expression, this skewness equation potentially can be used to calculate parameter contributions to the total skewness, but this analysis is not carried out here.

3.5.2 Uncertainty Contributions

The variances of the concentration PDFs provide a measure of the net uncertainties in the modeled concentrations induced by uncertainties in the model parameters. The analysis of the variance is taken one step further, because the net concentration uncertainties are sums of uncertainty contributions from the individual parameters and combinations of parameters. By arranging these variance contributions according to magnitude, the key parameters contributing the largest amounts of uncertainty are easily identified. This, in turn, allows for a potential reduction of model error by gaining better knowledge about a subset of the model parameters rather than blindly trying to improve the full parameter set.

Of the three variance estimates from the previous section, only the DIM-S and PCM expressions (equations 3.21 and 3.23) are used to compute variance contributions because their variance expressions are explicitly in terms of summations of model parameters. These fractional variance contributions are specified by:

$$\overbrace{\frac{\left(\partial\eta/\partial\varrho_j\right)^2\sigma_j^2}{\sigma_{\hat{\eta}}^2}}^{\text{DIM-S}}, \quad \overbrace{\frac{\alpha_{1,j}^2 + 2\,\alpha_{2,j}^2 + 6\,\alpha_{3,j}^2}{\sigma_{\hat{\eta}}^2}}^{\text{PCM-homogeneous}}, \text{ and } \quad \overbrace{\frac{\beta_{j,k}^2}{\sigma_{\hat{\eta}}^2}}^{\text{PCM-cross}}, \tag{3.26}$$

where j and k are parameter indices ($j \neq k$) and the partial derivative in the DIM-S expression is the first-order local sensitivity coefficient. These expressions clearly show an important advantage of PCM over DIM-S, because PCM accounts for uncertainty contributions from pairs of model parameters. Thus, PCM is useful for evaluating the effects of uncertain coupled processes on the overall concentration uncertainties.

3.5.3 Uncertainty Dependence on Temperature

Temperature impacts the uncertainties of the DMS-related species in two distinct ways. First, many of the model parameters in Table 3.1 are exponential functions of temperature, which results in reaction rates that depend strongly on temperature. For instance, the rate of DMS oxidation by OH changes considerably as temperature increases from low values, where OH-addition is favored, to relatively high values, where H-abstraction is dominant. Therefore, at low temperatures the sulfur-based concentration uncertainties are less likely to have contributions from the uncertain DMS+OH abstraction rate constant. Second, not only do the reaction rates depend on temperature, but many of the parameter uncertainties –as shown by equation 3.5– are also explicit exponential functions of temperature. These parameter uncertainty functions are formulated on the premise that the photochemical rate constants are most certain at room temperature, and less certain at other temperatures.

These two temperature-uncertainty effects may offset at one temperature and reinforce at another, because a particular reaction rate may decrease with falling temperature while its uncertainty increases. The DMS+OH abstraction reaction is a prime example, because the reaction rate decreases as temperature falls from 298 K, while the uncertainty in the rate constant increases. These two effects lead to possible non-linearities in the temperature-dependence of the concentration uncertainties. These potential non-linear temperature effects are diagnosed by calculating the sulfur-based concentrations and concentration uncertainties over a temperature range of 250-310 K, keeping all of the other conditions in Table 3.2 fixed.

3.6 Results and Discussion

The model is integrated until a repetitive diurnal cycle is achieved for all of the gas-phase sulfur-based species. The following sensitivity and uncertainty analysis is carried out for the final day of this integration. Recall, DIM integrates the concentration and concentration sensitivity ODEs nearly continuously with time (see equations 3.1 and 3.10), so explicit diurnal profiles

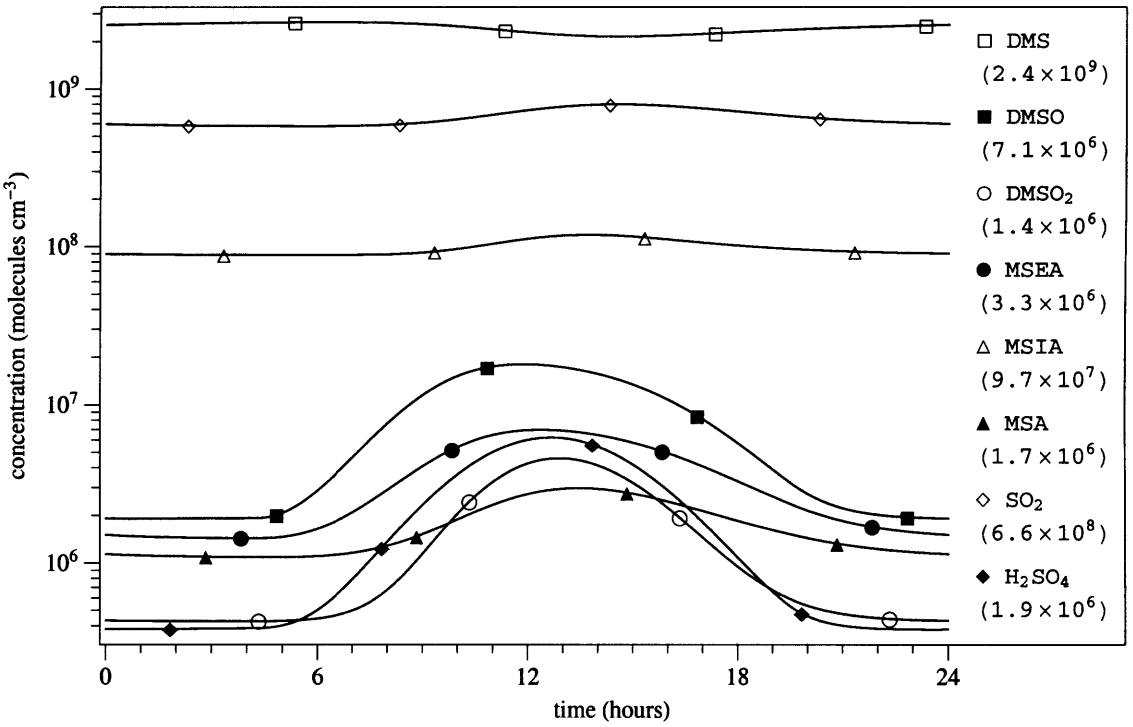

Figure 3-4: Diurnal cycles of the number concentrations (molecules cm^{-3}) of DMS, DMSO, $DMSO_2$, MSEA, MSIA, MSA, SO_2, and H_2SO_4. The labels on the individual profiles are given to the right and the daily average concentrations are given in parentheses.

are shown for the DIM-based solutions. PCM, on the other hand, is applied instantaneously in time. Therefore, two times are chosen for the PCM analysis, corresponding to the instantaneous values at 12:00 and 18:00. These two times allow for a detailed comparison between periods of active (12:00) and relatively in-active (18:00) photochemistry.

3.6.1 Concentrations

Diurnal Concentration Cycles

The diurnal cycles for the major DMS-related species calculated using DIM are displayed in Figure 3-4. As shown in the figure, DMS, SO_2, and MSIA exhibit diurnal cycles with noticeably smaller amplitudes (less than a factor of 2) than the cycles for the other species. Although DMS, SO_2, and MSIA are directly oxidized by OH, they are also strongly affected by non-photochemical processes –such as mixing into or out of the RMBL– that "dampen" the diurnal affects of OH oxidation. The species with large amplitudes, on the other hand, have sources

and/or sinks dominated by chemistry, so their amplitudes are greatly affected by changes in OH concentrations.

Besides the amplitudes, the phases of the diurnal cycles are also indicative of the major processes affecting the DMS-related species. For instance, species with cycles that have large amplitudes tend to peak at or near local noon, which indicates that photochemistry is a major factor driving their production. The cycles for DMS, SO_2, and MSIA, however, have inflection points near local noon, which indicates that non-photochemical processes play important roles.

The diurnal cycle of DMS is also strongly anti-correlated with the cycles for SO_2 and MSIA, which results from the photochemical conversion of DMS into these species. The DMS-SO_2 anti-correlation in the RMBL has been both observed and modeled (Davis et al., 1999; Chen et al., 2000), and serves as primary evidence that SO_2 in the marine environment is photochemically produced from DMS oxidation. The phases of the simulated DMS and SO_2 diurnal cycles in Figure 3-4 agree with the modeled cycles by Davis et al. (1999) and Chen et al. (2000); in particular the maxima and minima occur at roughly the same times. The diurnal amplitudes of DMS and SO_2 in Figure 3-4, however, are smaller than the amplitudes in the Davis et al. (1999) and Chen et al. (2000) studies. These amplitude differences are probably due to the different strengths of the OH cycles, because their studies are for the equatorial Pacific compared to the mid-latitude Pacific conditions employed here.

Concentration Correlations

Before comparing the sensitivities and uncertainties of the DMS-related species, it is important to first ensure that the PCE approximations of the output concentrations using PCM are consistent with the concentrations calculated by directly integrating the true model using DIM. The PCEs are tested by comparing the concentrations from the two methods (equation 3.1 from DIM versus equation 3.7 from PCM) for common sets of randomly sampled parameters from the parameter PDFs.

Using sample sizes of 10^3, two separate groups of correlations for the instantaneous concentrations at 12:00 and 18:00 were generated and are shown in Figure 3-5. Also shown are the coefficient of determination (R^2) and index of agreement (d), which are two common measures of the statistical agreement between the concentrations. First note that the concentrations at 12:00 are either smaller or larger than the 18:00 values as determined by the phases and peaks of the previously displayed diurnal cycles. Next, as indicated in the figure, both groups of correlations are very high because the values of R^2 and d are close to unity for all of the species. Also,

these strong concentration correlations hold by as much as four orders of magnitude for many of the species. These strong correlations, overall, suggest that using PCEs with third-order pure terms and second-order cross terms sufficiently represent the true model concentrations at 12:00 and 18:00. Further, because there are also no significant biases towards the DIM- or PCM-generated concentrations, any subsequent differences between DIM- and PCM-based sensitivities and uncertainties are likely due to the inherent ability of PCM to capture model non-linearities.

Concentrations in ξ-Space

Applying PCM at 12:00 and 18:00 leads to the set of PCEs for the DMS-related species shown in Table 3.4. These PCEs are functions of the ξ's described in Section 3.3. Due to a lack of space, only the six largest PCE coefficients after the leading term are shown in the table. Note that the leading PCE terms are the concentrations at the parameter means given by equation 3.20. The signs of the PCE coefficients $(+/-)$ indicate whether the concentrations depend positively or negatively on the specified parameter. The signs of the non-linear PCE coefficients also signal whether the concentration PDFs generated from these PCEs will be skewed to the left $(-)$ or right $(+)$ of the mean. Even in their truncated forms, these PCEs indicate that non-linearities and parameter couplings play an important role in determining the concentrations. For instance, the concentration of SO_2 in ξ-space depends on non-linear combinations of heterogeneous removal (ξ_{53}), DMS emissions (ξ_{55}), and RMBL mixing (ξ_{56}).

By evaluating the PCEs in Table 3.4 as functions of the ξ's, the dependencies of the sulfur-based concentrations on the uncertain parameters are ascertained. Because these PCEs are functions in a 56-dimensional parameter space, it is difficult to directly interpret them. However, by looking at 1-D slices through the 56-dimensional space, preliminary information about concentration sensitivities, uncertainties, and non-linearities is obtained. To do this, a single ξ_q is allowed to vary while all other ξ_r's $(r \neq q)$ are set to zero –which expresses variations in a single model parameter and equates all others to their mean values.

Figure 3-6 shows 1-D slices of the DMS-related concentrations at 12:00 and 18:00 as the DMS+OH abstraction and addition rate constants (ξ_1 and ξ_3) vary over $|\xi| \leq 1$. The curves cross at $\xi = 0$, where the concentrations are at the mean values of all the model parameters. Positive and negative slopes in the figure are related to the concentration sensitivities.

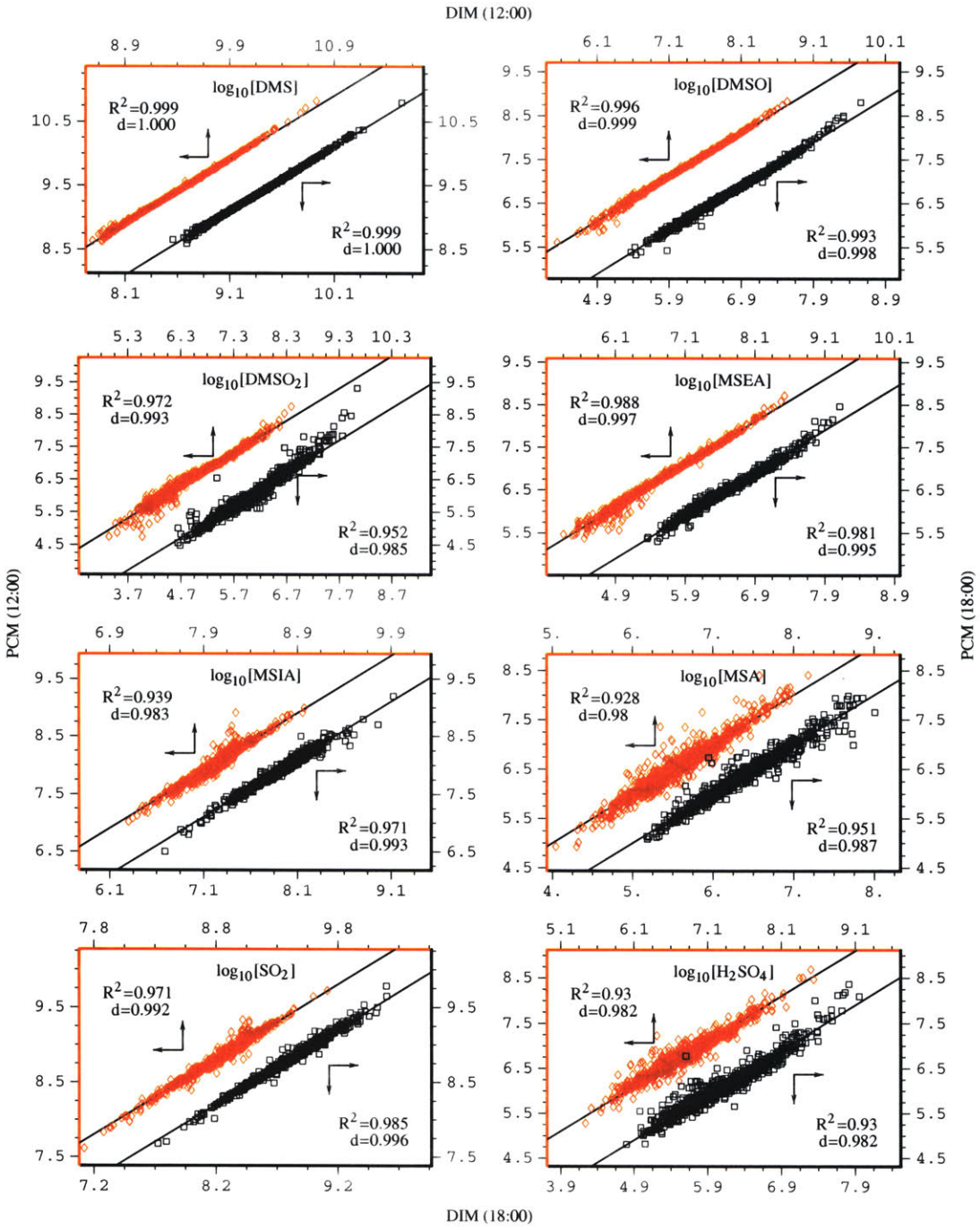

Figure 3-5: Logarithmic concentration correlations at 12:00 and 18:00 using DIM and PCM. The correlations at 12:00 are displayed by the red diamonds using the upper/left axes. The correlations at 18:00 are displayed by the black squares using the lower/right axes. The correlations were calculated using common sets of randomly sampled parameters for a sample size of 10^3. Also shown are the 1:1 lines, the coefficients of determination (R^2), and the indices of agreement (d).

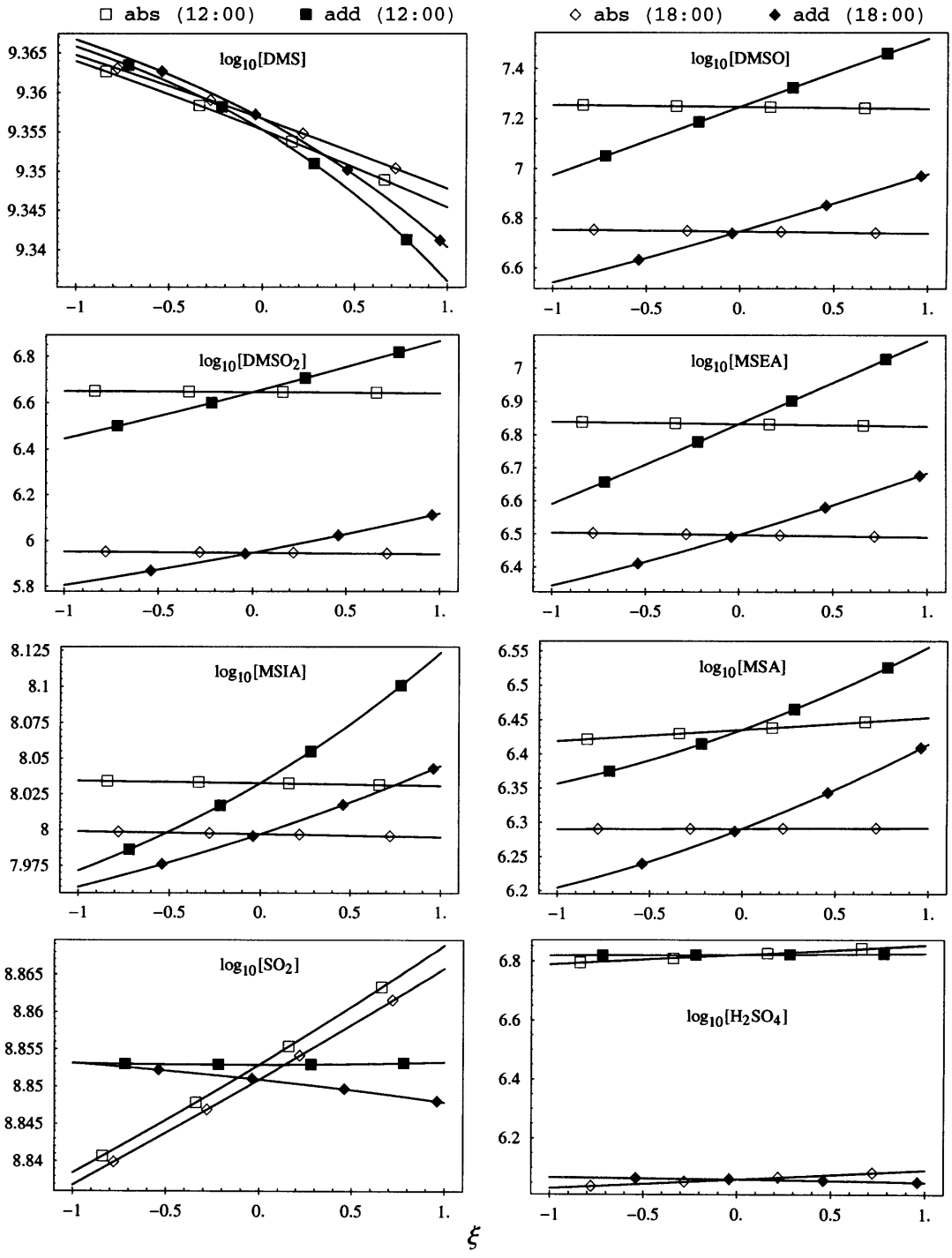

Figure 3-6: Changes in the DMS-related concentrations at 12:00 (squares) and 18:00 (diamonds) for variations in the DMS+OH abstraction (empty) and addition (filled) rate constants. The rate constants are varied as a function of ξ, where $|\xi| = 1$ is 1-σ from the rate constant mean.

Table 3.4: Polynomial Chaos Expansions of the DMS-Related Species

12:00

$$\hat{\eta}(\text{DMS}) \approx 9.36 + 0.339\,\xi_{55} - 0.129\,\xi_{56} + 0.028\,\xi_{55}^2 - 0.020\,\xi_{55}\,\xi_{56} - 0.014\,\xi_3 + 0.010\,\xi_4 + \cdots$$

$$\hat{\eta}(\text{DMSO}) \approx 7.25 + 0.323\,\xi_{55} + 0.274\,\xi_3 - 0.161\,\xi_4 - 0.132\,\xi_{56} - 0.123\,\xi_{48} + 0.067\,\xi_5 + \cdots$$

$$\hat{\eta}(\text{DMSO}_2) \approx 6.65 - 0.261\,\xi_9 + 0.251\,\xi_{55} + 0.237\,\xi_8 - 0.219\,\xi_{49} + 0.213\,\xi_3 - 0.134\,\xi_4 + \cdots$$

$$\hat{\eta}(\text{MSEA}) \approx 6.83 + 0.312\,\xi_6 + 0.291\,\xi_{55} + 0.247\,\xi_3 - 0.170\,\xi_{14} - 0.152\,\xi_4 - 0.122\,\xi_{56} + \cdots$$

$$\hat{\eta}(\text{MSIA}) \approx 8.03 - 0.176\,\xi_{51} + 0.084\,\xi_{55} + 0.075\,\xi_3 + 0.053\,\xi_{56} - 0.052\,\xi_{55}\,\xi_{56} - 0.042\,\xi_3\,\xi_{56} + \cdots$$

$$\hat{\eta}(\text{MSA}) \approx 6.44 - 0.235\,\xi_{52} + 0.217\,\xi_{55} + 0.125\,\xi_{47} + 0.119\,\xi_6 + 0.110\,\xi_{40} + 0.100\,\xi_3 + \cdots$$

$$\hat{\eta}(\text{SO}_2) \approx 8.85 - 0.182\,\xi_{53} + 0.089\,\xi_{55} - 0.055\,\xi_{55}\,\xi_{56} + 0.041\,\xi_{56} - 0.036\,\xi_{53}^2 + 0.028\,\xi_{55}^2 + \cdots$$

$$\hat{\eta}(\text{H}_2\text{SO}_4) \approx 6.82 - 0.236\,\xi_{54} + 0.207\,\xi_{55} - 0.170\,\xi_{25} + 0.139\,\xi_{45} + 0.139\,\xi_{24} - 0.087\,\xi_{53} + \cdots$$

18:00

$$\hat{\eta}(\text{DMS}) \approx 9.36 + 0.339\,\xi_{55} - 0.116\,\xi_{56} + 0.028\,\xi_{55}^2 - 0.020\,\xi_{55}\,\xi_{56} - 0.013\,\xi_3 + 0.010\,\xi_4 + \cdots$$

$$\hat{\eta}(\text{DMSO}) \approx 6.75 - 0.315\,\xi_{48} + 0.263\,\xi_{55} + 0.221\,\xi_3 - 0.129\,\xi_4 - 0.088\,\xi_{56} + 0.051\,\xi_5 + \cdots$$

$$\hat{\eta}(\text{DMSO}_2) \approx 5.95 - 0.458\,\xi_{49} + 0.186\,\xi_8 + 0.175\,\xi_{55} + 0.155\,\xi_3 - 0.151\,\xi_9 + 0.104\,\xi_{49}\,\xi_{56} + \cdots$$

$$\hat{\eta}(\text{MSEA}) \approx 6.50 + 0.225\,\xi_6 + 0.208\,\xi_{55} + 0.173\,\xi_3 - 0.133\,\xi_{50} - 0.133\,\xi_{47} - 0.101\,\xi_4 + \cdots$$

$$\hat{\eta}(\text{MSIA}) \approx 8.00 - 0.234\,\xi_{51} + 0.050\,\xi_{56} + 0.049\,\xi_{56} + 0.046\,\xi_{55} + 0.042\,\xi_3 - 0.041\,\xi_{51}^2 + \cdots$$

$$\hat{\eta}(\text{MSA}) \approx 6.29 - 0.347\,\xi_{52} + 0.160\,\xi_{55} + 0.116\,\xi_6 + 0.115\,\xi_{47} + 0.105\,\xi_3 + 0.092\,\xi_{46} + \cdots$$

$$\hat{\eta}(\text{SO}_2) \approx 8.85 - 0.228\,\xi_{53} + 0.077\,\xi_{55} + 0.046\,\xi_{53}\,\xi_{56} - 0.043\,\xi_{55}\,\xi_{56} - 0.042\,\xi_{53}^2 + 0.023\,\xi_{56} + \cdots$$

$$\hat{\eta}(\text{H}_2\text{SO}_4) \approx 6.06 - 0.276\,\xi_{54} + 0.217\,\xi_{55} - 0.176\,\xi_{25} + 0.172\,\xi_{45} + 0.171\,\xi_{24} - 0.146\,\xi_{12} + \cdots$$

PCEs are in terms of the standard normal random variables ξ_k, where k denotes the parameter number listed in Table 3.1. The leading term in the PCEs equals $\hat{\eta}$ evaluated at $\xi = 0$ as given by equation 3.20. PCEs are ordered by the magnitudes of the coefficients and are truncated after the sixth largest coefficient. The full PCEs are available upon request.

Positive slopes, for instance, indicate concentrations that increase as the DMS+OH rate constants increase. With increasing DMS+OH rate constants, therefore, the concentration of DMS decreases and the other species mainly increase.

The magnitudes of the slopes in Figure 3-6 indicate the degree of sensitivity of the concentrations to the DMS+OH addition and abstraction reactions. In one trend, the sensitivities of most of the species to these reactions decrease from 12:00 to 18:00 because the species are less dependent on chemistry away from the noontime peak in photochemistry. Another obvious trend is related to branching of the oxidized sulfur-based products in the DMS oxidation mechanism. For instance, DMSO, DMSO_2, MSEA, and MSIA lie solely along the OH-addition branch, so they show a large sensitivity to DMS+OH addition and negligible sensitivity to DMS+OH abstraction. That is, their slopes for OH-addition are larger than their H-abstraction slopes.

Likewise, SO_2 and H_2SO_4 –which lie primarily lie along the H-abstraction branch– show stronger sensitivities to the DMS+OH abstraction reaction.

The magnitudes of the slopes also highlight the amount of uncertainty that the uncertain DMS+OH reactions contribute to the sulfur-based concentrations. For example, the uncertainty in DMS+OH addition imparts significant uncertainty in DMSO, $DMSO_2$, and MSEA, but only minor to negligible uncertainty in the other species. The qualitative sensitivity and uncertainty issues touched on here are quantified in the following sections.

3.6.2 Sensitivities

Diurnal First-Order Local Sensitivity Cycles

Given that the model is forced by OH concentrations that vary with time, the first-order local concentration sensitivities also vary with time. Figures 3-7 and 3-8 show the diurnal cycles of the normalized, first-order local sensitivity coefficients for the major species in the DMS mechanism. These plots were derived by solving the sensitivity ODEs using DIM (equation 3.10) and normalized using equation 3.11. The key model parameters that influence the concentrations of the DMS-related species are the sensitivity coefficients with the largest magnitudes highlighted in the figures.

It is readily apparent from Figures 3-7 and 3-8 that the majority of the sensitivity coefficients are extremely time-dependent. Many of the sensitivity coefficients change rapidly in magnitude near midday and some even change their sign (i.e., from positive to negative or visa versa). Although this time-dependence is very complex, some common features occur throughout the set of sensitivity coefficients that simplify the analysis. These features are related to the type of model parameter –chemical production or loss, mixing into or out of the RMBL, heterogeneous loss, or DMS emissions– as described below:

1. Reactions that influence the production (loss) of a particular species yield positive (negative) sensitivity coefficients with magnitudes that peak at or near midday and diminish at other times. Two examples include the sensitivity of DMSO concentrations to reactions involving OH-addition to DMS (parameter 3) and DMSO (parameter 7). Physically, this behavior is due to the fact that many of the reaction rates are largest during midday when the photochemistry is most active.

2. The magnitude and sign of the sensitivity to the RMBL mixing coefficient (parameter 56) depends on the magnitude and sign of the difference $(\bar{n} - n)$ in equation 3.1. Considering

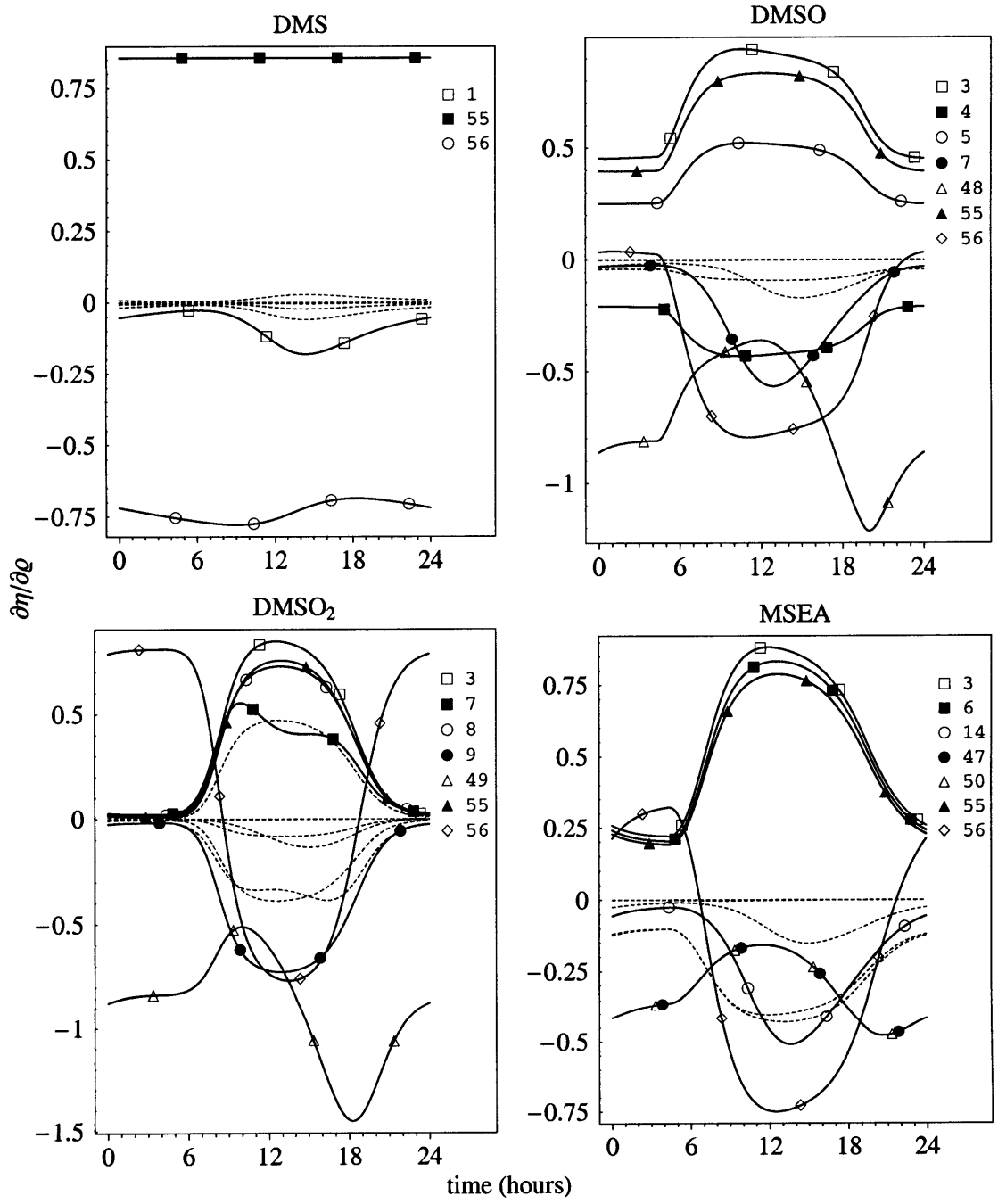

Figure 3-7: Diurnal cycles of the normalized, first-order local sensitivity coefficients for DMS, DMSO, $DMSO_2$, and MSEA calculated using equations 3.10 and 3.11. The sensitivity coefficients with the largest magnitudes are shown by the dark solid lines and are individually labeled on the right. All other sensitivities are shown using gray+dashed lines. Refer to Table 3.1 for the processes corresponding to the parameter numbers.

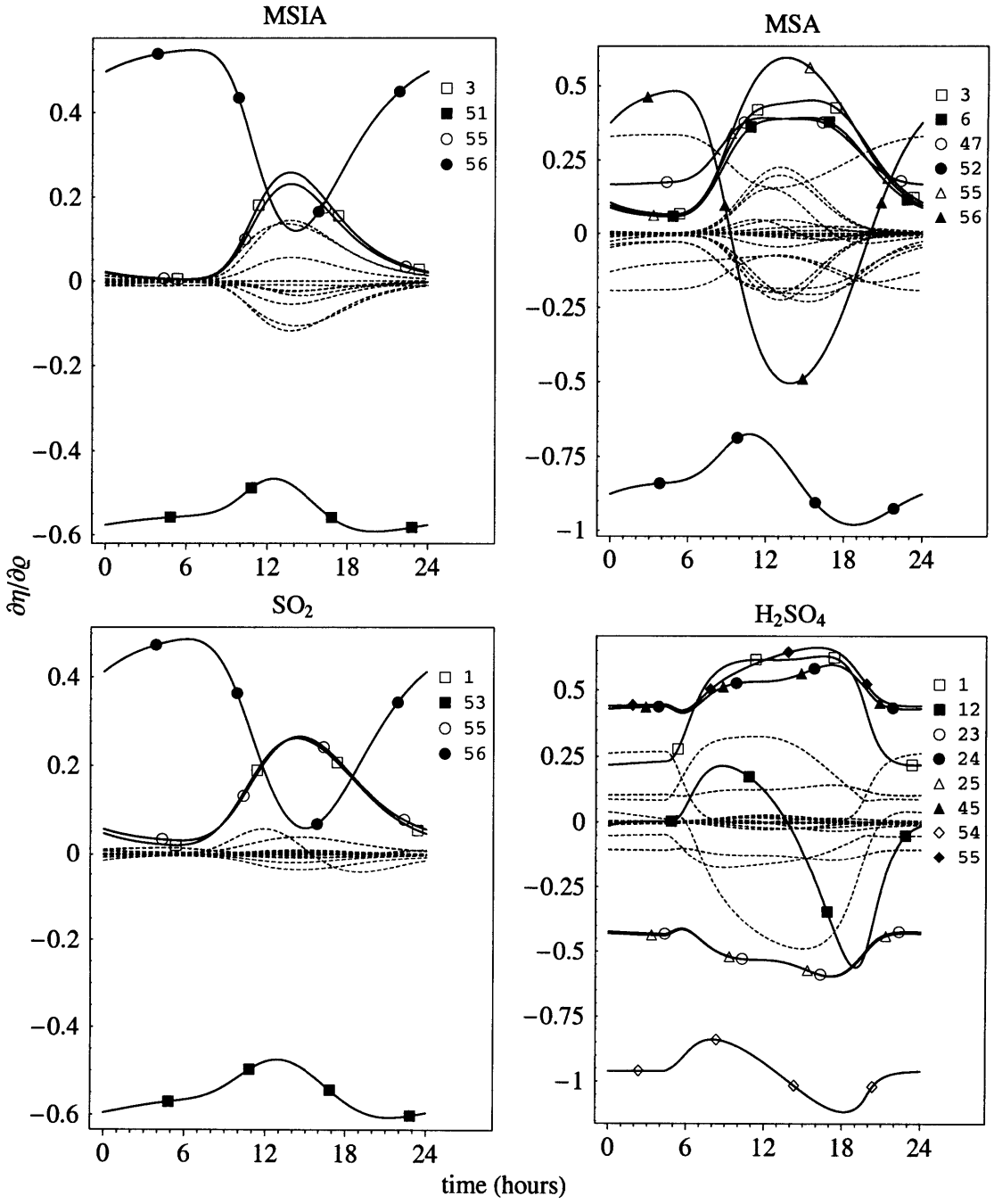

Figure 3-8: Same as Figure 3-7 for MSIA, MSA, SO_2, and H_2SO_4.

$DMSO_2$ for instance, during the early and late portions of the day $\bar{n} \gg n$, so the flux of $DMSO_2$ into the RMBL is large during these times. This results in a large and positive sensitivity of $DMSO_2$ to the RMBL mixing coefficient at the beginning and end of the day. At midday, however, $DMSO_2$ levels are built up in RMBL yielding $\bar{n} \ll n$. This results in a large flux out of the RMBL and a sensitivity of $DMSO_2$ to the mixing coefficient that is large and negative. Many of the other species show similar trends in their sensitivity to RMBL mixing, with magnitudes that are smallest at midday and larger otherwise.

3. The sensitivities of the oxidized sulfur-based species to heterogeneous removal (parameters 48-54) are always negative, but have magnitudes that are smallest between morning and noon. The magnitudes of these sensitivities decrease during this time because the active photochemistry dominates the changes to the concentrations.

4. Although all of the species are positively sensitive to changes in DMS emissions (parameter 55), only the sensitivity of DMS concentrations to DMS emissions does not exhibit a diurnal cycle. This sensitivity is linear because a change in DMS emissions always results in a proportional change in the concentration of DMS. For the other species, however, a change in DMS emissions results in a change in concentration of DMS, which is then subject to photochemical oxidation. Thus, the sensitivities of the other species to DMS emissions have cycles that follow the photochemical cycle.

One common application of sensitivity analyses is to rank the parameters affecting a model output from very important to non-influential on the basis of the magnitudes of the sensitivity coefficients. Because the sensitivity coefficients in Figures 3-7 and 3-8 are strong functions of time, the identity of the most important parameters also changes with time. For example, the concentration of H_2SO_4 is nearly equally sensitive to the DMS+OH abstraction (parameter 1) and CH_3SO+O_2 (parameter 24) reaction rate constants during the day. In the early morning and late evening, however, H_2SO_4 is much more sensitive to the latter than the former.

Despite the fact that the ratings of the sensitivities change with time, some general conclusions can still be drawn about the key parameters that influence the DMS-related concentrations over the course of a day. Using Figures 3-7 and 3-8 as a guide, and referring to the parameter numbers in Table 3.1, these key parameter sensitivities are:

- DMS is primarily sensitive to the parameters for oceanic emissions and mixing out of the RMBL, and moderately sensitive to the DMS+OH abstraction rate constant. The rate

constant for the oxidation of DMS by NO_3 is not a key sensitivity, even at night, because the concentration of NO_3 is sufficiently low and does not contribute to the loss of DMS.

- DMSO is sensitive to parameters for DMS emissions, RMBL mixing, heterogeneous removal, and chemical reaction rate constants involving the formation and loss of the DMS-OH adduct and DMSO.

- $DMSO_2$ is sensitive to parameters for DMS emissions, RMBL mixing, heterogeneous removal, the DMS+OH addition reaction, and rate constants involving the formation and loss of the DMSO-OH adduct.

- MSEA is sensitive to parameters for DMS emissions, RMBL mixing, heterogeneous removal, DMS+OH addition, and the production and loss reaction rate constants of MSEA.

- MSIA is sensitive to parameters for DMS emissions, RMBL mixing, heterogeneous removal, and the DMS+OH addition rate constant.

- MSA is mainly sensitive to parameters for DMS emissions, RMBL mixing, heterogeneous loss, the rate constant for DMS+OH addition, the rate constants associated with the formation of MSEA, and the parameterized rate constant converting MSEA into MSA.

- SO_2 is markedly sensitive to parameters related to DMS emissions, RMBL mixing, heterogeneous loss, and the DMS+OH abstraction rate constant. Note that SO_2 does not show any significant sensitivity to CH_3SO_2 dissociation (parameter 38) even though it is a direct precursor to SO_2. This finding contradicts Saltelli and Hjorth (1995), who found CH_3SO_2 dissociation to be a critical reaction for both SO_2 and H_2SO_4. The major reason for this difference involves the fact that Saltelli and Hjorth (1995) did not include non-photochemical processes in their study.

- H_2SO_4 is sensitive to many parameters, including those for DMS emissions, heterogeneous loss, and the rate constants for DMS+OH abstraction, the reaction between CH_3SCH_2OO and NO, reactions of CH_3SO with O_2 and O_3, and the isomerization of $CH_3S(O)OO$ into CH_3SO_3.

Another discernible feature in Figures 3-7 and 3-8 is related to the number of parameters a given sulfur-based species is sensitive to. From the figures, highly oxidized species tend to be sensitive to more parameters than less oxidized species. For instance, DMS and MSEA are sensitive to a smaller number of chemical reaction rate constants than $DMSO_2$ and MSA. This

characteristic is merely a consequence of the number of precursors affecting a given species. To illustrate, DMS shows appreciable sensitivity to only one rate constant (DMS+OH abstraction), while $DMSO_2$ shows large sensitivities to many. For this reason, all of the species are sensitive to some degree to the rate constants for the H-abstraction and/or OH-addition reactions with DMS.

Finally, by identifying the largest sensitivity coefficients, the number of parameters required in the mechanism can potentially be reduced. For global atmospheric chemical modeling, accurate reduced-form mechanisms are attractive alternatives to full mechanisms because the chemical calculations typically consume large portions of computer time. But, as indicated in Figures 3-7 and 3-8, the DMS-related species have significant sensitivities to many parameters. This means that it is difficult to reduce the DMS scheme down to a small number of reactions. For instance, if only those model parameters are kept that cause concentration sensitivities within 50% of the largest sensitivity for each species, then the original mechanism is reduced by less than half, from 56 to 34 parameters. Reducing the number of required parameters in the DMS chemistry model depends on the species of interest, however. If DMS and SO_2 are the only desired species, then the model could possibly be reduced down to just a few parameters. To properly model H_2SO_4, on the other hand, requires many reactions and processes.

Comparison of First-Order Local Sensitivities

Although DIM provides concentration sensitivities as a function of time, practical applications of DIM to atmospheric chemical mechanisms are limited to first-order local sensitivities. Alternatively, PCM can readily analyze higher-order sensitivities. Before analyzing these higher-order sensitivities, however, the reliability of the PCM-based sensitivities must first be tested. This section scrutinizes the PCM sensitivities by comparing the first-order local sensitivity coefficients calculated independently using DIM and PCM at 12:00 and 18:00.

Recall that the first-order PCM-based concentration sensitivities are of a probabilistic nature because the partial derivatives are functions of ξ. Setting $\xi = 0$ in equation 3.12 gives the local sensitivities at the parameter means (see equation 3.13), which then allows for a direct comparison with the corresponding sensitivities in DIM. This comparison is shown in Figure 3-9 for DIM and PCM at 12:00 and 18:00. Due to the large number of model parameters, comparisons are made only for the concentration sensitivities with the largest magnitudes.

The DIM and PCM sensitivity coefficients in Figure 3-9 agree in sign and magnitude for all of the DMS-related species and parameters. The agreement even holds over time, as exemplified

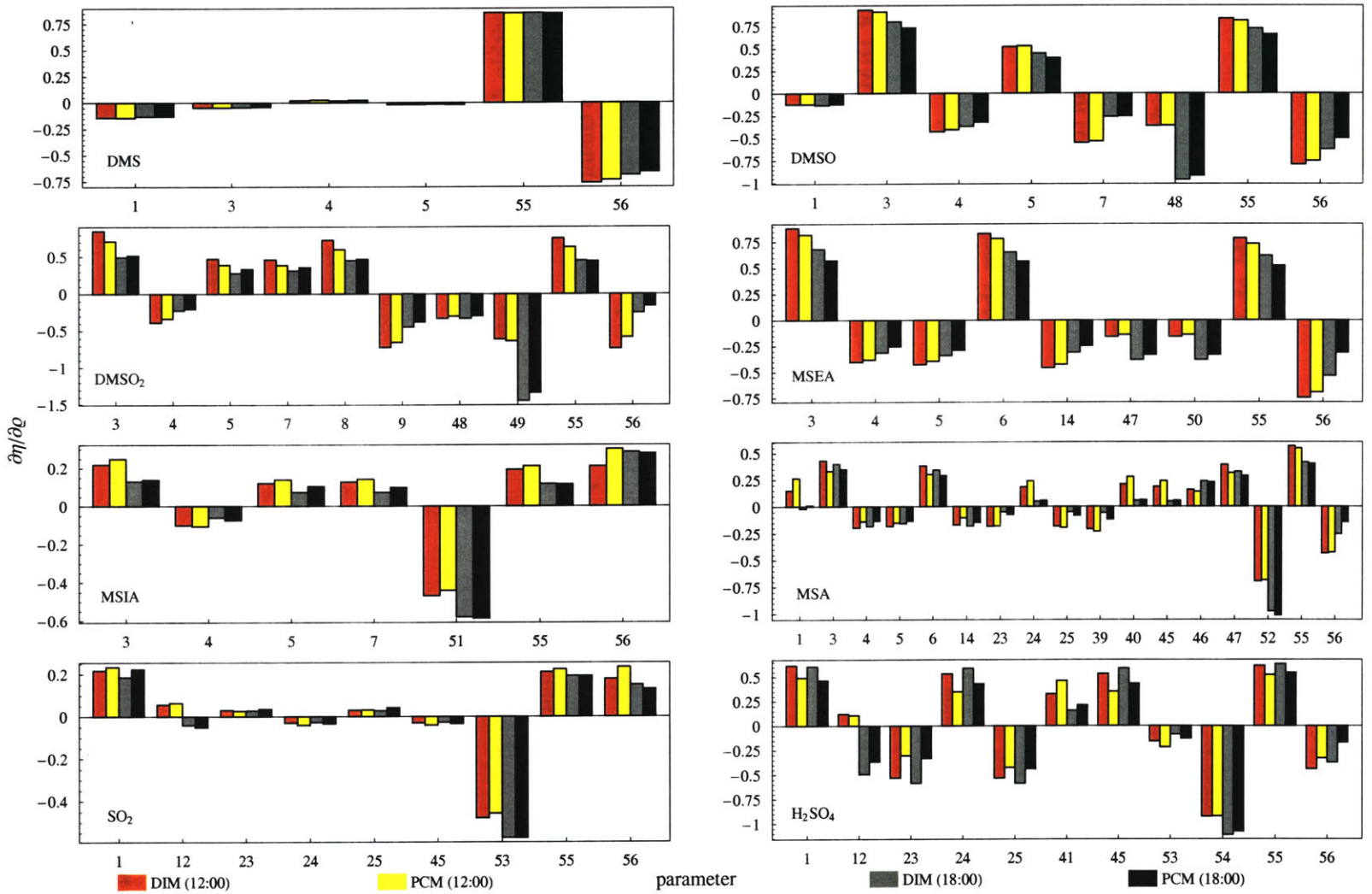

Figure 3-9: Comparison of the normalized, first-order local sensitivity coefficients for DMS-related species at 12:00 and 18:00 using DIM and PCM. The DIM sensitivities are shown in red (12:00) and gray (18:00). The PCM sensitivities are shown in yellow (12:00) and black (18:00). The PCM sensitivities are calculated using equation 3.13. The DIM sensitivities are the values at 12:00 and 18:00 shown in Figures 3-7 and 3-8. Refer to Table 3.1 for the processes corresponding to the parameter labels.

by the sensitivity of H_2SO_4 to the CH_3SCH_2OO+NO reaction rate constant (parameter 12), which is positive at 12:00 and negative at 18:00. Though the overall agreement is excellent, there are some slight systematic differences for some of the species. For instance, many of the H_2SO_4 concentration sensitivities using DIM are systematically larger than the corresponding PCM-based sensitivities. These systematic differences are not related to the PCE fits though, because the concentration correlations in Figure 3-5 do not show any significant biases towards DIM or PCM. Rather, the differences must be due to the first-order versus higher-order nature between DIM and PCM, respectively. Nevertheless, the generally good level of agreement between the DIM and PCM sensitivities lends credence to the identification of the important parameters affecting the DMS-related species identified in the previous section. Additionally, the good agreement allows for a confident assessment of the probabilistic and higher-order concentration sensitivities using PCM in the next section.

First-Order Probabilistic Sensitivities in ξ-Space

Using DIM, first-order local sensitivity coefficients are calculated by running the DMS chemistry model at the mean values of the parameters. Because many of the parameters have large uncertainties, the magnitudes of the sensitivity coefficients are likely to change if the sensitivities are re-evaluated away from the parameter means. This is not an issue if the DMS-related species depend linearly on the model parameters, because then the first-order sensitivities are independent of the parameter values. In reality, however, the sulfur-based species depend non-linearly on the parameters, so the sensitivity coefficients are expected to vary with the model parameters.

In principle, these sensitivity coefficient variations can be determined using a DIM-based approach by solving equations 3.1 and 3.10 multiple times for randomly sampled sets of model parameters. In practice, however, this requires extensive DIM runs to map out the 56-dimensional model parameter space. A more efficient alternative is to apply equation 3.12 derived from PCM, which specifies each first-order sensitivity coefficient as a polynomial that is quadratic in the parameter of interest and linear in all of the other parameters. That is, the sensitivity of $\hat{\eta}$ to ϱ_q is quadratic in ξ_q and linear in ξ_k (for $k \neq q$). Because the PCM sensitivity polynomials are 56-dimensional, directly interpreting them is difficult. But by setting all of the model parameters to their mean values except for the parameter of interest (that is, by setting $\xi_k = 0$ $\forall\ k \neq q$), the first-order PCM-based sensitivities become 1-D quadratic polynomials that are readily analyzed. Referring to equation 3.12, this amounts to keeping only the first summation

because the all of the cross terms in the second summation drop out for $\xi_k = 0$.

Figures 3-10 and 3-11 display the magnitudes of the PCM-based first-order sensitivity coefficients at 12:00 as the individually labeled parameters are varied between $-1 \leq \xi \leq 1$ (i.e., between $\bar{\varrho} \pm \sigma$). At $\xi = 0$, the sensitivities in these figures are equivalent to the PCM-based sensitivities at 12:00 shown in Figure 3-9. To interpret these plots, an increase in the vertical scale denotes an increased sensitivity to the indicated model parameter, and the vertical ordering from top to bottom rates the parameters from most to least influential. In general, the majority of the displayed sensitivities increase as the parameters increase, as shown by the positive sloping curves. This enhanced sensitivity with increasing ξ implies that changes in the parameters tend to have a larger effect on the concentrations at higher values of the parameters. For example, DMS, $DMSO_2$, MSIA, and MSA are more sensitive to the DMS+OH addition reaction (parameter 3) at larger values of the rate constant.

Not all of the sensitivities increase as the parameters increase, however. For instance, DMSO and $DMSO_2$ are less sensitive to the reaction between O_2 and DMS-OH (parameter 5) and MSA is less sensitive to CH_3SO_3 dissociation (parameter 39) as the respective rate constants increase. Essentially, the slope of $|\partial\hat{\eta}/\partial\varrho_q|$ versus ξ_q depends on whether the process of interest competes with other processes or is a rate-limiting step. Consider the addition of O_2 to DMS-OH as an illustration. This addition competes with DMS-OH dissociation. Therefore, by increasing the rate constant for addition, the competition with DMS-OH dissociation decreases, and the sensitivity of DMSO to the DMS-OH+O_2 reaction decreases. As another example, the CH_3SCH_2OO+NO reaction (parameter 12) is a rate-limiting step along the H-abstraction branch. By increasing this rate constant, the sensitivities of the affected species (SO_2 and H_2SO_4) to this reaction decrease.

The slopes and magnitudes of $|\partial\hat{\eta}/\partial\varrho_q|$ versus ξ_q also have important implications for rating the influence of the model parameters on the DMS-related species. The previous two sections indicated that, based on their magnitudes, DMS is more sensitive to emissions (parameter 55) than to the RMBL mixing coefficient (parameter 56). But according to Figure 3-10, because of their slopes in ξ-space, DMS is slightly more sensitive to RMBL mixing than to emissions near $\xi = -1$. Similar changes occur for the other species, but in a much more dramatic fashion. Take $DMSO_2$ as an example. The sensitivity of $DMSO_2$ to heterogeneous loss (parameter 49) has a large slope in ξ-space. This results in heterogeneous loss being the most influential parameter to $DMSO_2$ at $\xi = 1$, but only the fifth most influential parameter at $\xi = -1$. As another example, the sensitivities of MSA to CH_3SO_3 dissociation and RMBL mixing have large,

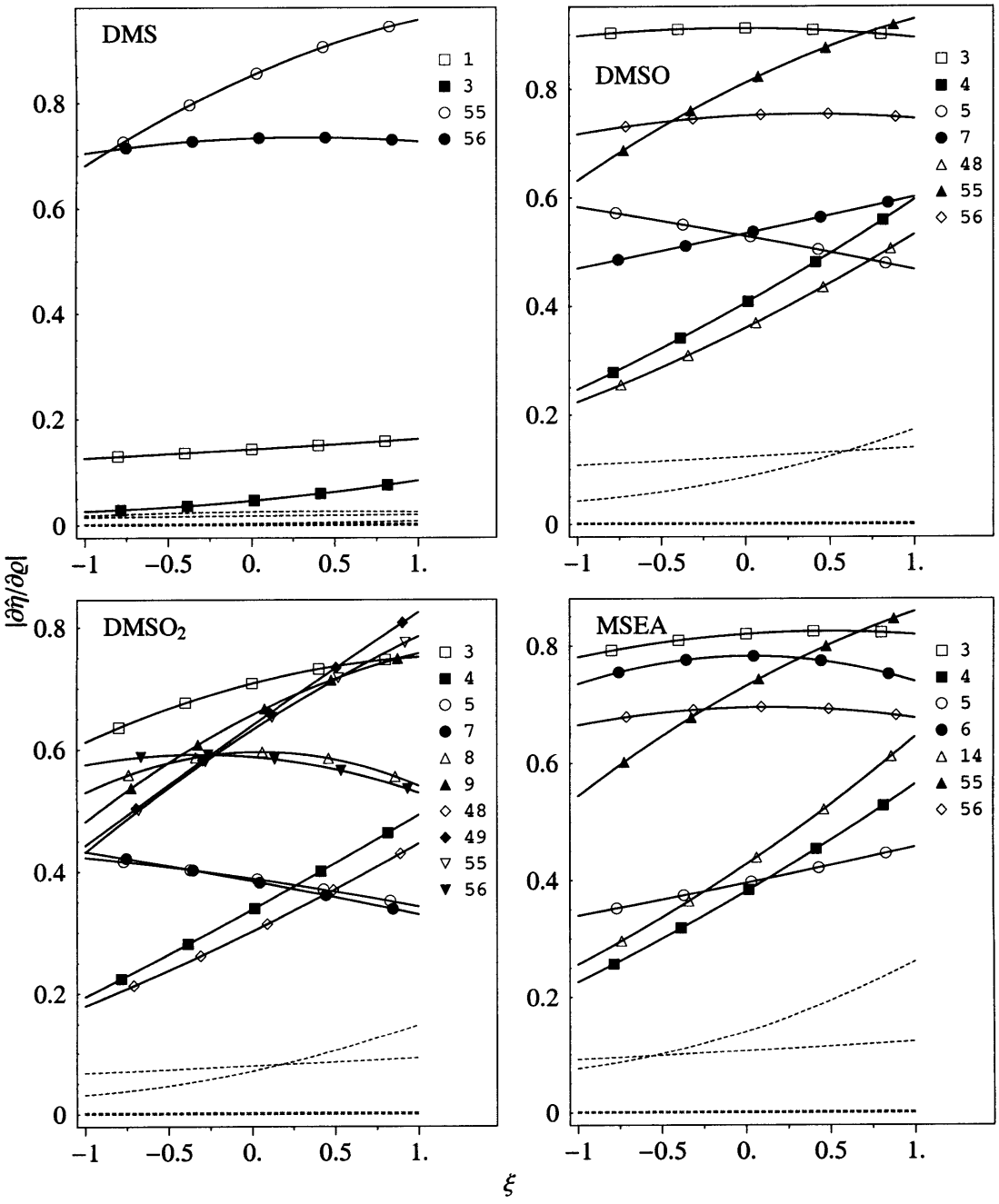

Figure 3-10: Magnitudes of the PCM-based first-order concentration sensitivities at 12:00 as a function of ξ for DMS, DMSO, $DMSO_2$, and MSEA. Only the labeled parameter is varied while all other parameters are set to their mean values ($\xi = 0$). The sensitivities with the largest magnitudes are shown using solid lines and symbols, as noted on the right. The remaining sensitivities are shown using gray+dashed lines.

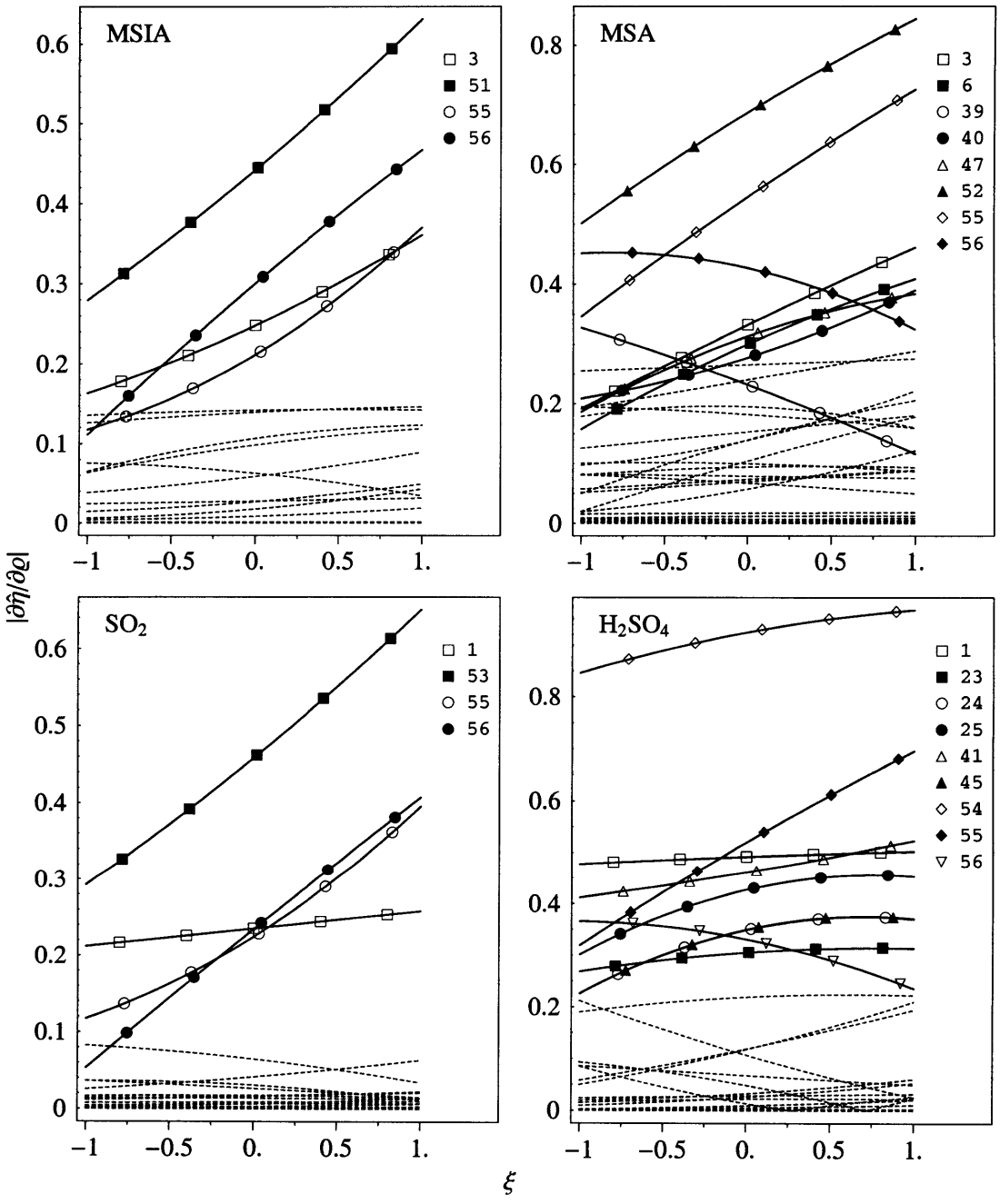

Figure 3-11: Same as Figure 3-10 for MSIA, MSA, SO_2, and H_2SO_4.

negative slopes in ξ-space, resulting in these parameters being highly influential at $\xi = -1$ and relatively insignificant at $\xi = 1$. Examples of other key changes in the ratings of the influential parameters are as follows:

- The RMBL mixing coefficient is fairly important at $\xi = -1$ for $DMSO_2$, MSA, and H_2SO_4, but of minor importance at $\xi = 1$.
- The DMS emission rate is one of the two most influential parameters for DMSO, $DMSO_2$, MSEA, and H_2SO_4 at $\xi = 1$, but is much less influential at $\xi = -1$.
- The DMS+OH addition rate constant is the most influential parameter at $\xi = -1$ for DMSO, $DMSO_2$, and MSEA, but is less important at $\xi = 1$. The opposite occurs for MSA, where this reaction rate constant shifts from being important at $\xi = 1$ to moderate at $\xi = -1$.
- The DMS+OH abstraction rate constant is the second most important parameter for SO_2 and H_2SO_4 at $\xi = -1$, and the fourth most important parameter at $\xi = 1$.
- MSEA is relatively insensitive to the rate constants for the oxidation by OH and the loss of OH from DMS-OH at $\xi = -1$, but is much more sensitive to these reaction rate constants at $\xi = 1$.

It is also important to note that many of the changes in $|\partial\hat{\eta}/\partial\varrho|$ with ξ shown in Figures 3-10 and 3-11 are as large as, or even larger than, the diurnal changes to the magnitudes of the sensitivities in Figures 3-7 and 3-8. For example, the magnitude of the sensitivity of SO_2 to the heterogeneous loss parameter (parameter 53) changes by about 0.15 over a day and 0.4 over $|\xi| < 1$. This implies that the concentration sensitivity to a given parameter may depend more on the level of uncertainty for that parameter than on the daily variations of the process described by that parameter.

Finally, besides the changes to the ratings of the influential parameters, the changes of the magnitudes of the sensitivities in ξ-space give a glimpse into the non-linearities inherent in the cycling of DMS chemistry in the RMBL. For example, if the sensitivity of $\hat{\eta}$ to ϱ_q is approximately constant in ξ-space –such as the sensitivity of DMSO to the DMS+OH addition rate constant– then $\hat{\eta}$ has a nearly linear dependence on ϱ_q. Likewise, if the sensitivity of $\hat{\eta}$ to ϱ_q undergoes a large change in magnitude with ξ –such as the sensitivities of MSA and SO_2 to their heterogeneous removal coefficients– then $\hat{\eta}$ depends non-linearly on ϱ_q. A more

quantitative treatment of parameter non-linearities is made through the analysis of higher-order sensitivities, which is the topic of the next section.

Higher-Order Sensitivities

Higher-order sensitivity coefficients are useful for a variety of purposes. They can be used to gauge the non-linear dependence of the concentrations on the model parameters, to determine how first-order sensitivities respond to changes in the parameters, and to estimate the moments of the concentration distributions. The effects of co-varying parameters on the concentrations are also ascertained through higher-order cross term sensitivities. Though higher-order sensitivities have many uses, they are rarely calculated because most computational techniques used to estimate them are too costly.

PCM, however, allows for an easy analysis of higher-order sensitivities simply by taking the higher-order derivatives of the concentration PCEs. These higher-order derivatives are calculated using equation 3.15, which expresses the PCM-based second- and third-order sensitivity coefficients. These expressions are evaluated at two different times (12:00 and 18:00) and the three largest magnitudes of each type are displayed in Figure 3-12. The first-order sensitivities from equation 3.13 are also displayed for comparison. To interpret Figure 3-12, large second- and third-order sensitivities denote significant quadratic and cubic dependencies of the concentration PCEs, respectively, while large second-order cross sensitivities designate important couplings between process parameters in the DMS chemistry model.

As shown in Figure 3-12, the first-order sensitivities tend to be larger than the higher-order terms for all of the species. This indicates that the concentration PCEs are mainly linear in the model parameters. However, there are many extremely large second- and third-order sensitivities, which illustrates the presence of significant non-linear parameter dependencies. In particular, MSEA, MSIA, and SO_2 have higher-order sensitivities that are nearly as large as their largest first-order sensitivity coefficient. Upon inspection, the most significant higher-order sensitivities are related to the RMBL mixing parameter. This emphasizes the important role that vertical transport plays in regulating the RMBL concentrations of the DMS-related species. The major non-linearities and parameter couplings derived from Figure 3-12 are summarized below:

- The DMS-related species have a quadratic or cubic dependence on the RMBL mixing coefficient, and this dependence is particularly large for $DMSO_2$, MSEA, MSIA, MSA, and SO_2.

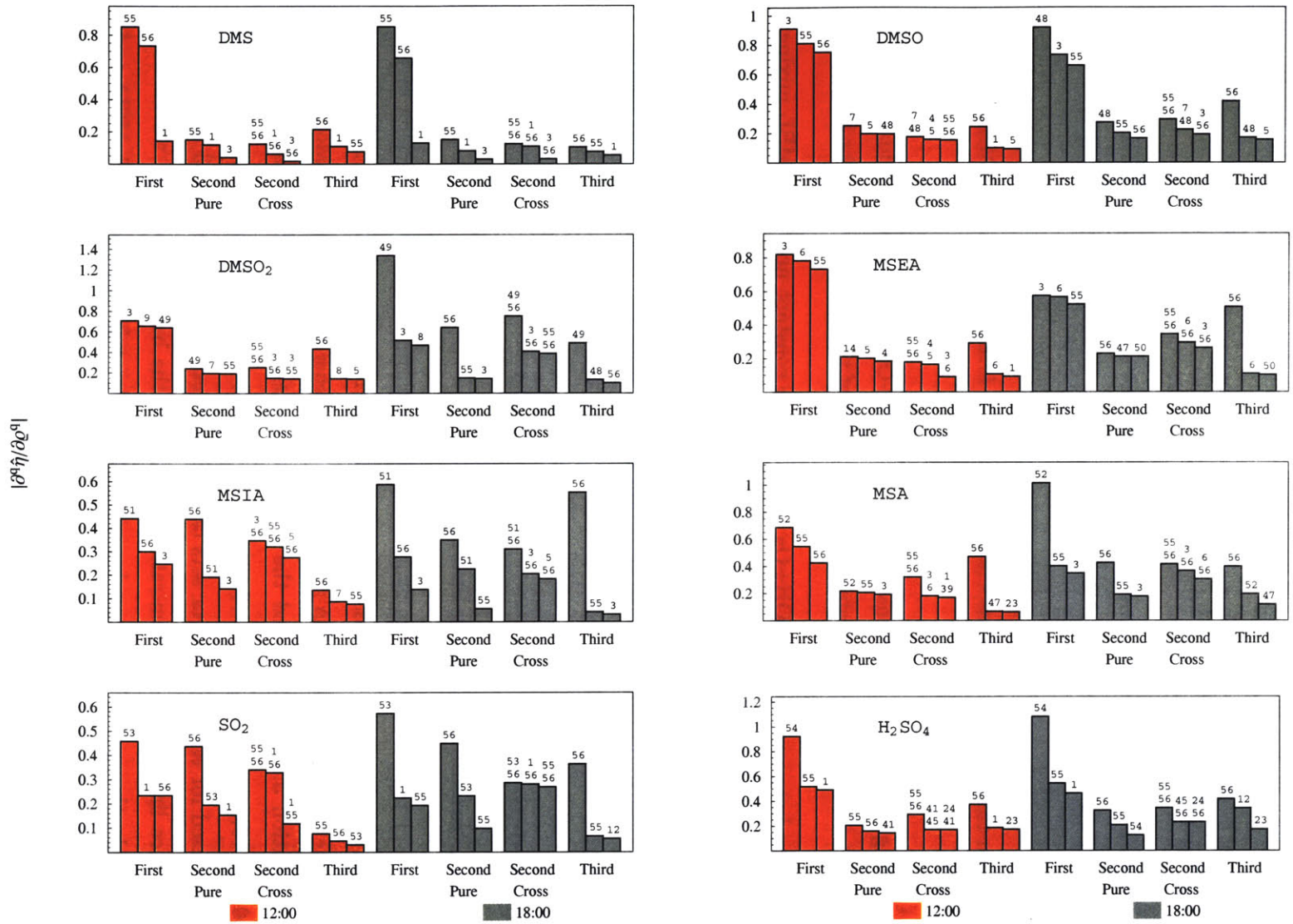

Figure 3-12: Comparison of the three largest magnitudes of the first-, second-, and third-order sensitivity coefficients for the DMS-related species using PCM at 12:00 (red) and 18:00 (gray). The parameter numbers are noted at the top of each bar, and ξ is set to zero where applicable.

- The oxidized sulfur-based species have a quadratic and/or cubic dependence on the heterogeneous removal parameter.
- The coupling between the DMS emission rate and RMBL mixing parameters is important, especially for MSEA, MSIA, and SO_2.
- The second-order co-variation between the heterogeneous removal rate and RMBL mixing coefficient in the late afternoon (18:00) is significant for $DMSO_2$, MSIA, and SO_2.
- In the late afternoon, MSEA and MSA have a fairly large dependence on the interaction between the rate constants associated with MSEA formation and the RMBL mixing parameter.
- The coupling between the rate constants for the DMS+OH abstraction or addition reactions with the RMBL mixing parameter influences all of the species except for H_2SO_4.
- The coupling between the DMS-OH+O_2 reaction rate constant and the RMBL mixing coefficient is important to MSIA.

Non-linear interactions are also important in the analysis of uncertainties, because products of uncertain parameters contribute to concentration uncertainties and lead to skewed concentration PDFs. These issues are thoroughly addressed in the following section.

3.6.3 Uncertainties

Concentration Probability Density Functions

The first portion of the uncertainty analysis involves generating concentration PDFs of the important DMS-related species and calculating the first three moments of these PDFs. The concentration PDFs, which are shown in Figure 3-13, were generated by applying Monte Carlo sampling to equation 3.1 (DIM-M) and the PCEs in equation 3.7 (PCM) for two different times (12:00 and 18:00). A sample size of 10^4 independent and randomly chosen sets of model parameters was used for each of the four sets of concentration PDFs. Figure 3-13 also shows the 95% confidence limits of the concentration PDFs. On the basis of the PDF widths and confidence intervals, the uncertainties are deemed to be moderately large for DMS, MSIA and SO_2, and extremely large for the other species.

With time, the most probable values of the PDFs –except those for DMS, MSIA, and SO_2– visibly shift from higher to lower concentrations between midday and afternoon. These shifts

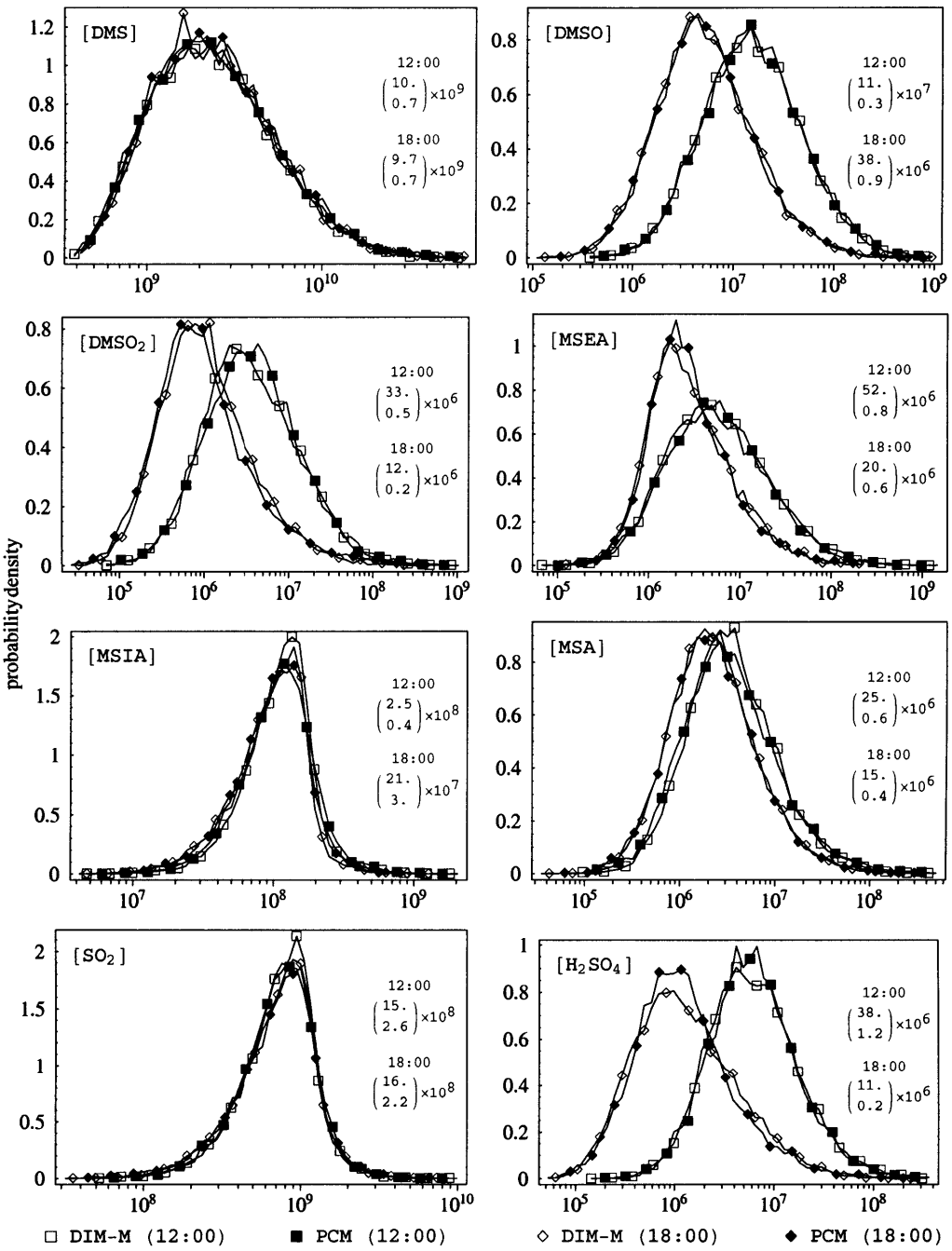

Figure 3-13: DMS-related concentration (molecules cm^{-3}) probability density functions using DIM-M (empty) and PCM (filled) at 12:00 (squares) and 18:00 (diamonds). Sample sizes of 10^4 were used for each set of PDFs. The PDFs were normalized over 50 equally spaced bins ranging from the minimum to maximum concentrations. Shown in the upper right hand corner are the 95% confidence limits averaged between DIM-M and PCM.

are related to the amplitudes of the diurnal cycles of the DMS-related concentrations relative to the concentration uncertainties. According to Figures 3-4 and 3-13, for instance, SO_2 has a small diurnal amplitude and a large uncertainty. This results in nearly overlapping PDFs for SO_2 at 12:00 and 18:00.

While some of the most probable values undergo large changes in time, the overall widths and shapes of many of the PDFs are largely invariant between 12:00 and 18:00. The widths and shapes of the PDFs are related to the combinations of parameter uncertainties and concentration sensitivities. If a given species has sensitivities that are constant in time and parameter uncertainties that are small, then the shape and width of the PDF for that species will be time invariant. This occurs for DMS, which, according to Figure 3-7, has sensitivities with small time variations. The shapes of the PDFs for $DMSO_2$ and MSEA, on the other hand, are noticeably different between 12:00 and 18:00. These large changes occur for $DMSO_2$ and MSEA because of the transition from photochemical to non-photochemical processing.

Finally, just as the strong DIM versus PCM concentration correlations in Figure 3-5 allowed for quantitative comparisons between the DIM- and PCM-based sensitivities, the excellent agreement between the DIM-M and PCM-based concentration PDFs in Figure 3-13 allows for quantitative assessments of the moments of these PDFs. The first three PDF moments are listed in Table 3.5 and are described in more detail below.

Comparison of Statistical Moments

First Moment The DIM-S, DIM-M, and PCM-based mean values were calculated using expressions 3.17-3.19 and are listed in Table 3.5. The DIM-M and PCM mean values agree nearly perfectly at the given precision at 12:00 and 18:00. This implies that the zeroth-order PCE coefficients are excellent estimators of the mean values. Comparing the DIM-M and PCM means with DIM-S, however, shows that the truncated term in the DIM-S equation 3.17 involving second-order derivatives leads to quantitative differences for DMSO and $DMSO_2$ at 12:00, H_2SO_4 at 18:00, and MSEA and MSA at both times. Recalling that the values listed in the table are in terms of logarithmic concentrations, these apparently small differences between the DIM-S and DIM-M/PCM estimates of the mean values for these species actually leads to as much as a 30% difference between the concentrations. This indicates that concentrations calculated using the mean values of the model parameters are not necessarily good estimates of the mean values of the concentrations. This conclusion is further supported using the PCM-based expression 3.7, which gives nearly the same results as the DIM-S mean values listed in

Table 3.5: Moments of the Logarithmic DMS-Related Concentration PDFs

Species	Mean			Variance			Skewness	
	DIM-S	DIM-M	PCM	DIM-S	DIM-M	PCM	DIM-M	PCM
				12:00				
DMS	9.36	9.38	9.38	0.13	0.12	0.12	0.38	0.49
DMSO	7.25	7.19	7.19	0.26	0.24	0.25	0.17	0.15
$DMSO_2$	6.63	6.55	6.56	0.42	0.31	0.32	0.31	0.25
MSEA	6.84	6.75	6.75	0.36	0.31	0.32	0.30	0.26
MSIA	8.05	8.03	8.03	0.050	0.060	0.070	-0.37	-0.28
MSA	6.43	6.55	6.53	0.23	0.22	0.26	0.35	0.48
SO_2	8.86	8.85	8.85	0.046	0.054	0.058	-0.61	-0.56
H_2SO_4	6.78	6.79	6.80	0.28	0.21	0.20	0.31	0.39
				18:00				
DMS	9.36	9.38	9.38	0.13	0.12	0.12	0.44	0.49
DMSO	6.76	6.72	6.72	0.29	0.23	0.24	0.30	0.38
$DMSO_2$	5.98	6.02	6.00	0.39	0.29	0.36	0.57	0.96
MSEA	6.52	6.45	6.46	0.26	0.21	0.22	0.60	0.82
MSIA	8.00	7.97	7.97	0.061	0.071	0.074	-0.62	-0.75
MSA	6.27	6.36	6.36	0.22	0.22	0.24	0.41	0.48
SO_2	8.85	8.84	8.84	0.059	0.066	0.071	-0.64	-0.69
H_2SO_4	6.03	6.11	6.10	0.37	0.27	0.26	0.45	0.71

the table.

Second Moment Figure 3-13 indicates that some of the PDFs are very wide (e.g., $DMSO_2$), while others are more moderately wide (e.g., MSIA and SO_2). These widths are related to the second moment, or variance. The variances are estimated using the DIM-S, DIM-M, and PCM-based expressions 3.21-3.23 and are listed in Table 3.5. As with the concentration means, there is good agreement between the DIM-M and PCM-based variances, which gives confidence in the calculations of the absolute uncertainties. Additionally, there are systematic differences between the DIM-M/PCM variances and the DIM-S estimates for the two times. For instance, the DIM-S variances for $DMSO_2$ are 30% larger than the corresponding DIM-M and PCM-based estimates. These differences indicate, not surprisingly, that the linear DIM-S approach does not capture any of the non-linearities contained in the neglected higher-order sensitivity coefficients. However, the DIM-S variances are still reasonable enough to provide a basis for estimating the diurnal variations in the concentration uncertainties shown in a following section.

Third Moment Some of the concentration PDFs in Figure 3-13 are nearly symmetric, while others are highly skewed. The skewness is calculated using the DIM-M and PCM-based expressions 3.24 and 3.25 and the values are listed in Table 3.5. The two sets of skewness values qualitatively match and indicate that the PDFs for MSIA and SO_2 are skewed to the left of the mean, the PDFs for DMSO are nearly symmetric, and the PDFs for the remaining species are skewed to the right. With time, the PDFs tend to be more skewed at 18:00 than 12:00.

The differences between the DIM-M and PCM estimates of the third moment are larger than their differences for the first and second moments, especially for $DMSO_2$ at 18:00. A large part of these differences are likely due to the fact that estimates of higher moments are less robust than estimates of lower moments. Press et al. (1992), for instance, suggest that only skewness values many times larger than $\sqrt{15/S}$ are significant for normal distributions with a sample size S. Applying the same criterion here means that differences between the DIM-M and PCM skewness values of less than about 0.1 are probably not significant. These differences may also arise from important cubic or quartic interactions not represented by the chosen truncated set of PCEs.

Nevertheless, the fairly good agreement between DIM-M and PCM is sufficient for drawing important conclusions about the relationship between PDF symmetries and non-linearities in the DMS chemistry model. The relationship follows from the central limit theorem of probability theory, which states that a sum of independent random variables tends towards a normal distribution regardless of the shapes of the PDFs of the individual random variables. Moreover, a product of random variables tends towards a lognormal distribution. Thus, the PDFs in Figure 3-13 are merely convolutions of normal and lognormal distributions because the DMS-related species depend on sums and products of the random model parameters.

In this regard, PCM is a powerful technique because the PCEs explicitly decompose the concentrations into sums and products of random variables. By examining the magnitudes of the PCE coefficients for the non-linear terms, one can predict *a priori* whether the resulting concentration PDFs are likely to be asymmetric. Furthermore, the non-linear combinations leading to any PDF asymmetries are readily identified. To give a couple of examples, the magnitudes of the PCE coefficients for DMS listed in Table 3.4 indicate that the PDF asymmetry stems from non-linearities involving the DMS emission rate, while the strong asymmetries for MSIA and SO_2 involve non-linear combinations of the parameters related to heterogeneous removal, DMS emissions, RMBL mixing, and the DMS+OH addition rate constant.

Variance Contributions

The contributions of the uncertain parameters to the concentration uncertainties are identified and calculated in this section. These contributions are computed for the DIM-S and PCM-based variances using equation 3.26 at 12:00 and 18:00. The resulting contributions are displayed in Figure 3-14 as percentages of the total variance for the most important uncertainty contributions, including contributions from pairs of uncertain parameters using PCM.

The differences between Figures 3-9 and 3-14 illustrate an important distinction between sensitivity and uncertainty analyses. According to Figure 3-9, SO_2 shows significant sensitivity to the DMS+OH abstraction reaction rate constant. Figure 3-14 indicates, however, that the uncertainty in this rate constant is not a large contributor to uncertainties in SO_2. Thus, after factoring in parameter uncertainties, parameters that greatly influence a given concentration based on sensitivities alone may not contribute significantly to the uncertainty in the concentration of that species.

As shown in Figure 3-14, the DIM-S and PCM-based estimates of the variance contributions generally agree for most of the species at midday and in the evening. The agreement is extremely good for DMS and DMSO (within 3%), and moderately good for MSEA and MSA (within 6%). For $DMSO_2$, MSIA, and SO_2, however, the DIM-S and PCM-based contributions from heterogeneous removal differ by as much as 15%. Although these larger discrepancies may, in principle, be partially due to the fact that PCM is a numerical approximation to the true model, it is more likely that they result from non-linearities. To illustrate, consider the variance contribution from heterogeneous removal (parameter 49) to $DMSO_2$ at 18:00. Both the DIM and PCM-based sensitivities to this parameter in Figure 3-9 and the total variances (DIM-S and PCM) listed in Table 3.5 match up very well. Therefore, numerical differences between the DIM and PCM-based sensitivities and total variances alone can not account for these large variance contribution discrepancies.

Figure 3-14 also shows the presence of some systematic differences between the DIM-S and PCM-based variance contributions. H_2SO_4 has, for instance, DIM-S contributions from uncertain rate constants involving $CH_3S(O)OO$ (parameters 24, 25, and 45) that are systematically larger than the PCM-based estimates at 12:00 and 18:00. These biases result from the inability of DIM-S to capture variance contributions from pairs of parameters, as exemplified by the large number of PCM-based contributions from pairs of parameters for H_2SO_4.

Even though there are fairly large and systematic differences between the individual DIM-S and PCM-based variance contributions in Figure 3-14, the memberships of the groups of pa-

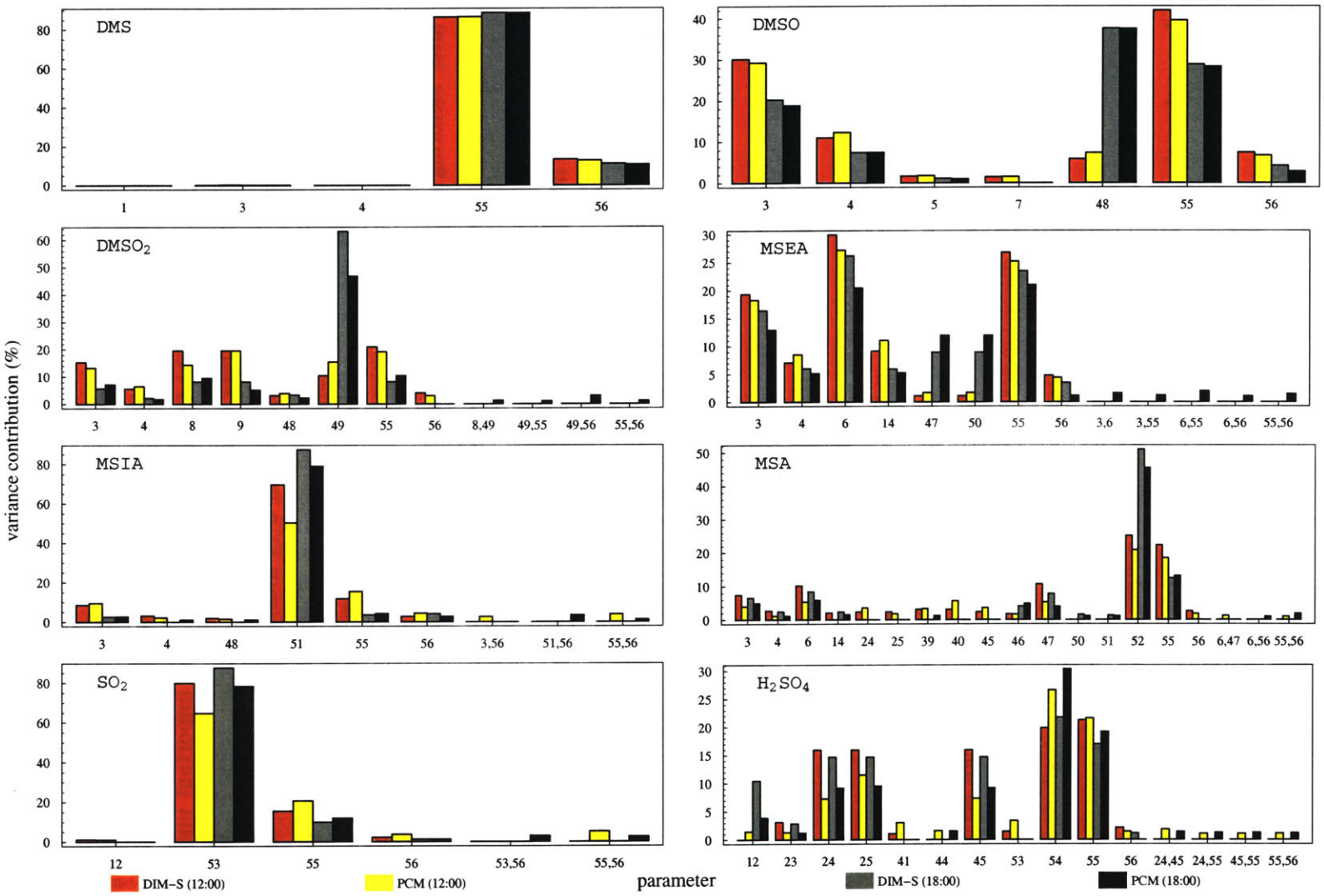

Figure 3-14: Parameter variance contributions (%) for DMS-related species using DIM-S and PCM. The DIM-S contributions are shown in red (12:00) and gray (18:00) and the PCM-based contributions in yellow (12:00) and black (18:00). Only contributions >1% are displayed, except for DMS which shows contributions > 0.05%. Pure and cross contributions are represented by a single parameter and pairs of parameters, respectively.

rameters contributing to the uncertainties are fairly robust. This means that the concentration uncertainties can be reduced by targeting these groups of parameters. From Figure 3-14 it is clear that an increased level of understanding of DMS emissions (parameter 55) and heterogeneous removal (parameters 48-54) will go a long way towards reducing the overall uncertainties in modeling the concentrations of DMS oxidation products. Other important conclusions from Figure 3-14 include:

- Many of the species have important uncertainty contributions from a multitude of parameters, particularly $DMSO_2$, MSEA, MSA, and H_2SO_4.
- The parameter for the emission rate of DMS contributes at least 10% of the uncertainty for all of the species, and more than 80% for DMS.
- The uncertainties in the DMS-related concentrations are not greatly influenced by the uncertainty in the DMS+OH abstraction rate constant.
- The rate constants for the reversible addition of OH to DMS are a source of uncertainty for DMSO, $DMSO_2$, MSEA, MSIA, and MSA.
- Rate constants for the reactions involving MSEA are important sources of uncertainty for MSEA.
- Rate constants of the loss reactions of DMSO-OH are important sources of uncertainty for $DMSO_2$.
- The rate constant for the conversion of MSEA to MSA is an important source of uncertainty for MSA.
- Rate constants for the reactions involving $CH_3S(O)OO$ are large sources of uncertainty for H_2SO_4.
- Uncertain heterogeneous removal parameters account for more than 50% of the uncertainty in MSIA and SO_2.

Only the most important variance contributions are shown in Figure 3-14, which makes it difficult to gauge the net impact of coupled uncertain parameters to the concentration uncertainties. To see these effects, the PCM-based percent variance contributions from the individual pure and cross terms have been summed and the totals are displayed in Table 3.6. Even though

Table 3.6: Percent Variance Contributions from Pure and Cross Terms Using PCM

Species	Pure								Cross	
	first		second		third		total			
	12:00	18:00	12:00	18:00	12:00	18:00	12:00	18:00	12:00	18:00
DMS	98.3	98.3	1.2	1.3	0.1	0.1	99.6	99.6	0.4	0.4
DMSO	96.9	93.7	2.4	3.1	0.1	0.1	99.4	97.0	0.6	3.0
$DMSO_2$	93.5	82.8	2.9	1.1	0.2	0.6	96.7	84.6	3.3	15.4
MSEA	95.9	84.5	2.7	5.7	0.2	0.3	98.8	90.5	1.2	9.5
MSIA	78.8	86.4	7.0	5.4	0.3	0.1	86.0	91.9	14.0	8.1
MSA	75.4	82.9	4.2	3.2	0.2	0.3	79.7	86.4	20.3	13.6
SO_2	83.8	86.1	8.0	6.7	0.2	0.2	92.0	93.0	8.0	7.0
H_2SO_4	84.8	83.8	3.1	2.2	0.5	1.2	88.4	87.2	11.6	12.8

pure parameters dominate the variance contributions, Table 3.6 indicates that coupled parameters (shown by the cross terms) make up more than 10% of the total variance for MSIA at 12:00, for MSA and H_2SO_4 at 12:00 and 18:00, and for $DMSO_2$ at 18:00. In fact, uncertain coupled parameters account for more than 20% of the uncertainty in MSA at midday. This means that efforts to reduce the MSA concentration uncertainty by improving the knowledge in just one or two individual parameters will have only a marginal effect. The higher-order terms in Table 3.6 also provide a measure of non-linearity in the DMS model. MSIA and SO_2, for instance, have fairly large net second-order contributions and highly-skewed PDFs in Figure 3-13.

Uncertainty Variations with Temperature

Because many of the reaction rates and parameter uncertainties are exponential functions of temperature, the temperature-dependence of the DMS-related concentrations and concentration uncertainties are assessed over a range of 250-310 K. These temperature-dependencies are calculated using DIM. Although DIM does not account for parameter interactions and other higher-order effects, the reasonable agreement between the DIM-S, DIM-M, and PCM-based variances in Table 3.5 provides confidence in applying equation 3.21 to estimate the absolute concentration uncertainties. Recall that DIM provides solutions as a function of time, so temperature- and time-dependencies are shown for the concentrations and concentration uncertainties.

Time-temperature contours of the DMS-related concentrations for temperatures between

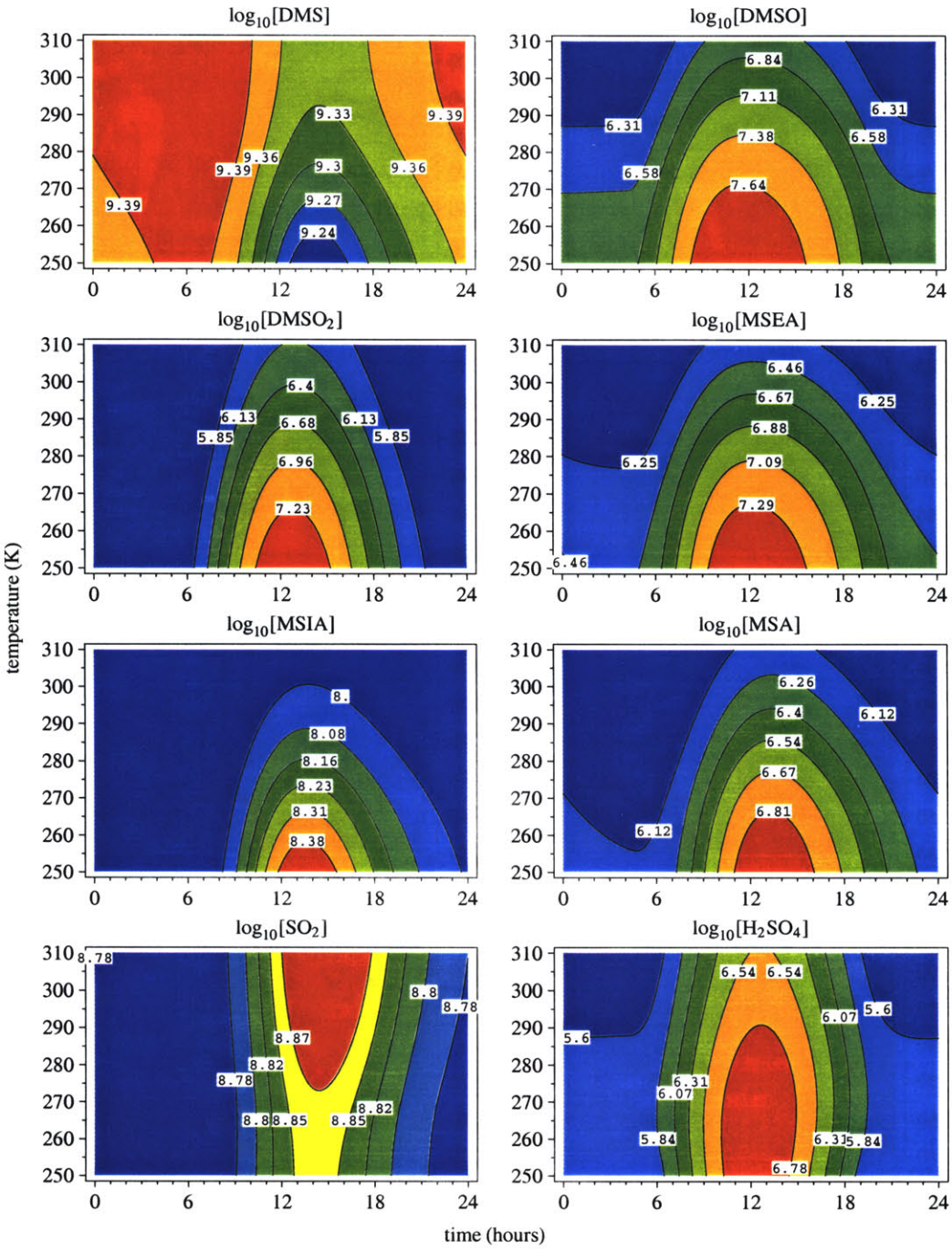

Figure 3-15: Time-temperature contours of the concentrations of the major DMS-related species over a daily cycle and temperature range of 250-310 K. The contours are in logarithmic concentration space ($\log_{10}$ (molecules cm^{-3})), maximum/minimum values are denoted by red/blue, and the value of each contour is labeled.

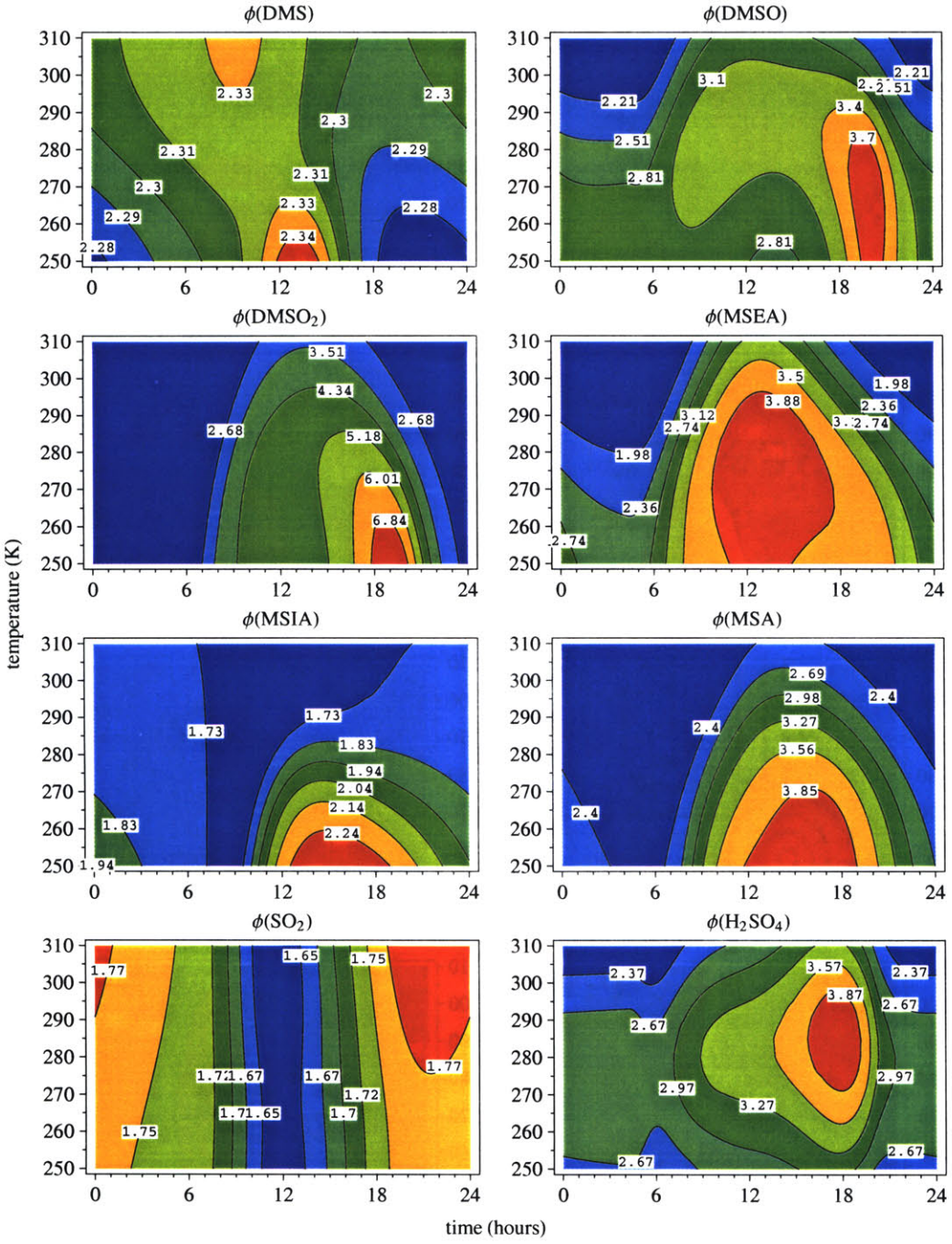

Figure 3-16: Time-temperature contours of the uncertainty factors of the major DMS-related concentrations over a daily cycle and temperature range of 250-310 K. The uncertainty factors are calculated using the relationship $\log \phi = \sigma_\eta$, where ϕ is the uncertainty factor and σ_η is the square root of expression 3.21. The maximum/minimum values are denoted by red/blue and the value of each contour is labeled.

250-310 K are shown in Figure 3-15. The most obvious feature in the figure is that the concentrations of DMS and SO_2 maximize at higher temperatures, while all of the other concentrations maximize at lower temperatures. These trends are simply related to the variations of the DMS+OH addition and abstraction reactions with temperature and the positions of the end products along the addition or abstraction branch.[4] For example, DMSO and $DMSO_2$ are products along the OH-addition channel, so their concentrations increase as the temperature decreases.

On the basis of the magnitudes of the contours in Figure 3-15, DMS and SO_2 are relatively insensitive to temperature changes, H_2SO_4 is moderately sensitive, and the remaining species are highly sensitive. Also, the concentrations are more sensitive to temperature near midday than at other times, as shown by the time of the minimum concentration of DMS and maximum concentrations of the other species. This enhanced sensitivity to temperature at noon is due to the greater temperature-dependence of photochemistry than the other processes. Overall, however, the sulfur-based concentrations change more rapidly with time than temperature, as suggested by the tighter contours along the time axis.

Though not readily obvious, Figure 3-15 also shows that all of the DMS-related concentrations, except for H_2SO_4, change monotonically with temperature. Thus, at a single time these concentrations either increase or decrease with temperature, but not both. This monotonic behavior results from the important temperature-dependent reactions affecting these species. The concentration of SO_2, for instance, is controlled by the DMS+OH abstraction and CH_3SO_2 dissociation reactions, both of which have rate constants with a positive ($\uparrow$) temperature-dependence. Considering H_2SO_4, on the other hand, the slight non-monotonic behavior –as exhibited by the largest concentrations at approximately 265 K– is due to a combination of three reaction rate constants having positive and negative temperature-dependencies (DMS+OH abstraction $\uparrow$, CH_3SO_2 dissociation $\uparrow$, and CH_3SO+O_2 addition $\downarrow$).

Time-temperature contours of the concentration uncertainties for temperatures between 250-310 K are shown in Figure 3-16. The concentration uncertainties in the figure are displayed as uncertainty factors.[5] One characteristic immediately apparent from the figure is that the concentration uncertainties are complex non-linear functions of temperature. Many of the uncertainty factors are also non-monotonic with temperature. The two sources of these

[4]Refer to Figure 2-4 in Chapter 2 for the temperature-dependence of the OH-addition and H-abstraction branches.

[5]Uncertainty factors are defined by $\phi = 10^{\sigma_\eta}$, where ϕ is the uncertainty factor and σ_η^2 is calculated using equation 3.21.

temperature variations are from changes to reaction rates through temperature-dependent rate constants and directly from parameter uncertainty factors that are exponential functions of temperature (see equation 3.5). As previously noted, the concentration uncertainties are non-linear because these two sources have temperature-dependencies that can reinforce at one temperature and cancel at another.

By examining the concentration uncertainty maxima in Figure 3-16, an assessment can be made regarding the relative importance of reaction rates versus equation 3.5 to the overall temperature-dependence. According to expression 3.5, many DMS-related rate constants are most certain at room temperature and less certain away from 298 K. Therefore, concentration uncertainties dominated by equation 3.5 should follow a similar trend. Figure 3-16 shows, however, that only the DMS uncertainty near noon –with two maxima at the highest and lowest temperatures– exhibits this behavior. In fact, the H_2SO_4 uncertainty has its maximum very close to room temperature, where the rate constants are most certain. These results clearly show that the temperature effects of the reaction rate constants dominate the temperature trends of their uncertainty factors.

On the basis of their magnitudes, the concentrations of DMS, MSIA, and SO_2 have the smallest uncertainty factors (1.6 to 2.3), while the remaining species have fairly large uncertainty factors (2 to 7). Additionally, the uncertainty factors for DMS and SO_2 concentrations remain practically constant versus temperature, while the uncertainty for $DMSO_2$ changes from a factor of about 2 at high temperatures to a factor of 7 at 250 K. The other species along the OH-addition branch (e.g., DMSO) have temperature trends similar to $DMSO_2$, with uncertainty factors that are smallest at high temperatures and largest at low temperatures. These trends are explained by the DMS+OH addition reaction, which has a larger rate constant at lower temperatures.

It is also interesting to note that, with time, the concentration uncertainty factors do not maximize at noon, when the photochemistry peaks. Rather, the concentration uncertainties peak after 12:00. Heterogeneous removal is the prime reason for this behavior –as shown in the diurnal local sensitivity profiles in Figures 3-7 and 3-8– because it is the largest sink in the afternoon when the concentrations are large and the photochemistry is weak.

3.7 Summary and Conclusions

The sensitivities and uncertainties of sulfur-containing concentrations to 56 uncertain parameters have been analyzed using a diurnally-varying model of comprehensive DMS chemistry in

the RMBL. Two separate methods are used to independently assess the parametric sensitivities and uncertainties of the important DMS-related species. The first technique uses a *direct integration method* to calculate concentrations and first-order local concentration sensitivities. When combined with Monte Carlo sampling, DIM also yields concentration PDFs of the important DMS-related species. The second technique utilizes the *probabilistic collocation method* to approximate the DMS-related concentrations as polynomial chaos expansions of orthogonal polynomials of the model parameters. These PCEs are then used to analyze probabilistic first- and higher-order sensitivities, concentration PDFs, and the contributions of uncertain parameters to the uncertain concentrations. DIM solves for the concentrations and sensitivities continuously with time, which allows for a diurnal analysis. However, DIM is computationally limited to first-order local sensitivities. PCM, on the other hand, advantageously represents the DMS chemistry model over a wide range in the probabilistic space of model parameters and effortlessly diagnoses important inter-dependencies between processes and other non-linearities. Also, PCM does not require additional computations to estimate higher-order sensitivities.

At the parameter means, the oxidized sulfur-containing species are particularly sensitive to the parameters describing DMS emissions, mixing into/out of the RMBL, heterogeneous removal, and the rate constants for the addition or abstraction reactions between DMS and OH. The species along the DMS+OH addition branch –which include DMSO, $DMSO_2$, MSEA, and MSIA– show additional sensitivities to reaction rate constants involving DMS-OH, DMSO, and DMSO-OH. MSA is also sensitive to reaction rate constants involving MSEA and moderately sensitive to a large number of other rate constants. H_2SO_4 is sensitive to numerous chemical rate constants, which emphasizes the limited capability of using highly parameterized DMS mechanisms to compute gas-phase sulfuric acid levels. Some of the additional sensitivities for H_2SO_4 include rate constants associated with the reaction between CH_3SCH_2OO and NO, reactions of CH_3SO with O_2 and O_3, and the isomerization of $CH_3S(O)OO$ into CH_3SO_3.

Away from the parameter means, however, these key sensitivities undergo dramatic changes in magnitude due to the large uncertainties in the parameters and the underlying non-linearities in the DMS chemistry. For instance, at 1-σ below the parameter means, the DMS-related species are much more sensitive to chemistry relative to non-photochemical processes. In fact, heterogeneous loss is no longer a dominant sensitivity for many of the species at 1-σ below the means. These results show that the proper identification of the key DMS model parameters requires the use of the probabilistic sensitivity techniques demonstrated by PCM.

For the uncertainty analysis, sulfur-based concentration PDFs were generated and their first

three moments and 95% confidence limits quantified. On the basis of the second moments (i.e., variances) and confidence intervals, the concentrations of DMS, MSIA and SO_2 have modest uncertainties, while the remaining species have rather large uncertainties. For instance, the net uncertainty for H_2SO_4 concentrations is about a factor of 3 for the typical RMBL-conditions used in the model. Moreover, only ~20% of this H_2SO_4 uncertainty is attributable to uncertainties in DMS emissions. This implies that, collectively, indeterminate parameters associated with gas-phase chemistry and heterogeneous removal limit the prediction of sulfuric acid concentrations more than the uncertainty associated with parameterizations of the sea-to-air flux of DMS. Furthermore, this large H_2SO_4 uncertainty amplifies the already extreme uncertainties in the nucleation of sulfate aerosols, thereby creating an enormous range of plausible rates of new particle production.

Although the parameters describing DMS emissions and heterogeneous removal are the main uncertainty contributors to the DMS-related species, many uncertain chemical reaction rate constants also contribute significantly. The key reactions contributing to the H_2SO_4 uncertainty involve parameters in the formation and loss of $CH_3S(O)OO$. For the other species, some important uncertainty-contributing rate constants include the reversible addition of OH to DMS, loss of the DMSO-OH adduct, and the formation and loss of MSEA. These key uncertainty contributions differ from the important sensitivities because they take parameters uncertainties into account. One example of this occurs for the relatively well constrained DMS+OH abstraction reaction, which was identified as an important sensitivity, but not as a crucial uncertainty contribution.

Non-linear uncertainty contributions were also quantified, including those from coupled process parameters. Though not as large as the linear contributions, total non-linearities account for 15-25% of the variances in the concentrations of $DMSO_2$, MSEA, MSIA, MSA, SO_2, and H_2SO_4. Of these non-linear contributions, coupled parameters make up 10-20% of the variances of $DMSO_2$, MSIA, MSA, and H_2SO_4. These rather large contributions suggest that efforts aimed at greatly reducing the concentration uncertainties for these species require a detailed understanding of many, simultaneous processes.

An analysis of the third moments of the concentration PDFs (i.e., skewness) also highlights the extent of non-linearity in the DMS chemistry model. This analysis makes use of the multiplicative central limit theorem, which relates the symmetries of the concentration PDFs to the presence or absence of higher-order and/or coupled parameters in the concentration PCEs. According to this analysis, the highly-skewed concentration PDF for DMS stems

from non-linearities involving DMS emissions. Additionally, this analysis ascribed the strongly-asymmetric concentration PDFs for MSIA and SO_2 to parameter combinations of heterogeneous removal, DMS emissions, the RMBL mixing coefficient, and the DMS+OH addition rate constant.

Given the exponential dependencies of the chemical rate constants and rate constant uncertainties on temperature, the uncertainties in the sulfur-containing concentrations were also computed over a range 250-310 K. On the basis of the temperature of maximum concentration uncertainty, this analysis finds that the temperature-dependent chemistry plays a larger role than the explicit temperature-containing expressions for rate constant uncertainties (i.e., $\phi = \phi_{298} \exp|\varepsilon(1/T - 1/298)|$ as suggested by DeMore et al. (1997) and Atkinson et al. (1997)). Thus, the temperature-dependence of the concentration uncertainties are largely determined by the temperature-dependent branching in the DMS oxidation mechanism (e.g., DMS+OH addition versus abstraction). This analysis also shows that the concentration uncertainties for DMS, MSIA, and SO_2 remain nearly constant (about factors of 2) over the full temperature range; the concentrations of DMSO, MSEA, MSA, and H_2SO_4, have uncertainties that vary with temperature by factors of 2 to 4; and the uncertainty for the $DMSO_2$ concentration varies from a factor of 2 to 7 from high to low temperatures, respectively, as controlled by the DMS+OH addition reaction.

Chapter 4

Mechanistic Studies in an Observationally-Constrained Atmospheric Column

4.1 Introduction

Dimethylsulfide (CH_3SCH_3, DMS) oxidation chemistry is an active area of research because of the significant ocean-to-air fluxes of DMS in the marine environment and because of the links between DMS oxidation products and background tropospheric aerosols. Oceanic DMS emissions account for the largest source of natural sulfur to the global atmosphere and may serve as the largest overall source of sulfur in the Southern Hemisphere (Spiro et al., 1992; Bates et al., 1992). In the atmosphere, DMS undergoes a complex series of gas-phase reactions, the oxidized products of which have a strong tendency to interact with water and aerosols. These interactions include the creation of new particles through particle nucleation or the alteration of existing aerosols through condensation and multiphase chemistry. Given these large sulfur fluxes and connections to aerosols, the atmospheric DMS cycle may significantly affect the radiative budget of the background atmosphere.

The major gas-phase DMS oxidation products include SO_2, dimethylsulfone ($CH_3S(O)CH_3$, DMSO), dimethylsulfoxide ($CH_3S(O)_2CH_3$, $DMSO_2$), methanesulfonic acid (CH_3SO_3H, MSA), sulfuric acid (H_2SO_4), and possibly methanesulfenic acid (CH_3SOH, MSEA) and methanesulfinic acid ($CH_3S(O)OH$, MSIA). Quantifying the impacts these species have on tropospheric aerosols requires a mechanism that produces the correct gas-phase yields because each species

interacts with aerosols in a different manner. For instance, H_2SO_4 is known to play a prominent role in the nucleation of fresh particles in the atmosphere (Raes and Van Dingenen, 1992; Kulmala et al., 1995), while MSA does not (Kreidenweis and Seinfeld, 1988; Van Dingenen and Raes, 1993). However, DMSO, $DMSO_2$, MSA, and H_2SO_4 all have relatively large solubilities (Sander, 1997) and readily condense on to existing aerosols at rates controlled by species-dependent mass accommodation coefficients and by the available aerosol surface area. Because condensation leads to aerosol growth, which increases aerosol surface area, the condensation of species such as $DMSO_2$ and MSA hinders H_2SO_4-H_2O particle nucleation by increasing the loss of H_2SO_4 onto existing aerosols. Thus, dynamic studies of aerosol growth and nucleation rely on knowledge of the yields of all of the major products in the DMS oxidation chain.

Laboratory-based investigations of DMS oxidation using chemical kinetic and reaction chamber techniques have provided many mechanistic details. A few recent kinetic studies include the DMS+OH reversible reaction (Barone et al., 1996; Turnipseed et al., 1996), the DMSO+OH reaction (Urbanski et al., 1998), and reactions of the methylsulfonyl radical CH_3SO_2 (Kukui et al., 2000). Even though these kinetic studies have been essential in the development of the DMS oxidation mechanism, many more reactions need to be characterized before a complete elementary reaction picture of DMS oxidation emerges. To fill in these gaps, laboratory reaction chamber studies provide information about the products yields for various reactions and conditions. Some recent chamber studies include observations of the major end products from the DMS+OH reaction in the presence of NO_x (Sørensen et al., 1996), under NO_x-free conditions (Barnes et al., 1996), and as NO_x is varied between 0 and 1.8 ppmv (Patroescu et al., 1999). In another chamber study, the rates of the OH-induced decay of DMSO and $DMSO_2$ were measured (Falbe-Hansen et al., 2000). Drawbacks to these chamber studies include a general disagreement between different groups because of differing chamber environments, problems in applying the results to the real atmosphere because of the pseudo-atmospheric chamber conditions, and difficulty in defining mechanisms at the elementary reaction level.

To complement laboratory investigations, field observations of DMS and its oxidation products can be used to deduce mechanistic information. Some studies have directly analyzed field observations to obtain DMS-SO_2 correlations and SO_2 yields (Putaud et al., 1992; Bandy et al., 1992, 1996). However, the direct interpretation of field data is often difficult because photochemical changes have to be separated from the transport tendencies, aerosol-cloud interactions, and other physical processes that are occurring simultaneously. Modeling approaches overcome this difficulty by incorporating these additional processes into a model containing a

DMS oxidation mechanism. The resulting model simulations can then be compared with the field observations and used to assess the mechanism.

There have been many recent modeling studies using both comprehensive (Koga and Tanaka, 1993; Hertel et al., 1994; Saltelli and Hjorth, 1995; Campolongo et al., 1999) and parameterized (Chin et al., 1996; Davis et al., 1999; Mari et al., 1999; Chen et al., 2000) versions of DMS oxidation mechanisms. The comprehensive mechanisms, which are modified or reduced forms of the Yin et al. (1990b) mechanism, are summarized below. The parameterized mechanisms, which use fixed branching ratios and yields, are not discussed further because a comprehensive mechanism is the focus of this report. Detailed reviews of comprehensive DMS oxidation mechanisms can be found in Yin et al. (1990b), Turnipseed and Ravishankara (1993), and Urbanski and Wine (1999).

Yin et al. (1990b) assembled the first comprehensive mechanism of DMS oxidation (146 reactions, 48 species) using all of the available kinetic and thermochemical information at that time. However, their mechanism was designed for testing chamber experiments under high NO_x conditions, so it includes many reactions not relevant in the remote marine atmosphere. Koga and Tanaka (1993) used a mechanism with 40 sulfur reactions and 23 sulfur species in a boundary layer box model to study the latitudinal distribution of DMS products. They added two new hypothetical MSA production reactions relative to the Yin et al. (1990b) scheme, although the reactions they proposed are not kinetically feasible (e.g., the formation of MSA from MSEA+O_2 in one-step). DMS oxidation in the semi-polluted coastal marine boundary layer was studied by Hertel et al. (1994) using a one-dimensional model with a mechanism involving 58 sulfur reactions and 26 sulfur species. They altered the Yin et al. (1990b) mechanism by fixing the yields of MSA (83%) and H_2SO_4 (17%) for many of the reactions, by decreasing the CH_3SO_2 thermal dissociation rate constant by a factor of 10^3 to 10^4, and by eliminating the CH_3SO_3 radical from their scheme. Campolongo et al. (1999) modeled the impacts of multiphase chemistry on the latitudinal distribution of DMS products by adding aqueous-phase reactions to a gas-phase mechanism (37 reactions, 18 species) initially developed by Saltelli and Hjorth (1995). Major gas-phase mechanistic changes relative to Yin et al. (1990b) included a factor of 100 decrease in the thermal dissociation rate of CH_3SO_3 and a large first-order transformation rate of CH_3SO_3 to MSA.

Because all of these comprehensive studies modified the Yin et al. (1990b) scheme by arbitrarily increasing the MSA production rates, each in a different manner, this indicates that MSA production is currently poorly understood. This is further exemplified in the recent study

by Capaldo and Pandis (1997), which compared five different DMS mechanisms with each other and with nine sets of observations. The study found that the MSA predictions varied dramatically between the mechanisms and that no single mechanism reproduced all sets of observations.

This report assesses the current DMS oxidation mechanism, with a focus on the MSA production paths, using an observationally constrained one-dimensional model of DMS chemistry and vertical mixing. Simultaneous observations from Flight 24 aboard the C-130 aircraft during the First Aerosol Characterization Experiment (ACE-1) (Bates et al., 1998a) are used in this study. The ACE-1 Flight 24 observations provide a unique opportunity to examine the DMS mechanism because the dataset constrains many factors important to DMS cycling in the remote marine atmosphere and includes gas-phase measurements of DMS, SO_2, H_2SO_4, and MSA, which are useful for directly evaluating the model. In addition, because the Flight 24 observations were made under clear-sky, daytime conditions, the effects of multiphase chemistry are minimized and the gas-phase oxidation is most active. This allows for a simple model design that concentrates on the gas-phase pathways.

The DMS mechanism is assessed in two different ways in this chapter. First, seven scenarios of the DMS mechanism are tested. The first scenario represents a baseline case, and the remaining scenarios include isomerizations of key sulfur-containing radicals and five new MSA production pathways. A schematic of the baseline mechanism and the additional paths is shown in Figure 4-1. Second, parametric probability distribution functions (PDFs) are constructed from uncertainty estimates of the model parameters. Each of the seven scenarios is evaluated stochastically via Monte Carlo sampling, which produces output PDFs for DMS, SO_2, H_2SO_4, and MSA. Comparison between these output PDFs and the observations determines if the model parameters are sufficient to explain the observations, or whether new chemical pathways are required for statistical agreement.

4.2 DMS Chemistry and Mixing Model

4.2.1 Model Description

The one-dimensional model of DMS oxidation chemistry uses 69 parameters to describe the following processes: vertical mixing, chemical production and loss (55 reactions, 28 species), condensation onto background aerosols (6 species), surface loss (6 species), and DMS emissions. The model inputs are constrained by 8 sets of observations from ACE-1 Flight 24 that define

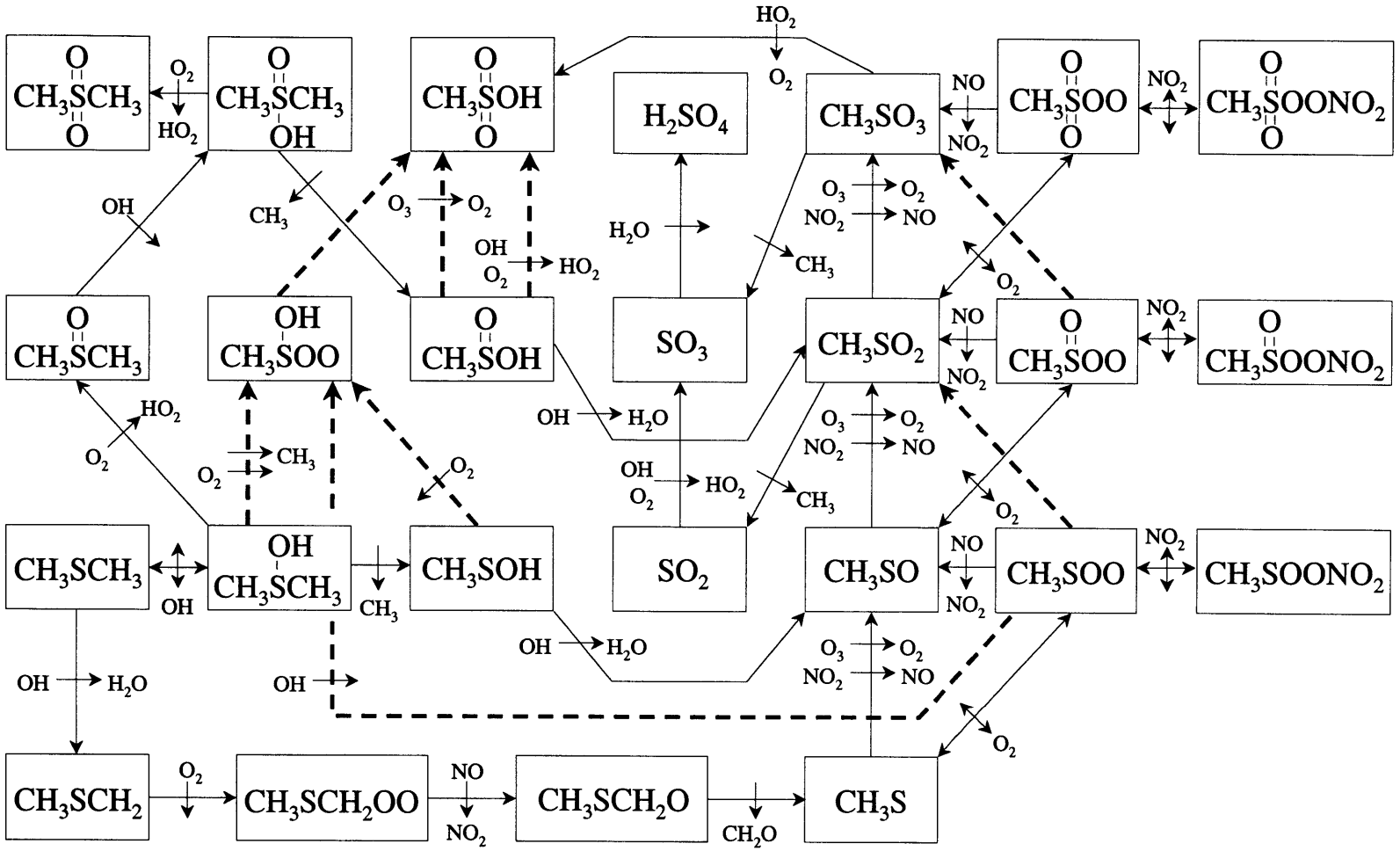

Figure 4-1: The DMS oxidation mechanism in the remote marine atmosphere. The thin black arrows represent the baseline scenario. Additional scenarios are also shown using the dashed arrows, including three isomerization reactions and five hypothesized MSA production paths.

the meteorological, oxidative, and aerosol properties of the atmosphere. Gas-phase number concentrations are predicted using the following continuity equation:

$$\frac{\partial N_i}{\partial t} = \frac{\partial}{\partial z}\left(K_z \frac{\partial N_i}{\partial z}\right) + (P_i - L_i) - \mathbb{C}_i N_i - S_i N_i + E_i \tag{4.1}$$

where N_i is the number concentration of species i, K_z is the vertical mixing coefficient, $(P-L)$ is the net chemical production, $\mathbb{C}$ defines the loss due to condensation, S is the surface loss frequency, and E is the surface emission rate. The surface terms S and E are applied in the lowest model layer and zero flux conditions are used at the upper and lower boundaries.

Vertically, the model resolves the surface to 6 km in twenty layers, using ten 100-meter-thick layers to represent the lowest one kilometer and ten 500-meter-thick layers to represent the remaining five kilometers. This model grid is based on the spatial resolution of the Flight 24 observations because the model grid density is greater where the majority of the aircraft measurements were made (in lowest 1 km), and the 100-meter-thick layers coincide with the aircraft altitude transects roughly spaced 100 meters apart in the vertical. Equation 4.1 is solved using the operator-splitting technique in which the vertical diffusion is split from the other terms. The diffusive tendency is solved using the semi-implicit Crank-Nicholson scheme (Press et al., 1992), where K_z and the layer thickness are both altitude dependent. The net chemical production, condensation, DMS emissions, and surface loss terms make up a fully-coupled system of ordinary differential equations (ODEs), which is solved using the sparse-matrix version of the Livermore Solver for Ordinary Differential Equations (LSODES) (Hindmarsh and Radhakrishnan, 1993). Temporally, LSODES uses a variable time step that depends on the stiffness of the ODE system, and the species concentrations are passed from LSODES to the diffusion routine every five minutes.

4.2.2 Net Chemical Production

The net chemical production during Flight 24 is calculated using a DMS oxidation mechanism designed for the cloud-free, daytime, remote marine atmosphere. This specific set of conditions simplifies the mechanism in the following ways. First, cloud-phase chemistry is neglected because of the clear-sky conditions. The only heterogeneous paths included are irreversible deposition onto aerosols and the ocean surface. Second, the initial oxidation of DMS by NO_3 is not included because the chemistry is occurring during the day. Third, anthropogenic influences are minimized and NO_x levels are low in the remote marine atmosphere, so the DMS

oxidation cycle is primarily driven by HO_x and O_3. Further simplifications are made using the Flight 24 measurements (OH, O_3, H_2O_2, and CH_3OOH) either as direct inputs or to diagnostically calculate other required species. Driving DMS oxidation with observations removes the complications, and possible extra sources of error, associated with calculating photolysis and background HO_x-NO_x-O_x-CH_4 chemistry, and eases the computational burden of the model.

The reactions used to calculate the net chemical production for the seven scenarios are given in Table 4.1. All species in the mechanism that contain a sulfur atom are treated prognostically, all others are either set using the observations or are calculated diagnostically. Rate constant uncertainty factors are also listed in Table 4.1, where the logarithm of the uncertainty factor defines the one-sigma deviation of the lognormal rate constant PDFs used in the Monte Carlo analysis ($\mu \pm \sigma = \log k \pm \log \phi$, where μ and σ are the mean value and standard deviation of the PDFs respectively, and k and ϕ are the rate constant and uncertainty factor respectively). The uncertainty factors were either derived from DeMore et al. (1997) and Atkinson et al. (1997), or estimated using reported spreads of experimentally determined rate constants, or generously assigned a value of 2.5 when no other information was available.

Table 4.1: DMS Oxidation Mechanism

Reaction	Rate Constant	Uncertainty Factor	Refs
	Baseline Chemistry		
$CH_3SCH_3 + OH \rightarrow CH_3SCH_2 + H_2O$	$1.2 \times 10^{-11} \exp\left(\frac{-260}{T}\right)$	$1.15 \exp\left\|100\left(\frac{1}{T} - \frac{1}{298}\right)\right\|$	[1,1]
$CH_3SCH_3 + OH \rightarrow CH_3S(OH)CH_3$	k_f	2.0	[2,2]
$CH_3S(OH)CH_3 \rightarrow CH_3SCH_3 + OH$	k_r	2.5	[3,*e*]
$CH_3S(OH)CH_3 + O_2 \rightarrow CH_3S(O)CH_3 + HO_2$	5×10^{-13}	1.34	[4,3]
$CH_3S(OH)CH_3 \rightarrow CH_3SOH + CH_3$	5×10^{5}	2.5	[5,*e*]
$CH_3S(O)CH_3 + OH \rightarrow CH_3S(O)(OH)CH_3$	$6.3 \times 10^{-12} \exp\left(\frac{800}{T}\right)$	1.3	[6,6]
$CH_3S(O)(OH)CH_3 + O_2 \rightarrow CH_3S(O)_2CH_3 + HO_2$	1×10^{-13}	2.5	[*e*,*e*]
$CH_3S(O)(OH)CH_3 \rightarrow CH_3S(O)OH + CH_3$	2×10^{6}	2.5	[7,*e*]
$CH_3S(O)OH + OH \rightarrow CH_3SO_2 + H_2O$	1×10^{-12}	2.5	[*e*,*e*]
$CH_3SCH_2 + O_2 \rightarrow CH_3SCH_2OO$	5.7×10^{-12}	1.07	[1,1]
$CH_3SCH_2OO + NO \rightarrow CH_3SCH_2O + NO_2$	$7.9 \times 10^{-12} \exp\left(\frac{128}{T}\right)$	2.5	[4,*e*]
$CH_3SCH_2O \rightarrow CH_3S + CH_2O$	3.3×10^{4}	2.5	[4,*e*]
$CH_3SOH + OH \rightarrow CH_3SO + H_2O$	5×10^{-11}	2.5	[*e*,*e*]
$CH_3S + NO_2 \rightarrow CH_3SO + NO$	$2.1 \times 10^{-11} \exp\left(\frac{320}{T}\right)$	$1.15 \exp\left\|100\left(\frac{1}{T} - \frac{1}{298}\right)\right\|$	[1,1]
$CH_3S + O_3 \rightarrow CH_3SO + O_2$	$2.0 \times 10^{-12} \exp\left(\frac{290}{T}\right)$	$1.15 \exp\left\|100\left(\frac{1}{T} - \frac{1}{298}\right)\right\|$	[1,1]
$CH_3S + O_2 \rightarrow CH_3SOO$	$1.4 \times 10^{-16} \exp\left(\frac{1550}{T}\right)$	2.0	[2,2]
$CH_3SOO \rightarrow CH_3S + O_2$	$1.5 \times 10^{11} \exp\left(\frac{-3910}{T}\right)$	2.0	[2,2]

continued on next page

continued from previous page

Reaction	Rate Constant	Uncertainty Factor	Refs
$CH_3SOO + NO \rightarrow CH_3SO + NO_2$	1.1×10^{-11}	$2.0 \exp\left\|100\left(\frac{1}{T} - \frac{1}{298}\right)\right\|$	[1,1]
$CH_3SOO + NO_2 \rightarrow CH_3SOONO_2$	2.2×10^{-11}	$2.0 \exp\left\|100\left(\frac{1}{T} - \frac{1}{298}\right)\right\|$	[2,1]
$CH_3SOONO_2 \rightarrow CH_3SOO + NO_2$	4×10^{-3}	2.5	[e,e]
$CH_3SO + NO_2 \rightarrow CH_3SO_2 + NO$	1.2×10^{-11}	1.4	[1,1]
$CH_3SO + O_3 \rightarrow CH_3SO_2 + O_2$	6.0×10^{-13}	1.5	[1,1]
$CH_3SO + O_2 \rightarrow CH_3S(O)OO$	$2.6 \times k_{CH_3S+O_2}$	2.5	[e,e]
$CH_3S(O)OO \rightarrow CH_3SO + O_2$	$2.6 \times k_{CH_3SOO}$	2.5	[e,e]
$CH_3S(O)OO + NO \rightarrow CH_3SO_2 + NO_2$	8×10^{-12}	2.5	[5,e]
$CH_3S(O)OO + NO_2 \rightarrow CH_3S(O)OONO_2$	1×10^{-12}	2.5	[5,e]
$CH_3S(O)OONO_2 \rightarrow CH_3S(O)OO + NO_2$	4.2×10^{-3}	2.5	[5,e]
$CH_3SO_2 + NO_2 \rightarrow CH_3SO_3 + NO$	2.2×10^{-12}	1.5	[8,8]
$CH_3SO_2 + O_3 \rightarrow CH_3SO_3 + O_2$	5×10^{-15}	2.5	[5,e]
$CH_3SO_2 + O_2 \rightarrow CH_3S(O)_2OO$	$0.86 \times k_{CH_3S+O_2}$	2.5	[e,e]
$CH_3SO_2 + OH \rightarrow CH_3SO_3H$	5×10^{-11}	2.5	[5,e]
$CH_3S(O)_2OO \rightarrow CH_3SO_2 + O_2$	$0.86 \times k_{CH_3SOO}$	2.5	[e,e]
$CH_3S(O)_2OO + NO \rightarrow CH_3SO_3 + NO_2$	1×10^{-11}	2.5	[5,e]
$CH_3S(O)_2OO + CH_3O_2 \rightarrow CH_3SO_3 + CH_2O + HO_2$	5.5×10^{-12}	2.5	[5,e]
$CH_3S(O)_2OO + NO_2 \rightarrow CH_3S(O)_2OONO_2$	1×10^{-12}	2.5	[5,e]
$CH_3S(O)_2OONO_2 \rightarrow CH_3S(O)_2OO + NO_2$	4.2×10^{-3}	2.5	[5,e]
$CH_3SO_2 \rightarrow CH_3 + SO_2$	$k_{CH_3SO_2}$	2.5	[9,e]
$CH_3SO_3 \rightarrow CH_3 + SO_3$	1.6×10^{-1}	2.5	[5,e]
$CH_3SO_3 + HO_2 \rightarrow CH_3SO_3H + O_2$	5×10^{-11}	2.5	[5,e]
$SO_2 + OH \rightarrow HOSO_2$	k_{SO_2+OH}	$\sqrt{k^+/k^-}$	[1,1]
$HOSO_2 + O_2 \rightarrow SO_3 + HO_2$	$1.3 \times 10^{-12} \exp\left(\frac{-330}{T}\right)$	$1.2 \exp\left\|200\left(\frac{1}{T} - \frac{1}{298}\right)\right\|$	[1,1]
$SO_3 + H_2O \rightarrow H_2SO_4$	$k_{SO_3+H_2O}$	$2.0 \exp\left\|110\left(\frac{1}{T} - \frac{1}{298}\right)\right\|$	[10,10]
	Isomerizations		
$CH_3SOO \rightarrow CH_3SO_2$	1×10^{0}	2.5	[e,e]
$CH_3S(O)OO \rightarrow CH_3SO_3$	8×10^{-2}	2.5	[e,e]
$CH_3S(OH)(OO) \rightarrow CH_3SO_3H$	1×10^{-6}	2.5	[e,e]
	Branch A		
$CH_3S(OH)CH_3 + O_2 \rightarrow CH_3S(OH)(OO)CH_3$	1×10^{-13}	2.5	[e,e]
$CH_3S(OH)(OO)CH_3 \rightarrow CH_3S(OH)(OO) + CH_3$	1×10^{4}	2.5	[e,e]
$CH_3S(OH)(OO)CH_3 \rightarrow CH_3S(OH)CH_3 + O_2$	$10^{-4} \times k_{CH_3SOO}$	2.5	[e,e]
	Branch B		
$CH_3SOH + O_2 \rightarrow CH_3S(OH)(OO)$	1×10^{-23}	2.5	[e,e]
$CH_3S(OH)(OO) \rightarrow CH_3SOH + O_2$	0.0	2.5	[e,e]
	Branch C		
$CH_3SOO + OH \rightarrow CH_3S(OH)(OO)$	$10^{5} \times k_{SO_2+OH}$	2.5	[e,e]

continued on next page

continued from previous page

Reaction	Rate Constant	Uncertainty Factor	Refs
$CH_3S(OH)(OO) \rightarrow CH_3SOO + OH$	0.0	2.5	[e,e]
	Branch D		
$CH_3S(O)OH + O_3 \rightarrow CH_3SO_3H + O_2$	2×10^{-18}	2.5	[e,e]
	Branch E		
$CH_3S(O)OH + OH \rightarrow CH_3S(O)(OH)(OH)$	$0.5 \times k_{SO_2+OH}$	2.5	[e,e]
$CH_3S(O)(OH)(OH) + O_2 \rightarrow CH_3SO_3H + HO_2$	$2.0 \times k_{HOSO_2+O_2}$	2.5	[e,e]

First-order and second-order rate constants have units of s^{-1} and cm^3 $molecule^{-1}$ s^{-1}. Temperature has units of K. Concentrations are in units of molecules cm^{-3}. The first and second entries in the References column are for the rate constant and uncertainty factor. 1=DeMore et al., 2=Atkinson et al., 3=Barone et al., 4=Turnipseed et al. (1996), 5=Yin et al., 6=Hynes and Wine, 7=Urbanski et al. (1998), 8=Ray et al., 9=Kukui et al., 10=Lovejoy et al., e=estimated here.

[a] The forward addition of OH to DMS is given by $k_f = \frac{1.7\times10^{-42}[O_2]\exp(7810/T)}{1+5.5\times10^{-31}[O_2]\exp(7460/T)}$.

[b] The reverse reaction is calculated using $k_r = k_f/K_{eq}$, where K_{eq} is the temperature dependent equilibrium constant given by $K_{eq} = 8.3 \times 10^{-29} T \exp(5136/T)$ cm^3 $molecule^{-1}$.

[c] The *ab initio* rate constant calculated by Kukui et al. is used in the model.

[d] The effective second-order rate constant reported in DeMore et al. is used for the SO_2+OH association reaction. The uncertainty is estimated using $0.5\left(\log k^+ - \log k^-\right)$, where k^+ and k^- are the upper and lower limits respectively of the rate constant using the uncertainty ranges given in DeMore et al..

[e] The reaction rate is second-order in water vapor, which is specified using the following equivalent second-order rate constant $k_{SO_3+H_2O} = 2.26 \times 10^{-43} T \exp(6544/T)[H_2O]$. The uncertainty factory for this reaction rate is estimated from the measurements of Lovejoy et al. (1996).

Baseline Chemistry The baseline chemistry in Table 4.1 is a reduced form of the Yin et al. (1990b) mechanism, where the reduced mechanism includes only the most efficient reactions occurring in the clear-sky, daytime, remote marine atmosphere. A few notable exceptions are some NO_x reactions that are kept to maintain unique pathways. The baseline reactions have been updated using many recently reported rate constants as listed in Table 4.1. Key changes or updates from Yin et al. (1990b) include the following:

1. The temperature and pressure dependent reverse addition of OH to DMS has been estimated by combining the reported forward rate constant (Atkinson et al., 1997) with the equilibrium constant calculated using the experimental data of Barone et al. (1996).

2. The forward and reverse reactions $CH_3S(O)_x + O_2 \rightleftharpoons CH_3S(O)_xOO$ rapidly reach equilibrium giving a $[CH_3S(O)_xOO]/[CH_3S(O)_x]$ ratio linearly dependent on pressure and exponentially dependent on temperature. The forward and reverse rate constants for the $x = 0$ case have been individually fit to experimental data from Turnipseed et al. (1992), which yields a ratio that varies from 0.77 at the surface to 2.2 at 6 km for Flight 24 conditions. The same ratio is assumed for $x = 1$ and 2. This is the first modeling study to account for the temperature variations of this ratio.

3. Reactions of the CH_3SO_2 radical are believed to play an important role in the branching between SO_2 and MSA. The *ab initio* pressure and temperature dependent dissociation rate constant of CH_3SO_2 calculated and experimentally confirmed by Kukui et al. (2000) is adopted in this study.

4. Reactions of the DMSO-OH adduct are important for branching between $DMSO_2$ and MSIA. The formation rate of $CH_3S(O)(OH)CH_3$ and the subsequent decay into MSIA have been updated using recent measurements (Hynes and Wine, 1996; Urbanski et al., 1998). The formation rate of $DMSO_2$ has been lowered to maintain the Yin et al. (1990b) ratio of MSIA formation to $DMSO_2$ formation.

5. Rate constants for the oxidation reactions of MSEA and MSIA with OH have been decreased from the Yin et al. (1990b) values to enhance the production of MSA along the DMS+OH addition branch.

Isomerization Reactions The isomerization scenario looks at the impacts of adding the following two isomerization reactions to the baseline chemistry:

$$CH_3SOO \rightarrow CH_3SO_2 \quad \text{(R1)}$$

$$CH_3S(O)OO \rightarrow CH_3SO_3 \quad \text{(R2)}$$

These reactions are driven by the large thermodynamic difference in stability between the reactants and products. At 298 K for example, reaction R1 has an enthalpy change of ΔH_{rxn} = −314 kJ/mole (DeMore et al., 1997). Kinetically, the reactions should be slow due to the large energy barriers associated with the three-center transition states. However, the reactant concentrations should be sufficient to compensate for the large barriers and make the rates competitive. Reaction R1 has been measured in room temperature solutions, $k = 2\times10^3$ s^{-1} (Zhang et al., 1994), and an upper limit has been set in the gas-phase, k = 20-25 s^{-1} (Turnipseed et al., 1993). Reaction R1 has been used in previous modeling studies (Saltelli and Hjorth, 1995; Campolongo et al., 1999), while reaction R2 has not.

Branch A The branch A scenario increases MSA production by the addition of O_2 to the DMS-OH adduct, followed by dissociation into $CH_3S(OH)(OO)$, which then isomerizes into MSA:

$$CH_3S(OH)CH_3 + O_2 \rightleftharpoons CH_3S(OH)(OO)CH_3 \quad \text{(R3)}$$

$$CH_3S(OH)(OO)CH_3 \rightarrow CH_3S(OH)(OO) + CH_3 \quad \text{(R4)}$$

$$CH_3S(OH)(OO) \rightarrow CH_3SO_3H \quad \text{(R5)}$$

Koga and Tanaka (1993) proposed a similar pathway, but suggested that the dissociation and MSA isomerization occurred in one-step (reactions R4+R5). Reaction R3 was reported by Yin et al. (1990b) and that rate constant is used here. Reaction R4 has not been previously reported, though a similar reaction involving CH_3 dissociation from $CH_3S(O)(OH)CH_3$ has been experimentally confirmed and measured (Urbanski et al., 1998). The MSA isomerization reaction R5 is based on analogy to reactions R1 and R2, and is used in the branch A-C scenarios.

Branch B Hatakeyama and Akimoto (1983) first proposed that MSEA+O_2 can form MSA in one-step, a reaction later exploited by Koga and Tanaka (1993) to increase MSA production rates. However, this is unlikely to occur as a one-step reaction due to the strength of the O_2 double bond. Alternatively, the process can be written in two elementary steps, O_2 addition to MSEA as shown below, followed by reaction R5.

$$CH_3SOH + O_2 \rightarrow CH_3S(OH)(OO) \quad \text{(R6)}$$

Reaction R6 is proposed by analogy to similar O_2 addition reactions known to occur with CH_3S and $CH_3S(OH)CH_3$.

Branch C The branch C scenario increases MSA production through two steps. First, OH adds to CH_3SOO as shown below, which is followed by isomerization reaction R5.

$$CH_3SOO + OH \rightarrow CH_3S(OH)(OO) \quad \text{(R7)}$$

Reaction R7 is reported here for the first time and is based on analogous OH-addition reactions with DMS, DMSO, and SO_2.

Branch D The branch D scenario increases MSA production through the oxidation of MSIA by ozone:

$$CH_3S(O)OH + O_3 \rightarrow CH_3SO_3H + O_2 \quad \text{(R8)}$$

Reaction R8 has not been previously proposed and is based on the similar CH_3SO_x+O_3 reactions. Reaction R8 may provide a significant source of MSA at higher altitudes given that MSIA may have a relatively large lifetime and that ozone typically increases with altitude.

Branch E The branch E scenario oxidizes MSIA to MSA by the following two steps:

$$CH_3S(O)OH + OH \rightarrow CH_3S(O)(OH)OH \quad \text{(R9)}$$

$$CH_3S(O)(OH)OH + O_2 \rightarrow MSA + HO_2 \quad \text{(R10)}$$

These reactions are modeled for the first time in this report. Reactions R9 and R10 are based on the analogous set of reactions that oxidize SO_2 to SO_3, and the rate constants are proportional to those of the analogous reactions.

4.2.3 Scavenging by Aerosols

The clear-sky (i.e., cloud-free but not aerosol-free) conditions and low liquid water content during ACE-1 Flight 24 imply that gas-to-aerosol transfer is efficient only for the most soluble sulfur species. These species in the DMS cycle include DMSO, $DMSO_2$, MSA and H_2SO_4. The solubility properties of MSEA and MSIA have not been characterized, but they are also assumed to undergo loss by condensation in the model simulations. The loss of SO_2 to sea-salt aerosols during Flight 24 is also important as shown by Mari et al. (1999), but this loss is not explicitly calculated using the methodology in this section. Rather, the loss of SO_2 to sea-salt aerosols at the surface is factored into an empirically determined first-order surface removal rate coefficient that accounts for both dry deposition and aerosol scavenging (see Section 4.2.4).

The net loss by condensation for DMSO, $DMSO_2$, MSA, MSEA, MSIA, and H_2SO_4 is calculated using the expression:

$$\mathbb{C}_i = 4\pi D_i \sum_j \left(\frac{n_{j,j+1}}{\Delta r_{j,j+1}} \int_{r_j}^{r_{j+1}} r \; f(Kn_i, \alpha_i) dr \right) \quad (4.2)$$

where $\mathbb{C}_i$ is the first-order loss coefficient for the condensation of species i, D_i is the molecular diffusion coefficient, $n_{j,j+1}$ is the particle number concentration (particles cm^{-3}) for particles with a radius between r_j and r_{j+1} in the j-th bin of the aerosol size distribution, Kn_i is the Knudsen number defined as the ratio of the mean free path of i (λ_i) to the particle radius, α_i is the mass accommodation coefficient, and $f(Kn_i, \alpha_i)$ is a correction factor accounting for flux

changes between the kinetic and bulk regimes and imperfect mass accommodation.

The gas-phase molecular diffusion coefficient is calculated using the expression

$$D_i = \frac{3}{8N_{air}\sigma_{i,air}^2}\sqrt{\frac{RT}{2\pi}\left(\frac{m_i + m_{air}}{m_i m_{air}}\right)} \tag{4.3}$$

where N_{air} is the air number density, $\sigma_{i,air}$ is the collision diameter (set at 4.5×10^{-10} m), R is the gas constant, T is the temperature, and m is the molar mass (Jacobson, 1999). The mean free path is approximated by

$$\lambda_i = 3D_i\sqrt{\frac{\pi m_i}{8RT}} \tag{4.4}$$

and the correction factor is calculated using

$$f(Kn,\alpha) = \frac{f_1\alpha(1+Kn)}{Kn^2 + (1+f_2\alpha)Kn + f_1\alpha} \tag{4.5}$$

with f_1=0.75 and f_2=0.283 (Fuchs and Sutugin, 1971). The mass accommodation coefficients of DMSO, $DMSO_2$, and MSA are calculated using the temperature dependent expression

$$\alpha(T) = \frac{g(T)}{1+g(T)} \tag{4.6}$$

where $g(T) = \exp\left[-\frac{1}{RT}(\Delta H - T\Delta S)\right]$, and ΔH and ΔS are given in De Bruyn et al. (1994). Mass accommodation uncertainty factors of 2.0 have been assigned for DMSO, $DMSO_2$, and MSA (DeMore et al., 1997). For H_2SO_4 a constant value of $\alpha = 0.65$ is used along with an estimated uncertainty factor of 1.5 (Pöschl et al., 1998). For MSEA and MSIA values of $\alpha = 1 \times 10^{-3}$ and 2×10^{-4} are used respectively, each with an uncertainty factor of 2.0. These values are based on the upper and lower limits for the mass accommodation of organic acids onto $(NH_4)_2SO_4$ as measured by Wagner et al. (1996).

The $n_{j,j+1}$ and $\Delta r_{j,j+1}$ in equation 4.2 are directly supplied by Flight 24 observations of particle size distributions (see Section 4.3.4), while all the other terms are explicitly calculated using observations of T and p. The integral in equation 4.2 has known analytical solutions which are used in the model. The observationally constrained loss coefficients for condensation as a function of altitude are shown in Figure 4-2. We also estimate the uncertainties in $\mathbb{C}$ using

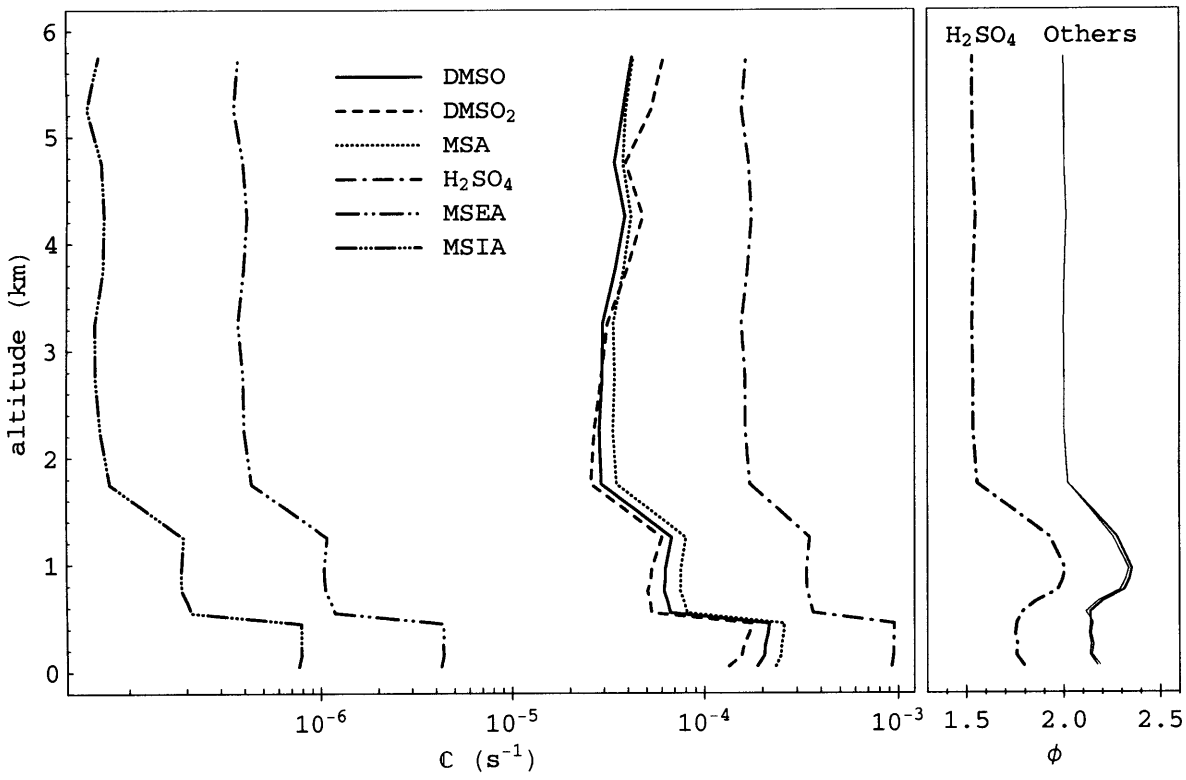

Figure 4-2: The left panel displays the coefficients for the loss of DMSO, $DMSO_2$, MSA, H_2SO_4, MSEA, and MSIA onto aerosols as a function of altitude. The right panel displays the corresponding uncertainty factors as a function of altitude. The aerosol observations used to calculate these profiles are discussed in Section 4.3.4.

the following expression:

$$\log \phi_{\mathbb{C}} = \sqrt{(\delta \log \mathbb{C})^2 + \left(\frac{\partial \log \mathbb{C}}{\partial \log \alpha} \log \phi_\alpha\right)^2} \tag{4.7}$$

where $\delta \log \mathbb{C}$ is the difference in the condensation rate using two independent observed aerosol size distributions and ϕ_α is the mass accommodation uncertainty factor. The uncertainty expression is further simplified by setting $\partial \log \mathbb{C} / \partial \log \alpha = 1$, which is an upper limit for the aerosols most affected by mass accommodation. The uncertainty factors for $\mathbb{C}$ as a function of altitude are also shown in Figure 4-2.

Table 4.2: Surface Flux and Vertical Mixing Parameters

Parameter	Value	ϕ
	Emission Rate (molecules cm^{-3} s^{-1})	
E_{DMS}	9.5×10^4	2.5
	Surface Loss (s^{-1})	
S_{DMSO}	1.0×10^{-5}	2.5
S_{DMSO_2}	1.0×10^{-5}	2.5
S_{SO_2}	5.0×10^{-5}	2.5
S_{MSIA}	2.0×10^{-5}	2.5
S_{MSA}	2.5×10^{-5}	2.5
$S_{H_2SO_4}$	1.0×10^{-5}	2.5
	Vertical Mixing Coefficient (cm^2 s^{-1})	
K_z (boundary layer)	5×10^4	1.4
K_z (buffer layer)	5×10^3	1.4
K_z (free troposphere)	3×10^3	1.4

ϕ = uncertainty factor

4.2.4 Surface Fluxes and Vertical Mixing

DMS Surface Emissions The only significant source of sulfur in the remote marine atmosphere is the sea-to-air flux of DMS. This flux was directly estimated by Bates et al. (1998b) during ACE-1 aboard the research vessel Discoverer through measurements of the sea-surface and atmospheric concentrations of DMS and the surface wind speed. These measurement-based flux estimates range between 0.8 and 5×10^9 molecules cm^{-2} s^{-1} during the time corresponding to Flight 24 and depending on the flux parameterization used. However, because the Discoverer and C-130 aircraft did not correspond exactly in space, this range is only representative of the typical DMS fluxes over the region sampled by the aircraft. This discrepancy was addressed by Suhre et al. (1998) and Mari et al. (1999) in which the DMS sea-surface measurements were interpolated on to the Flight 24 trajectory and the wind speeds calculated along the trajectory, resulting in an approximate DMS flux range of 0.9 to 4×10^9 molecules cm^{-2} s^{-1} for the flux parameterization most consistent with observations. In a more recent evaluation, Shon et al. (2001) used a mass-balance photochemical model to estimate the Flight 24 DMS flux to be 1.6×10^9 molecules cm^{-2} s^{-1}.

In this report a time-independent DMS emission rate is estimated by adjusting the rate until

the model predicted atmospheric DMS concentrations in the lowest model layer agree with the observed values. The resulting DMS emission rate is shown in Table 4.2 and has an equivalent surface flux value of 9.5×10^8 molecules cm^{-2} s^{-1}, which lies at the lower end of the previously reported flux ranges. The listed uncertainty factor of 2.5 reflects the uncertainties associated with different flux parameterizations and gives a one-sigma flux range of 0.4 to 2×10^9 molecules cm^{-2} s^{-1}.

Surface Losses Loss at the ocean surface is modeled using the time-independent, first-order surface loss coefficients and uncertainty factors listed in Table 4.2. These surface loss frequencies are applied in the lowest model layer and physically represent dry deposition removal of DMSO, $DMSO_2$, H_2SO_4, MSA, and MSIA, and dry deposition and sea-salt scavenging of SO_2. The loss frequencies, except for SO_2, correspond to deposition velocities with a one-sigma range of 0.04 to 0.625 cm s^{-1}, which are representative of the relatively stable atmospheric conditions during Flight 24. The mean SO_2 surface loss frequency was adjusted to provide good agreement between the model predictions and observations in the boundary layer. This SO_2 loss frequency has a corresponding deposition velocity of 0.5 cm s^{-1} if dry deposition was the only SO_2 surface removal path. Also, this SO_2 loss frequency provides a surface sink that is comparable to the sum of the SO_2 dry deposition and sea-salt sinks at the surface in the Flight 24 simulations of Mari et al. (1999). Finally, the assumption of no SO_2 sea-salt processing above the lowest model layer may overestimate the SO_2 concentrations or SO_2+OH removal rate there, but this will reinforce the major conclusions from this study as discussed later.

Vertical Mixing The turbulent mixing characteristics during Flight 24 of the ACE-1 campaign were analyzed in detail by Russell et al. (1998) and Wang et al. (1999a,b). These studies revealed the existence of the following three distinct layers: the boundary layer (BL, $z \leq 0.5$ km), the buffer layer (FL, $0.5 < z \leq 1.5$ km), and the free troposphere (FT, $z > 1.5$ km). These studies also showed that there was little change in the depths of these layers during the course of the flight. In addition, Russell et al. (1998) found large, positive bulk Richardson numbers in the FL, thus indicating stably stratified conditions there, while Wang et al. (1999a) found evidence for mesoscale variability in the BL mixing during Flight 24.

A simplified, diagnostic approach to vertical mixing is adopted in this study to ensure consistency between all species and with observations of sulfur compounds. Based on the findings of Russell et al. (1998) and Wang et al. (1999b) the model atmosphere is segregated into three mixing layers: the BL is represented by the lowest five model layers, the FL by the

next six layers, and the FT by the remaining nine layers. Within each mixing layer a separate time-independent K_z is set using DMS as a tracer for a given DMS sea-to-air flux. DMS serves as an ideal tracer because its vertical mixing time in the BL and FL is shorter than its chemical lifetime. The K_z values were then adjusted until the modeled vertical profile of DMS matched the observed profile. This procedure provides consistent mixing in the BL and FL because of sufficient DMS observations. However, K_z in the FT was estimated by extrapolation from the BL and FL because of a lack of DMS observations above the FL. The resulting K_z values are shown in Table 4.2. The uncertainty factors cover K_z ranges that yield modeled DMS profiles in statistical agreement with observations.

4.3 Observational Constraints

The ACE-1 Flight 24 measurements used to constrain the model runs include: meteorological parameters (temperature T, relative humidity RH, and pressure p), gas-phase measurements (OH, O_3, H_2O_2, and CH_3OOH), and aerosol size distributions. This flight occurred during the local time (LT) period 05:18 to 14:36 LT on 8 December 1995. The measurements included samplings of air from the BL up to an altitude of 5.5 km and were made under daytime and primarily clear-sky conditions. Because the model is constructed for clear-sky conditions, episodes of cloudiness were filtered from the observational database. This filtering uses an analysis of cloud encounters in which a cloud is defined to exist whenever the number concentration of particles with a diameter in the size range of 2.0 to 47 μm is greater than 5 particles cm^{-3} for a period 5 seconds or greater. Additionally, cloud fringe effects were removed by taking ∓ 15 minutes before and after the defined cloud period. Applying the cloud filter removes the data from 14:11:11 LT to the end of the flight.

The Flight 24 observations have one of the following three characteristics: the constraint is mainly a function of space, a function of time, or a function of time and space. Time-series of the observations were analyzed and used to categorize the constraints. These time-series, which are illustrated in Figure 4-3, show that over the course of Flight 24 p, T, RH, and O_3 are largely time invariant, OH is primarily a function of time, and that H_2O_2 and CH_3OOH vary in both time and space. Aerosol number concentrations are also largely time-independent, and the processed aerosol number distributions are shown in Section 4.3.4.

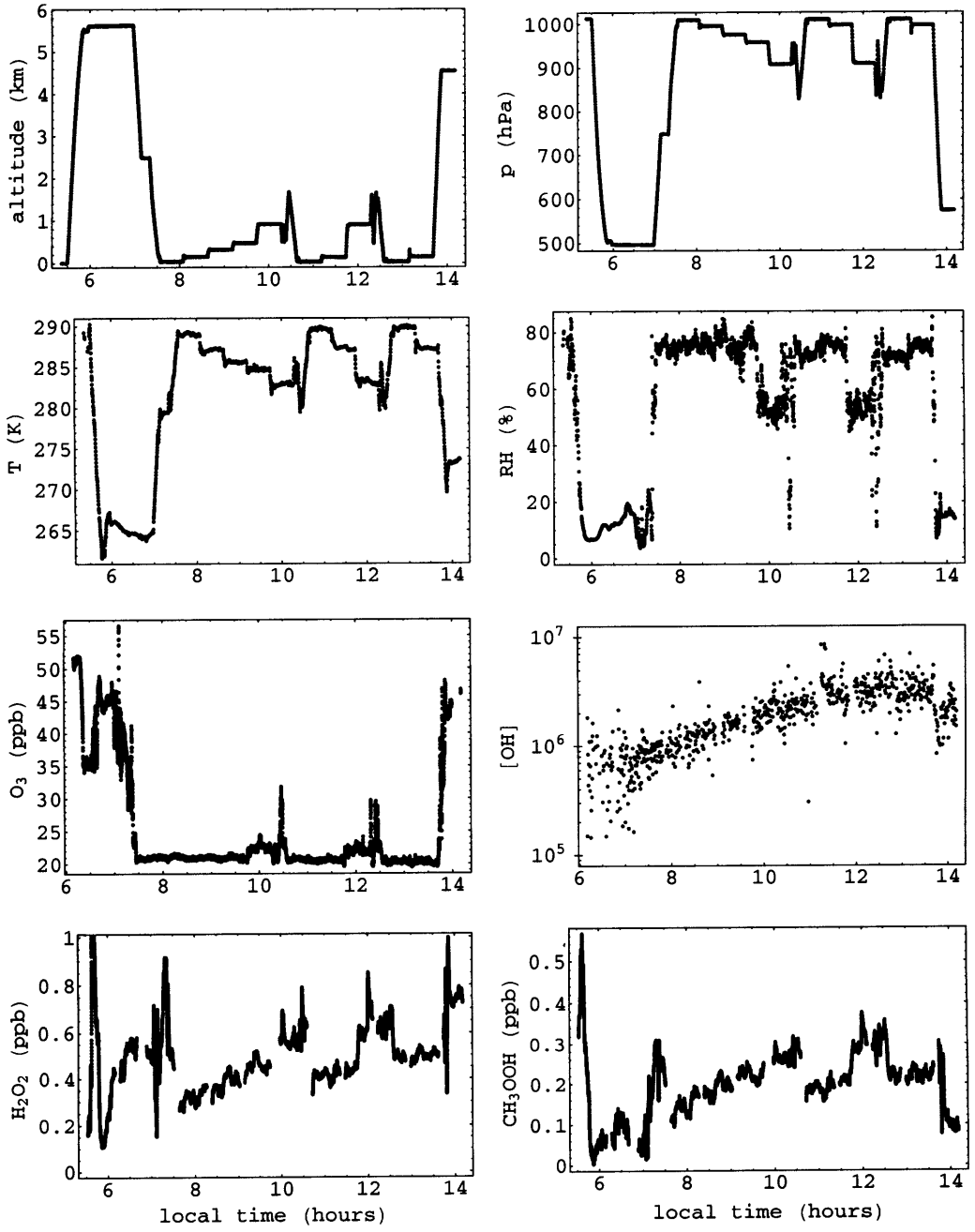

Figure 4-3: ACE-1 Flight 24 measurements of altitude, pressure, temperature, relative humidity, O_3 mole fraction, OH concentration, H_2O_2 mole fraction, and CH_3OOH mole fraction as a function of time. Concentration is in molecules cm^{-3} and mole fractions are in parts per billion (ppb).

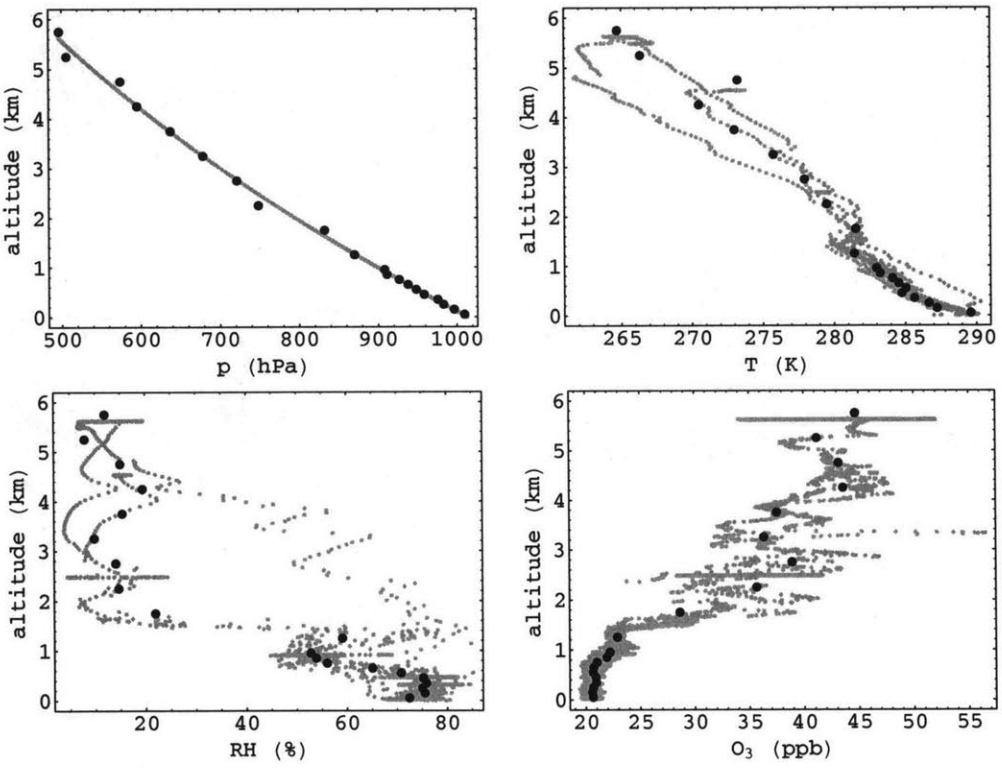

Figure 4-4: Vertical profiles of observed p, T, RH, and O_3 mole fraction during Flight 24. The small gray points are the direct observations, while the larger black points are the binned median values of the observations in each model layer.

4.3.1 p, T, RH, and O_3 Levels

Based on Figure 4-3 p, T, RH, and O_3 are assumed to be fixed in time throughout the model integrations. To capture the strong spatial variations in these quantities, they were binned in altitude layers defined by the model spatial resolution. The median values within each layer were then calculated. The resulting median value vertical profiles are shown in Figure 4-4 and define the observational constraints for p, T, RH, and O_3.

4.3.2 OH Concentrations

In the daytime, remote marine atmosphere, reaction with OH is the dominant DMS sink and drives much of the subsequent oxidation chemistry. In this study, time-dependent *in situ* OH observations from ACE-1 Flight 24 (Mauldin III et al., 1998) have been fit to 'forcing functions'

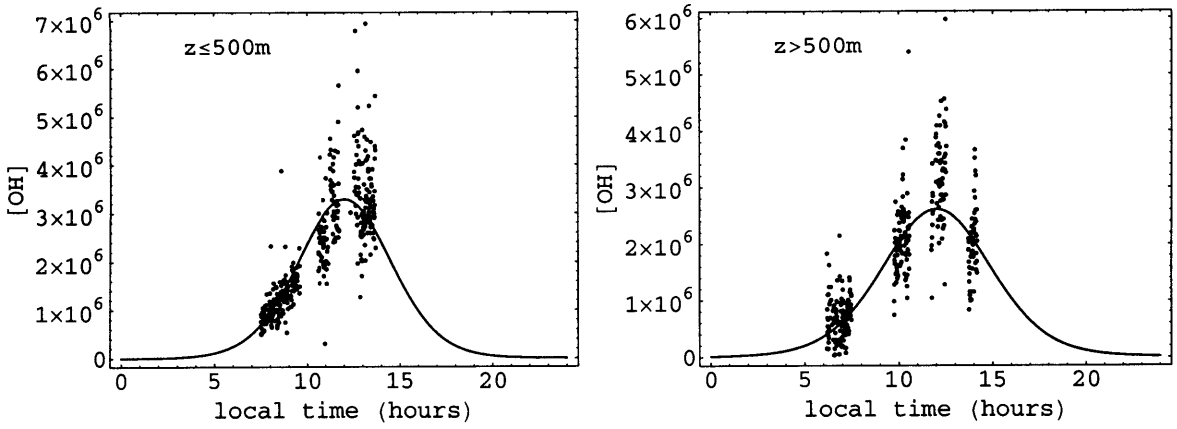

Figure 4-5: Observed and fit OH concentrations (molecules cm^{-3}) for the boundary layer and above. The fitted values for the coefficients in Equation 4.8 in the boundary layer are $A = 1.665$ and $B = 4.853$. Above the boundary layer the fitted values are $A = 1.263$ and $B = 5.153$.

which are used to drive the net chemical production. This scheme captures the oxidative state of the atmosphere during the flight without introducing additional complexities and uncertainties associated with predicting OH using HO_x-NO_x-O_3-CH_4 chemistry. The OH data has been fit specifically to the following function:

$$\log [\mathrm{OH}] = A \sin \left[\frac{\pi}{d} (t - s) \right] + B \tag{4.8}$$

where t is the local time in hours, d is the number of daylight hours, s is the sunrise in hours, A is the amplitude of the OH diurnal cycle, and B is the nighttime OH background concentration. A and B were adjusted in the fits, and $d \approx 15.2$ hours and $s \approx 4.4$ hours were set using the location of the flight and time of year. Figure 4-5 shows the OH observations and fits for the BL ($z \leq 500$ m) and above ($z > 500$ m).

4.3.3 Peroxide Mole Fractions

The H_2O_2 and CH_3OOH time-series in Figure 4-3 clearly show a mole fraction altitude dependence. These species are also slightly time-dependent as shown by the mole fraction increase in the lowest model layer (z = 0 to 50 m) from 07:45-11:00 to 13:00 LT. To capture the dependencies in time and space, the peroxide observations have been fit to fourth-order polynomial

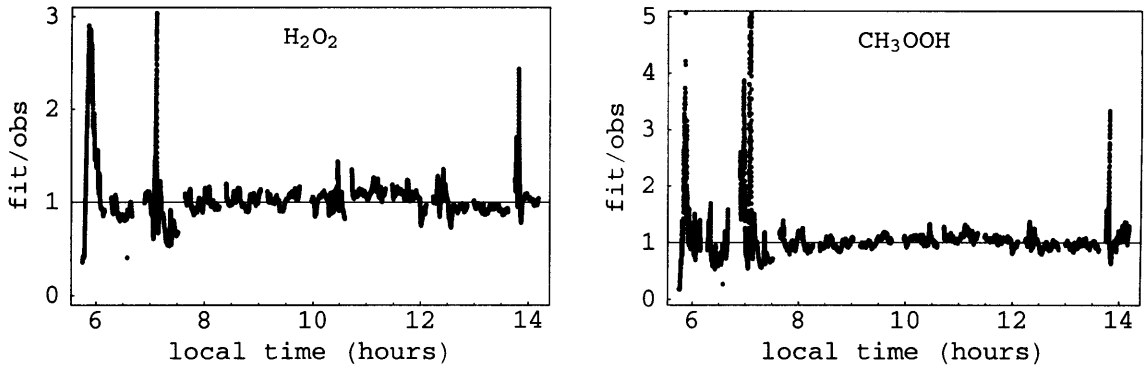

Figure 4-6: Ratios of the functional fits to the Flight 24 mole fraction observations of H_2O_2 and CH_3OOH. The coefficients of the H_2O_2 functional fit (Equation 4.9) are: $\zeta_0 = 0.4612$, $\zeta_1 = 0.1341$, $\zeta_2 = 0.1069$, $\zeta_3 = -0.05263$, $\zeta_4 = 0.005858$. The coefficients of the CH_3OOH functional fit are: $\zeta_0 = 0.2046$, $\zeta_1 = 0.1353$, $\zeta_2 = -0.01901$, $\zeta_3 = -0.01283$, $\zeta_4 = 0.002102$.

functions in altitude modulated by a sinusoidal function in time:

$$ROOH(z,t) = \sin\left[\frac{\pi}{d}(t-s)\right]\sum_{i=0}^{4}\zeta_i z^i \tag{4.9}$$

where $ROOH(z,t)$ represents the peroxide mole fraction in ppb, d and s are the same as in equation 4.8, and ζ_i are the coefficients of the polynomial fit. Separate functions were fit to the H_2O_2 and CH_3OOH observational data. To prevent negative mole fractions, 0.017 $ROOH(z, s+\frac{d}{2})$ was used for all nighttime values, where the factor of 0.017 provides a nearly continuous change from the low daytime values to the nighttime values. The residuals for the resulting fits are shown in Figure 4-6. The anomalous observations before t=6.75 hours are ignored in the fit. This time frame corresponds to high altitude measurements and a period of rapid aircraft ascent.

4.3.4 Aerosol Number Distributions

The loss of condensable gas-phase sulfur is constrained using two independently measured aerosol number distributions from ACE-1 Flight 24. These aerosol spectra each provide the $n_{j,j+1}$ and $\Delta r_{j,j+1}$ required in equation 4.2. The coefficients for loss by condensation are calculated by averaging the two spectra, while the difference ($\delta \log \mathbb{C}$) is used for uncertainty estimates.

The first aerosol distribution data comes from the composite particle probe spectra (CPP). The CPP spectra require no size adjustments for changes in T or RH because the measurements were made under ambient conditions. The CPP spectra were constructed by overlapping the data from four wing-mounted particle probes, resulting in a distribution covering a diameter size range of 0.16 to 600 μm in 43 sections (Baumgardner and Clarke, 1998; Clarke et al., 1998). To compute the aerosol surface area, the spectra were binned in three altitude layers corresponding to the BL, FL, and FT, and the average values calculated within each layer. Corrections were made for a possible air leak in the probe registering the first three sections of the CPP spectra (0.16 to 0.30 μm). The air leak affected the measurements when the aircraft climbed from low to high altitudes (high to low particle concentrations). Time-series of the first three sections indicate that the early-morning measurements were not affected by the air leak, so the contamination is avoided by using the data collected between 05:36 and 09:06 LT. The additional 40 channels in the CPP spectra were not affected by the air leak.

The second set of aerosol distribution data comes from an inboard laser optical particle counter (OPC) (Clarke et al., 1998). The OPC instrument measured particle number concentrations in 233 bins ranging in size from 0.14 to 7.0 μm of aerosols dried to 25% RH and preheated to 40, 150, and 300°C. For this study the sizes of the 40°C samples were adjusted to the ambient RH and T using the Köhler equation at each of the model levels. The samples at 150 and 300°C were not used because of the possible loss of volatile components at these higher temperatures. As with the CPP measurements, the OPC number concentrations were binned in the three altitude layers corresponding to the BL, FL, and FT and the average values computed. After adjusting for ambient conditions, the dry OPC spectra in the BL grew by nearly a factor of two to a diameter size range of 0.25 to 12 μm. The processed CPP and OPC number distributions used to compute the aerosol surface area are displayed in Figure 4-7.

4.3.5 Diagnostic Constraints

The Flight 24 observations do not fully constrain the DMS oxidation model. In particular, the peroxy radicals HO_2 and CH_3O_2 are required for the production and loss of CH_3SO_3, while NO_2 oxidizes CH_3SO_x to CH_3SO_{x+1}. These species are diagnostically calculated from observations assuming steady-state conditions. First, the production and loss of H_2O_2 in the background atmosphere is described by reactions D1 to D3 listed in Table 4.3. From this set of reactions and corresponding rate constants, HO_2 is expressed diagnostically as the following function of observed levels of H_2O_2 and OH, where the subscripts o and e indicate observed and estimated

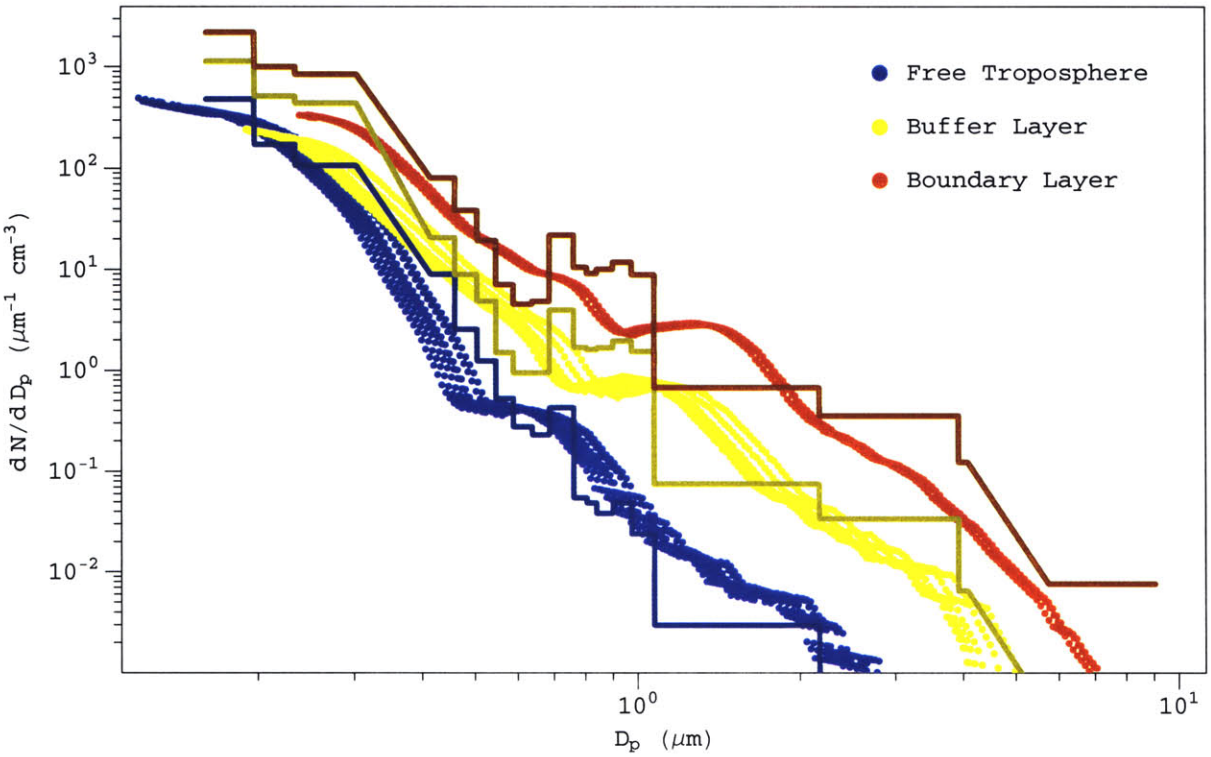

Figure 4-7: Aerosol number distributions from the CPP (lines) and OPC (dots) as a function of particle diameter D_p (μm) in the boundary layer, buffer layer, and free troposphere. The diagonal portions of the CPP distributions represent size gaps in the dataset. The multiple OPC distributions in the BL, FL, and FT result from the size adjustments to ambient conditions at each model layer.

species respectively:

$$[HO_2]_e = \sqrt{\frac{[H_2O_2]_o(k_{D2}[OH]_o + J_{D3})}{k_{D1}}}. \tag{4.10}$$

Production and loss of CH_3OOH in the background atmosphere is controlled by reactions D4 to D7, which yields the following diagnostic expression for CH_3O_2:

$$[CH_3O_2]_e = \frac{[CH_3OOH]_o(J_{D5} + k_{D6}[OH]_o + k_{D7})}{k_{D4}[HO_2]_e}. \tag{4.11}$$

NO_2 is estimated using reactions D8 to D11 and the following diagnostic relationship relating NO_2 to NO, O_3, and peroxy radicals (Seinfeld and Pandis, 1998, p.249):

$$[NO_2]_e = [NO]_o \frac{k_{D9}[O_3]_o + k_{D10}[HO_2]_e + k_{D11}[CH_3O_2]_e}{J_{D8}}. \tag{4.12}$$

Table 4.3: Diagnostic Reactions and Rate Constants

Reaction	Rate Constant	Ref [a]
D1 $HO_2 + HO_2 \rightarrow H_2O_2 + O_2$	k_1 = See Note [b]	[1]
D2 $H_2O_2 + OH \rightarrow HO_2 + H_2O$	$k_2 = 2.9 \times 10^{-12} \exp(-160/T)$	[1]
D3 $H_2O_2 \xrightarrow{h\nu} 2\ OH$	$J_3^* = 7.7 \times 10^{-6}$ [c]	[2]
D4 $CH_3O_2 + HO_2 \rightarrow CH_3OOH + O_2$	$k_4 = 3.8 \times 10^{-13} \exp(800/T)$	[1]
D5 $CH_3OOH \xrightarrow{h\nu,O_2} CH_2O + HO_2 + OH$	$J_5^* = 5.7 \times 10^{-6}$ [c]	[2]
D6 $CH_3OOH + OH \rightarrow CH_3O_2 + H_2O$	$k_6 = 2.66 \times 10^{-12} \exp(200/T)$	[1]
D7 $CH_3OOH \rightarrow CH_2O + H_2O$	$k_7 = 1.14 \times 10^{-12} \exp(200/T)$	[1]
D8 $NO_2 \xrightarrow{h\nu,O_2} NO + O_3$	$J_8^* = 8.8 \times 10^{-3}$ [c]	[2]
D9 $NO + O_3 \rightarrow NO_2 + O_2$	$k_9 = 2.0 \times 10^{-12} \exp(-1400/T)$	[1]
D10 $NO + HO_2 \rightarrow NO_2 + OH$	$k_{10} = 3.5 \times 10^{-12} \exp(250/T)$	[1]
D11 $CH_3O_2 + NO \xrightarrow{O_2} CH_2O + HO_2 + NO_2$	$k_{11} = 3.0 \times 10^{-12} \exp(280/T)$	[1]

[a] References: [1] = DeMore et al. (1997), [2] = Jacobson (1999).

[b] The reaction has bimolecular and termolecular components and a water correction. The overall rate constant is given by: $k_1 = k_a\,(k_b + k_c)$, where $k_a = 1 + 1.4 \times 10^{-21}[H_2O]\exp(\frac{2200}{T})$, $k_b = 2.3 \times 10^{-13}\exp\left(\frac{600}{T}\right)$, and $k_c = 1.7 \times 10^{-33}[M]\exp(\frac{1000}{T})$.

[c] J-value diurnal variations are calculated using $\log_{10} J = (\log_{10} J^* - A) + A\sin\left[\frac{\pi}{d}(t-s)\right]$, where J^* is the midday maximum given in the table, A is the amplitude (set to 1.24), $(\log_{10} J^* - A)$ represents the background value, and d and s are as given in equation 4.8. The J^* are for clear-sky, 0° solar zenith angle, and UV surface albedo of 0.03.

Although NO was measured during the ACE-1 C-130 flights, most of the Flight 24 levels fell below the detection limit (5 pptv). NO levels were fixed arbitrarily at the detection limit for all the model integrations used in this study. Also, the photolysis reactions take diurnal variability into account using the same functional form for the OH forcing function.

4.4 Analysis and Discussion

The model is integrated for a ten day period, the last day of which is used in this analysis. After ten days a steady daily cycle is achieved in the BL and FL. The following seven model runs, corresponding to seven mechanism scenarios, were carried out: (1) baseline, (2) isomerizations, and (3) to (7) branches A to E. Note that the isomerizations run also includes the baseline chemistry, and the branch A-E runs include both the baseline and isomerization reactions.

4.4.1 Model Uncertainties

The seven model scenarios were randomly evaluated using a Monte Carlo sampling method with a sample size of 6000. This results in a set of output species PDFs that are well resolved and nearly lognormal. The standard deviations of these output PDFs define the uncertainties in the model predictions due to uncertainties in the model parameters. Figure 4-8 shows examples of daily average, boundary layer PDFs for the major species in the DMS cycle for the branch D scenario. The mean values that are displayed were calculated directly from the output PDFs and are almost identical to the values obtained from a run of the model using the mean values of the parameters. The figure also shows that these species have uncertainty factors that range between 2.5 and 2.9.

Additionally, using the following equation we calculated the contributions from the parameter uncertainties to the overall model uncertainties to determine the importance of each parameter to the model predictions.

$$(\Delta \log N_i)^2 = \sum_j \left(\frac{\partial \log N_i}{\partial \log \mathrm{p}_j} \log \phi_j \right)^2 \tag{4.13}$$

This equation expresses the total variance as a sum of the variance contributions from all of the uncertain parameters, where the partial derivative term characterizes the sensitivity of species N_i to model parameter p_j and ϕ_j is the uncertainty factor for p_j. We evaluated this expression for the branch D case by running a reference case at the parameter means and additional cases in which each parameter was multiplied by the corresponding uncertainty factor. The resulting variance contributions are shown in Table 4.4. The results in the table indicate that the uncertainty in DMS emissions is the main source of uncertainty for all of the species and accounts for nearly all of the uncertainty in the DMS predictions. Other parameters that contribute more than 10% to the species uncertainties are losses to aerosols, surface losses, the DMS+OH reversible addition reaction, and other reactions as noted. The table also shows that, except for DMS and SO_2, three or more parameters contribute significantly to the overall uncertainty. This increases the complexity of studies trying to reduce the overall uncertainties because many parameters have to be simultaneously monitored. Finally, it is worth noting that the vertical mixing coefficients are not major contributors to the overall uncertainties because the model is insensitive to large changes in K_z. For instance, changing K_z by a factor of 3.0 (more than three standard deviations from the mean) results in uncertainty contributions that are smaller than 3% for DMS and even smaller for the other species.

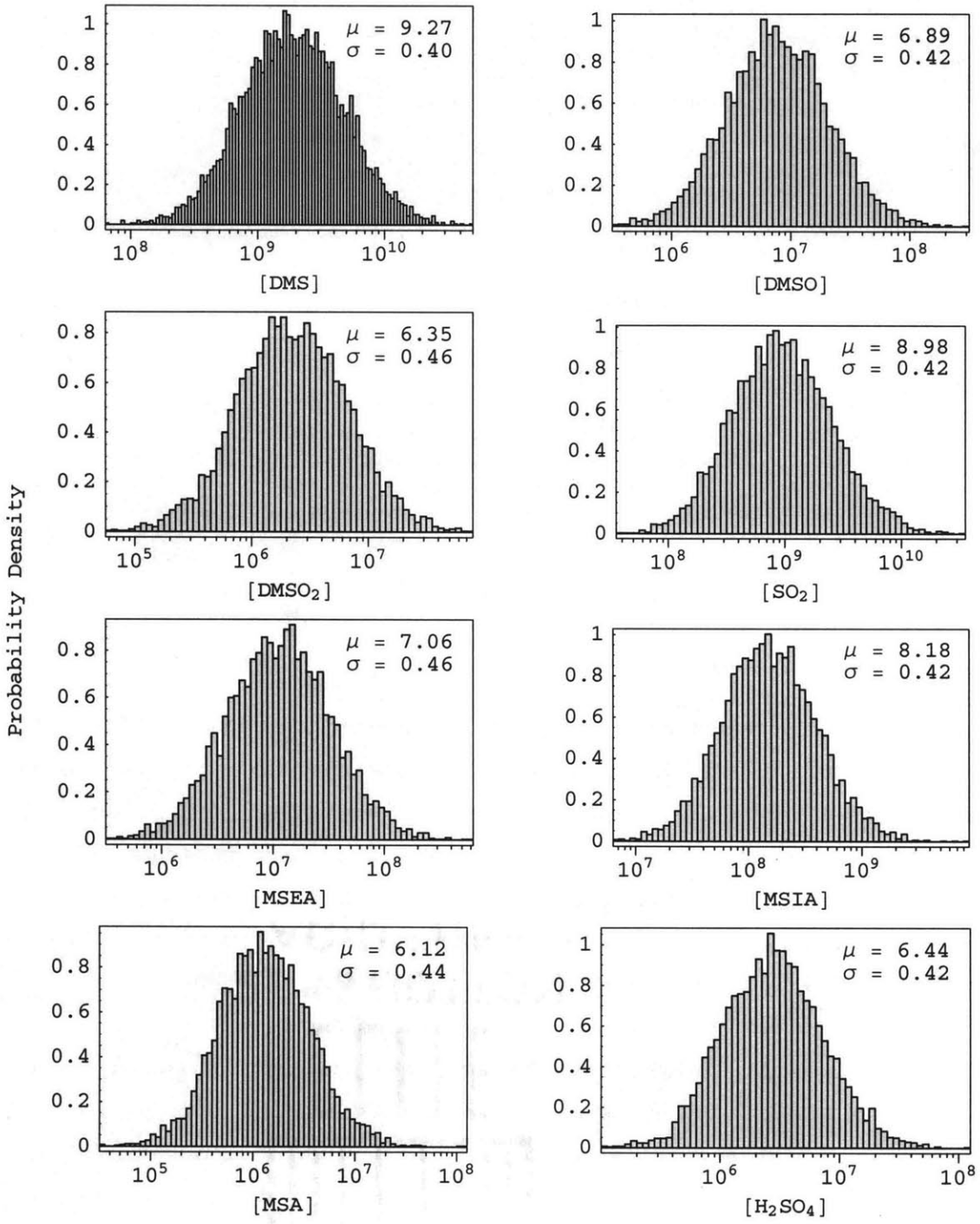

Figure 4-8: Daily average, boundary layer PDFs for concentrations (molecules cm^{-3}) of DMS, DMSO, $DMSO_2$, SO_2, MSEA, MSIA, MSA, and H_2SO_4 for the branch D case. The PDF mean (μ) and standard deviation (σ) is shown in the upper right hand corner.

Table 4.4: Five Largest Contributions to the Total Variance (Percent) *

Species	1st	2nd	3rd	4th	5th
DMS	92.8^a	4.8^b	1.2^c	0.8^d	0.2^e
DMSO	54.4^a	15.7^f	14.5^b	11.3^c	1.4^g
$DMSO_2$	27.3^a	20.0^h	19.6^i	13.6^j	7.2^b
SO_2	59.8^a	31.0^k	2.4^l	2.4^m	2.0^b
MSEA	31.9^a	29.1^n	22.5^g	7.9^b	6.4^c
MSIA	43.5^a	11.7^b	11.4^o	9.7^c	7.2^f
MSA	32.3^a	26.0^p	13.2^q	5.5^b	4.7^o
H_2SO_4	46.3^a	19.4^r	9.4^l	9.3^m	6.5^s

*The variance contributions are for the branch D daily average boundary layer PDFs in Figure 4-8.
a=DMS emissions, b=DMS+OH addition, c=DMS+OH reverse addition, d=DMS+OH abstraction, e=K_z in the Buffer Layer, f=DMSO to aerosols, g=DMS-OH to MSEA, h=DMSO-OH to MSIA, i=$DMSO_2$ to aerosols, j=$DMSO_2$ formation, k=SO_2 surface loss, l=Isomerization to CH_3SO_3, m=CH_3SO+O_2 addition, n=MSEA+OH oxidation, o=MSIA surface loss, p=MSA to aerosols, q=MSIA + O_3, r=H_2SO_4 to aerosols, s=CH_3SO+O_2 reverse addition.

4.4.2 Model-Observation Comparisons

We have tested our model assumptions by comparing time-series measurements of DMS, SO_2, H_2SO_4, and MSA from ACE-1 Flight 24 with the seven sets of model integrations. Because the DMS and SO_2 measurements were reported in mole fractions (parts per trillion), while H_2SO_4 and MSA measurements were reported in number concentrations (molecules cm^{-3}), the observed DMS and SO_2 mole fractions were transformed to number concentrations so that all the species are on a common scale. This transformation was accomplished using the following fit of air density to the Flight 24 observations of p and T: $N_{air} \approx 2.56 \times 10^{19} \exp(-0.112\ z)$, where N_{air} is the air density (molecules cm^{-3}) and z is the altitude (km).

In addition, a complication arises because the model predictions are on a regular space-time grid, while each of the observations was uniquely sampled along the Flight 24 trajectory. In order to make direct comparisons between the observations and the model, the model output is interpolated from the model grid on to the corresponding observational trajectory in time and space using a cubic interpolation function. This is done for each species independently because each has a unique space-time trajectory. The model errors, which are also functions of time and space, are similarly interpolated along the observation trajectories.

For comparisons, the goodness of the fits between the seven model scenarios and the obser-

Table 4.5: Boundary and Buffer Layer RMSR Factors [a]

Scenario	DMS [b]	SO_2 [c]	H_2SO_4 [d]	MSA [d]
Baseline	1.26	1.22	2.0	19,900
Isomerizations	1.26	1.18	1.3	9.3
Branch A	1.25	1.19	1.3	2.4
Branch B	1.26	1.19	1.3	3.0
Branch C	1.26	1.20	1.3	2.7
Branch D	1.26	1.19	1.3	2.1
Branch E	1.26	1.18	1.3	2.6

[a] Periods of rapid aircraft ascent and descent are excluded and are individually defined for each species.

[b] The outlier at 10:43 LT is not included.

[c] Measurements after 07:26 LT were used.

[d] Measurements between 07:26 and 13:43 LT were used.

vations are expressed as a multiplicative factor (RMSR) defined using the following root-mean-square residual difference between the common logarithms of the observed and mean model concentrations:

$$\log(\text{RMSR}) = \sqrt{\frac{1}{N}\sum_{i=1}^{N}\left(\log\frac{[\overline{x}_m]_i}{[x_o]_i}\right)^2} \tag{4.14}$$

where x_o represents the observed value, $\overline{x}_m$ represents the interpolated model mean value, and N is the number of observations in the time-series. The RMSR statistical measure captures unestimated model structural errors and is used to distinguish which of the seven mean model scenarios provides the best fit with the observations. The model-observation results for DMS, SO_2, H_2SO_4, and MSA are discussed below.

DMS It is important to first ensure that the modeled vertical DMS profile matches the observations because DMS is the primary sulfur source in the remote marine atmosphere and because the chemical lifetime of DMS in the BL is long enough (roughly 2 to 3 days based on the reaction with OH) for transport to influence vertical variations of all of the products of DMS destruction. Modeled and observed vertical profiles for DMS are displayed in Figure 4-9. The figure shows that, within the parametric errors, the model reproduces successfully the DMS vertical profile in the BL and FL, except for one outlier near the surface. This

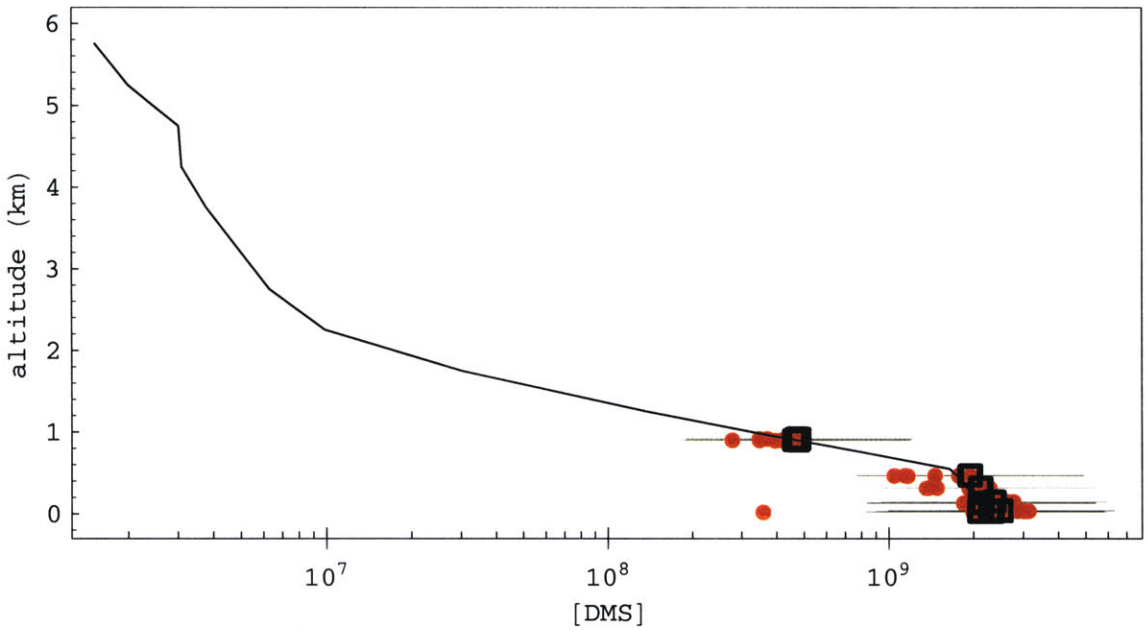

Figure 4-9: Vertical profiles of observed (red dots) and modeled (black boxes) DMS concentrations (molecules cm^{-3}) during Flight 24 for the baseline scenario. The one-sigma model errors are also shown (in gray), along with the daily average model vertical DMS profile (thin black line).

agreement is expected because the DMS observations were used to constrain the BL and FL mixing coefficients and the DMS surface flux. The figure also shows that the FT mixing rate is not constrained due to a lack of DMS observations above the FL. However, because the majority of the Flight 24 sulfur observations lie within the BL and FL, the FT mixing rate is not a large factor for these model-observation comparisons.

The DMS observed and modeled time-series are illustrated in Figure 4-10 for the baseline chemistry case. The other model cases are not shown because they are either identical or very similar to the baseline case. The large DMS concentration difference below and above 500 m confirms the BL/FL structure previously reported (Russell et al., 1998; Wang et al., 1999b,a) and is well-represented in the model. However, larger differences between the model and observations are found in the DMS time dependence. Within the BL the DMS observations decrease by a factor of three with time between 07:30 and 10:00 LT and show little time dependence thereafter, while the model shows a weaker time dependence throughout the time-series. The modeled DMS time dependence is due only to the OH forcing function, while the observed time dependence may result from a combination of the OH cycle with horizontal and temporal inhomogeneities in DMS emissions and vertical mixing. Horizontal variations in

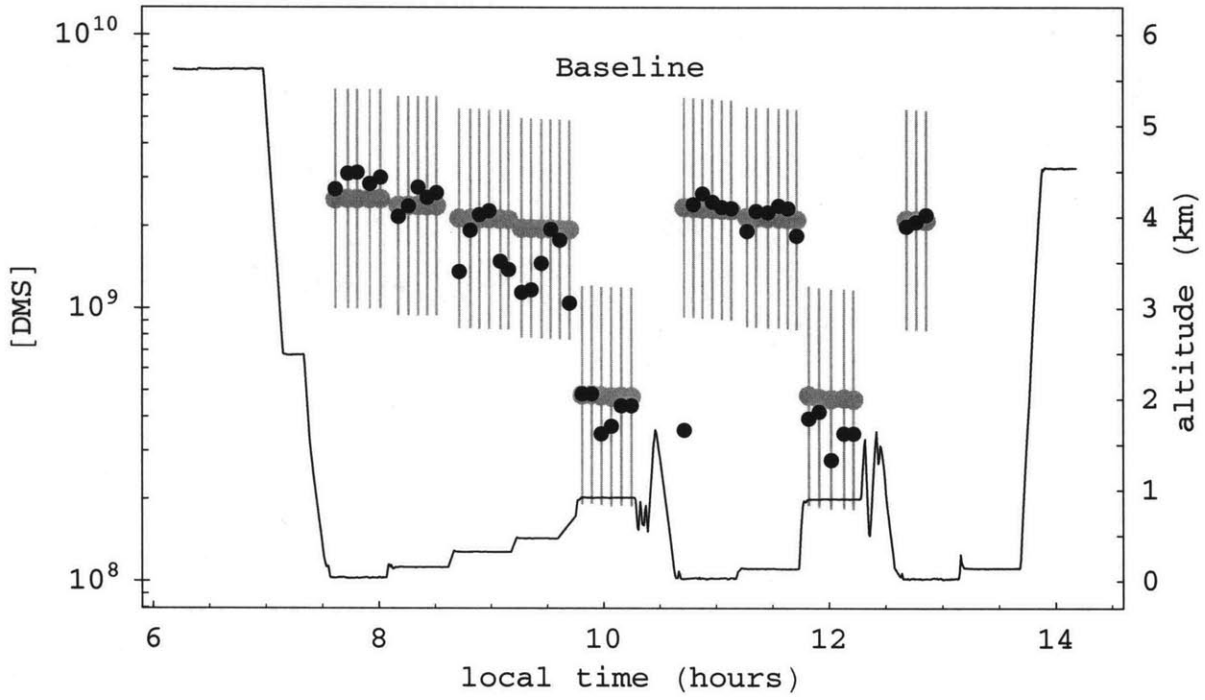

Figure 4-10: Modeled and observed time-series for DMS concentrations (molecules cm^{-3}) in the baseline scenario. Observations are displayed as black dots, the model evaluations are shown in gray (gray dots are at the parameter means and the gray bars are the one-sigma deviations). Also shown is the aircraft altitude (thin black line).

sea-surface temperature were encountered during Flight 24, which may have influenced DMS emissions and vertical mixing horizontally (Wang et al., 1999a).

In spite of these time dependence differences, the baseline run agrees statistically with the DMS observations for the given parameter PDFs. Overall, the RMSR measure between the mean model run and the observations for this case is a factor of 1.26 as shown in Table 4.5. The table also shows that all of the other model cases, except for branch A, have exactly the same RMSR. They are the same because these other time-series are essentially identical to the baseline run time-series, which indicates that the additional chemistry has a negligible impact on DMS cycling. The RMSR for branch A is slightly different because Reactions R3 and R4 reduce the lifetime of the DMS-OH adduct, and hence reduce the rate of the reverse DMS+OH addition reaction. The other model scenarios do not change the loss rate of the DMS-OH adduct.

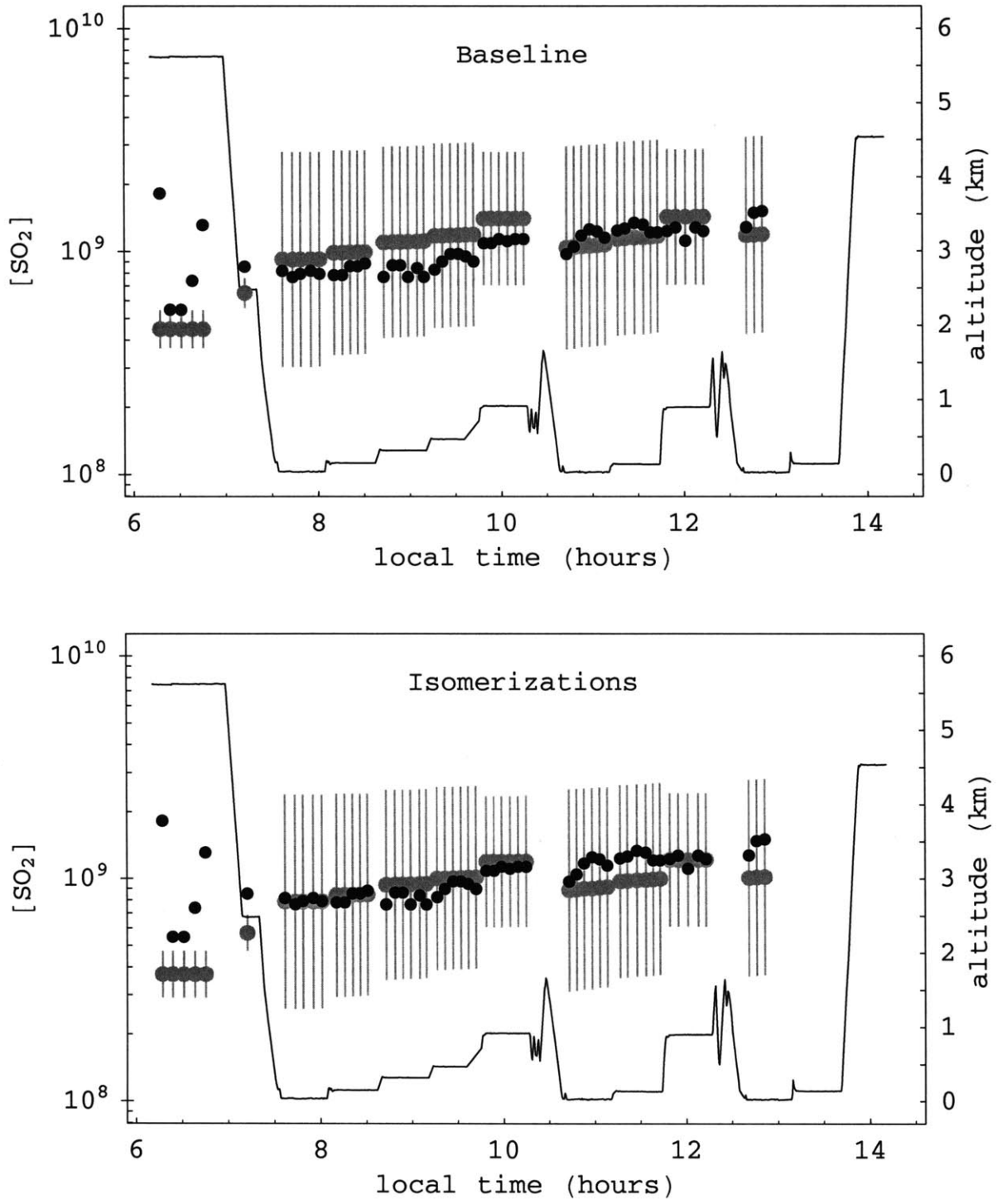

Figure 4-11: Same as Figure 4-10 except for the baseline and isomerization scenarios for SO_2 concentrations (molecules cm^{-3}).

SO_2 The measured SO_2 time-series and the modeled baseline and isomerization time-series are shown together in Figure 4-11. The branch A to E cases are not displayed because they are nearly indistinguishable from the isomerizations run. The figure shows that unlike DMS, SO_2 does not exhibit a large gradient between the BL and FL. For DMS there is only a surface source combined with atmospheric destruction by OH, which leads to the decay of DMS with height. For SO_2 however, loss at the surface and the photochemical source aloft lead to a slight BL to FL increase in the observed and modeled SO_2. The individual terms in the SO_2 and DMS budgets describing this behavior are given quantitatively in Section 4.4.3. The figure also shows that the modeled and observed SO_2 increases with time during the day, which is due to the daytime photochemical conversion of DMS to SO_2. This conversion efficiency is calculated in Section 4.4.3.

Figure 4-11 also indicates that, except for a few measurements before 07:30 LT, each of the modeled points agrees statistically with the observations. The early morning measurements correspond to free tropospheric altitudes where SO_2 is more likely to be influenced by long-range horizontal transport not represented in the model. The figure also shows that the SO_2 parametric errors decrease with altitude, which occurs because loss by reaction with OH is the dominant SO_2 sink above the FL and this term has a smaller error than the other terms in the SO_2 budget.

Excluding the early morning FT measurements, the RMSRs in Table 4.5 for all of the mean model runs are about a factor of 1.2. The largest RMSR difference occurs between the baseline scenario and the other model cases. In the baseline run the model overestimates SO_2 between 07:30 and 10:00 LT, but has better agreement afterwards. Inclusion of the isomerization reactions reduces SO_2 throughout the time-series, resulting in an improved fit in the morning and a slightly worse fit in the afternoon. The isomerization reactions decrease SO_2 because the conversion of $CH_3S(O)OO$ to CH_3SO_3 reduces the flux of sulfur through the CH_3SO_2-SO_2 channel.

Because the modeled DMS and SO_2 both agree with the BL and FL observations within the parametric uncertainties for all of the model runs, this implies that the modeled flow of sulfur through the system connecting DMS to SO_2 is correct. If so, any large systematic deviations between observed and modeled H_2SO_4 and MSA are likely due to systematic errors in the flow of sulfur either downstream of SO_2 or along branches that do not impact SO_2. Also, our assumption of no SO_2 loss to sea-salt aerosols above the lowest model layer does not jeopardize the ability to achieve a good fit between the modeled and observed SO_2 concentrations. This

is expected from a previous finding where the SO_2 concentrations showed little change (< 5%) when sea-salt aerosols were added to and removed from Flight 24 simulations (Mari et al., 1999).

H_2SO_4 Observed and modeled gas-phase H_2SO_4 time-series are shown in Figure 4-12. As with the modeled SO_2 runs, only the baseline and isomerization scenarios are displayed because the branch A-E cases are very similar to the isomerization case. With respect to time, the figure shows that both the modeled and observed H_2SO_4 increase throughout the morning, peak near local noon, then start to drop off in the early afternoon. Because the modeled H_2SO_4 time dependence is driven by the OH forcing function and because the modeled and observed time trends match quite well, this suggests that the OH fit is sufficient for capturing diurnal variations in the model.

Figure 4-12 also shows that the model agrees parametrically with most of the observations, the exceptions being FT measurements at the beginning and end of the time-series and some BL observations that lie just above the one-sigma range in the baseline case. More interesting however are the large systematic differences in the BL between the baseline model and the observations. These differences indicate a large BL to FL gradient in the baseline case that is not seen in the observations.

The controlling terms in the modeled H_2SO_4 budget are production from the oxidation of SO_3 and loss due to scavenging by aerosols (see Section 4.4.3). The large BL to FL gradient calculated in the baseline model is a consequence of the decreasing aerosol surface area, and hence condensation rates, with height (see Figure 4-2). To reduce the altitude gradient in the baseline model and achieve a better fit with the observations, either gas-phase production needs to be increased or loss to aerosols decreased in the BL. As the loss to aerosols is directly constrained using two independent sets of aerosol number distributions, the systematic differences are more likely due to the chemical production term. The chemical production of H_2SO_4 involves the reaction between SO_3 and H_2O, the precise nature of which is unknown, but is believed to depend quadratically on water vapor concentrations (Lovejoy et al., 1996). Because H_2O is also observationally constrained, increases in the BL production rate require increases in SO_3. As shown in Figure 4-1, SO_3 is produced either from oxidation of SO_2 or by the dissociation of CH_3SO_3. The oxidation mechanism of SO_2 to SO_3 is well known and involves OH, which is also constrained by observations. Additionally, the modeled SO_2 in the BL matches the observations very well.

Together these lines of evidence suggest that the large systematic underestimation of H_2SO_4

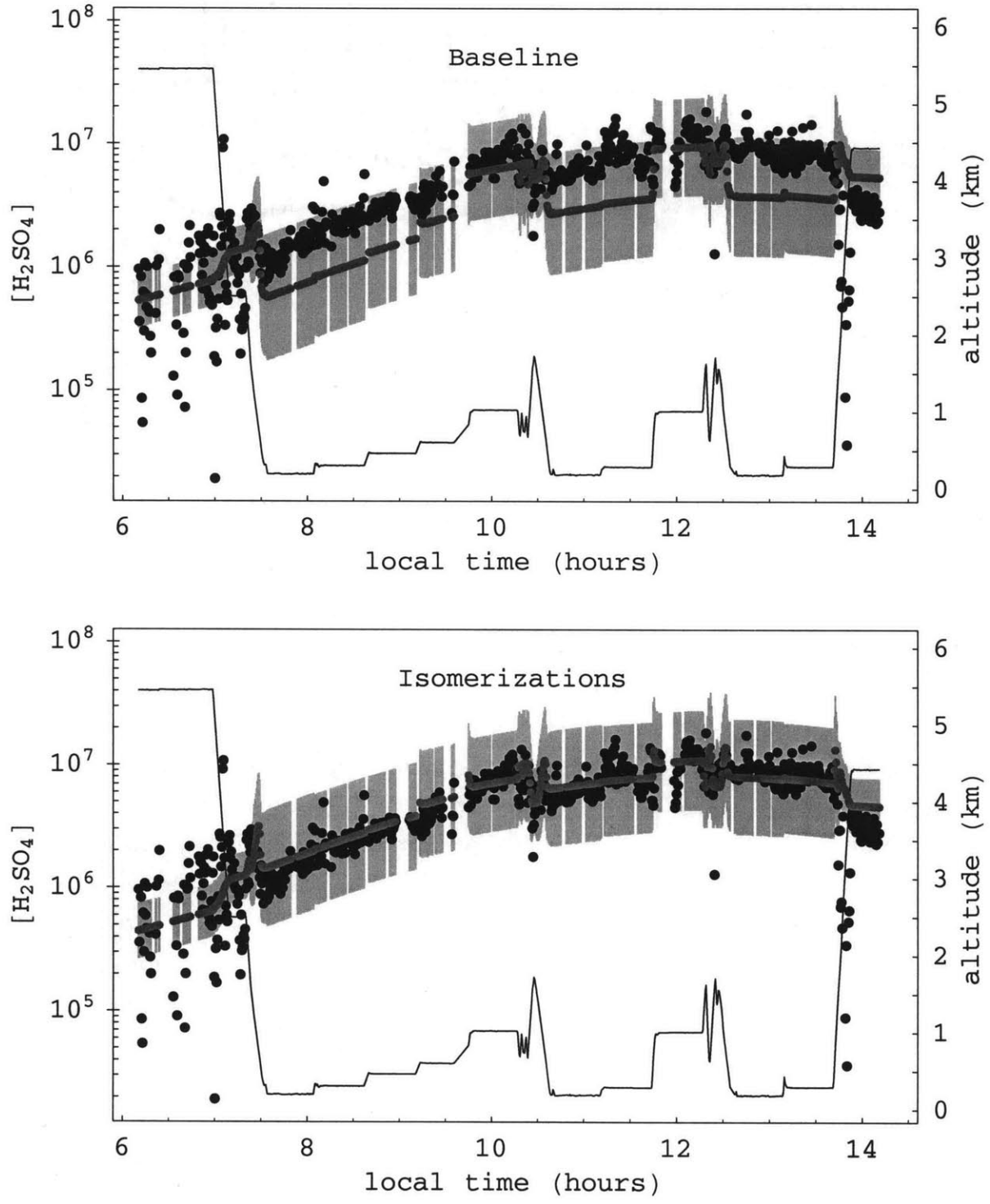

Figure 4-12: Same as Figure 4-10 except for the baseline and isomerization scenarios for H_2SO_4 concentrations (molecules cm^{-3}).

in the BL by the baseline model is due to underestimation of the production rate of SO_3 from CH_3SO_3 dissociation. To compensate for the low H_2SO_4, the production rate of SO_3 through the CH_3SO_3 channel has to be increased to values that are either comparable to or larger than the rates through the SO_2 channel. This in turn implies the existence of a major formation pathway for gas-phase H_2SO_4 in the remote marine atmosphere that does not involve SO_2. To further bolster this argument, the chemical production of H_2SO_4 from SO_2 may be overestimated in the model because the loss of SO_2 to sea-salt aerosols is not included above the lowest model layer. If included, the additional sea-salt loss of SO_2 would decrease the production of H_2SO_4 through the SO_2 channel, which would require an even larger flux through the CH_3SO_3-SO_3 path.

This finding supports a report by Bandy et al. (1992), who suggested that the CH_3SO_3-SO_3-H_2SO_4 branch plays a large role in sulfate formation, yet disagrees with the conclusion by Saltelli and Hjorth (1995) that this branch is not important. The disagreement with Saltelli and Hjorth (1995) likely occurs because reaction R2 was not included in their study. In addition, this result has important implications for aerosol nucleation because the formation of H_2SO_4 through CH_3SO_3-SO_3 proceeds without the intervention of multiphase chemistry, while homogeneous H_2SO_4 formation through SO_2 can be short-circuited by the aqueous phase oxidation of SO_2 in the presence of clouds. Also, because SO_2 is relatively long-lived while CH_3SO_3 is formed *in situ* from DMS oxidation, the nucleation of new particles may be more related to the local levels of DMS than to the amount of transported SO_2.

Figure 4-12 illustrates how the additional SO_3 production influences the modeled H_2SO_4 in the isomerization and branch A-E cases. The major change is due to the isomerization reaction $CH_3S(O)OO \rightarrow CH_3SO_3$, which enhances the production rate of SO_3 by increasing the levels of CH_3SO_3. This significantly improves the modeled H_2SO_4 in the BL and results in one-sigma model ranges that cover all but a few of the BL and FL observations. The additional reactions in the branch A-E scenarios do not directly affect CH_3SO_3, so their cumulative impacts are negligible. These changes are summarized in the RMSR table which lists a factor of 2.0 for the baseline scenario and a factor of 1.3 for the other model cases.

MSA The modeled and observed MSA time-series for all of the model cases are displayed in Figures 4-13 and 4-14. All of the cases are shown because they differ significantly from one another. Focusing in on the observations, there are two main features that distinguish MSA from H_2SO_4. First, MSA exhibits a weak diurnal cycle as compared to the strong H_2SO_4 diurnal trend. This suggests that the major MSA production route does not directly involve

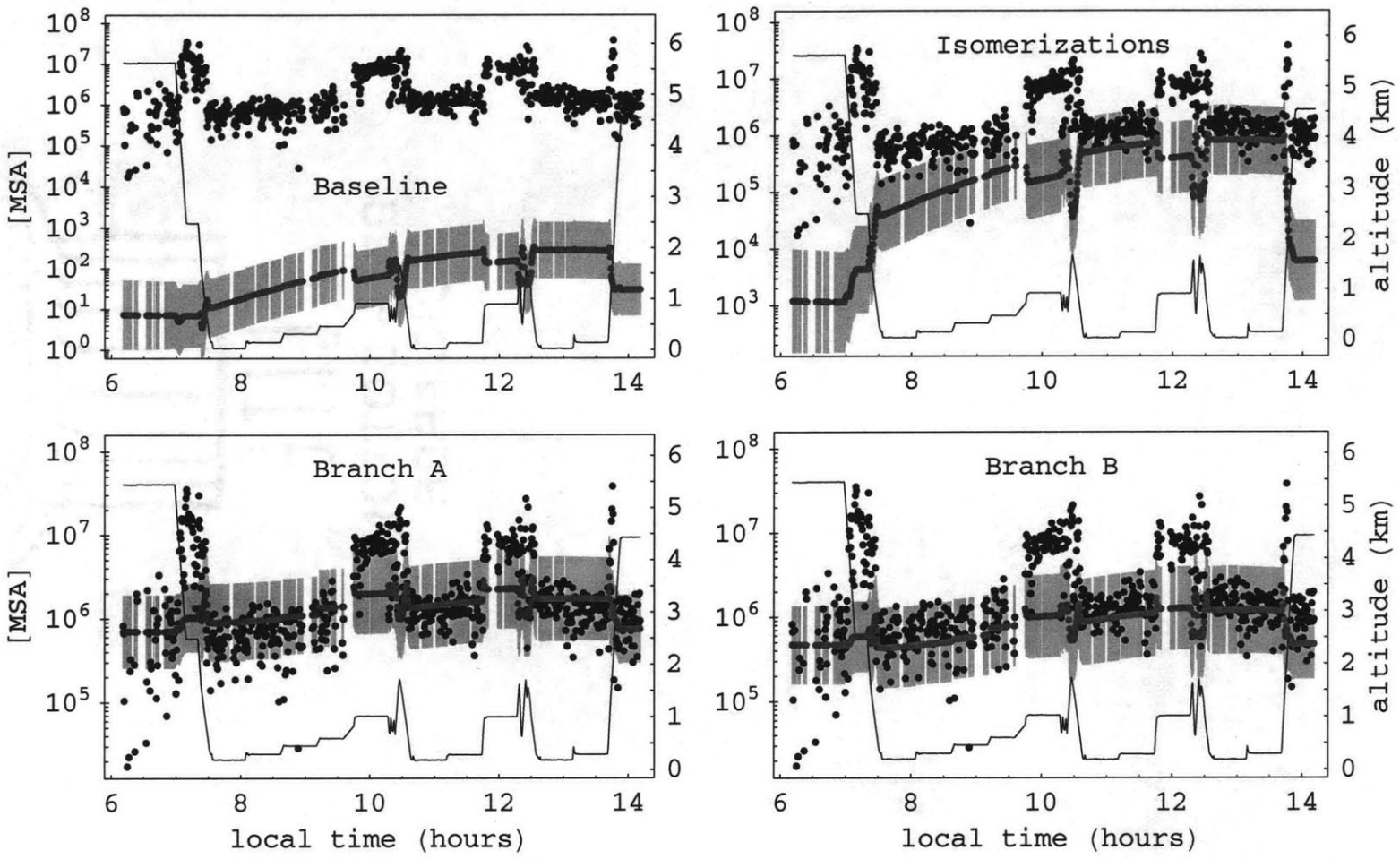

Figure 4-13: Same as Figure 4-10 except for the baseline, isomerization, and branch A and B scenarios for MSA concentrations (molecules cm^{-3}).

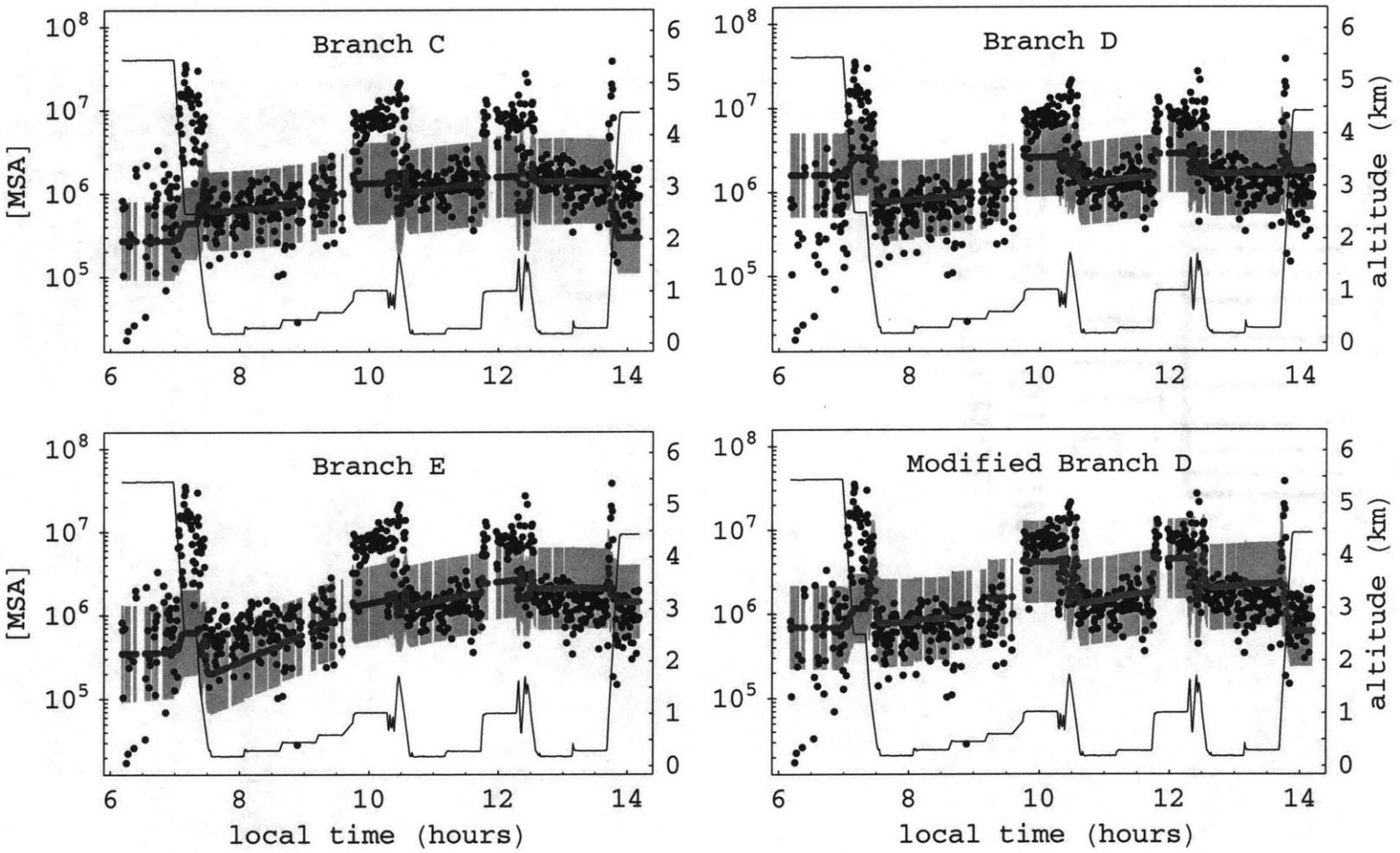

Figure 4-14: Same as Figure 4-10 except for the branch C to E scenarios for MSA concentrations (molecules cm^{-3}). Also, a modified version of the branch D scenario is shown on the lower right.

photooxidants with large daily cycles such as HO_x because the largest loss term in the MSA budget, the observationally constrained loss to aerosols, has small diurnal variations. Second, the observations indicate a roughly one order of magnitude increase in the MSA concentration from the BL to the FL. A large gradient is expected due to the decreasing rate of loss to aerosols with height (see Figure 4-2). However, loss of MSA to aerosols cannot account for the observed magnitude of this gradient because this loss only drops off by a factor of 3 from the BL to the FL. For a gradient this large, enhanced MSA production in the FL relative to the BL is required. Three possible ways of achieving this are: (1) MSA precursors that have a large sink in the boundary layer (e.g., through condensation and/or surface loss), (2) MSA precursors that react with species that increase with altitude, and (3) MSA formation rate constants that have large negative activation energies so that the reaction rate increases as the altitude increases (temperature decreases).

The most striking feature of the MSA time-series in Figure 4-13 is the large difference between the baseline predictions and the observations. The figure shows that the baseline model underestimates the observations by nearly 4.5 orders of magnitude. This large discrepancy is statistically very significant. Other factors that may contribute to this large difference, such as the transport of MSA-rich air into the region or model parameters that actually lie far outside of the uncertainty ranges of the parameter PDFs, can be ruled out. The transport of MSA-rich air into the region can be ruled out on the basis that DMS oxidation is the only known source of atmospheric MSA, that the DMS observations are well within the parametric uncertainties, and that the MSA lifetime for Flight 24 conditions is less than 7 hours (based on the condensation onto aerosols displayed in Figure 4-2).

That the large MSA deficit in the baseline case is due to model parameters that are orders of magnitude away from their best-estimate values can be ruled out by considering the MSA budget. In the baseline run, the MSA burden is controlled by loss to aerosols and reactions involving CH_3SO_2 and CH_3SO_3. For loss to aerosols, large changes are not likely because the MSA accommodation coefficient has been measured (De Bruyn et al., 1994) and the aerosol surface area is constrained by observations. The agreement for H_2SO_4 also indicates that the aerosol loss is probably modeled correctly. For the reactions with CH_3SO_2 and CH_3SO_3, multiple order of magnitude changes to the rate constants are very unlikely because they have either been measured, as in the case of CH_3SO_2 dissociation (Kukui et al., 2000), or have been carefully assigned based on thermochemical data or analogous reactions, as in the case of CH_3SO_3 dissociation (Yin et al., 1990b). Furthermore, the baseline model simulates ob-

served SO_2 and H_2SO_4 reasonably well, so large changes to the rate constants of reactions of CH_3SO_2 and CH_3SO_3 that increase MSA will worsen the fits of modeled SO_2 and H_2SO_4 with observations.

Therefore, by ruling out other possibilities, it is concluded that the four order of magnitude MSA deficit for the baseline scenario is due to missing gas-phase chemistry in the DMS oxidation mechanism. This finding provides the impetus for the new MSA chemical production routes suggested and tested in this report. This finding also explains the low level of agreement between the MSA predictions from the various DMS oxidation mechanisms diagnosed by Capaldo and Pandis (1997). The same arguments used above can also be used to determine where the additional MSA reactions are likely to occur in the DMS oxidation scheme. For instance, these production reactions probably originate from the DMS+OH addition branch because the chemistry along this branch will not perturb the modeled SO_2 and H_2SO_4. Along the addition route, the most likely MSA precursor candidates are MSEA and MSIA because they are structurally similar with MSA and because the baseline model predicts that they are present in large concentrations. The oxidation reactions required to convert MSEA and MSIA into MSA are modeled by analogy to other known oxidation steps in the mechanism, and these make up the various branches that are discussed below.

Figure 4-13 shows that inclusion of the isomerization reactions improves the modeled MSA by a factor of 10^3 as compared to the baseline case. This improvement results from a factor of 10^3 to 10^4 increase in the production rate of CH_3SO_3 from reaction R2. This in turn increases the production rate of MSA by the same factor through the reaction $CH_3SO_3 + HO_2 \rightarrow CH_3SO_3H + O_2$. In spite of the great improvement, the overall agreement is still poor with an RMSR of nearly a factor of 10. There are two major reasons for the continued poor agreement. First, the modeled time-series displays a larger time-dependence than the observations because of the strong daily cycle of HO_2. Second, and more importantly, the model grossly underestimates MSA in the FL and FT because MSA precursors are not efficiently transported out of the BL. This implies that either the modeled vertical transport of DMS is incorrect or that some other species are long-lived and serve as MSA precursors. Because the vertical profile of DMS matches the BL and FL observations (see Figure 4-9), then it is much more likely that some other long-lived species is participating in MSA production. Combined with the fact that SO_2 is the only species along the DMS+OH abstraction route of sufficient longevity to be affected by transport, this provides additional evidence that the major MSA precursors lie along the DMS+OH addition branch. Of the species along the addition branch, MSIA is perhaps the

most likely candidate because OH reacts rapidly with both DMSO (lifetime < 2 hours) and MSEA (lifetime < 6 hours) in the BL.

In addition to the improvement associated with the isomerizations case, Figures 4-13 and 4-14 illustrate the further improvements for the branch A to E cases due to the extra MSA production routes. These improvements bring the overall modeled MSA in the BL and FL to within a factor of 2 to 3 of the observations according to the RMSR values in Table 4.5. With respect to the parametric uncertainties, the majority of the BL observations now lie within the modeled one-sigma bounds for branches A-E. However, many of the FL observations lie above the modeled parametric error range, which indicates the difficulty in modeling the large BL to FL gradient and implies that some significant structural errors are still present in the model. For the branch A-C cases, the MSA production rate is increased by reactions that oxidize the DMS-OH adduct and MSEA into the $CH_3S(OH)(OO)$ intermediate, which then isomerizes into MSA. Given the large barrier for rearrangement into MSA, the isomer builds up to significant concentrations and is efficiently transported out of the BL. Of the three branches involving this isomer, branch A has the largest BL to FL gradient, which results in the MSA time-series that agrees best with observations according to the RMSR statistic.

For the branch D and E cases, reactions that oxidize MSIA to MSA increase the MSA production rate substantially. Note that both DMSO and MSIA, which are precursors to MSA through these branches, are efficiently lost in the BL through scavenging by aerosols and surface deposition. This leads to positive BL to FL gradients for DMSO, MSIA, and MSA. The branch D case enhances the vertical gradient further for another reason. MSIA is oxidized by O_3, which increases with altitude (see Figure 4-4) and is not strongly time-dependent. In comparison to the other modeled cases, the branch D case has the largest BL to FL gradient and the lowest RMSR. The observations, however, show a much larger vertical MSA gradient than in the branch D case. The inability of the branch D case to resolve the large MSA gradient could be due to relatively low rates for the loss of DMSO and MSIA at the surface and the production of MSA from the MSIA+O_3 reaction. Increasing these three rates should result in an increased vertical gradient for MSA. This hypothesis is tested by applying factor-of-5 increases to the surface removal frequencies of DMSO and MSIA and the MSIA+O_3 rate constant. Note that these increases fall outside of the assumed uncertainty ranges for these parameters. The resulting modeled time-series for MSA is labeled 'Modified Branch D' and is shown on the bottom right of Figure 4-14. This simulation yields enhanced MSA concentrations in the FL that agree statistically with most of the observations there, and results in a slightly improved

RMSR factor of 2.0. Thus, the modified branch D case provides evidence that MSA production involves precursors that are efficiently scavenged at the surface. Finally, the branch E case, which involves the oxidation of MSIA by OH in a manner analogous to the SO_2 to SO_3 path, has a greater diurnal cycle than the observations and supports the presumption that the major production route of MSA does not depend on rapidly varying species such as HO_x.

4.4.3 Branch Sensitivities

We examine the sensitivities of the oxidized DMS products to the choice of oxidation branch by calculating daily average budgets in the BL and FL, diurnal cycles in the BL, and daily average vertical profiles for the seven mechanism scenarios. This analysis shows the key laboratory reactions and field observations that, if measured, may be used to distinguish between the proposed branches for additional MSA production. Because we wish to highlight the impacts of the individual branches, only the mean parameter runs for the seven model scenarios are used.

Daily Average Budgets Daily average burdens and process tendencies for the major sulfur species in the BL and FL are shown in Table 4.6. The table shows the branch D budgets, which have the lowest RMSR for MSA, along with all additional mechanism scenario budgets that differ significantly from branch D. As shown in the table, the budgets of DMS, DMSO, $DMSO_2$, SO_2, and MSIA are relatively insensitive to the additional MSA pathways because all of the budget terms for all of the cases are within a factor of two from the branch D budgets. The MSEA budget is also moderately insensitive because the branch B burden and loss to aerosols in the BL and FL, and vertical mixing in the BL differ by slightly more than a factor of 2.0 from the corresponding branch D terms. Similarly, the H_2SO_4 baseline burden, chemical production, loss to aerosols, and surface loss terms in the BL differ from branch D by slightly more than a factor of two. Overall, the greatest changes are in the MSA budget, where four order of magnitude changes to all of the budget terms occur between the baseline case and the branch A-E cases. In spite of the large changes in the magnitudes of the MSA tendencies, the percent contributions of the individual tendencies to the total source and sink are fairly insensitive. For example, MSA chemical production contributions to the total MSA source vary between 90% and 94% in the BL for all of the mechanism cases. Likewise, the loss of MSA to aerosols is the dominant sink and is fixed at 98% of the total BL sink for all of the scenarios. These budgets indicate that the various scenarios cause large changes to the magnitude of the MSA budget

terms without greatly affecting the budgets of the other species or the MSA percent budget contributions. In the rest of this section we describe the major sulfur fluxes and branching points in the DMS mechanism and how these relate to the budgets in Table 4.6.

Referring to the initial branching point at DMS+OH in Figure 4-1 and noting the budgets in Table 4.6, 64% of the DMS emitted into the BL reacts with OH by abstraction and addition (including the reverse addition of OH to DMS), while the remaining 36% is mixed out of the BL. Of the amount that reacts with OH, roughly two-thirds undergoes OH-abstraction (70% in the BL, 68% in the FL) and one-third is lost through OH-addition (30% in the BL, 32% in the FL). Along the OH-abstraction route, the sulfur flows irreversibly and without branching to CH_3S, which is then oxidized to CH_3SO_2 predominantly by reactions involving CH_3SO_x+O_3. The CH_3SO_2 then thermally dissociates and serves as the major source of SO_2 (80% of the total source in the BL, 100% in the FL). The fate of SO_2 is surface loss in the BL (91% of the total loss), mixing between the BL and FL (20% of the total source in the BL, 69% of the total loss in the FL), and oxidation to H_2SO_4 (9% of the total loss in the BL, 31% in the FL). This SO_2 budget agrees with that reported by Mari et al. (1999), who found that during Flight 24 and over an altitude range from the surface to 2.5 km, 24% of SO_2 is lost through oxidation with OH and 76% is lost to sea-salt aerosols, mixing, and dry deposition combined. When averaged over the same altitude range, we calculate that 28% of SO_2 is oxidized by OH to H_2SO_4 and 72% is lost to surface processing. The only significant change along the OH-abstraction route for the various mechanism scenarios occurs when the isomerization reaction $CH_3S(O)OO \rightarrow CH_3SO_3$ is added. When included, the burden of CH_3SO_3 increases by a factor of $10^{3.7}$, which subsequently increases the production rates and burdens of SO_3 and H_2SO_4.

Along the DMS+OH addition route there are four branching points that influence the product yields. The first occurs at $CH_3S(OH)CH_3$, where the chemical loss is partitioned among three channels. The major loss channel leads to DMSO (72% branch A, 83-84% all others), while the two minor channels lead to MSEA (14% branch A, 16-17% all others) and $CH_3S(OH)(OO)$ (14% branch A). MSEA provides a second branching point with separate paths leading to CH_3SO (58% branch B, 100% all others) and the MSA isomer (42% branch B). Continuing along the major channel from DMS-OH, the production of DMSO is mainly balanced by losses due to reaction with OH (47% of the total loss in the BL, 64% in FL) and condensation on aerosols (52% of the total loss in the BL, 30% in FL). The reaction between OH and DMSO yields the third branching point at $CH_3S(O)(OH)CH_3$, with routes leading to $DMSO_2$ (20-21%) and MSIA (79-80%). MSIA is the fourth branching point with separate paths

Table 4.6: Daily Average Budgets

Species	DMS	DMSO	$DMSO_2$	SO_2	MSEA		MSIA	MSA				H_2SO_4	
Scenario	D	D	D	D	B	D	D	S	I	B	D	S	D
Boundary Layer													
species burden	9.3	6.9	6.3	9.0	6.6	7.0	8.3	1.8	5.3	5.8	6.1	6.1	6.4
chemical production	...	3.5	2.5	3.9	2.8	2.8	3.1	-1.8	1.7	2.2	2.4	3.0	3.3
chemical loss	4.1	3.2	...	2.9	2.7	2.7	2.6	...	...	...	...	...	...
flux convergence	3.8	1.9	1.5	3.3	0.8	1.1	2.2	-3.0	0.6	1.2	1.5	1.7	1.9
loss to aerosols	...	3.2	2.5	...	1.3	1.7	2.2	-1.8	1.7	2.2	2.5	3.0	3.3
surface tendency	4.3	1.2	0.6	4.0	...	...	2.9	-3.5	0.0	0.5	0.7	0.3	0.6
Buffer Layer													
species burden	8.9	6.8	6.4	9.1	6.4	6.8	8.3	1.9	5.4	6.0	6.4	6.5	6.6
chemical production	...	3.1	2.2	3.5	2.4	2.4	2.8	-2.2	1.3	2.0	2.3	3.0	3.2
chemical loss	3.7	2.9	...	3.0	2.4	2.4	2.6	...	...	...	...	...	...
flux convergence	3.7	1.9	1.5	3.3	0.3	0.5	2.4	-3.0	0.5	1.1	1.4	1.6	1.9
loss to aerosols	...	2.6	2.1	...	0.4	0.8	1.6	-2.2	1.2	1.9	2.3	3.0	3.1

Budget terms are displayed for the branch D scenario and all other scenarios that contain at least one term that differs from branch D by more than a factor of 2.0. Individual scenarios are labeled S=baseline, I=isomerizations, B=branch B, and D=branch D. Burdens and tendencies have units of $\log_{10}$ (molecules cm^{-3}) and $\log_{10}$ (molecules $cm^{-3}s^{-1}$) respectively. Sinks are underlined, sources are not. The flux convergence is due to vertical mixing and can be either positive or negative.

leading to CH_3SO_2 (47% branch D, 68% branch E, 100% all others) and MSA (53% branch D, 32% branch E). Overall, the most significant changes occur at the DMS-OH, MSEA, and MSIA branching points because new pathways that enhance MSA production open up at these points. In addition, the large flows of sulfur into MSEA and MSIA suggest a mechanism for cross-over between the OH-addition and OH-abstraction pathways because MSEA and MSIA are oxidized by OH to form CH_3SO_x. However, the magnitude of the production of CH_3SO_x from MSEA and MSIA is much smaller than the production from the OH-abstraction path, so the OH-abstraction and OH-addition paths are essentially decoupled.

Finally, Table 4.6 indicates that the SO_2 budget is not greatly affected by any of the additional chemistry. The SO_2 budget is insensitive because Reactions R1 and R2 are the only additional reactions that affect SO_2 precursors, and these reactions hardly change the chemical production rate of the SO_2 precursor CH_3SO_2. Thus, the production of SO_2 is essentially controlled by the level of DMS emissions, vertical mixing of DMS, and the initial branching between OH-addition and OH-abstraction. This direct connection between DMS and SO_2 is used to estimate the photochemical conversion efficiency of DMS to SO_2, where the efficiency is given by the ratio of the daily average chemical production rate of SO_2 to the daily average net chemical destruction rate of DMS. Using this definition, the calculated conversion efficiency in both the BL and FL has a range of 63 to 66% for the isomerization and branch A-E runs, which is similar to the Flight 24 conversion efficiency of 60% reported by Mari et al. (1999) and the average 70% efficiency for ACE-1 conditions suggested by Shon et al. (2001). For the baseline case, the calculated efficiency is slightly larger, 76 and 78% in the BL and FL respectively, because the production rate of CH_3SO_2 is slightly larger in the absence of reaction R2.

Boundary Layer Diurnal Cycles Daily cycles of H_2SO_4, MSEA, and MSA in the boundary layer for all of the model runs are shown in Figure 4-15. The diurnal cycles are from the last day of the ten day model integration and were averaged over the lowest five model layers representing the BL. The cycles for DMS, DMSO, $DMSO_2$, SO_2, and MSIA are not shown because the different model runs do not significantly change the BL cycles. Relative to the baseline run, the other H_2SO_4 diurnal cycles are shifted up by about a factor of two because of the additional production of CH_3SO_3 and SO_3 from reaction R2. However, the time-dependence of the H_2SO_4 cycles, which is caused by OH forcing, does not change. For MSEA, the magnitude and time-dependence of the branch B case is radically different from the other model cases. The branch B case is shifted to lower values and has a factor of six variation from peak to trough, while the other cases show variations of less than a factor of 1.5. The small MSEA cycles are a

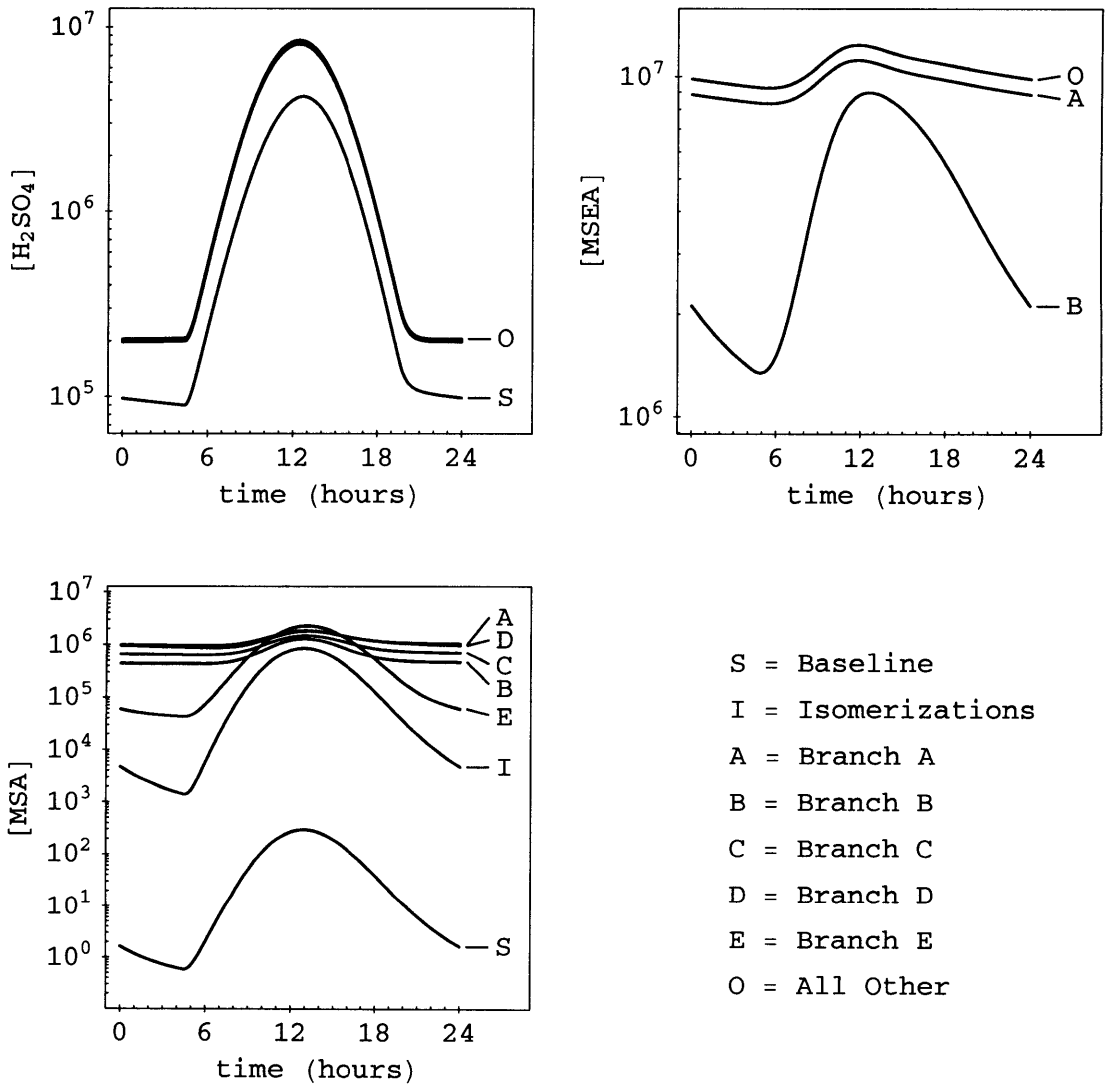

Figure 4-15: Modeled diurnal cycles of the concentrations (molecules cm^{-3}) of H_2SO_4, MSEA, and MSA in the boundary layer for all scenarios. The individual scenarios are labeled in the figure.

result of net source and sink terms that are similar in time, resulting in a source-sink difference that has an overall small time dependence. For the branch B case, however, the MSEA+O_2 reaction alters the net sink term, but not the source term, resulting in a source-sink difference with a stronger time variation. For MSA, there are large differences in the magnitudes of MSA and the amplitude of the diurnal cycle between the various model runs. The large changes in the magnitudes result from the additional MSA production routes, while the amplitude differences are related to the time-dependence of the main MSA source terms. The baseline, isomerization, and branch E model runs all exhibit large diurnal cycles because the main production terms involve reactions with HO_x, while the branch A-D runs do not. Also, the branch A and D cases are nearly identical, yet are a factor of 2.5 larger than the branch B case.

The differences in these diurnal cycles suggest that BL observations of MSEA, H_2SO_4, and MSA may help differentiate between some of the new chemical pathways proposed in this report. For instance, BL observations of MSEA that show a weak diurnal cycle would rule out the branch B pathway. Further, observations of MSA in the BL during the early morning or late evening may help to distinguish branch E from branches A-D.

Daily Average Vertical Profiles Vertical profiles of the ratios of the daily average concentrations of MSEA, MSIA, MSA, and H_2SO_4 to the daily average concentration of DMS for all of the model runs are displayed in Figure 4-16. Normalizing to DMS helps to remove the simple effects of differing DMS fluxes on sulfur compound concentrations. Profiles of DMSO, $DMSO_2$, and SO_2 are not shown because the various scenario choices have a negligible impact on the ratios. For MSEA, the branch B profile is shifted to lower values relative to the other model runs by a factor of two throughout the atmosphere because of the additional MSEA+O_2 loss channel. For MSIA, all of the model runs are similar below an altitude of 1.5 km. Above this altitude however, the MSIA concentrations in the branch D case are about a factor of two lower than the other cases because of the large increase in O_3 with altitude. For MSA, the profiles shift to larger values going from the baseline run to the isomerization run to the branch A-E runs as expected. Interestingly, the isomerization and branch A-E runs are within an order of magnitude of each other in the BL, while above the BL they differ by many orders of magnitude. This shows that the isomerization reactions contribute significantly to the production of MSA only in the BL, and not above. There are large MSA differences in the FT for the branch A-E profiles, the largest being nearly an order of magnitude separating branch C from branch D. For H_2SO_4, the profiles are nearly indistinguishable above the BL. Yet within the BL the baseline case for H_2SO_4 is a factor of two lower than all of the other cases because the isomerization

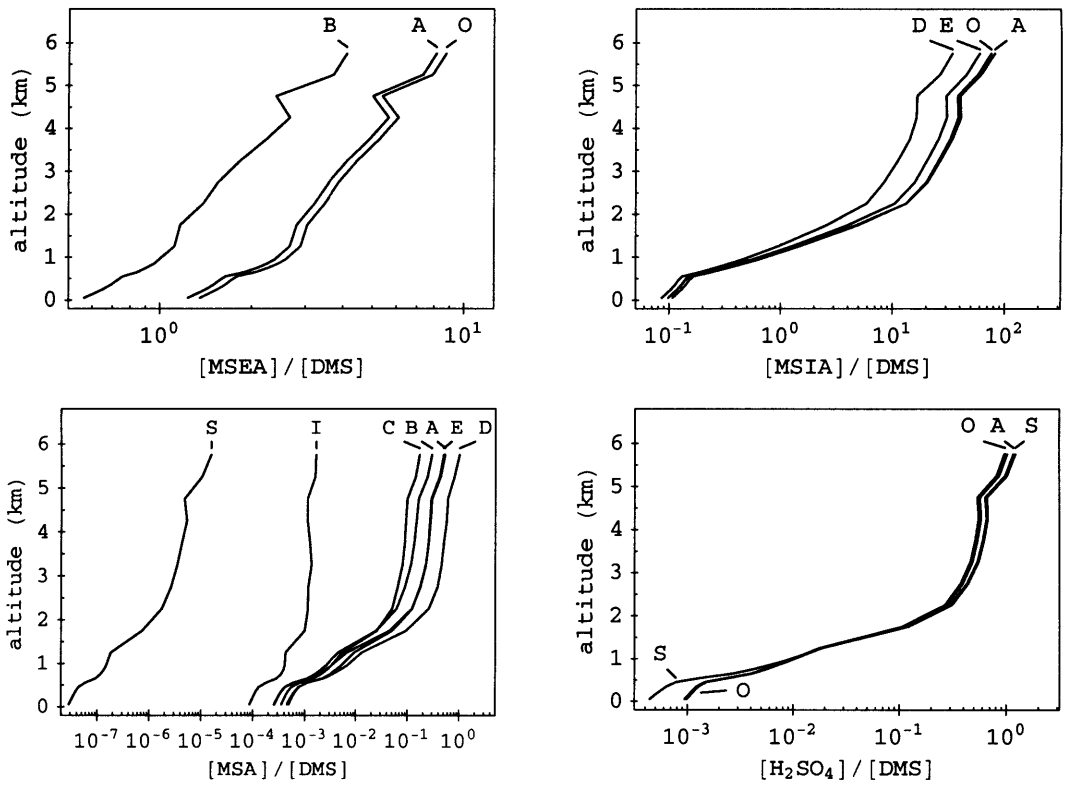

Figure 4-16: Daily average vertical profiles of the concentrations of MSIA, MSEA, MSA, and H_2SO_4 relative to DMS for all model scenarions. The individual scenarios are labeled the same as in Figure 4-15.

production of CH_3SO_3 is inactive.

Together, these vertical profiles suggest that measurements of MSEA relative to DMS at any point in the lower troposphere may help to determine the feasibility of branch B, while FT measurements of MSIA and MSA relative to DMS may help determine the possibility of MSA production from branches C and D. Also, additional BL measurements of H_2SO_4 can be used to test the proposed isomerization of $CH_3S(O)OO$ to CH_3SO_3. The lack of significant sensitivity of the DMSO, $DMSO_2$, and SO_2 profiles to scenario choices suggests that field observations of these species will not help to sort out the unknown MSA pathways.

4.5 Summary and Conclusions

A one-dimensional model of DMS oxidation chemistry and vertical mixing is used to examine the production routes of DMS oxidation products in the remote marine atmosphere. The model

is constrained by selected observations from Flight 24 of the ACE-1 campaign and the model predictions are compared with a corresponding set of Flight 24 observations of DMS, SO_2, H_2SO_4, and MSA. This study shows that the Yin et al. (1990b) mechanism, reduced for remote marine atmospheric conditions and updated with recently measured rate constants, yields DMS and SO_2 concentrations that agree well with observations, but produces gas-phase MSA levels four to five orders of magnitude smaller than what is observed. A Monte Carlo error analysis including all of the major parameter uncertainties shows that this large MSA deficiency is statistically extremely significant. By ruling out other possible sources for this large MSA difference, we conclude that the primary pathways of gas-phase MSA production in the DMS oxidation mechanism must be absent from current schemes. Furthermore, by noting the nature of the MSA observations and examining the sulfur fluxes in the Yin et al. (1990b) mechanism, this report suggests that the primary MSA production paths lie along the DMS+OH addition route and that MSEA and MSIA should be considered as likely MSA precursors.

The hypothesis that an additional and dominant MSA production path is required is tested by modeling the system using five new sets of hypothesized elementary reactions that produce MSA. Three of these sets involve a newly proposed MSA isomer $CH_3S(OH)(OO)$ and two sets involve the oxidation of MSIA. The modeling results indicate that the branch A and branch D cases provide the best overall fit with MSA observations, but that more studies are needed before eliminating the possibility of the other branches. Also, a modified version of the branch D case significantly enhances the vertical gradient for MSA and results in a better match with observations. The modified branch D case, therefore, suggests that MSA production involves precursors that are efficiently scavenged in the boundary layer. Laboratory and/or quantum chemistry studies of the proposed reactions, especially the formation and isomerization of $CH_3S(OH)(OO)$ and the reaction between MSIA and O_3, may conclusively support or rule out the proposed MSA production paths. Also, based on model sensitivity studies, additional field observations of MSA and MSEA diurnal cycles in the boundary layer may be useful for distinguishing branches B and E from the other cases, while free tropospheric measurements of MSIA and MSA relative to DMS may help to distinguish branches C and D. The sensitivity analyses also suggest that, while field observations of DMSO, $DMSO_2$, and SO_2 are helpful for gaining a more complete understanding of the full DMS oxidation mechanism, they do not allow differentiation between the proposed MSA production pathways.

Regarding the gas-phase production of H_2SO_4, the baseline simulations of this gas agree with the buffer layer observations very well, but show large systematic underestimations in

the boundary layer. We argue for enhanced production of H_2SO_4 through a route involving CH_3SO_3 and SO_3. This route increases the H_2SO_4 in the BL without affecting the good agreement between the modeled and observed SO_2. This proposed route is tested in the model by including the isomerization of $CH_3S(O)OO$ to CH_3SO_3. The resulting model predictions agree with observations in both the BL and FL. An analysis of the sulfur fluxes for this case shows that, relative to the SO_2 pathway, the CH_3SO_3-SO_3 pathway is the dominant H_2SO_4 production route in the BL and competitive in the FL. Together, these results provide evidence for an efficient production route of gas-phase H_2SO_4 in the remote atmosphere that does not involve SO_2. Laboratory measurements of the transformation rate of $CH_3S(O)OO$ into CH_3SO_3, and further field observations of MSA and H_2SO_4 in the BL are needed to support or discount the importance of this isomerization reaction to H_2SO_4 production.

Chapter 5

Three-Dimensional Global Studies of the DMS Cycle

5.1 Introduction

Dimethylsulfide (CH_3SCH_3, DMS) plays a significant role in the tropospheric sulfur cycle because oceanic DMS emissions are global in scale and comprise some 10 to 25% of the net flux of sulfur to the atmosphere (Bates et al., 1992; Kettle and Andreae, 2000). In the atmosphere DMS is oxidized to a variety of gas-phase species such as sulfur dioxide (SO_2), sulfuric acid (H_2SO_4), and methanesulfonic acid (CH_3SO_3H, MSA) that are known to interact with aerosols, and hence, climate (Charlson et al., 1987, 1992). For these reasons, DMS oxidation chemistry forms an integral component in models of the global sulfur cycle.

The mechanism describing the atmospheric oxidation of DMS, however, is highly-complex and involves many reactions. Simulating this complex chemistry places a high computational burden on global models. Furthermore, the DMS oxidation mechanism is fraught with many uncertainties, including both unknown reactions and unmeasured rate constants (Lucas and Prinn, 2002). Previous global modeling studies of the atmospheric sulfur cycle thus used highly-parameterized versions of DMS oxidation chemistry. Three recent examples are those by Pham et al. (1995), Chin et al. (1996), and Barth et al. (2000). These parameterized mechanisms connect DMS to SO_2, MSA, and sulfate using just a few of the many known DMS reactions. Although most parameterized DMS schemes typically resolve the branching between OH-addition and H-abstraction at the time of the initial reaction between DMS and OH, other branches in these schemes partition the oxidation products using fixed yields, many of which

are based on chamber studies at a single set of conditions. By excluding known temperature- and pressure-dependent chemistry and using fixed branching yields, these global models may be seriously mis-calculating the concentrations of DMS oxidation products.

This chapter addresses the issue of the accuracy of the parameterizations by calculating the global distributions of DMS-related species using comprehensive and parameterized mechanisms in a 3-D chemical transport model. In total, four DMS oxidation mechanisms are simulated. Two of the mechanisms are the parameterized versions used by Pham et al. (1995) and Chin et al. (1996). The remaining two are the *branch A* and *branch D* variations of the comprehensive mechanism described in Chapter 4 and Lucas and Prinn (2002). All four mechanisms include DMS, SO_2, MSA, and H_2SO_4. In addition, the comprehensive schemes include reactions that produce and destroy dimethylsulfoxide ($CH_3S(O)CH_3$, DMSO), dimethylsulfone ($CH_3S(O)_2CH_3$, $DMSO_2$), methanesulfenic acid (CH_3SOH, MSEA), and methanesulfinic ($CH_3S(O)OH$, MSIA) acid. Keeping all other factors the same –such as OH concentrations and scavenging rates by aerosols– the global distributions of DMS, SO_2, H_2SO_4, and MSA are calculated for the four mechanisms and the differences between them are quantified. These differences define the sensitivities of these species to the type of mechanism and the errors inherent in the previous global studies that used parameterized DMS chemistry. Note that this study represents the first attempt at modeling the global three-dimensional DMS cycle using a comprehensive DMS oxidation mechanism.

In addition to the sensitivity studies, the model output is also assessed by comparing to observations of gas-phase DMS-related species collected during the First Aerosol Characterization Experiment (ACE-1) and Pacific Exploratory Mission-Tropics A (PEM-TA) campaigns (Bates et al., 1998a; Hoell et al., 1999). The ACE-1 and PEM-TA campaigns were focused in the clean marine atmosphere of the Southern Ocean and equatorial tropical Pacific, respectively. ACE-1 and PEM-TA provide an excellent test of the model because their datasets also featured some of the first simultaneous measurements of DMS, SO_2, MSA and H_2SO_4 in the gas-phase. In order to make direct comparisons with the gaseous MSA and H_2SO_4 observations, the scavenging rates of these species on to background aerosols are explicitly calculated in the model. This, in turn, allows for the calculation of their gas-phase burdens. Note that the majority of previous global sulfur modeling studies did not keep track of gaseous H_2SO_4, but instead monitored aerosol-based sulfate. In contrast, our current study allows for the computation of the production rate of H_2SO_4-H_2O particles on a global scale, which is useful for understanding the contribution of DMS oxidation to the formation new particles in the atmosphere.

5.2 Model Description

The Model of Atmospheric Transport and Chemistry (MATCH) is adopted for the three-dimensional global simulations of DMS oxidation chemistry (Rasch et al., 1997).[1] MATCH has been widely used and well-tested for a variety of tracers in many applications. Some of these include inverse modeling of CCl_3F (Mahowald et al., 1997a), CO_2 and CH_4 (Chen, 2003), and the transport of aerosols (Collins et al., 2001; Rasch et al., 2001) and dust (Colarco et al., 2002). These cited studies involved primarily chemically-inert or nearly-inert tracers. A chemically-detailed version of MATCH at the Max-Planck-Institute für Chemie (MATCH-MPIC) also exists and has been used to study the HO_x-NO_x-O_3-CH_4 chemical cycles in the background troposphere (Lawrence et al., 1999; von Kuhlmann, 2001). The simulations in this chapter are carried out by adding DMS-related source and sink modules to the standard distribution of MATCH (version 3.4.18). As described later, the concentrations of important non-sulfur-bearing oxidants used to drive the DMS chemistry are from MATCH-MPIC.

Tracers are transported in MATCH using offline meteorological archives and the mass-conserving SPITFIRE advection algorithm. Here, the archives from the National Center for Environmental Prediction (NCEP) are used, which are available with a time resolution of six hours and a spatial resolution of T62 horizontally ($1.9° \times 1.9°$) and 28 sigma levels vertically (Kalnay et al., 1996).[2] Because the gas-phase DMS chemistry package used in our study is computationally expensive, the spatial resolution of the NCEP archives are degraded horizontally to T42 ($2.8° \times 2.8°$) which saves a factor of 2.2 in computer time. The NCEP archives are regridded to T42 using an interpolation routine internal to MATCH. Dynamical routines in the model are stepped forward in time using 40-minute time-steps by interpolating the NCEP archives, while the fast DMS-related chemistry is propagated forward using a smaller adaptive time-step that maintains the accuracy of the numerical solutions to the chemical ODEs.

The model is integrated from September 1995 to October 1996, and the last year of this period is used to calculate annual averages. A relatively short spin-up time is required because SO_2, which is the longest-lived species in the simulations, has an average global lifetime of only 7 to 10 days. And on the basis of the typical 1 to 3 hour transport time out of the boundary layer in the model, those DMS-related species that may have chemical lifetimes greater than this are transported during the model integrations. Eight such species are identified for the

[1] MATCH is publically-available at <http://www.cgd.ucar.edu/cms/match/new_website>.

[2] The mid-points of the sigma levels equal 2.7, 10.1, 18.3, 28.8, 41.8, 58, 78.2, 102.8, 132.6, 168.2, 210.1, 258.2, 312.5, 372, 435.7, 501.7, 568.1, 632.9, 694.3, 750.8, 801.4, 845.8, 883.8, 915.9, 942.5, 964.4, 982.1, and 995.

comprehensive mechanism cases and they are DMS, DMSO, $DMSO_2$, SO_2, MSEA, MSIA, MSA, and H_2SO_4. The remaining non-transported sulfur-containing species are diagnosed within the gas-phase chemistry routines. The major source and sink terms for the eight transported species are described in more detail in the following subsections.

5.2.1 DMS Emissions

Even though terrestrial ecosystems provide a source of atmospheric DMS, this contribution is known to be small relative to the dominant oceanic source.[3] Terrestrial-based DMS, therefore, is ignored in this study. For the oceanic source, the ocean-to-atmosphere flux of DMS is calculated dynamically as a function of the DMS concentrations in the ocean and atmosphere, the surface wind speed, and sea-surface temperature. This flux is expressed by

$$F_{\mathrm{DMS}} = v_t \left([\mathrm{DMS}] - p_{\mathrm{DMS}}\, H_{\mathrm{DMS}}\right) \tag{5.1}$$

where F_{DMS} represents the ocean-to-atmosphere flux (kg m^{-2} s^{-1}), v_t is the wind-dependent transfer velocity (m s^{-1}), [DMS] is the dissolved DMS sea-surface concentration (kg m^{-3}), p_{DMS} is the atmospheric partial pressure of DMS (Pa), and H_{DMS} is the Henry's law coefficient for DMS. A temperature-dependent value of $H_{\mathrm{DMS}} = 2.94 \times 10^{-4} \exp[3100(1/T_s - 1/298)]$ kg m^{-3} Pa^{-1} is used in these calculations (De Bruyn et al., 1995), where T_s is the sea surface temperature.

As defined, the ocean-to-air flux is typically positive because the ocean is supersaturated in DMS relative to the atmosphere. Sea-surface DMS concentrations from Kettle et al. (1999) are used in equation 5.1. The Kettle et al. (1999) fields represent climatological monthly averages of dissolved DMS sea-surface concentrations on a $1° \times 1°$ horizontal grid. Because the model is run at a lower spatial resolution, the sea-surface concentration fields are remapped to T42 using a conservative, area-weighted remapping algorithm (Jones, 1999). Samples of the remapped sea-surface concentrations for January and July are shown in Figure 5-1.

The transfer velocity (v_t) in equation 5.1 is calculated using a modified version of the wind-speed dependent parameterization from Liss and Merlivat (1986). The modification accounts for changes in the DMS Schmidt number ($Sc_{\mathrm{DMS}}=\nu_k/D_{\mathrm{DMS}}$ where ν_k is the kinematic viscosity and D_{DMS} is the molecular diffusion coefficient for DMS) with sea-surface temperature using

[3]For example, Table 1.1 in Chapter 1 lists 15-25 Tg S yr^{-1} as the oceanic source and 0.053-0.84 Tg S yr^{-1} as the terrestrial source.

the following expression from Gabric et al. (1996).

$$v_t = \begin{cases} (0.17\ u_H)\, c_1 & \text{for } u_H \leq 3.6 \\ (2.85\ u_H - 10.26)\, c_1 + 0.612\, c_2 & \text{for } 3.6 < u_H \leq 13 \\ (5.90\ u_H - 49.91)\, c_1 + 0.612\, c_2 & \text{for } u_H > 13 \end{cases} \tag{5.2}$$

In equation 5.2, the transfer velocity has units of cm h^{-1}, u_H is the horizontal wind speed (m s^{-1}) taken from the midpoint of the lowest level of the NCEP archives, and $c_1 = (600/Sc_{\mathrm{DMS}})^{2/3}$ and $c_2 = (600/Sc_{\mathrm{DMS}})^{1/2}$ are the Schmidt number corrections. The Schmidt number dependence on sea-surface temperature is calculated using

$$Sc_{\mathrm{DMS}} = 3628.5 - 234.58\ T_s + 7.8601\ T_s^2 - 0.1148\ T_s^3 \tag{5.3}$$

where T_s is the sea-surface temperature in °C (Gabric et al., 1996). Climatological monthly mean 2° × 2° sea-surface temperature fields are taken from Shea et al. (1990) and have been remapped to T42 in a manner similar to the DMS sea-surface concentrations. Note that the sea-surface temperature is also used in calculating H_{DMS}. Samples of DMS surface fluxes are also shown in Figure 5-1 using 1996 NCEP archives.

The one-year globally integrated oceanic DMS surface flux calculated over the simulation period is 15 Tg of sulfur, which is consistent with other evaluations that use the Kettle et al. (1999) fields and the Liss and Merlivat (1986) transfer velocity (Kettle and Andreae, 2000). This annual-global value lies at the lower end of the range given in Table 1.1 in Chapter 1. Using the Wanninkhof (1992) transfer velocity parameterization nearly doubles the flux and results in annual-global DMS emissions near the upper end of the range in Table 1.1.

5.2.2 Dry Deposition

Dry deposition at the planetary surface is a loss process for many of the products of DMS oxidation. Dry deposition is computed as a surface flux, where the flux is the product of the species concentration and dry deposition velocity (v_d). The budgets in Table 4.6 in Chapter 4 indicate that dry deposition is extremely important for SO_2 and mildly to moderately important for the other sulfur-containing species. On this point, v_d is calculated dynamically for SO_2 over the ocean as described below, while DMSO, $DMSO_2$, MSIA, MSA, and H_2SO_4 use prescribed orographic-dependent dry deposition velocities. Over land, ocean, and snow/ice surfaces these non-SO_2 species have assumed deposition velocities of 0.1, 0.25, and 0.01 cm s^{-1}, respectively,

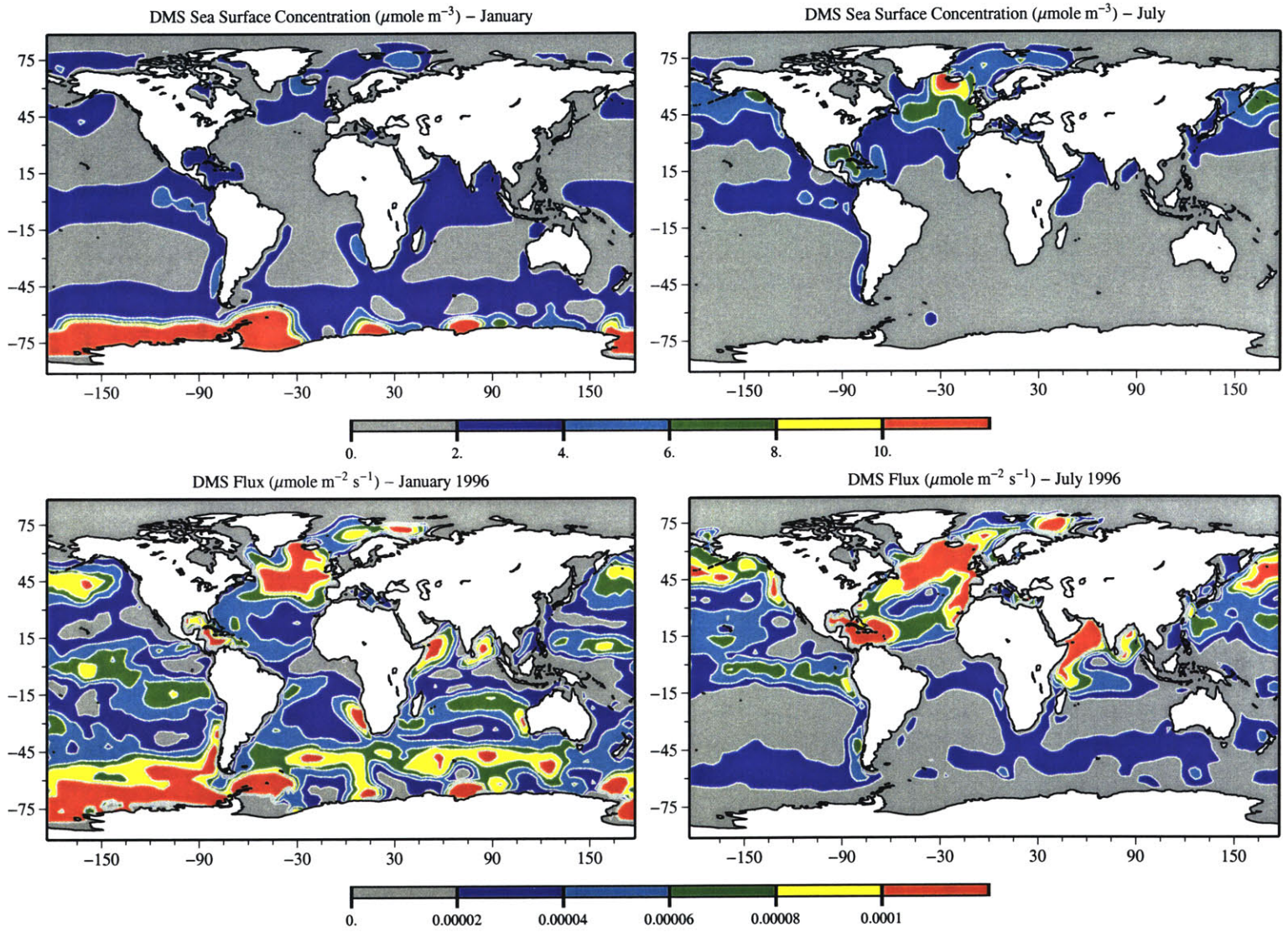

Figure 5-1: Sea surface concentrations (μmole m^{-3}) and wind-forced surface fluxes (μmole m^{-2} s^{-1}) of DMS for January and July. The NECP winds for 1996 are used to calculate these DMS fluxes.

which are based on the values for methylhydroperoxide used by Hauglustaine et al. (1994).

Dry Deposition Velocities for SO_2

Because the DMS cycle is focused on the ocean, we simply assume prescribed constant SO_2 dry deposition velocities over land (1.0 cm s^{-1}) and snow/ice surfaces (0.05 cm s^{-1}). Over oceanic grid cells the SO_2 dry deposition velocity is calculated dynamically at each time-step using a resistance-in-series method. In this method, the oceanic dry deposition velocity is expressed as the reciprocal sum of aerodynamic (r_a), quasi-laminar (r_q), and surface resistances (r_s):

$$v_d = (r_a + r_q + r_s)^{-1} \tag{5.4}$$

where r_a defines the aerodynamic resistance to the turbulent transport from the bulk atmosphere to the planetary surface, r_q represents the resistance to the molecular-scale transport across a quasi-laminar layer adjacent to the surface, and r_s is related to specific surface properties such as surface reactivity and surface type (for example, vegetated land, barren land, or water).

The aerodynamic resistance is determined using the standard expression from Monin-Obukhov similarity theory:

$$r_a = \int_{z_o}^{z_r} \frac{\phi(\zeta)}{\kappa u_* z} dz \tag{5.5}$$

where z is the altitude, z_o is the roughness height, z_r is a reference height, κ is the von Karman constant (set to 0.4), u_* is the friction velocity, ζ is the ratio z/L where L = Monin-Obukhov length, and ϕ is the dimensionless vertical potential temperature gradient. The boundary layer scheme in MATCH explicitly determines u_* and L using the methodology of Holtslag and Boville (1993) that is employed in the NCAR Community Climate Model. Note that L and u_* are calculated at the mid-point height of the bottom layer, and so, for consistency, z_r is defined at that level. The following function for ϕ is used (Holtslag and Boville, 1993), which is divided into three stability classes:

$$\phi(\zeta) = \begin{cases} 1 + 5\zeta & \text{stable: } 0 \leq \zeta \leq 1 \\ 5 + \zeta & \text{very stable: } \zeta > 1 \\ (1 - 15\zeta)^{-1/2} & \text{unstable: } \zeta < 0 \end{cases} \tag{5.6}$$

Integrating equation 5.5 between z_o and z_r using the above definition for ϕ gives

$$r_a = \begin{cases} \frac{1}{\kappa u_*}\left[5\left(\zeta_r - \zeta_o\right) + \ln\frac{z_r}{z_o}\right] & \text{stable} \\ \frac{1}{\kappa u_*}\left[\left(\zeta_r - \zeta_o\right) + 5\ln\frac{z_r}{z_o}\right] & \text{very stable} \\ \frac{1}{\kappa u_*}\left[\ln\frac{\sqrt{1-15\,\zeta_r}-1}{\sqrt{1-15\,\zeta_r}+1} - \ln\frac{\sqrt{1-15\,\zeta_o}-1}{\sqrt{1-15\,\zeta_o}+1}\right] & \text{unstable} \end{cases} \tag{5.7}$$

where ζ_r and ζ_o are z_r/L and z_o/L, respectively. The roughness height is calculated using $z_o = \frac{D_{SO_2}}{\kappa u_*}$, where D_{SO_2} is the molecular diffusion coefficient for SO_2 in air. The quasi-laminar resistance is calculated using the expression from Wesely (1989)

$$r_q = \frac{5Sc^{2/3}}{u_*} \tag{5.8}$$

where as before Sc is the Schmidt number defined by the ratio ν_k/D_{SO_2}, and ν_k is the kinematic viscosity of air. The surface resistance over the ocean is based on the following parameterization from Sehmel (1980), which is a function of turbulence and air-sea partitioning,

$$r_s = \frac{2.54 \times 10^4}{H^*_{SO_2} T\, u_*}. \tag{5.9}$$

In this expression, $H^*_{SO_2}$ is the effective Henry's law constant for SO_2 listed in Table 5.3, and T is the surface air temperature (K). A constant surface seawater pH of 8.2 is used to calculate $H^*_{SO_2}$ in this equation. As an illustration of the resistance-in-series calculations, the monthly-mean SO_2 dry deposition velocities for September 1995 are shown in Figure 5-2.

5.2.3 Chemical Production and Loss

Because the DMS oxidation cycle involves species with a wide range of atmospheric lifetimes, a stiff ordinary differential equation solver is required to calculate the net chemical production.[4] Initially, the GEAR-based LSODE solver –which is highly stable and accurate (Hindmarsh and Radhakrishnan, 1993)– was tested, but was found to be too computationally expensive for our 3-D integrations. An implementation of LSODE using sparse matrix techniques was also tested and found to be too expensive. Numerical benchmarks by Sandu et al. (1997a,b) showed that the Rosenbrock-class of ODE solvers are relatively efficient and accurate for solving large atmospheric chemical systems, thus a fourth-order Rosenbrock solver is used to integrate the DMS

[4]For example, approximate lifetimes of the DMS-related species range from 10^1 to 10^6 seconds.

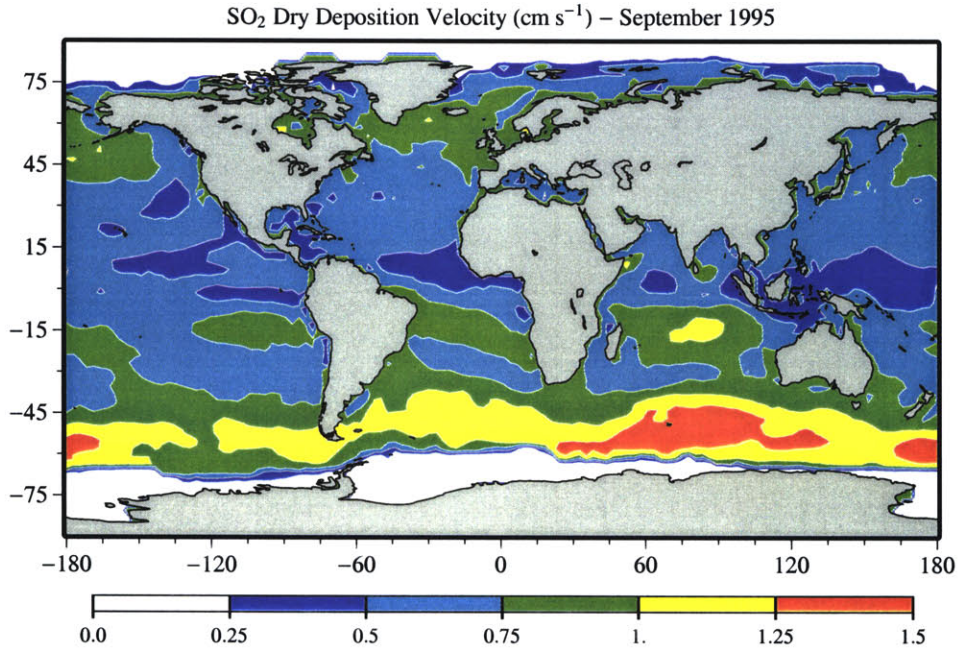

Figure 5-2: Monthly-mean dry deposition velocities for SO_2 (cm s^{-1}) using the September 1995 NCEP archives. The oceanic deposition velocities are calculated dynamically, while the deposition velocities over land and ice are fixed at 1.0 and 0.05 cm s^{-1}, respectively.

mechanisms described below (Press et al., 1992). Note that the chemical solver is initialized by the eight transported species while the remaining species are diagnosed internally.

Parameterized DMS Oxidation Mechanisms

The two parameterized DMS oxidation mechanisms used in these simulations are taken from the recent 3-D global sulfur models of Chin et al. (1996, modified[5]) and Pham et al. (1995). These mechanisms are representative of the highly-simplified DMS oxidation schemes typically employed in global sulfur models to enable computational feasibility. For the remainder of this chapter, the modified Chin et al. (1996) and the Pham et al. (1995) parameterized mechanisms are referred to as 'P_1' and 'P_2', respectively. These schemes are shown in Figure 5-3 and their reactions and rate constants are listed in Table 5.1. P_1 and P_2 use only four to five reactions to

[5]Note that Chin et al. (1996) also introduced an unknown species labeled 'X' as an additional DMS oxidant, but that pathway is not included here.

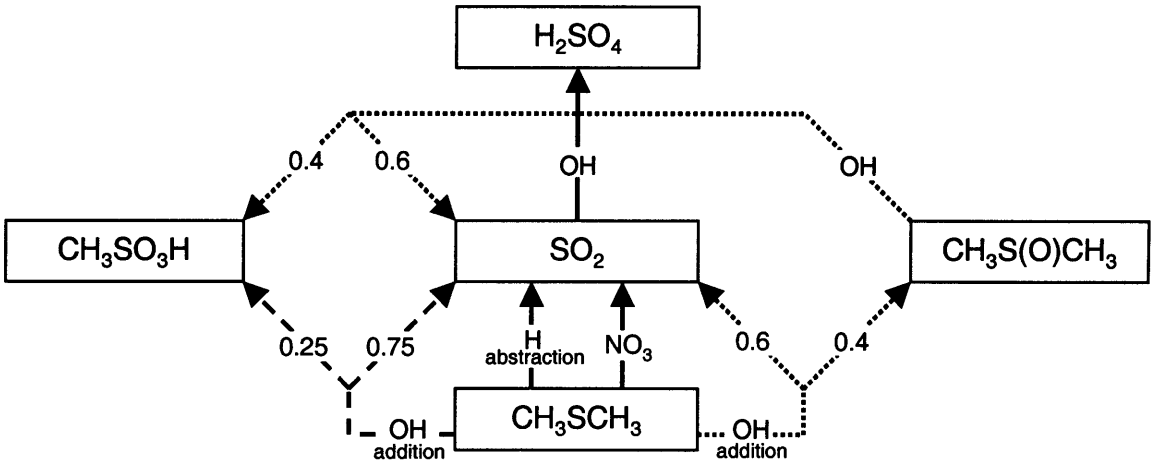

Figure 5-3: Diagram of the two parameterized DMS mechanisms used in MATCH. The pathways unique to P_1 are shown using dashed arrows, those unique to P_2 are shown using dotted arrows, and the paths common to both schemes are shown using the solid arrows.

describe the oxidation of DMS to SO_2, H_2SO_4, and MSA. Despite their simplicity, P_1 and P_2 do resolve the branching between OH-addition and H-abstraction. Further, as with the more comprehensive mechanisms, the products along the H-abstraction branch are SO_2 and H_2SO_4 while the OH-addition branch gives a mixture of MSA and SO_2. As is the case with many parameterized DMS mechanisms, however, these two versions use constant yields at some of the key branching points. Though similar, P_1 and P_2 do differ in their branching ratios and oxidation products. For example, P_2 includes DMSO –which undergoes oxidation to MSA and SO_2– while P_1 does not. Because DMSO is susceptible to wet and dry deposition, the MSA levels from P_1 and P_2 will differ even if their DMS-to-MSA branching ratios are similar.

Comprehensive DMS Oxidation Mechanisms

Of the seven comprehensive DMS oxidation mechanisms tested in Chapter 4, the *branch A* and *branch D* scenarios –which have different MSA production pathways– were found to give the best agreement with observations. These two mechanisms are therefore used to compute chemical production and loss in MATCH. Hereafter the *branch A* and *branch D* comprehensive mechanisms are referred to as 'C_1' and 'C_2', respectively. A brief summary of the major differences and similarities between the parameterized and comprehensive mechanisms is given

Table 5.1: Reactions and Rate Constants in the Parameterized DMS Oxidation Mechanisms

Mechanism	Reaction	Rate Constant (cm^3 $molecule^{-1}$ s^{-1})
$P_1 + P_2$	DMS + OH $\rightarrow$ SO_2	$9.6 \times 10^{-12} \exp(-234/T)$
P_1	DMS + OH $\rightarrow$ 0.75 SO_2 + 0.25 MSA	$\frac{1.7\times10^{-42}\exp(7810/T)[O_2]}{1+5.5\times10^{-31}\exp(7460/T)[O_2]}$
P_2	DMS + OH $\rightarrow$ 0.6 SO_2 + 0.4 DMSO	same as above
*$P_1 + P_2$	DMS + NO_3 $\rightarrow$ SO_2	$1.9 \times 10^{-13} \exp(500/T)$
P_2	DMSO + OH $\rightarrow$ 0.6 SO_2 + 0.4 MSA	5.8×10^{-11}
$P_1 + P_2$	SO_2 + OH $\rightarrow$ H_2SO_2	see DeMore et al. (1997)

* Chin et al. (1996) did not use NO_3 and the listed rate constant directly, but instead assumed that NO_3 was balanced between production from $NO_2 + O_3$ and loss by reaction with DMS. Because NO_3 fields are directly used here, the rate constant for the DMS + NO_3 reaction from DeMore et al. (1997) is used for P_1 and P_2.

below, while the detailed reactions and rate constants in C_1 and C_2 are found in Table 4.1 in Chapter 4. Note that the nighttime oxidation of DMS by NO_3, which was not included in Chapter 4, is used in C_1 and C_2 in this chapter.

Parameterized Versus Comprehensive DMS Mechanisms

Overall, the most significant differences between the parameterized and comprehensive schemes are the constant branching yields and missing intermediate species in P_1 and P_2. For example, P_1 partitions the OH-addition path into 25% MSA and 75% SO_2 at all temperatures and pressures. In C_1 and C_2, on the other hand, the gas-phase branching along the OH-addition path depends on a complex combination of temperature and pressure. Thus, the parameterized and comprehensive mechanisms may agree under certain atmospheric conditions, but significantly disagree at others. Missing intermediate species in P_1 and P_2, such as MSEA and MSIA, may also cause large differences because these species are influenced by non-photochemical processes. The loss of MSIA by wet deposition, for instance, affects the yield of MSA, and this effect is not captured by P_1 and P_2. Furthermore, some of the magnitudes of the branching ratios in the parameterized mechanisms are inconsistent with the comprehensive versions. As an example, P_2 constantly partitions the OH-addition path into 40% DMSO and 60% SO_2. But according to the analysis in Chapter 4 (also, see Figure 2-5 in Chapter 2), C_1 and C_2 favor DMSO production at this particular branching point. The parameterized schemes also lack the potentially important SO_2-independent H_2SO_4 production pathway discussed in Lucas and Prinn (2002). Finally, the differences between the parameterized and comprehensive mechanisms are likely to be largest

at low temperatures, because the OH-addition path is favored at temperatures below ~270 K, which accentuates the differences between the branching ratios.

Despite these large differences, some of the features in P_1 and P_2 are similar to C_1 and C_2. First, the four mechanisms use similar rate constants for the initial DMS+OH reactions, and hence their differences in the oxidation of DMS are expected to be small. Note that C_1 and C_2 have unique reactions involving the DMS-OH adduct, including its thermal decomposition back to DMS and OH, which slightly changes their oxidation rates of DMS relative to P_1 and P_2. Second, as a consequence of using similar H-abstraction rate constants, the four mechanisms are expected to produce comparable levels of SO_2 at high temperatures where the H-abstraction path is dominant. Third, P_1 and P_2 produce MSA solely through the OH-addition branch, which is also consistent with the majority of the MSA production by C_1 and C_2 as analyzed in Chapter 4.

Background Oxidants

The DMS chemistry in P_1 and P_2 is driven by reactions with OH and NO_3, while the chemistry in C_1 and C_2 requires specification of HO_x, NO_x, O_3, and CH_3O_2. Rather than computing the concentrations of all of these oxidants interactively in our model, our DMS chemistry is driven using concentrations calculated offline. This is reasonable because DMS chemistry is not strongly coupled to the background HO_x and NO_x cycles. For example, the lifetime of OH is determined mainly by CO, NO_2, and hydrocarbons, not by the DMS-related species. Using offline fields for the oxidants also has the obvious advantage of being computationally less expensive.

For consistency, the offline concentrations of the aforementioned species are taken from the chemically-detailed MATCH-MPIC. This version includes the standard HO_x-NO_x-O_3-CH_4 cycles and nonmethane hydrocarbon chemistry (Lawrence et al., 1999; von Kuhlmann, 2001). These fields were calculated for the year 1998 and are available as monthly means. As before, these fields have been remapped from T63 to T42 using the remapping algorithm of Jones (1999). Daily average values for these oxidants are calculated by linearly interpolating the monthly mean values.

Because diurnal variations in OH are important in DMS oxidation, a diurnal OH cycle is also imposed using

$$[\mathrm{OH}](t) = A\cos\theta(t) + \min \mathrm{OH} \tag{5.10}$$

where [OH](t) is the time-dependent local concentration of OH (molecules cm^{-3}), t is the local time (fraction of day between -0.5 and 0.5), $\theta(t)$ is the solar zenith angle, A is the amplitude of the cycle, and minOH is a minimum OH value adopted for numerical stability (set to 10 radicals cm^{-3}). The solar zenith angle is computed internally in MATCH as a function of location, time of day, and day of year. The amplitude A is calculated by setting the daily average OH equal to the average of the cycle defined by equation 5.10. This gives

$$\overline{\mathrm{OH}} = \frac{1}{t_2 - t_1} \int_{t_1}^{t_2} (A \cos\theta(t) + \min \mathrm{OH})\, dt \tag{5.11}$$

where $\overline{\mathrm{OH}}$ is the daily average OH concentration from the interpolated monthly mean fields, and t_1 and t_2 are the sunrise and sunset, respectively. Note, in expression 5.11, A is set to zero for $t < t_1$ and $t > t_2$. Modeled and observed diurnal OH cycles are compared in Section 5.3.4.

Lastly, the monthly mean OH fields have been scaled up uniformly by a factor of 1.5. As shown later, this scaling leads to better comparisons between measured and modeled OH concentrations. Further justification for this scaling is due to the fact that the version of MATCH-MPIC with the non-methane hydrocarbon chemistry package consistently overestimates methylchloroform (CH_3Cl_3) in the atmosphere (von Kuhlmann, 2001), which is indicative of deficient OH concentrations. Chen (2003) also found that an OH scaling factor of at least 1.25 is required to give a good fit to CH_3Cl_3 observations using the identical version of MATCH that is employed here.

5.2.4 Scavenging by Background Aerosols

Many of the gas-phase species in the DMS oxidation cycle are highly adsorbable and soluble, and thus are readily scavenged by background aerosols. This gas-to-aerosol loss is considered for SO_2, DMSO, $DMSO_2$, MSEA, MSIA, MSA, and H_2SO_4. Because of the rather large solubilities of these oxidized sulfur-containing species (see Table 5.3), it is assumed that this process is irreversible. This assumption of irreversibility allows for the exclusion of an aerosol dynamics package that would normally be required to keep track of aerosol-phase species concentrations. Among these scavenged sulfur-containing species, SO_2 is most affected by the irreversible loss assumption because it is the least soluble. Therefore, to prevent excessive scavenging for SO_2 its gas-to-aerosol loss is limited to sea-salt aerosols. Note, however, that reversible loss is considered for the uptake of gas-phase sulfur-containing species by cloud water as described in the wet

Table 5.2: Aerosol Components and Parameters

Component	$\bar{r}_w$				σ	N_∞	H
	a	b	c	d			
Insoluble	0.471	—	—	—	2.51	0	825
Water soluble	0.0203	0.0000792	0.0908	102.6	2.24	200	825
Soot	0.0118	—	—	—	2.00	0	825
Sea-salt, accumulation	0.199	0.00203	1.28	101.2	2.03	0	370
Sea-salt, coarse	1.67	0.0170	10.9	101.1	2.03	0	370
Mineral, nucleation	0.070	—	—	—	1.95	0	825
Mineral, accummulation	0.390	—	—	—	2.00	0	825
Mineral, coarse	1.90	—	—	—	2.15	0	825
Mineral, transported	0.50	—	—	—	2.20	0	825
Sulfate	0.0670	0.000485	0.278	101.4	2.03	200	130

Aerosol number distributions for the individual components are defined using equation 5.14, where $\bar{r}_w$ is the mean wet radius (in μm) and σ is standard deviation. The mean wet radius $\bar{r}_w$ is calculated as a function of relative humidity using equation 5.16. N_∞ is the high altitude, background aerosol number concentration (in particles cm^{-3}). H is the particle scale height (in m) for the vertical decay of the surface aerosol number concentrations.

deposition section that follows.

The gas-to-aerosol loss on background aerosols is described using a Fickian diffusion formulation that specifies the first-order scavenging loss rate by

$$C = -4\pi D \int_0^\infty r_w \, f(Kn, \alpha) \, n(r_w) \, dr_w \tag{5.12}$$

where C is the scavenging rate (s^{-1}), r_w is the wet particle radius at the ambient relative humidity (cm), D is the molecular diffusion coefficient ($cm^2\ s^{-1}$), $f(Kn, \alpha)$ is a unitless correction factor, and $n(r_w)$ is the aerosol number distribution (particles $cm^{-1}\ cm^{-3}$). The equations for D and $f(Kn, \alpha)$ and the values of the accommodation coefficients are given in Lucas and Prinn (2002). An accommodation coefficient of 0.11 is used for SO_2 (DeMore et al., 1997).

The aerosol number distributions are taken from the Global Aerosol Dataset (GADS) (Koepke et al., 1997). GADS is compiled from an interpolated set of surface measurements, and represents an aerosol climatology that is useful mainly for climate modeling applications. GADS provides biannual $5° \times 5°$ surface maps of ten aerosol number distributions representing

aerosols of different types and sizes. The GADS aerosol components are summarized in Table 5.2.

The net aerosol number distribution in equation 5.12 is expressed as the sum over the ten independent GADS number distributions

$$n(r_w) = \sum_{i=1}^{10} \tilde{n}_i(r_{w,i}) \tag{5.13}$$

where each GADS number distribution is given by

$$\tilde{n}(r_w) = \frac{N(z)}{\sqrt{2\pi}\, r_w \ln\sigma} \exp\left[-\frac{1}{2}\left(\frac{\ln r_w - \ln \bar{r}_w}{\ln\sigma}\right)^2\right]. \tag{5.14}$$

In equation 5.14, $N(z)$ is the altitude-dependent aerosol number concentration (particles cm^{-3}), and $\bar{r}_w$ and σ are the mean wet radius and standard deviation of the aerosol number distribution, respectively.

Because GADS only provides surface particle number concentrations (that is, $N(z)$ at $z = 0$), extrapolations to other altitudes are made using

$$N(z) = N_\infty + (N_o - N_\infty) \exp\left(\frac{-z}{H}\right) \tag{5.15}$$

where N_∞ represents the high-altitude background number concentration, N_o is the GADS surface aerosol number concentration, and H is the particle scale height. The background number concentrations and scale heights are listed in Table 5.2 and are approximately based on averages of the values given by Jaenicke (1993).

Also note that the water soluble, sea-salt, and sulfate aerosol number distributions vary with relative humidity due to changes in the size of their mean wet radii $\bar{r}_w$. GADS only provides the $\bar{r}_w$ at eight different relative humidities between 0 and 99%, not continuously across this range. By fitting the following function to the GADS values, however, the $\bar{r}_w$ at all relevant relative humidities are available:

$$\bar{r}_w = a + b\,\mathrm{RH} + \frac{c}{d - \mathrm{RH}} \tag{5.16}$$

In this expression, RH is the percent relative humidity, and a, b, c, and d are the coefficients of the fits as listed in Table 5.2.

In general, the integral in equation 5.12 cannot be evaluated exactly because of the cor-

rection factor term, and thus requires numerical approximation using quadrature. Brute-force quadrature methods are too expensive for calculating scavenging rates in a 3-D global model.[6] However, because the integrand has its maximum close to where the aerosol distribution is a maximum (at $\bar{r}_w$), the integral can be accurately estimated using a 'guided' quadrature method over six equally-spaced bins between $\ln \bar{r}_w \pm 3 \ln \sigma$. This method is computationally efficient and gives results that are within 5-10% of the values obtained using higher-order quadrature methods.

Finally, the condensation coefficients were scaled down by a factor of 0.4 to yield vertical profiles similar to those shown in Figure 4-2 in Chapter 4. This adjustment suggests that the GADS aerosol number concentrations are overestimated by more than a factor of two. Using a global mixed aerosol model, Wilson et al. (2001) similarly found that GADS overestimated particle number concentrations by a factor of 3 to 10. Samples of the aerosol number distributions and first-order condensation loss rates for H_2SO_4 are shown in Figure 5-4.

5.2.5 Wet Deposition

The hydrologic cycle in MATCH includes a prognostic, transported portion and a diagnostic, subgrid-scale portion. These two portions are used to define important quantities such as the amounts of cloud water and rain (stratiform and convective), rates of raindrop production and evaporation, and cloud volume estimates. These variables, in turn, are used to calculate scavenging tendencies for the wet removal of soluble gases. Rasch et al. (1997) describe the cloud microphysical parameterizations used in MATCH, while Barth et al. (2000) discuss the wet deposition routine implemented by MATCH. Briefly, the wet removal of soluble sulfur-containing gases is calculated using scavenging rates that account for in-cloud and below-cloud scavenging by liquid hydrometeors. Wet scavenging is initiated at the top of an atmospheric column and ends at the surface. Within a given level in this column, the inward flux of sulfur-containing precipitation is first determined, followed by local adjustments made assuming Henry's law equilibrium, and then the outward flux of precipitation is calculated. According to this scheme, 'sulfur-rich' precipitation falling into a 'sulfur-dry' layer can potentially release the sulfur-containing species back into the gas-phase. Permanent removal of the gas-phase species occurs through rainout at the surface. The sulfur-based species subjected to this procedure include DMSO, $DMSO_2$, SO_2, MSEA, and MSIA, and their Henry's law coefficients are given in Table 5.3. Because H_2SO_4 and MSA are even more soluble than these other species (see

[6]For example, the 31-point Gauss-Kronrod quadrature method was initially tested.

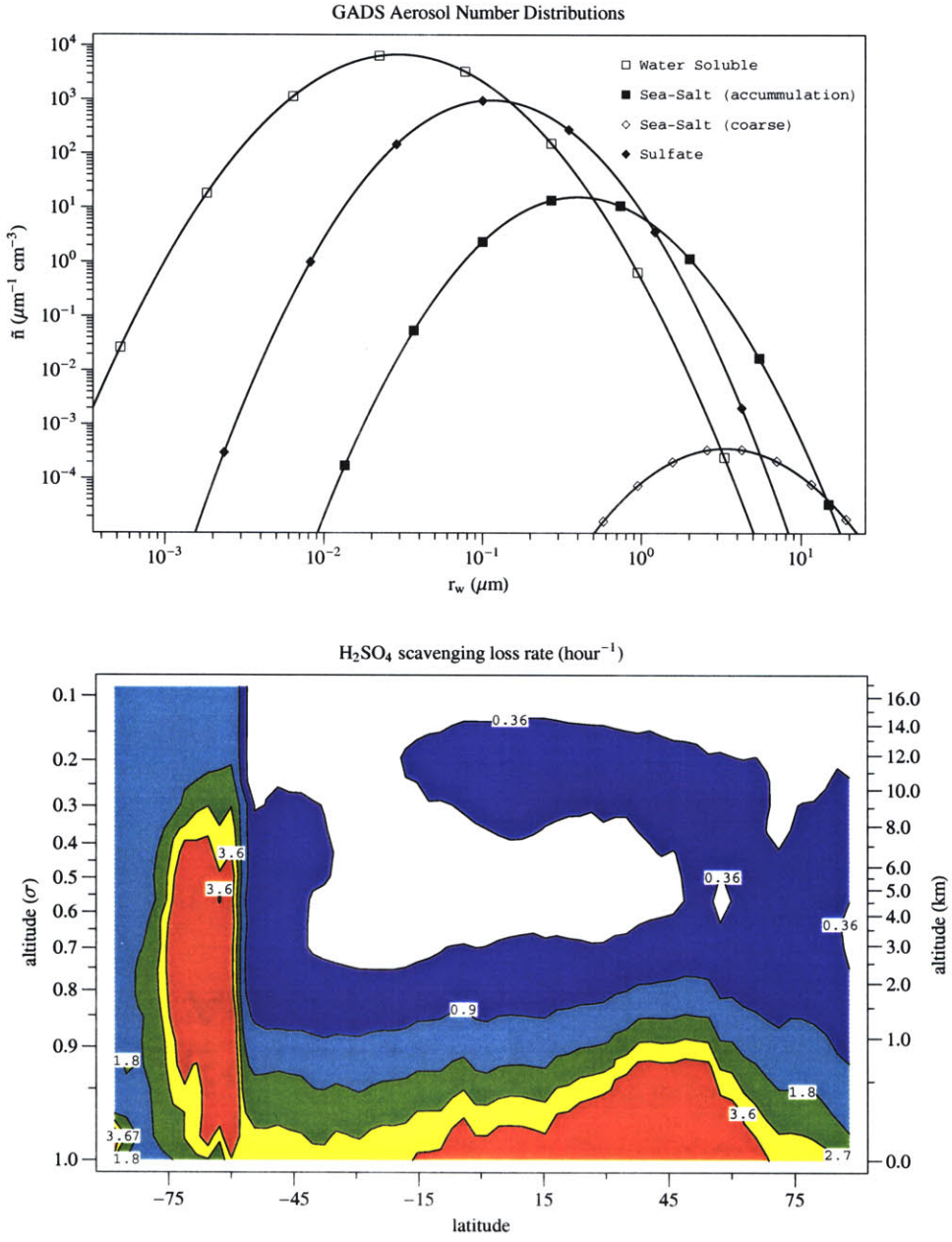

Figure 5-4: Samples of prescribed aerosol number distributions (equation 5.14) and aerosol scavenging rates (equation 5.12) for H_2SO_4. The aerosol number distributions are for Julian Day 151, (84.4°E, 37.7°S), an altitude of 500 m, and a relative humidity of 75%. The H_2SO_4 scavenging rates ($hour^{-1}$) are displayed as daily-zonal averages for September 1, 1995. Altitude is shown using σ-pressure coordinates on the left and the approximate height in km on the right.

Table 5.3: Henry's Law Coefficients

Equilibrium Reaction	Henry's Law Coefficient (M/atm)	Reference
SO_2 (g) $\rightleftharpoons$ S(IV) (aq)	$H^*_{SO_2} = H_{SO_2}\left(1 + K_1/[H^+] + K_1K_2/[H^+]^2\right)$	see note
DMSO (g) $\rightleftharpoons$ DMSO (aq)	$H_{DMSO} = 5.0 \times 10^4$	De Bruyn et al. (1994)
$DMSO_2$ (g) $\rightleftharpoons$ $DMSO_2$ (aq)	$H_{DMSO_2} = 5.0 \times 10^4$	De Bruyn et al. (1994)
MSEA (g) $\rightleftharpoons$ MSEA (aq)	$H_{MSEA} = 5.0 \times 10^4$	Assumed
MSIA (g) $\rightleftharpoons$ MSIA (aq)	$H_{MSIA} = 5.0 \times 10^4$	Assumed

$H^*_{SO_2}$ is the effective Henry's law coefficient for SO_2, which is a function of temperature and pH. In this expression, $H_{SO_2} = 3.64 \times 10^{-5}$ exp$(3100/T)$, $K_1 = 1.67 \times 10^{-5}$ exp$(1960/T)$, and $K_2 = 4.30 \times 10^{-10}$ exp$(1500/T)$ (Pandis and Seinfeld, 1989). Cloud-water and ocean surface pH are assumed to be 5.6 (i.e., in equilibrium with CO_2) and 8.2, respectively.

Table 2.1 in Chapter 2), their wet removal rates are instead estimated from the grid box fraction occupied by liquid water. That is, the first-order loss rate of gas-phase H_2SO_4 and MSA due to wet deposition equals $\Phi_w/\Delta t$, where Φ_w is the fraction of rain and cloud water contained in a grid box and Δt is the model time-step (40 minutes). Thus, if $\Phi_w = 1$, then all of the gaseous H_2SO_4 and MSA in that grid box is lost.

5.3 Model Results

The four DMS mechanism cases were integrated in MATCH between September 1995 and October 1996. This simulation period coincides with two measurement campaigns that are used to diagnose the model as described in Section 5.3.4. The simulation period also covers a full annual cycle because the DMS-related species are relatively short-lived and require only a short spin-up time. The last 12 months of the integrations, therefore, are used to define annual averages. We cannot practically show here all of the enormous amount of information available from the model runs. Instead, the model outputs for discussion and analysis are limited to the following two datasets: (1) Daily average mole fractions of the transported DMS-related species on the global 3-D grid (of these, DMS, SO_2, MSA, and H_2SO_4 are the species that the four mechanisms have in common, and these outputs are used to calculate zonal profiles and global and column burdens); (2) mole fractions of the transported sulfur-containing species in two different atmospheric sub-regions with a time-resolution of 40 minutes (these two sub-regions

Table 5.4: Annual-Global Atmospheric Gas-Phase Burdens (Gg S)

Species	MATCH				Chin et al.	Pham et al.
	P_1	P_2	C_1	C_2	(1996)	(1995)
DMS	43	43	46	46	59	50
DMSO	—	0.22	0.19	0.21	—	2‡
MSA	0.27	0.10	0.21	0.12	19‡	20‡
SO_2	63	61	40	40	†	†
H_2SO_4	0.27	0.27	0.39	0.39	†, ‡	†, ‡

† Although these species were included in the models of Chin et al. and Pham et al., they were affected by non-DMS-related sources such as anthropogenic emissions. It is not possible, therefore, to compare these burdens with those in the current version of MATCH.

‡ The models of Chin et al. and Pham et al. did not partition these species between the gas- and aerosol-phases, so that these burdens represent net amounts in the atmosphere. In the MATCH model, on the other hand, these burdens represent the gas-phase only amounts.

overlap with the focal areas during the ACE-1 and PEM-TA measurement campaigns).

5.3.1 Annual-Global Burdens

The annual-global atmospheric gas-phase burdens of DMS, DMSO, SO_2, MSA, and H_2SO_4 using the four mechanisms are shown in Table 5.4. Also shown are some of the DMS-related burdens computed in the models of Chin et al. (1996) and Pham et al. (1995). As noted, the global burden of DMS is similar using the comprehensive and parameterized mechanisms in MATCH. The DMS burdens are comparable because the initial oxidation rate constants –H-abstraction, OH-addition, and reaction with NO_3– are similar in the parameterized and comprehensive schemes. Notice that the DMS burdens for the comprehensive schemes C_1 and C_2 are slightly larger because these schemes include the thermal dissociation of the DMS-OH adduct, which slightly reduces the effective oxidation of DMS by OH-addition. The DMS burdens in the models of Chin et al. (1996) and Pham et al. (1995) are also similar to those in MATCH, even though these models used different emissions for DMS.

Other than the P_1 scheme, the MATCH-based burdens for DMSO are also similar to each other because the mechanisms do not have any effective branching between DMS and DMSO along the OH-addition path. There is, however, an order of magnitude difference between the DMSO burdens in Pham et al. (1995) and MATCH. This large difference is due to the fact that the MATCH-based burden represents DMSO only in the gas-phase, while the Pham et al. (1995)

burden includes DMSO in the gas- and aerosol-phases. This difference, therefore, provides a measure of the impact of scavenging by aerosols on atmospheric DMSO.

For SO_2 and H_2SO_4, the MATCH-based burdens differ significantly from each other. More specifically, the SO_2 and H_2SO_4 burdens differ by about a factor of 1.5 between the parameterized and comprehensive mechanisms. Interestingly, P_1 and P_2 systematically give higher SO_2 and lower H_2SO_4 burdens relative to C_1 and C_2. Normally, higher SO_2 implies higher H_2SO_4, but C_1 and C_2 contain the important isomerization reaction $CH_3S(O)OO \rightarrow CH_3SO_3$ that enhances H_2SO_4 production through an SO_2-independent channel. The parameterized schemes do not include this pathway. It is also important to point out that, relative to C_1 and C_2, the larger SO_2 burdens in P_1 and P_2 are due to higher yields of SO_2 production through the OH-addition channel, which will be discussed in more detail later on.

Finally, although there are significant differences for MSA, there is not a systematic distinction between the parameterized and comprehensive cases. Rather, P_1 and C_1 have larger MSA burdens than P_2 and C_2. This behavior is related to the MSA production routes. In all cases, MSA is produced through the OH-addition channel. In P_1 and C_1, however, MSA production occurs through a path that does not involve DMSO, whereas DMSO is an MSA-precursor in P_2 and C_2. Accordingly, the MSA burdens in P_2 and C_2 are lower because gas-phase DMSO is scavenged by aerosols. MSA also condenses on to aerosols, which causes the factor of 10^2 difference between the gas-phase MSA burdens computed in MATCH and the net gas- and aerosol-phase MSA burdens in the models of Chin et al. (1996) and Pham et al. (1995). A similar factor of 100 is observed between atmospheric concentrations of MSA in the gas-phase and methanesulfonate anion in aerosols.

5.3.2 Annual-Zonal Profiles and Annual-Column Burdens

The results in Table 5.4 highlight some of the differences between the parameterized and comprehensive DMS mechanisms, but many details are not captured by these annual-global burdens. For instance, the mechanisms may have better, or worse, agreement in some portions of the atmosphere than others because the comprehensive schemes have numerous temperature-dependent branching points that are not represented in the parameterized mechanisms. To glimpse into these differences in more detail, the annually and zonally averaged profiles and column burdens are analyzed in this section.

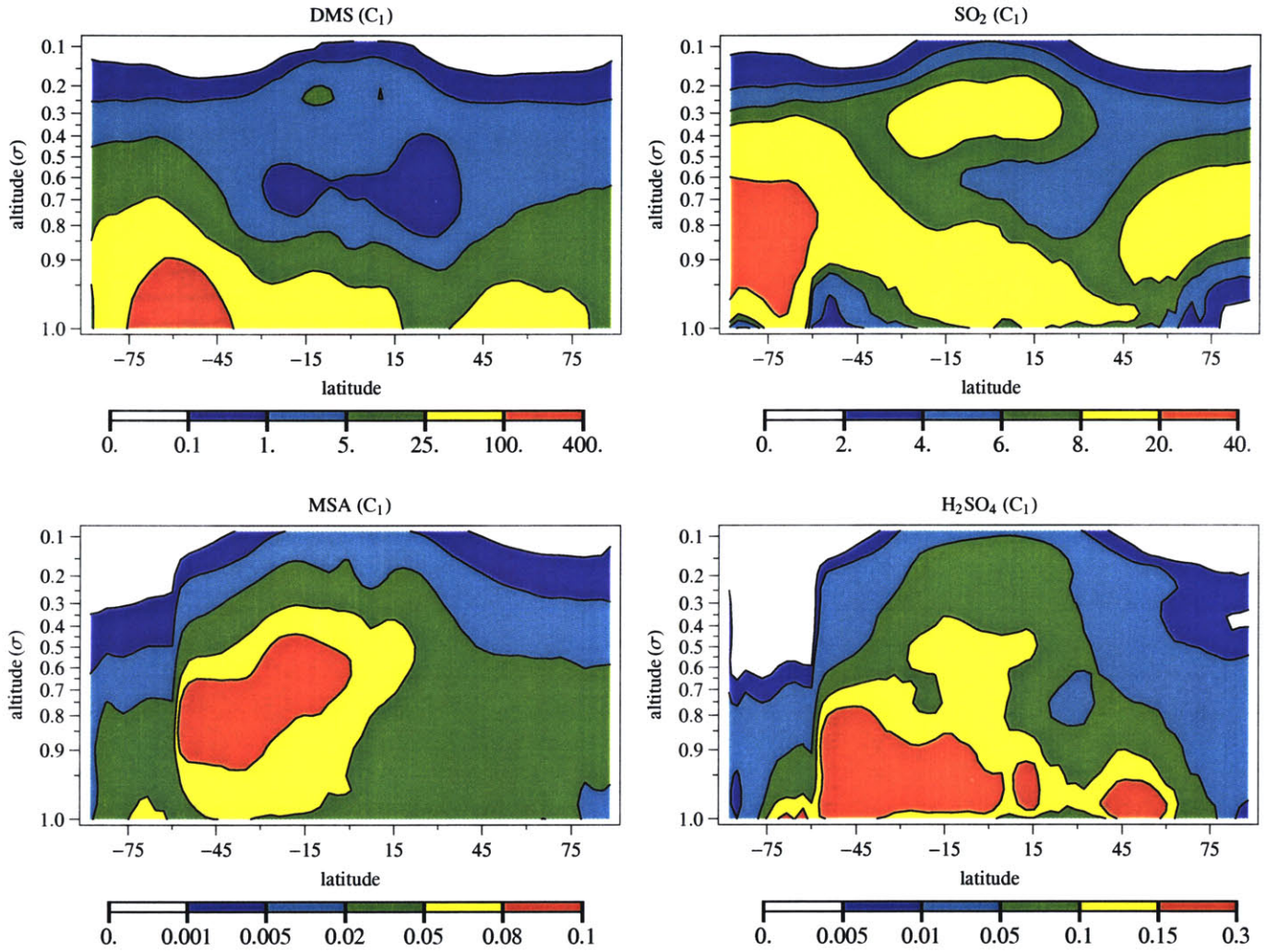

Figure 5-5: Annual-zonal average vertical profiles of the mole fractions (parts per 10^{12}, ppt) of DMS, SO_2, MSA, and H_2SO_4 using the C_1 mechanism. Altitude is shown using σ-coordinates. Refer to Figure 5-4 for the approximate altitude in km.

Annual-Zonal Profiles The annual-zonal profiles of the mole fractions of DMS, SO_2, MSA, and H_2SO_4 are shown in Figure 5-5 for the C_1 mechanism. Figure 5-6 displays the annual-zonal profiles of the three other mechanism cases as ratios relative to C_1, where a value of 1 denotes perfect agreement. Referring to the C_1 case in Figure 5-5, the zonal profile for DMS exhibits maximum surface values in the Southern Hemisphere and mole fractions that decay with altitude. These results are due to DMS having a source only at the surface and DMS sea surface concentrations that are largest in the Southern Ocean. Also note that the local minimum DMS mole fractions in the tropical middle troposphere follows from the fact that the maximum OH concentrations occur there. Referring to Figure 5-6, the DMS zonal profile using C_2 is nearly identical to C_1, while the parameterized schemes agree with C_1 to within a factor of 1.2 throughout most of the atmosphere. Note that the C_2-based DMS mole fractions are slightly larger everywhere because C_2 lacks the additional loss path for the DMS-OH adduct that is present in C_1. On a similar note, the DMS zonal profiles computed using P_1 and P_2 are typically smaller than using C_1 because these schemes do not include the thermal dissociation of DMS-OH that is used exclusively in C_1 and C_2.

As shown in Figure 5-5, the C_1-based SO_2 zonal profile is similar to the DMS profile because both display maximum mole fractions in the Southern Hemisphere and mole fractions that tend to decrease with altitude. One important distinction is that maximum SO_2 mole fractions are not found right at the surface because SO_2 is lost through dry deposition and sea-salt scavenging. Moreover, the vertical gradient for SO_2 is smaller than that for DMS because SO_2 has a longer lifetime and is produced photochemically throughout the atmosphere. Referring to Figure 5-6, the C_2 profile gives slightly larger and smaller SO_2 mole fractions in the lower and upper troposphere, respectively, when compared to C_1. In general, however, C_1 and C_2 agree well. Regarding the parameterized mechanisms, P_1 and P_2 are similar to each other and show the following important systematic differences relative to C_1. These cases agree best with C_1 in the equatorial lower troposphere and have larger disagreements elsewhere. At the polar surface, for example, P_1 and P_2 differ from C_1 by nearly a factor of two. The differences are even larger in the upper troposphere, where the SO_2 mole fractions from P_1 and P_2 are up to three times larger than those from C_1.

These SO_2 trends follow the zonal-mean temperature gradients, which points to differences in temperature-dependent SO_2 production as the cause. These temperature-dependent differences are not due to the rate constants for the initial DMS+OH reactions though, because all four chemical schemes use nearly identical values. There are two other mechanistic places

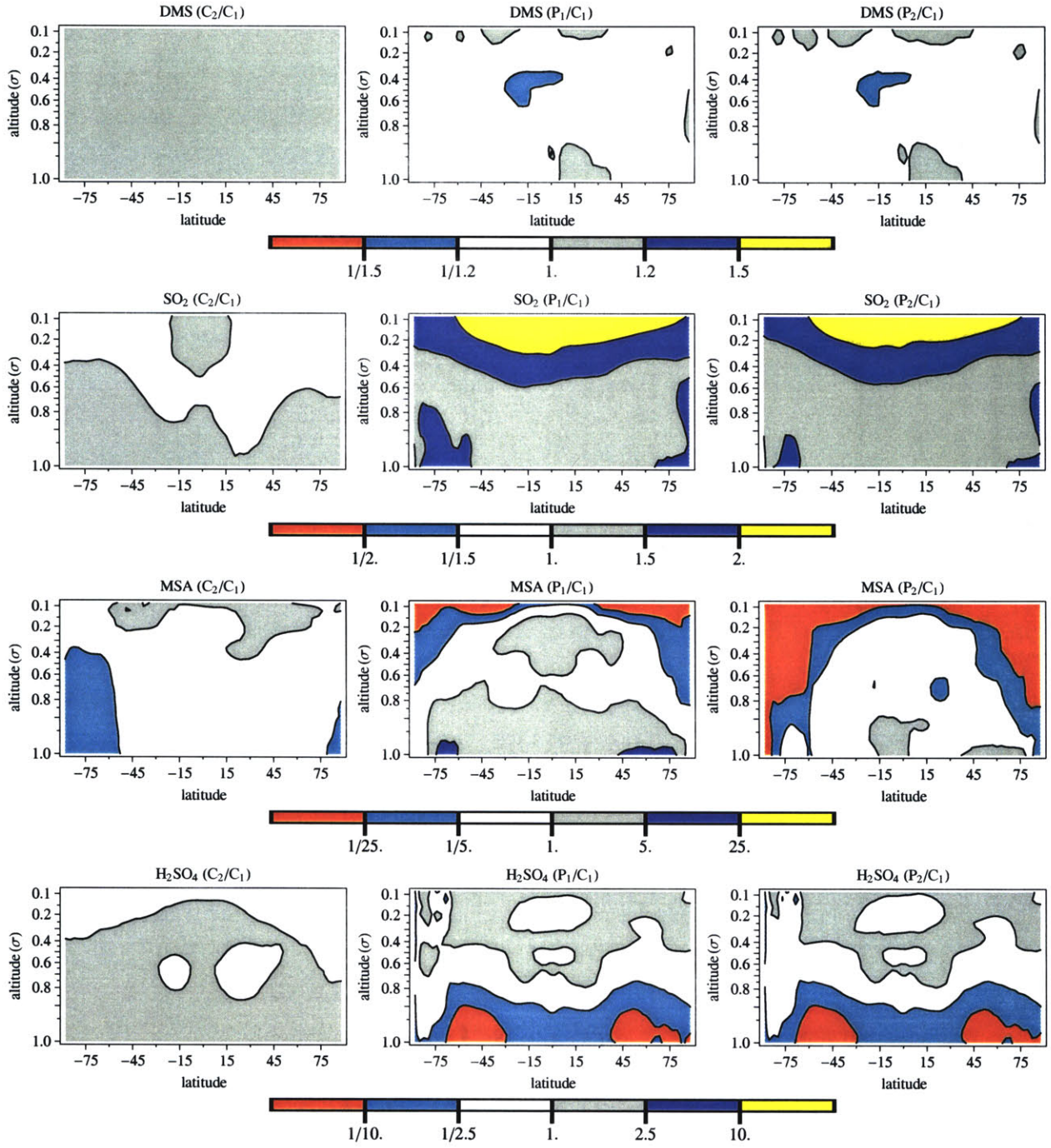

Figure 5-6: Annual-zonal average vertical profiles of the mole fractions of DMS, SO_2, MSA, and H_2SO_4 using the C_2, P_1, and P_2 mechanisms. The profiles for these mechanisms are shown as ratios relative to C_1 (see Figure 5-5), where a value of 1.0 denotes perfect agreement.

where these temperature-dependent differences arise. First, the OH-addition branch is favored over H-abstraction at colder temperatures, and along this branch P_1 and P_2 use fairly large constant yields for producing SO_2. Second, the comprehensive cases produce SO_2 through the thermal decomposition of the CH_3SO_2 radical, which has a positive temperature-dependence. This effect is not included in the parameterized schemes. To alleviate these differences the parameterized DMS mechanisms should use temperature-varying SO_2 yields that account for branching variations along the OH-addition path and changes in CH_3SO_2 dissociation.

Figure 5-5 displays the gas-phase annual-zonal H_2SO_4 mole fractions using C_1. Although H_2SO_4 is produced from SO_2, the sulfuric acid profile differs from SO_2 in significant ways. First, the H_2SO_4 mole fractions maximize in the equatorial region, unlike DMS and SO_2. This occurs because the production of H_2SO_4 is influenced by reaction with OH, which also has its maximum in the equatorial region. Second, there is a steep meridional gradient between $-55°$ and $-60°$ latitude. This gradient is caused by the enhanced loss of gas-phase H_2SO_4 on polar aerosols prescribed by the GADS aerosol climatology. Relative to C_1, the C_2 case has good agreement and differs by less than a factor of 2.5 everywhere in the atmosphere. The parameterized schemes, on the other hand, have regions of extremely poor agreement with C_1. In the boundary layer, P_1 and P_2 have two large areas centered around the mid-latitudes with mole fractions smaller than C_1 by more than an order of magnitude. The most interesting feature of these latter two areas is that they coincide with regions of relatively larger SO_2 mole fractions produced using P_1 and P_2. Higher SO_2 normally results in higher H_2SO_4, which suggests that P_1 and P_2 should have more H_2SO_4, not less. This apparent paradox is resolved by recalling that the comprehensive mechanisms have an H_2SO_4 production pathway that is independent of SO_2. In these near-surface mid-latitude regions the SO_2-independent pathway is comparatively more efficient than the SO_2-dependent path because SO_2 is quickly lost to the GADS sea-salt aerosols, which are most abundant at the mid-latitudes. The major conclusion is that even though an atmospheric sulfur model may produce reasonable levels of SO_2, slight changes to the structure of the chemical mechanism can cause profound changes in gas-phase H_2SO_4, which is important for issues related to H_2O-H_2SO_4 binary nucleation.

The C_1-based gas-phase MSA zonal mole fraction profile in Figure 5-5 has some features in common with H_2SO_4. Both have maximum levels near the equator and both incur significant losses to polar aerosols in the Southern Hemisphere. Unlike H_2SO_4, however, the maximum MSA mole fractions occur well above the surface, which results from its slower condensation rate and hence longer atmospheric lifetime. Relative to C_1, the other three mechanisms exhibit

MSA profiles with large disagreements in some regions by an order of magnitude. Moreover, the MSA profiles in P_1 and P_2 also significantly differ from each other, which is not the case for the other species. For instance, P_1 has relatively more MSA than C_1 throughout most of the lower troposphere, while P_2 has less. These results show that MSA is very sensitive to the details of the mechanism, even to the slight structural differences between C_1 and C_2. Regarding the C_2-based MSA, it is within a factor of 5 of C_1 everywhere except the polar regions. The C_2-based MSA is lower in these regions because it is produced through a pathway involving DMSO and MSIA as precursors, both of which undergo wet and dry deposition and scavenging by polar aerosols. The precursors in the C_1-based production of MSA, on the other hand, do not have these sinks. Having a DMSO-precursor also explains why P_2 is typically depleted in MSA relative to C_1. This implies that refined gas-phase observations of MSA may be useful in determining whether MSA is produced through pathways that do or do not involve DMSO. Finally, there is one important systematic feature between the parameterized and comprehensive mechanisms. P_1 and P_2 are comparatively much lower in the upper troposphere than C_1 and C_2. These patterns of disagreement do not resemble the zonal temperature profile as was noted for the P_1- and P_2-based SO_2. Rather, these patterns are similar to the annual zonal and vertical OH profile. In P_1 and P_2, MSA is a direct product of OH oxidation reactions, whereas MSA production in C_1 and C_2 occurs through non-OH-based reactions of intermediary species. The MSA in the comprehensive mechanisms, therefore, is less sensitive to gradients in OH.

Annual-Column Burdens The annual zonal and vertical mole fraction profiles in the previous section are useful for diagnosing differences between the mechanisms because of the strong gradients in annual-average temperature and OH with latitude and altitude. There may also be large differences at a given latitude, however, because DMS emissions have important longitudinal variations. These longitudinal variations may highlight potential locations for future observations of the DMS-related species that can distinguish between the four mechanisms. On this note, the annually-averaged column burdens of DMS, SO_2, MSA, and H_2SO_4 as functions of longitude and latitude using the C_1 mechanism are shown in Figure 5-7. As with the zonal and vertical profiles, the column burdens of the other three mechanisms are displayed as ratios relative to C_1 in Figure 5-8.

Referring to the C_1-based DMS column burdens in Figure 5-7, the most obvious features are the low/high DMS burdens over the continents/oceans, which are due to the lack of DMS emissions over land. Another obvious feature is the band of maximum values in the Southern Hemisphere high latitudes. This is caused by the peak DMS surface oceanic fluxes during the

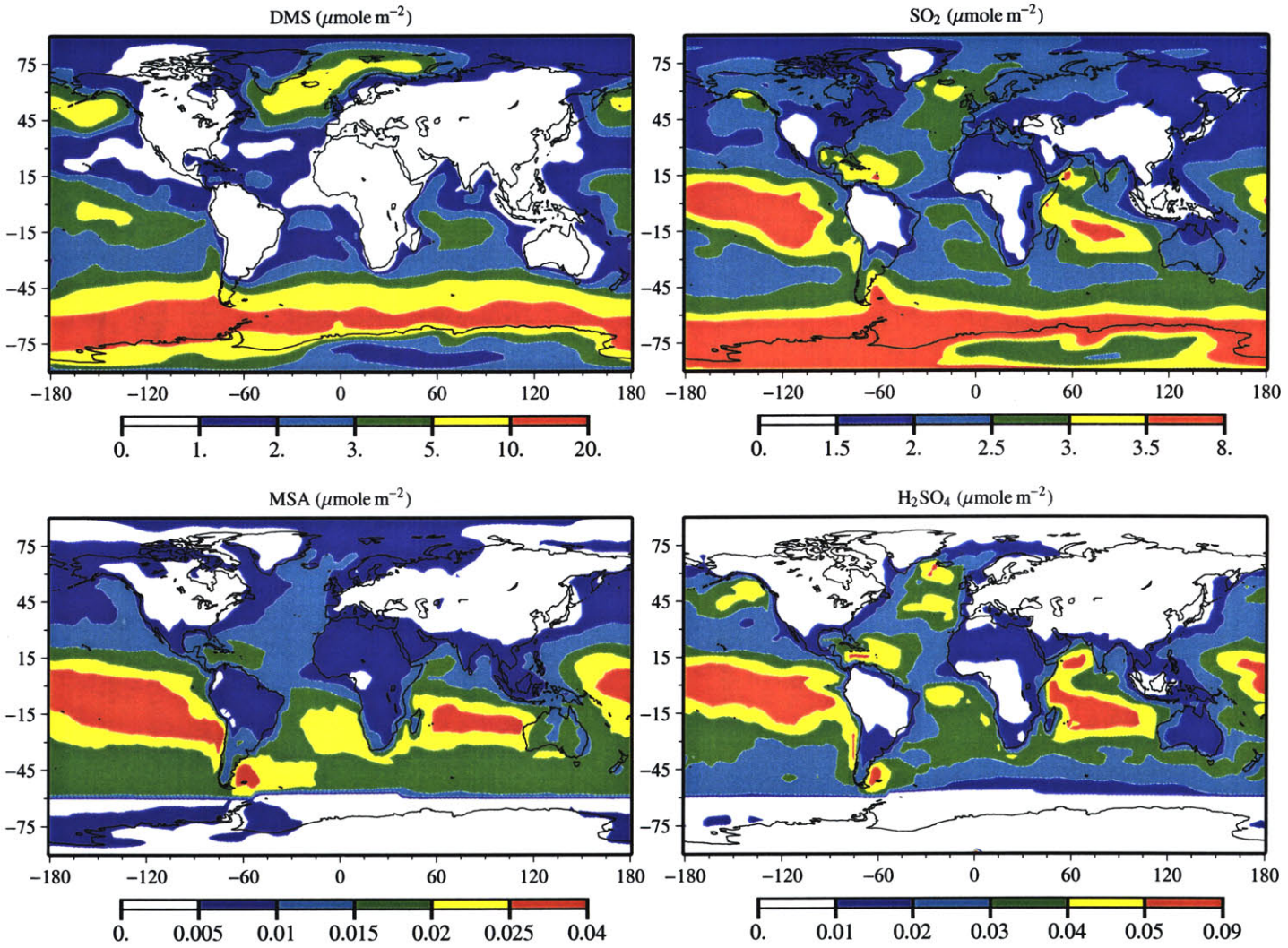

Figure 5-7: Annual average column burdens (μmole m^{-2}) of DMS, SO_2, MSA, and H_2SO_4 using the C_1 mechanism.

austral summer, as shown in Figure 5-1, and the relatively small high-latitude OH concentrations. Fairly large burdens are also found off the southeastern coast of Greenland. This local maximum is caused by the relatively large DMS surface fluxes that occur through most of the year in this area. Relative to C_1, the other mechanisms produce DMS column burdens that are quite similar. More specifically, the P_1 and P_2 DMS columns are within a factor of 1.3 of C_1 everywhere, while the C_2/C_1 ratio is nearly unity. These small differences largely reflect the slight differences in the initial DMS+OH rate constants used in the various mechanisms.

The C_1-based annual SO_2 column burdens in Figure 5-7 mimic the DMS column burdens, having maximum values in the high latitude Southern Hemisphere and minimum values over the continents. There is also a local SO_2 maximum in the equatorial Pacific, which results from the product of relatively large DMS surface fluxes and high OH levels. In addition, as noted for the annual-zonal SO_2 profile, the gradient between the minimum and maximum values is much less pronounced than the corresponding DMS gradient. This occurs because SO_2 has a longer lifetime than DMS. As for the other mechanisms, Figure 5-8 indicates that the SO_2 burdens from C_2 are nearly identical to those from C_1 everywhere. The burdens from P_1 and P_2, however, are similar to each other, but larger than the C_1 burdens by as much as a factor of two. The largest deviations of P_1 and P_2 from C_1 are found in the western equatorial Pacific. In terms of measurement locations, DMS-derived SO_2 over the equatorial Pacific may be useful for distinguishing between the parameterized and comprehensive mechanisms.

As was the case for DMS and SO_2, the C_1-based column burdens for gas-phase H_2SO_4 in Figure 5-7 have minimum and maximum values over land and sea, respectively. Contrary to DMS and SO_2, however, the largest H_2SO_4 burdens do not occur in the Southern Hemisphere because of the efficient scavenging by the GADS-prescribed polar aerosols. The maximum H_2SO_4 burdens occur over the equatorial Pacific and tropical Indian Oceans because of the significant levels of SO_2 and OH. Turning to the other mechanisms in Figure 5-8, the C_2/C_1 ratio for H_2SO_4 is less than a factor 1.1 globally (not shown on the scale in the figure), showing again that the comprehensive mechanisms are very similar to each other. Moreover, P_1 and P_2 are nearly identical to each other, but disagree significantly with C_1 and C_2 in the high-latitude oceanic regions. Some of these disagreements approach an order of magnitude. It is interesting to note that, relative to C_1, P_1 and P_2 overestimate SO_2 at the mid-to-high latitudes, but grossly underestimate H_2SO_4 there. This is the same behavior that was noted in the annual zonal profiles whereby P_1 and P_2 do not have the SO_2-independent H_2SO_4 production pathway used in the comprehensive schemes. Overall, these discrepancies suggest that gas-phase observations

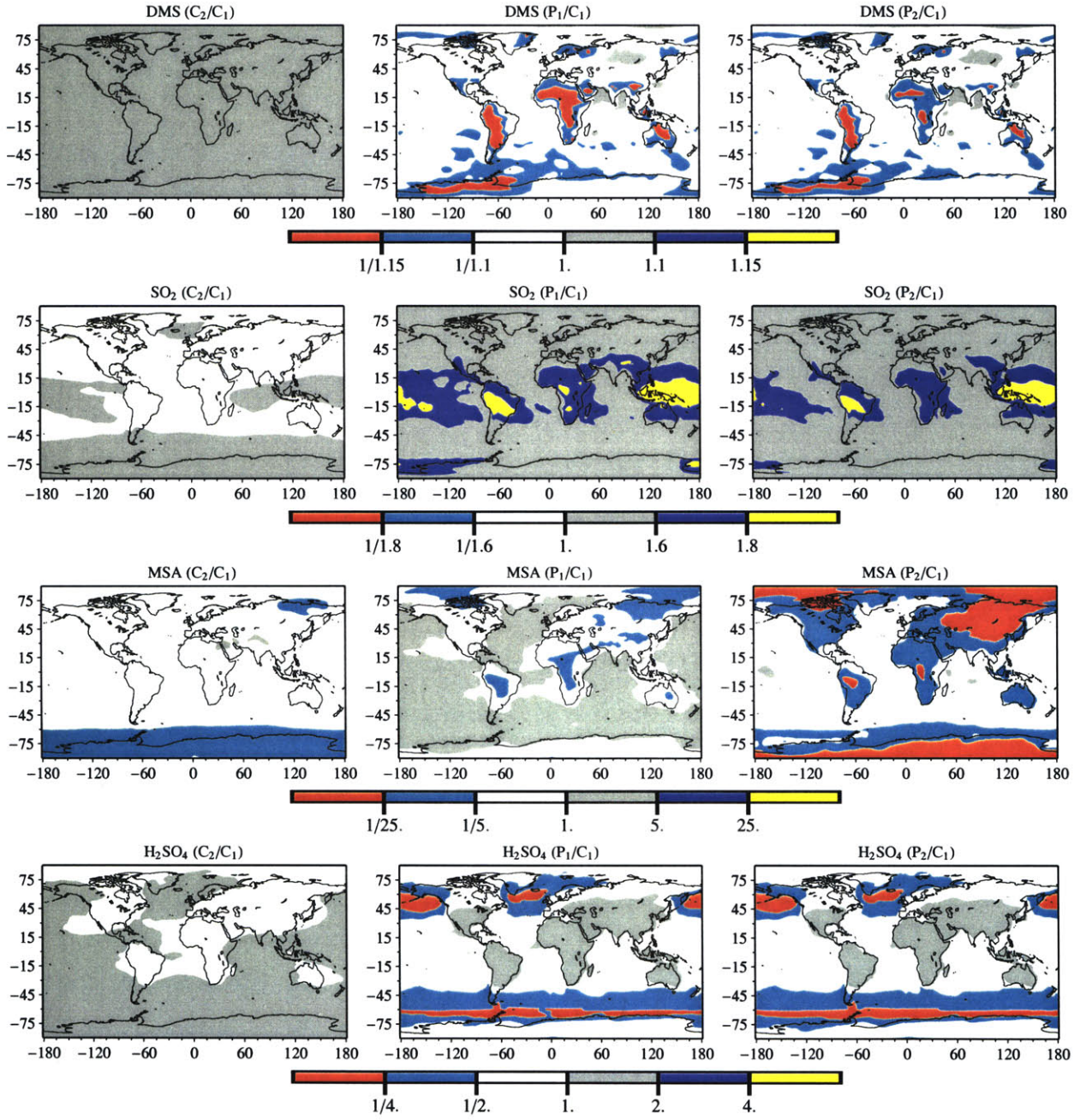

Figure 5-8: Annual average column burdens of DMS, SO_2, MSA, and H_2SO_4 using the C_2, P_1, and P_2 mechanisms. The burdens for these mechanisms are shown as ratios relative to C_1 (see Figure 5-7), where a value of 1.0 denotes perfect agreement.

of H_2SO_4 over the mid-to-high latitude oceans may be useful for testing some of the DMS oxidation pathways.

Lastly, the C_1-based annual column burdens of gas-phase MSA in Figure 5-7 closely match the trends for H_2SO_4. As with H_2SO_4, MSA has maximum burdens near the equator due to high photochemical activity and minimum values at the high latitudes in the Southern Hemisphere due to scavenging by polar aerosols. Relative to C_1, the MSA burdens using the other mechanisms have varying degrees of agreement over different regions. Over the open oceans, C_2 and P_2 are similar in that they have smaller MSA burdens, while P_1 tends to have larger burdens. Over the continents, excluding Antarctica and the boreal high latitudes, the C_2/C_1 ratio is close to one. Over the same continental regions, P_1 and P_2 have smaller MSA burdens by factors as large as 5 and 25, respectively. The similarities between C_2 and P_2 also extend to Antarctica and the surrounding oceans because both have large areas with smaller MSA burdens. As previously mentioned, the similarities between C_2 and P_2 is a result of their use of DMSO as a precursor to MSA. Considering the patterns of these ratios suggests the following MSA sampling strategy for distinguishing between the various mechanisms. Observations of MSA over Central Africa and South America, for instance, may be useful for distinguishing C_1 and C_2 from P_1 and P_2. Additional MSA observations at the high southern latitudes may be useful for differentiating C_1 and P_1 from C_2 and P_2, and hence the role of DMSO in the production of gas-phase MSA.

5.3.3 Implications for Aerosol Nucleation

Binary nucleation between gaseous H_2O and H_2SO_4 is an important source of secondary sulfate aerosols in the atmosphere (Raes and Van Dingenen, 1992; Easter and Peters, 1994; Pirjola and Kulmala, 1998). The creation of new H_2O-H_2SO_4 particles is described in terms of a nucleation rate that depends nonlinearly on temperature and the vapor-phase concentrations of H_2O and H_2SO_4. Because theoretical nucleation rates depend nonlinearly on H_2SO_4, small changes to the gas-phase concentration of H_2SO_4 can have a profound impact on the calculated formation rate of new particles in the atmosphere. The nucleation rate parameterization by Vehkamäki et al. (2002), for instance, has an approximately cubic dependence on the concentration of sulfuric acid at 236 K and 55% relative humidity. This translates into a factor of 10^3 change in the nucleation rate for a factor of 10 change in H_2SO_4 under these conditions. The goal of this section, therefore, is to quantify the changes to the nucleation rates for the differences in the H_2SO_4 concentrations from the four mechanisms.

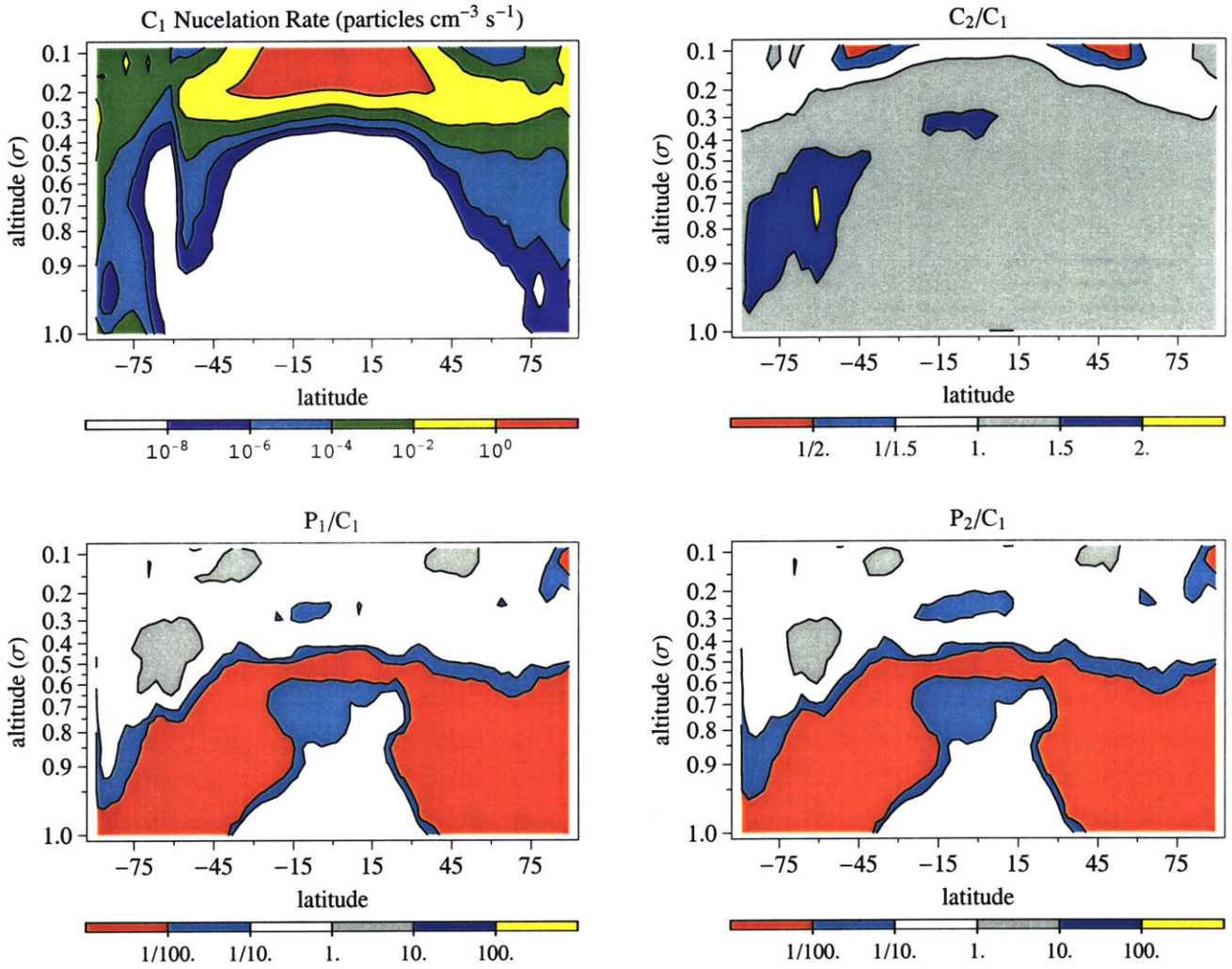

Figure 5-9: Annual zonal average profiles of H_2SO_4-H_2O binary nucleation rates as functions of latitude and altitude. The nucleation rates (particles cm^{-3} s^{-1}) using the C_1 are shown in the upper left. The nucleation rates for the other mechanisms are displayed as ratios relative to C_1. Altitude is shown using σ-coordinates. Refer to Figure 5-4 for the approximate altitude in km.

The most recent parameterization from Vehkamäki et al. (2002) is used to compute the H_2O-H_2SO_4 particle production rate. Their parameterization is designed for typical atmospheric conditions (temperature 230 to 305 K, relative humidity 0.01 to 100%) and is within the errors of experimental results at room temperature and relative humidities above 30%. This parameterization expresses the nucleation rate by

$$J_N = f(T, \text{RH}, N_{H_2SO_4}) \tag{5.17}$$

where J_N is the nucleation rate in particles cm^{-3} s^{-1}, T is the temperature in degrees K, RH is the relative humidity in percent, and $N_{H_2SO_4}$ is the gaseous sulfuric acid number density in molecules cm^{-3}. The nucleation rates have been calculated using the H_2SO_4 concentrations produced by the four mechanisms and the meteorological fields from NCEP. For consistency, the relative humidities were processed using the standard water vapor saturation subroutines in MATCH.

The latitude/altitude sensitivities of J_N to the four mechanisms are shown in Figure 5-9 as annual zonal averages. As with the previous comparisons, the C_1 mechanism is the reference case and the three other mechanisms are shown as ratios relative to C_1. Focusing on C_1, the nucleation rate peaks in the upper tropical troposphere and at high latitudes. These trends more closely mimic the zonal average temperature than the RH or H_2SO_4 concentrations. This, in turn, suggests that particle nucleation is most sensitive to temperature for the typical zonal distributions of T, RH, and H_2SO_4.

Considering the other three mechanisms, Figure 5-9 indicates that the nucleation rates using the C_2-generated H_2SO_4 are slightly larger throughout the mid-to-lower troposphere, but generally agree with C_1. Secondary particle formation, therefore, is relatively insensitive to the H_2SO_4 changes between C_1 and C_2. The H_2SO_4 concentrations from the parameterized mechanisms, however, yield nucleation rates that are many orders of magnitude lower in much of the mid-to-lower troposphere. These extreme differences are caused by smaller production rates of H_2SO_4 in P_1 and P_2, which lack the SO_2-independent H_2SO_4 production path. Although the uncertainties in the nucleation rate parameterization are already large, these results indicate that the uncertainties associated with the DMS oxidation mechanism also profoundly impact the calculated nucleation rates.

Finally, as a frame of reference, a value of J_N=1 particle cm^{-3} s^{-1} is typically used as a lower bound denoting significant particle production. Using this measure, Figure 5-9 indicates that H_2SO_4 derived from DMS using all four mechanisms only contributes to significant secondary

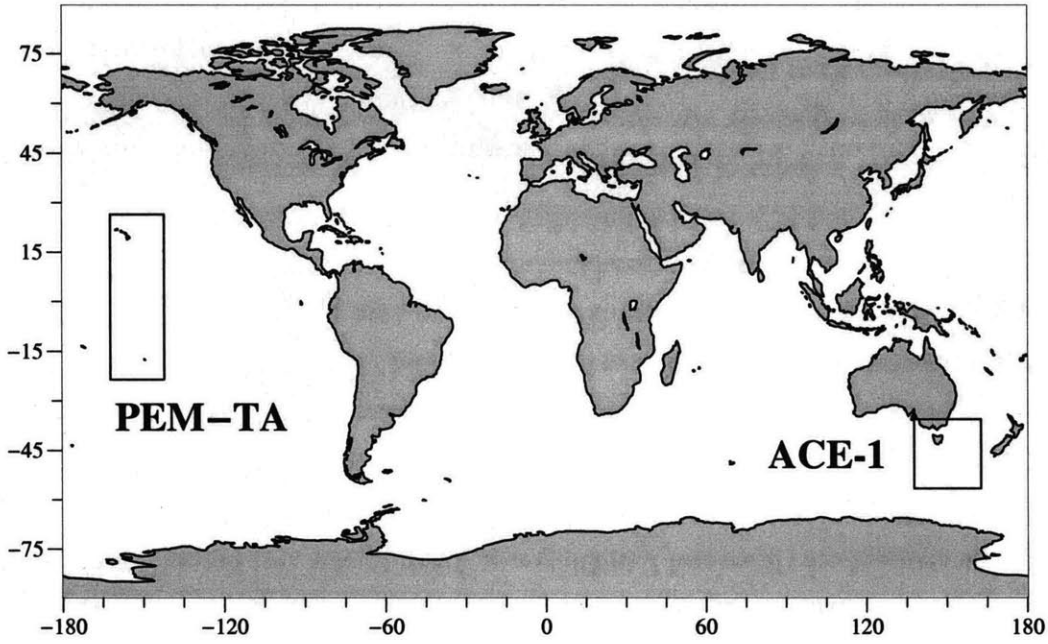

Figure 5-10: The focal regions of the ACE-1 and PEM-Tropics A measurement campaigns are shown in the rectangular areas. The high-time-resolution model output is compared to the observations within these rectangles.

aerosol formation in the tropical upper troposphere. Whether or not new particle production occurs in the remote marine boundary layer from DMS oxidation is a hotly contested issue. Some studies suggest that it can occur (Russell et al., 1994; Yoon and Brimblecombe, 2002), while others indicate that it does not (Raes, 1995; Cainey and Harvey, 2002). Clearly, this study agrees with the latter studies.

5.3.4 Comparisons With Campaign Measurements

The model predictions of gas-phase DMS, SO_2, MSA, and H_2SO_4 are compared with atmospheric observations made during the First Aerosol Characterization Experiment (ACE-1) and Pacific Exploratory Mission-Tropics A (PEM-TA) measurement campaigns. These two campaigns took place within a year of each other, featured some of the first atmospheric measurements of gas-phase MSA and H_2SO_4, and were located in distinctly different climatological regions of the remote marine atmosphere. The focal regions for these campaigns are displayed in Figure 5-10. Unless noted otherwise, all of the subsequent comparisons with ACE-1 and PEM-TA utilize the high-time-resolution output of MATCH in the two focal regions in Figure

5-10.[7]

In comparing to observations, previous versions of MATCH using observationally-based winds successfully simulated high-resolution time series of both long- and short-lived tracers.[8] To repeat that exercise here would require excellent knowledge of the sources and sinks of the DMS-related species. There are three factors, however, that severely limit the knowledge of these sources and sinks, which thus precludes the ability to recreate (without tuning) the high-resolution time series of DMS-related species. First, the DMS source is defined using monthly-mean, climatologically-derived DMS sea surface concentrations. Second, the photochemical sinks (for example, OH and NO_x) are limited to monthly averages. Third, the crude representation of multi-component aerosol distributions from GADS defines the crucial aerosol-based scavenging.

Due to these limitations, the main goal of this section is not to successfully reproduce the high temporal resolution features of the ACE-1 and PEM-TA measurements. Rather, the major goals are to: (1) check that the model in its various chemical mechanistic forms gives reasonable values for DMS, SO_2, MSA, and H_2SO_4; (2) quantify any large, systematic differences between the parameterized and comprehensive mechanisms; (3) determine the degree to which the observations can be used to differentiate between the four mechanisms.

Model-Observation Comparison Methodology

The subsequent model-observation comparisons are performed by interpolating the model values to the space-time coordinates of the measurements. Linear and cubic functions are used to interpolate the mole fractions in time and space, respectively, and logarithmic mole fractions are used to avoid non-physical negative values. Interpolations to the mobile measurement platforms –that is, the research vessel and aircraft– make use of the space-time coordinates of the meteorological observations rather than the DMS-related species. This results in better defined trajectories because the meteorological measurements were made at a higher-frequency than the data for the DMS-related species.

Another facet of the model-observation comparisons involves the estimation of an important error resulting from the coarse spatial resolution of the model. That is, given the spatially-inhomogeneous nature of the sources and sinks in the DMS cycle and the rather short lifetimes of many of the participating species, the gradients of the DMS-related quantities may be sub-

[7]That is, the model output with a time-resolution of 40 minutes.

[8]For example, see the ^{222}Rn and CCl_3F studies by Mahowald et al. (1997a,b).

stantial over dimensions comparable to the size of a grid-cell in MATCH. This creates a spatial 'mis-match' between the volume-averaged quantities produced by MATCH and the point measurements made during the campaigns. This mis-match error is estimated using

$$\Delta^2 = (\delta_x)^2 + (\delta_y)^2 + (\delta_z)^2 \tag{5.18}$$

where Δ is the error in the model-based value at a given point and δ_i is the gradient of the model value in the i-direction. The longitudinal and latitudinal gradients are estimated conservatively as differences in the model values between $x \pm 1.4°$ and $y \pm 1.4°$, which roughly corresponds to the horizontal dimension of a MATCH grid-cell. Altitude gradients are only used for comparing to aircraft measurements, where they are computed as the model differences between $z \pm 5$ hPa. Thus, five model-interpolated trajectories are computed for surface platform data, one for the mean value and four used to define the horizontal mis-match error. Likewise, seven model-interpolated trajectories are computed for the aircraft data.

Comparisons with ACE-1

ACE-1 was a large-scale, multi-platform measurement campaign whose one of many goals was to simultaneously observe many components involved in sulfur cycling in the pristine marine atmosphere. A comprehensive overview of the ACE-1 campaign is presented by Bates et al. (1998a). The ACE-1 operations were carried out during the austral summer in 1995 with measurements focused in the region shown in Figure 5-10. This region provided a clean atmosphere that was relatively free of continental contamination, and had fairly large DMS fluxes resulting in relatively large amounts of DMS oxidation products. Among the various measurement platforms employed during ACE-1, four are most relevant to this study. Two of these are the surface stations at Cape Grim, Tasmania (40.7° S, 144.7° E) and Macquarie Island (54.5° S, 159.0° E). Unfortunately, only measurements of DMS are available at these two sites. The other two ACE-1 platforms are mobile and include the research vessel *Discoverer* and NCAR C-130 aircraft. Simultaneous measurements of DMS and SO_2 were made aboard the *Discoverer*, while gas-phase measurements of DMS, SO_2, MSA, and H_2SO_4 were taken aboard the C-130. The spatial coverage of the land surface, shipboard and aircraft platforms during ACE-1 are shown in Figure 5-11.

ACE-1 – *Discoverer* – DMS Surface Fluxes De Bruyn et al. (1998) measured the concentrations of DMS in the ocean and atmosphere aboard the *Discoverer* during ACE-1. Bates

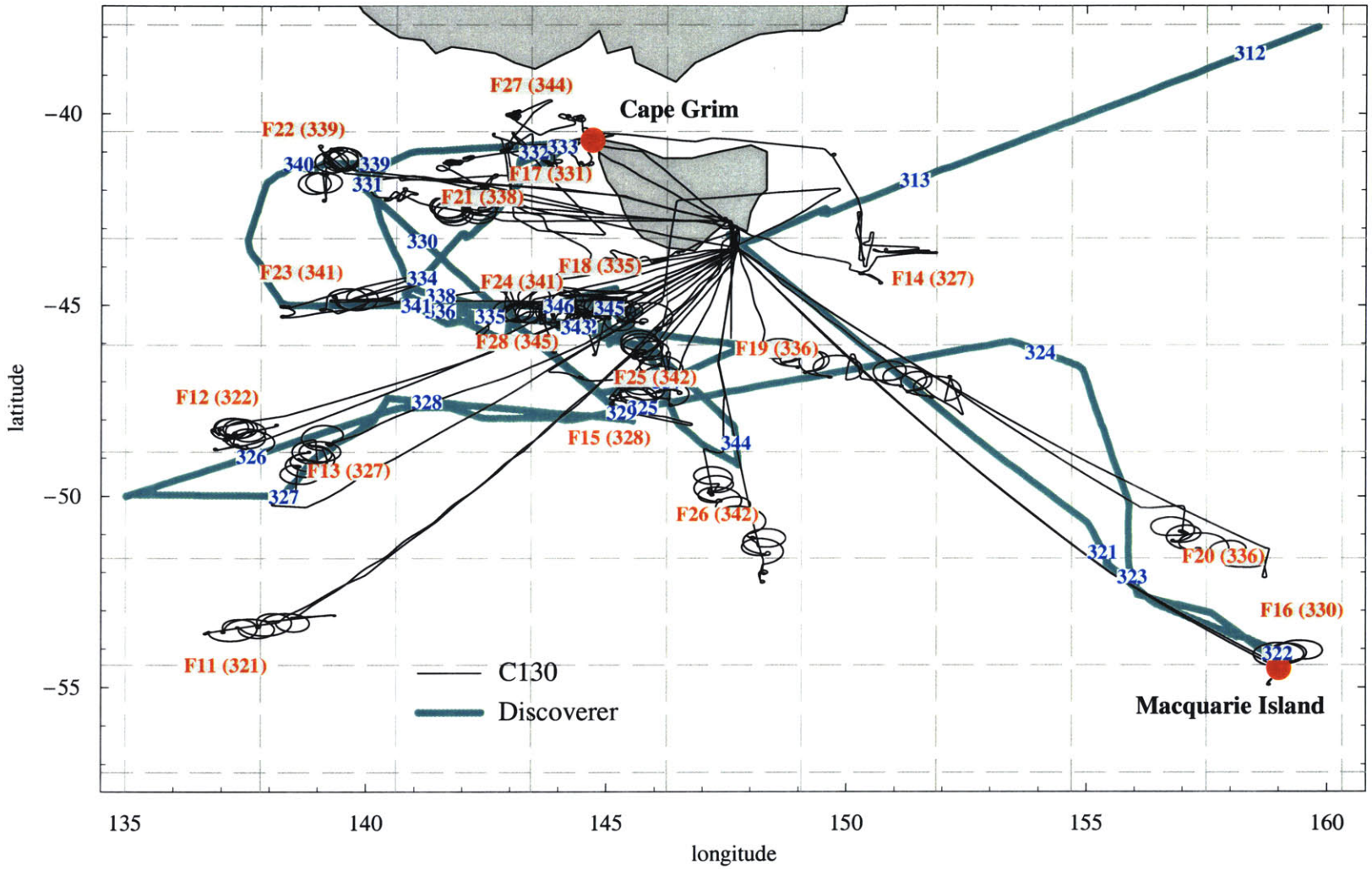

Figure 5-11: Relevant measurement platforms in the focal region of ACE-1. The surface stations at Cape Grim and Macquarie Island are shown by the red dots. The *Discoverer*'s ship track is shown in blue with its position in time noted by the blue numbers (day of year). The C-130 aircraft flight trajectories are shown in black with the flight numbers and take-off times (day of year) noted by the red numbers. The intersections of the dashed lines show the grid points in MATCH.

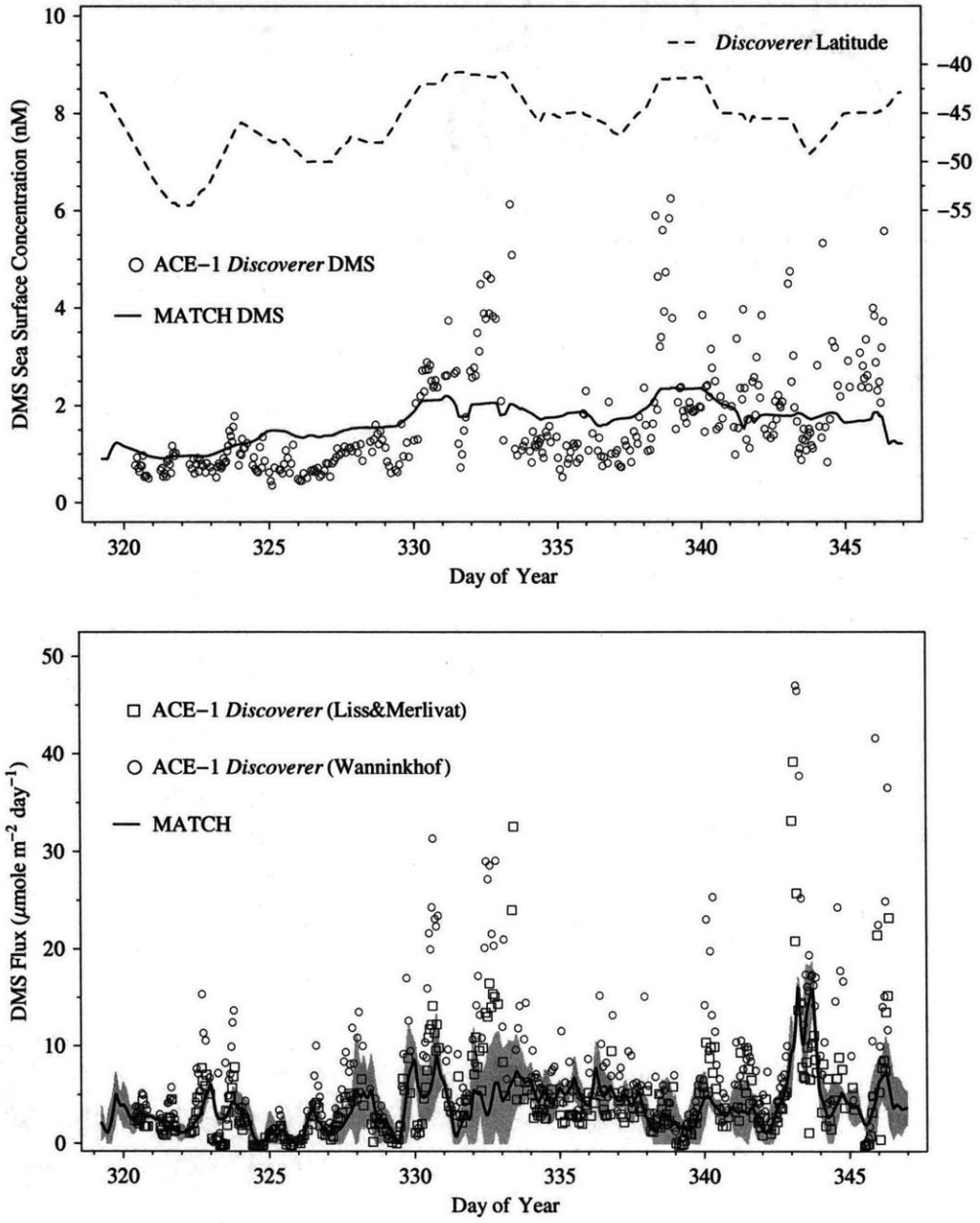

Figure 5-12: Observed and modeled DMS sea surface concentrations and sea-to-air fluxes versus day of year along the *Discoverer* ship track during ACE-1. The model-based sea surface concentrations are interpolations from Kettle et al. (1999). The modeled fluxes are interpolations using the P_2 mechanism. The estimated spatial mis-match errors for the fluxes are shown in gray. Observationally-based fluxes are shown using the Liss and Merlivat (1986) and Wanninkhof (1992) transfer velocity parameterizations. For reference, the latitude of the *Discoverer* is shown by the dashed line in the upper figure.

et al. (1998b) used these oceanic DMS measurements, along with observations of the surface wind speed, to estimate the sea-to-air flux of DMS for the two most common parameterizations of the transfer velocity (Liss and Merlivat, 1986; Wanninkhof, 1992). The measurement-based DMS sea surface concentrations and DMS surface fluxes are shown in the upper and lower panels in Figure 5-12, respectively. For comparison, the model-based DMS sea surface concentrations and surface fluxes are also shown in the figure. The model values are interpolations onto the *Discoverer* ship track using the previously described methodology. The model fluxes are shown only for a single mechanism case (P_2) as the DMS surface fluxes are nearly invariant between the four mechanisms. Also note that the model-prescribed DMS sea surface concentrations vary smoothly with time because they are derived from monthly-mean fields, while the model-based DMS fluxes have higher frequency fluctuations through the action of the surface wind forcing using the 6-hourly NCEP archives.

As shown, the model-prescribed DMS sea surface concentrations are mainly within a factor of 2 of the *Discoverer* observations, although the large oceanic DMS concentrations near days 332 and 339 are not captured by the monthly-mean fields. As shown in Figures 5-11 and 5-12, the *Discoverer*'s ship track indicates that these large DMS sea surface concentrations occur when the vessel is near Tasmania. An oceanographic boundary between subtropical and subantarctic water was identified during ACE-1 just south of Tasmania (Bates et al., 1998b; Griffiths et al., 1999), and the Kettle et al. (1999) fields do not capture the DMS sea surface concentration changes across this boundary.

Regarding the sea-to-air DMS fluxes, the model values are also typically within a factor of two of the observations when considering the spatial mis-match errors. Furthermore, the model captures much of the variability in the measurement-based DMS fluxes, particularly the fluctuations between days 324-329 and 338-344. The peaks of these modeled fluxes, however, have smaller magnitudes than the observations because of the underestimated DMS sea surface concentrations. Overall, the modeled DMS surface fluxes are fairly consistent with the measurement-based values aboard the *Discoverer*, so no adjustments are made to the DMS sea surface concentrations. Also, as the next section shows, the fluxes using the Liss and Merlivat (1986) parameterization yield a better a fit to atmospheric DMS mole fractions, which is why this transfer velocity is used in equation 5.2.

ACE-1 – *Discoverer* – Atmospheric DMS and SO_2 The model-interpolated and measured DMS atmospheric mole fractions along the *Discoverer* ship track are displayed in the top panel of Figure 5-13. Recall that the OH concentrations from von Kuhlmann (2001) have

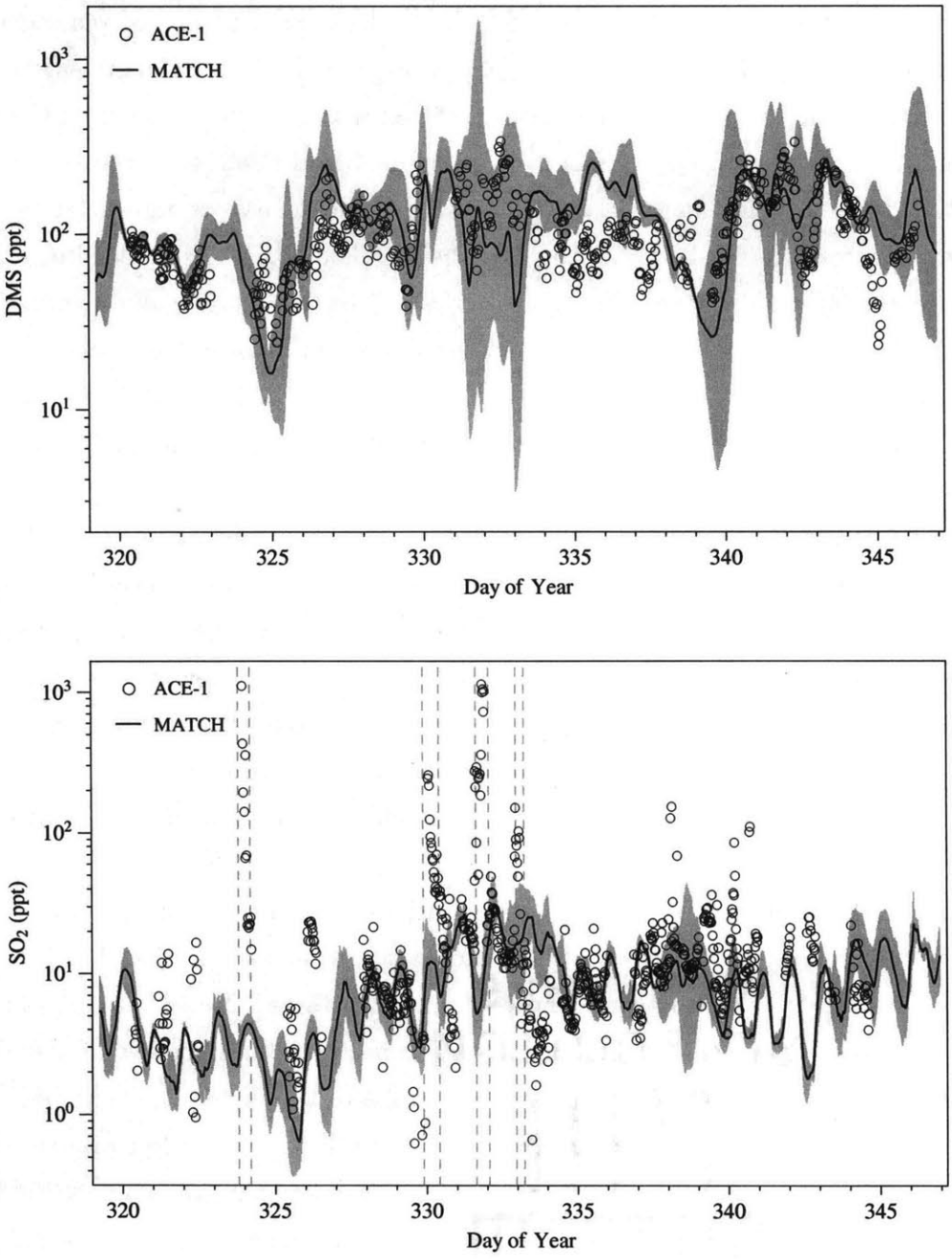

Figure 5-13: Observed and modeled atmospheric mole fractions (parts per 10^{12}, ppt) of DMS and SO_2 versus day of year along the *Discoverer* ship track during ACE-1. The observations are shown using open circles, the interpolated C_1-based model values are shown by the black lines, and the estimated model mis-match errors are shown as the gray shaded areas. Known periods of large continental and ship exhaust contamination for SO_2 are indicated by the vertical gray dashed lines.

been increased uniformly by a factor of 1.5. Without this adjustment, the modeled DMS mole fractions in Figure 5-13 would be larger by this amount. In addition, using the transfer velocity of Wanninkhof (1992) instead of Liss and Merlivat (1986) would increase the modeled DMS mole fractions by a factor of 2.

Using the scaled OH fields and Liss and Merlivat (1986) transfer velocity, the modeled DMS mole fractions along the *Discoverer* ship track are typically within a factor of 2 to 3 of the observations. Note that only the modeled DMS mole fractions using C_1 are shown because the four mechanisms produce similar levels of DMS in the atmosphere. In spite of the fairly good agreement, many of the DMS observations lie outside of the estimated error range. These discrepancies are attributable to differences between the prescribed and actual DMS sea surface concentrations, near-surface OH concentrations, or dynamical effects. Between days 324-329, for instance, the modeled DMS surface fluxes in are in agreement with observations, yet MATCH tends to overestimate the DMS mole fractions near day 327. This suggests that the model-based OH concentrations or ventilation from the boundary layer may be too low during this period. Aircraft observations of OH are used to analyze this feature in more detail in a following section. The larger modeled DMS mole fractions near day 336, however, appear to be due to prescribed DMS sea surface concentrations that are too large because the corresponding DMS fluxes in the model are also too large. To achieve a better fit between the model and observations, therefore, requires fine-scale adjustments to the DMS sea surface concentrations and concentrations of oxidants. There are two final comments worth mentioning. First, the large fluctuations in the modeled DMS mole fractions are strongly associated with latitude. Between days 337 to 340, for example, the *Discoverer* traversed 10 degrees in latitude (see the top panel in Figure 5-12). Second, the exceptionally large model mis-match errors (the gray shaded area) on days 331-333 and 339-340 occur when the *Discoverer* is in close proximity to land, and thus is a consequence of the large horizontal gradients in DMS mole fractions between land and sea.

De Bruyn et al. (1998) also measured the atmospheric concentrations of SO_2 aboard the *Discoverer*. These observations are displayed in the bottom panel in Figure 5-13, along with the modeled SO_2 mole fractions. As with DMS, only the C_1-based SO_2 mole fractions are shown because the other mechanisms yield similar levels of SO_2. Compared to the DMS model-observation comparisons, there are three notable differences for SO_2. First, the modeled mole fractions for SO_2 are more periodic than those for DMS because the SO_2 source in this model is solely photochemical. Second, the estimated model errors are much smaller for SO_2 because its longer lifetime and non-localized photochemical source leads to smaller atmospheric gradients.

Third, even though there is a reasonable level of agreement between the measured and modeled SO_2 mole fractions, many of the SO_2 observations exceed the model by a factor of 10 or more. The most extreme examples occur on days 324 and 332. Several large ^{222}Rn episodes were observed aboard the *Discoverer* (Whittlestone et al., 1998; Bates et al., 1998b), which implies that the SO_2 is of continental origin on days 330, 332, and 333. Because the runs of MATCH used here do not include anthropogenic sources of SO_2, these events are naturally not captured. The remaining events at days 324, 338, and 340 do not appear to be attributable to continentally-influenced SO_2 because the radon levels are low. Other than a few spurious measurements most of the observed and modeled SO_2 mole fractions at days 338 and 340 agree to within a factor of 2 to 3. The large model-observation discrepancy on day 324 has been identified as a period of ship exhaust contamination (De Bruyn et al., 1998).

ACE-1 – Surface Stations

Cape Grim The observed and modeled DMS mole fractions at the Cape Grim, Tasmania surface station during ACE-1 are shown in the upper panel in Figure 5-14. As before, only the C_1-based mole fractions are displayed because the four mechanisms yield nearly identical levels of DMS. First, note that the estimated model mis-match errors are very large at Cape Grim because of its location and highly variable winds. The station is in close proximity to two land masses with negligible DMS emissions (Australia and Tasmania), the Bass Strait with relatively small emissions, and the open Southern Ocean with fairly large emissions. Subtle shifts in the winds, therefore, bring air masses with dramatically different mole fractions of DMS. This causes large horizontal gradients in the DMS mole fractions when traversing away from Cape Grim by the length of a model grid box. These model errors at Cape Grim can be reduced by running MATCH at a higher spatial resolution.

Considering these rather large estimated model errors, the model does not disagree statistically with the observations throughout the time-series except for the early period between days 321-323. This period of disagreement is most likely due to some combination of overpredicted model fluxes and underpredicted OH concentrations. Unfortunately, the *Discoverer* was not near Cape Grim during this period, so the oceanic DMS fluxes near Cape Grim cannot be quantitatively assessed. Qualitatively, however, a potential explanation involves temporal changes in DMS sea surface concentrations related to the onset of a phytoplankton spring bloom. Aboard the *Southern Surveyor* research vessel Jones et al. (1998) measured mean DMS sea surface concentrations of 0.3 nM near Cape Grim on days 322-323. Just over one week later (days 331-333),

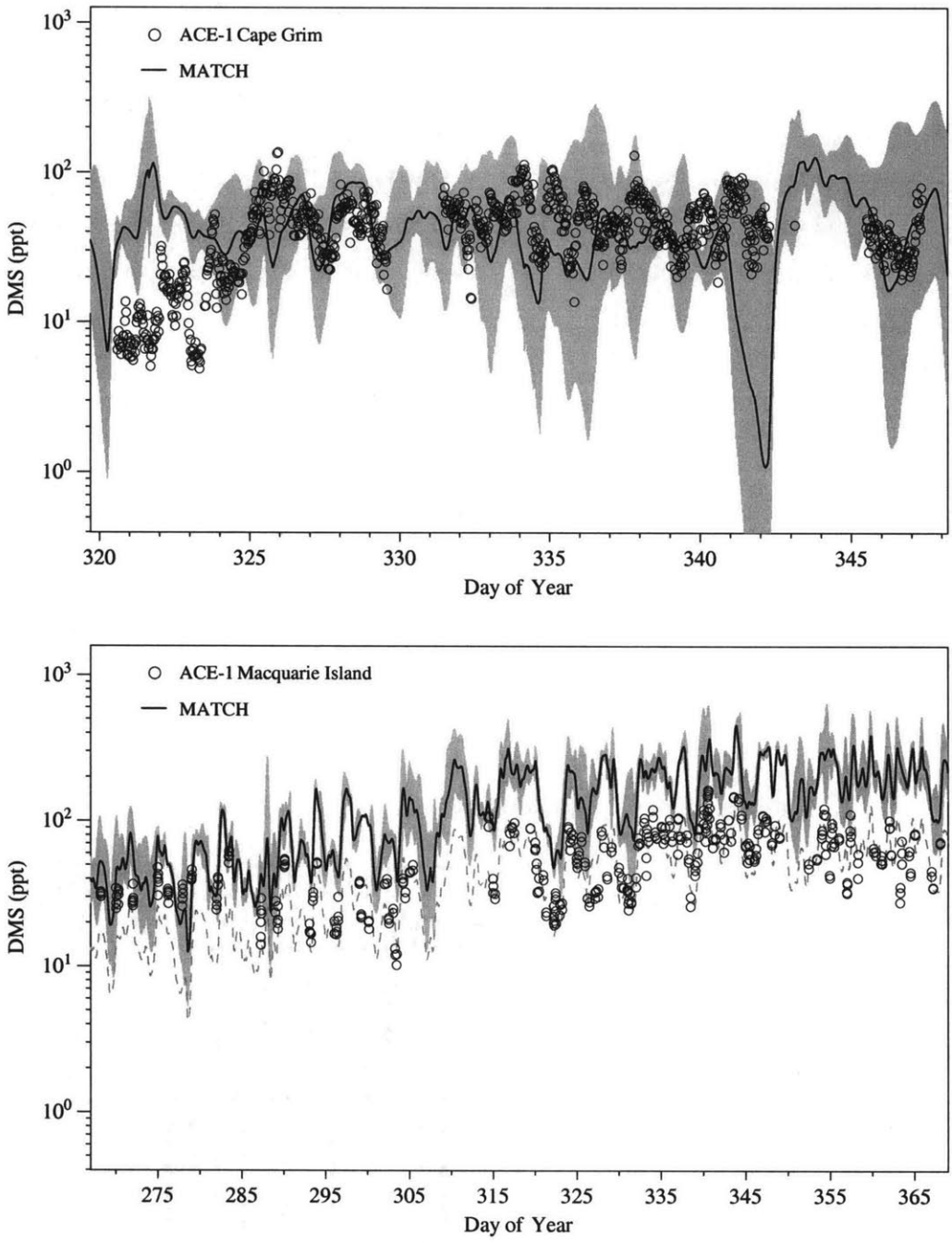

Figure 5-14: Observed and modeled mole fractions (ppt) of DMS versus day of year at Cape Grim, Tasmania and Macquarie Island during ACE-1. At Cape Grim the model errors are estimated by calculating the DMS gradients in only two directions (west and south) to avoid large continental-influences. Refer to Figure 5-13 for further explanation of the plot symbols.

the *Discoverer* measured mean sea surface concentrations of 2.84 nM in the same region. The monthly-mean Kettle et al. (1999) fields do not resolve this factor of 10 increase during this time period. As another possible resolution to this dilemma, Hainsworth et al. (1998) noted the passage of a synoptic front over Cape Grim on days 324-325. This front shifted the winds from having a Tasmanian origin to a marine-based origin, and hence potentially explains the large increase in the observed (but not modeled) DMS mole fractions. Although an analysis of the NCEP fields at Cape Grim during this period indicates that the model does seem to resolve this frontal event, slight differences in the actual versus archived wind speed and direction could contribute to the model overprediction.

Lastly, we note that the observed DMS mole fractions on days 341-342 remain steady in time, while the model interpolated-mean values fall and rise by more than an order of magnitude. The model behavior is caused by the NCEP wind speed, which in turn affects the model-calculated flux of DMS. Both the model-based and observed wind speeds were low on these days (< 8 m s^{-1}) (Whittlestone et al., 1998), which favors locally-emitted DMS over convergence of DMS due to long-range transport. Yet, the model-based wind speed was consistently lower than the observations, in some cases by as much as 6 m s^{-1}. This causes the locally-modeled DMS flux, and hence atmospheric mole fractions, to be 10 times smaller because the transfer velocity in equation 5.2 depends non-linearly on wind speed.

Macquarie Island The observed and modeled DMS mole fractions at Macquarie Island are displayed as a function of day of year in the lower panel of Figure 5-14. The observed DMS mole fractions were measured and partially analyzed by Brechtel et al. (1998). Notice that the Macquarie Island observations have a lower frequency and a longer duration relative to those at Cape Grim. Also note that there are two model-based time-series in the figure, one corresponding to a reference run using the C_1 mechanism and another where the mole fractions from the reference run have been reduced by a factor of three. Regarding the small estimated model errors, the horizontal mole fraction gradients for DMS are much smaller at Macquarie Island because of its remote location and relatively steady westerly winds. These smaller estimated model errors (if correct) are useful because they expose a systematic difference between the modeled and observed mole fractions. Although the reference case agrees with the observations during the first two weeks in the time-series, it is larger by a statistically significant factor-of-3 amount thereafter. This is clearly shown by the modeled time-series with the above factor-of-3 decrease, which is in excellent agreement with the observations for the majority of the time period.

The *Discoverer* was in close proximity to Macquarie Island on day 322 (see Figure 5-11), so the measurements from that period may shed some light on this apparent positive model bias. From Figures 5-12 and 5-13, the modeled and measurement-based DMS fluxes and atmospheric mole fractions match very well during day 322 aboard the *Discoverer*, and thus the same positive model bias is not present then and there. Between days 321.62 to 322.46 the *Discoverer* was within half a degree latitude and longitude of Macquarie Island, and over this period the modeled mole fractions at the two platforms were comparable with both ranging between 50-80 ppt. The observed mole fractions, however, drastically differ from each other. Aboard the *Discoverer* the measurements varied between 40-100 ppt, while at Macquarie Island they were 2 to 3 times lower (20-30 ppt). Thus, there seems to be an important feature at Macquarie Island other than its longitude and latitude that is not represented in the model. Regarding altitude, both platforms measured DMS at roughly the same height, so that is not a factor. Moreover, the wind directions were generally similar at the two platforms (Whittlestone et al., 1998), so they sampled comparable air masses. Unfortunately, the discussions of the atmospheric DMS measurements at Macquarie Island (Brechtel et al., 1998) and on the *Discoverer* (De Bruyn et al., 1998) do not comment on this discrepancy, and so a straightforward answer remains elusive.

ACE-1 – C-130 The NCAR C-130 aircraft participated in 33 missions during ACE-1. Of these, flight numbers F11-F28 occurred within the focal region in Figure 5-11 and took place between November 17 and December 11 (days 321-345). Considering the four ACE-1 measurement platforms, the observations from the C-130 aircraft provide the most useful diagnosis of the DMS mechanisms for three major reasons. First, the gas-phase concentrations of DMS, SO_2, MSA, and H_2SO_4 were simultaneously monitored. Second, the C-130 instruments had higher sampling frequencies, resulting in larger datasets. Third, the C-130 covered a larger spatial domain and encountered a larger variety of conditions.

In spite of these clear advantages, there are inherent difficulties in comparing the relatively coarse model output with the highly-transient nature of the aircraft-based measurements. For this reason, the high-frequency observations are not compared directly with the model results as was done for the other ACE-1 platforms. Rather, the model output and aircraft observations are compared for the following three important sets of space and time averages: (1) boundary layer values averaged over individual flights; (2) vertical profiles averaged over all of the flights in the intensive ACE-1 region; (3) composite diurnal profiles of important time-varying species.

Note that averaging over the aircraft flights adds a degree of variability in the aircraft-based

comparisons. This variability is defined by σ_{traj}, which is the standard deviation of the model-interpolated values or observations along the aircraft trajectory. This variability is directly shown for the observations as σ_{traj}, and for the model output it is added in quadrature to equation 5.18 using $(\Delta^2 + \sigma^2_{\text{traj}})^{1/2}$. Also note that all four DMS mechanism cases are shown in the following comparisons.

Boundary Layer The observed and modeled boundary layer average mole fractions of DMS and SO_2 for the individual ACE-1 flights are shown in Figure 5-15. Note that the model averages have larger uncertainties than the observations primarily because of the estimated spatial mis-match error of the model. In light of these large uncertainties, the modeled DMS mole fractions in the boundary layer agree with the observations for all of the flights except F13 and F25, which disagree by about a factor of two. Note also that the comprehensive and parameterized DMS mechanisms are nearly identical, but the parameterized schemes have slightly smaller DMS mole fractions. Overall, the generally good agreement for DMS suggests that the surface fluxes and boundary layer OH concentrations are consistent over a wide portion of the intensive ACE-1 region.

As for the model overestimates of DMS during F13, the measurements from the *Discoverer* on day 327 can be compared with F13 because both platforms were in the same vicinity at the same time. From Figure 5-13, the modeled DMS mole fractions near day 327 on the *Discoverer* were too large by roughly the same amount relative to the observations as computed during F13, so the two model results are wrong but consistent. The previous discussion for the *Discoverer* observations implicated low model-based OH concentrations or boundary layer ventilation as the most likely sources for this overestimation. Note that OH concentrations were measured aboard the C-130 (see Figure 5-18), and during F13 the average near-surface OH concentration ($\sigma > 0.95$ and $z \lesssim 500$ m) is 3.7×10^5 molecules cm^{-3} (Mauldin III et al., 1998). The corresponding model-prescribed value is roughly 6.6×10^5 molecules cm^{-3}, which exonerates OH as the cause of the excessive model-calculated DMS mole fractions. Dynamically, F13 was characterized by heavy clouds and a large mixed-layer depth that ranged between 1280 and 4300 meters as recorded in the ACE-1 flight records. The boundary layer height in MATCH, on the other hand, never exceeds 1000 meters in the same region and during the same time as this flight, which is indicative of inefficient boundary ventilation.

Turning to F25, the model again predicts larger DMS mole fractions relative to the observations. This time, however, the OH concentrations prescribed in the model appear to be too low. The F25 average over the measured near-surface OH concentrations is about 6×10^4 molecules

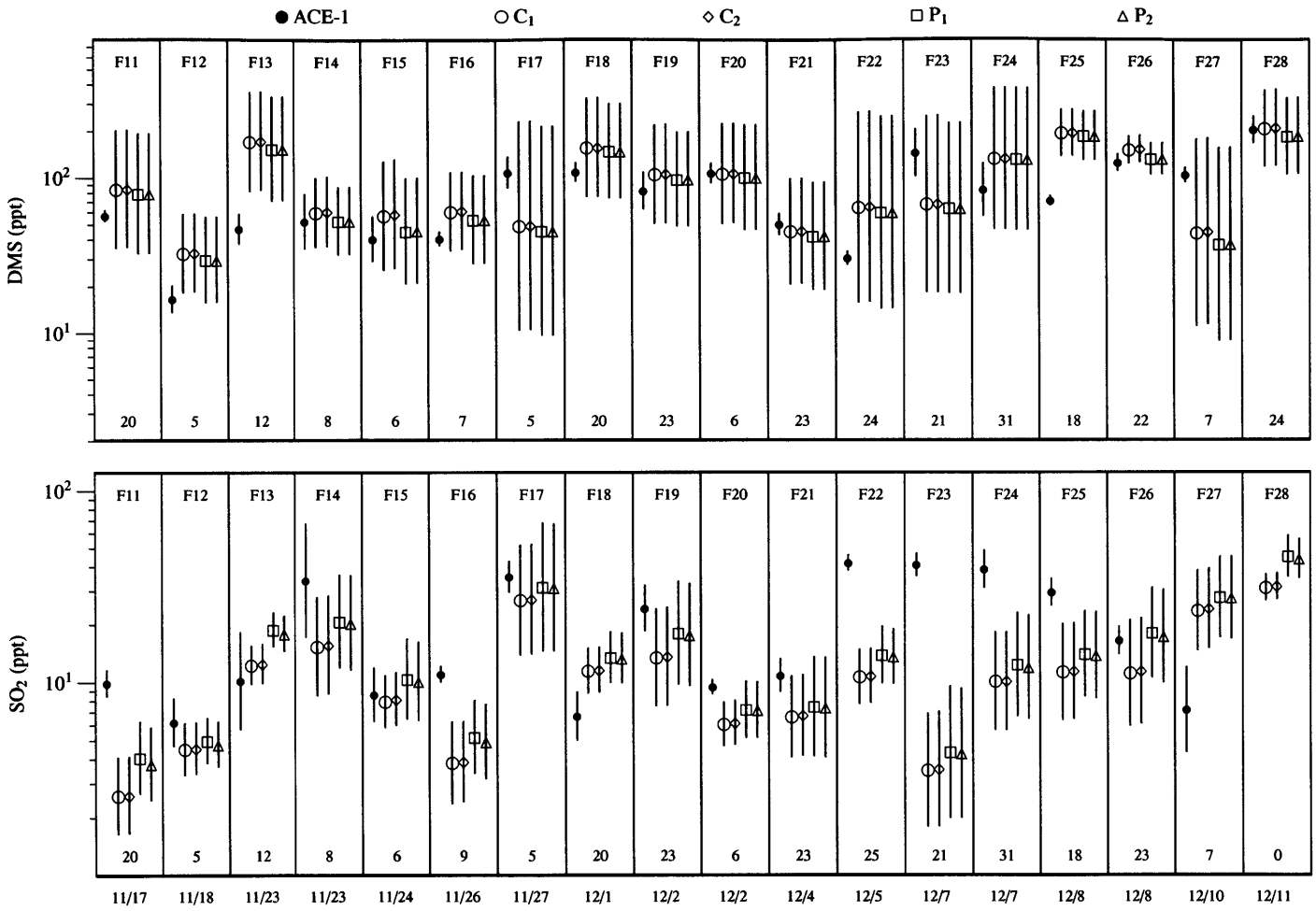

Figure 5-15: Observed and modeled boundary layer average mole fractions (ppt) of DMS and SO_2 for the individual ACE-1 flights. The observations and four model cases are noted by the symbols defined at the top of the figure. Vertical bars equal σ_{traj} for the observations and $(\Delta^2 + \sigma_{traj}^2)^{1/2}$ for the model. Individual flight numbers are labeled at the tops the boxes (for example, F11 equals flight 11). The number of boundary layer observations for each flight are shown at the bottoms of the boxes. The starting dates of each flight (UTC) are shown at the bottom of the figure. The boundary layer is taken to be $\sigma > 0.95$, which roughly corresponds to the lowest 500 m and the bottom 3-layers in MATCH.

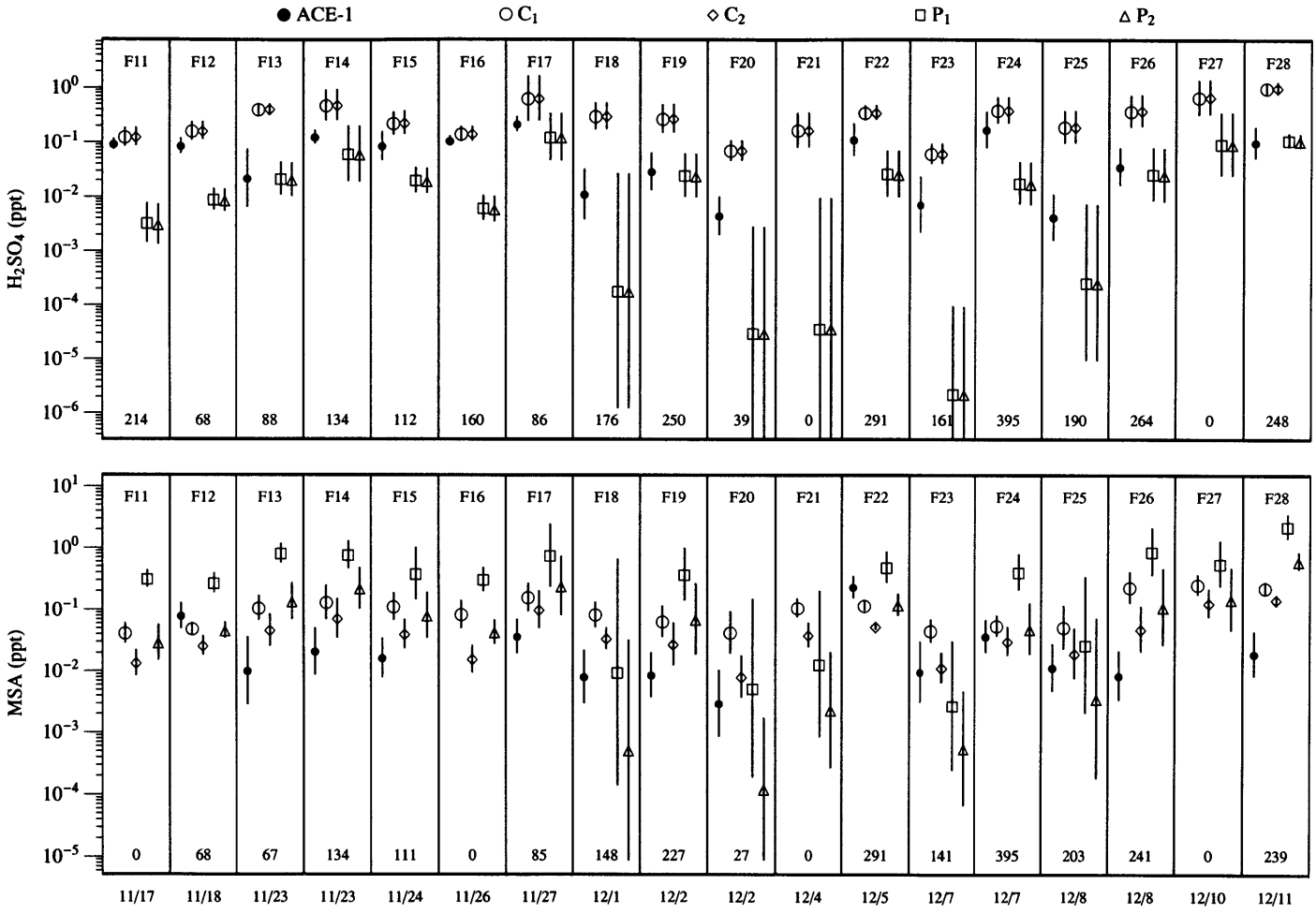

Figure 5-16: Same as Figure 5-15, but for H_2SO_4 and MSA.

cm^{-3}, and the corresponding model-based average is 100 times lower. These low values are due to the late starting time of the flight, which took off at approximately 18:00 local time. This sharp difference suggests that the model imposed OH cycle may change too rapidly near sunrise and sunset.

Unlike the excellent agreement for DMS displayed in Figure 5-15, the modeled boundary layer mole fractions for SO_2 do not agree with the observations on 7 out of the 17 flights that measured SO_2. Although most of these disagreements are within a factor of 2, the F23 observations exceed the model predictions ten-fold. Recall that the largest SO_2 mole fractions measured aboard the *Discoverer* were associated with continental pollution, which is not included in the model. Regrettably, radon was not measured aboard the C-130, so continental influences on the aircraft measurements of SO_2 are not readily identified. Back trajectories from the midst of the aircraft circles, however, suggest that of the flights recording larger SO_2 concentrations, perhaps only F25 encountered air of recent Australian origin.[9] For the remaining flights, the disagreements likely stem from many factors given the multiple sinks for SO_2 such as chemical oxidation, sea-salt scavenging, and dry deposition and the possibility that we have overestimated them. These poorly quantified multiple sinks make it difficult to pinpoint the exact sources of the discrepancies. As for F23, the aircraft was fairly close to the *Discoverer* at this time (day 341), and from Figure 5-13 the model similarly produced lower mole fractions of SO_2 than observed. Finally, it is worth pointing out that the comprehensive DMS mechanisms systematically predict lower levels of SO_2 than the parameterized cases. This feature was noted previously in Section 5.3.2, where it was ascribed to slightly different temperature-dependencies for the yield of SO_2.

The observed and modeled boundary layer average mole fractions of gas-phase H_2SO_4 and MSA for the individual ACE-1 flights are shown in Figure 5-16. Considering the four mechanism cases collectively with their estimated uncertainties, the model apparently performs well overall because MSA and H_2SO_4 both agree with the observations on all but one of the aircraft flights. The only disagreements occur on F28 for MSA and F23 for H_2SO_4. Considering the model cases separately, on the other hand, we must paint a different picture because of the large differences among the predictions with the various mechanisms. The H_2SO_4 observations, for instance, agree with the C_1 and C_2 mechanisms on 7 of the flights and P_1 and P_2 on 10 of the flights. This seems to imply that the parameterized mechanisms are a better fit to the H_2SO_4

[9]Back trajectories were analyzed for all of the ACE-1 measurement platforms and are available in the standard, distributed ACE-1 dataset. Examples of back trajectories at Cape Grim and Macquarie Island are found in Brechtel et al. (1998) and Whittlestone et al. (1998).

observations. This view is distorted though, because the modeled H_2SO_4 mole fractions from P_1 and P_2 are highly variable, while those from C_1 and C_2 appear to have a regular, positive offset. Thus, the comprehensive mechanisms are a better match to the boundary layer H_2SO_4 mole fractions if considering only their mean values. And, the variabilities of H_2SO_4 using C_1 and C_2 are more similar to the observed variabilities than using P_1 and P_2. Additionally, Figure 5-16 suggests that boundary layer observations of H_2SO_4 can potentially distinguish between the model cases if they are well-constrained given the large separation between the comprehensive and parameterized mechanisms.

The distinction between the comprehensive and parameterized mechanisms is not as clear for the boundary layer MSA mole fractions because there is no regular trend among the four model cases. The MSA mole fractions from P_1 and C_2 are typically the largest and smallest, respectively, but this is not always true. All said, this means that the boundary layer observations of MSA are not very useful for distinguishing between the four mechanisms. As far as which model cases are providing a better simulation, the MSA observations agree with C_1 and P_1 on 5 of the flights and with C_2 and P_2 on 11 of the flights. This suggests that the latter two mechanisms are better overall. But, as with H_2SO_4, the MSA mole fractions using the parameterized mechanisms are highly variable. Thus, the *mean values* of C_1 and C_2 provide a better match to the *mean values* of the observations. Also, the variabilities of MSA using C_1 and C_2 are more similar to the observed variabilities than using P_1 and P_2.

Vertical Profiles The observed and modeled vertical profiles of DMS, SO_2, MSA, and H_2SO_4 are shown in Figure 5-17. The vertical profiles are displayed as averages over all of the ACE-1 flights and within the lowest fourteen layers in MATCH, which spans the surface to about 7 km. Regarding DMS, the modeled mole fractions for the four mechanisms agree extremely well with the observations below 1.5 km. Above this level, however, the model-based DMS declines much more rapidly with altitude than the observations. The mid-tropospheric budget of DMS in the remote marine atmosphere is dominated mainly by vertical transport and oxidation with OH. The low modeled DMS mole fractions, therefore, are due to excessive OH concentrations, to inefficient transport from the lower troposphere, or to both. These two terms can be assessed because OH concentrations were measured aboard the C-130 during ACE-1. Vertical profiles of the measured and modeled OH concentrations are shown on the right side of Figure 5-18. This figure clearly shows that the model-based OH levels during ACE-1 are well within the observed variations and follow the observed vertical profile closely. This means that the large vertical gradients in the modeled DMS appear to be due to inefficient mixing

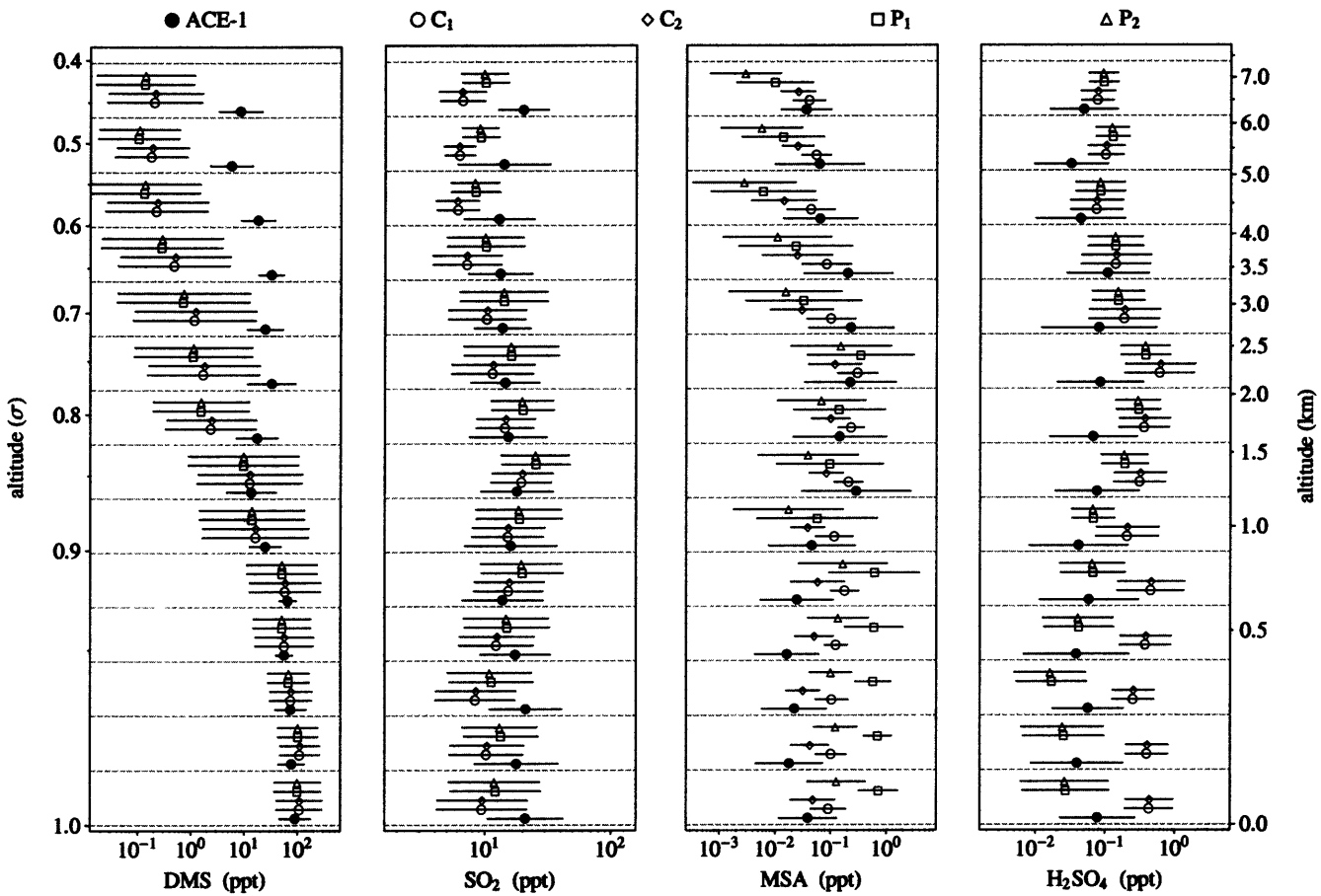

Figure 5-17: Observed and modeled vertical profiles of the mole fractions (ppt) of DMS, SO_2, MSA, and H_2SO_4 averaged over all ACE-1 flights. The symbols for the observations and four model cases are noted at the top. Vertical averaging is within the MATCH vertical grid layers, the interfaces of which are shown as the dashed gray lines. The altitudes are shown relative to the model interfaces with σ-pressure coordinates on the left and the approximate height in km on the right. The bottom-most values, for example, represent averages between $\sigma = 0.99$ and $\sigma = 1$. For MSA and H_2SO_4 the daytime observations and model values are selected for $0.4 \leq t \leq 0.6$, where t is the local fraction of the 24-hour day (0.5 is noon).

out of the lower troposphere. A similar 'surface-trapping' effect in the same transport version of MATCH has recently been encountered and is currently being diagnosed (Chen, 2003). Also note that MATCH has been used primarily for simulating continentally-emitted gases, so the vertical profiles above ocean-emitting grid cells have not been diagnosed before.

For SO_2, the four model-based mole fraction profiles are similar to each other and match the observations at all altitudes. The profiles for SO_2 do not have large vertical gradients compared to DMS because SO_2 is produced photochemically throughout the troposphere and has a longer lifetime for chemical loss. The SO_2 mole fractions from P_1 and P_2 are slightly larger than those from C_1 and C_2, but these differences are small and cannot be used to distinguish between the parameterized and comprehensive mechanisms. It is also interesting to note that the model-based SO_2 agrees with the observations even above the boundary layer where the modeled DMS was grossly underestimated. This probably occurs because SO_2 has a longer lifetime than DMS and is less sensitive to vertical mixing for the same reason that causes the shallow vertical SO_2 gradient. Hence, SO_2 is less prone to the boundary layer ventilation rate errors that plague DMS.

Turning to MSA, the model-based vertical profiles in Figure 5-17 display significant differences from one another. Within the boundary layer, the P_1-generated MSA is 10 times larger than from the other three mechanisms, while above the boundary layer the MSA from P_2 is much lower than the other cases. The MSA from the parameterized mechanisms consequently have steeper vertical gradients than from the comprehensive schemes. Compared to the measurements, the MSA mole fractions from C_1, C_2, and P_2 track the observations within their uncertainties, and overall the comprehensive schemes perform best. Given that the bulk of the MSA measurements are in the lower troposphere, the C_2 mechanism –which produces MSA through a reaction between MSIA and O_3– is closest to the observed profile. Also recall that the C_2 and P_2 mechanisms involve DMSO as an MSA precursor, while C_1 and P_1 do not. The vertical MSA profiles in the figure, however, can not differentiate between these mechanisms. Lastly, for reasons presumably similar to SO_2, the model-based MSA mole fractions do not have the large deficiencies in the mid-troposphere as noted for DMS.

Like MSA, the four model-generated H_2SO_4 mole fraction vertical profiles in Figure 5-17 exhibit large differences. Unlike MSA, these differences occur systematically between the comprehensive and parameterized mechanisms; specifically the H_2SO_4 profiles using C_1 and C_2 are larger than those using P_1 and P_2 from the lower to middle troposphere. The photochemical cause of this positive bias in C_1 and C_2 is related to the SO_2-independent production path, as

previously described in Section 5.2.3. This systematic bias implies that if the non-photochemical sources and sinks of H_2SO_4 are well constrained, then lower tropospheric observations of H_2SO_4 may help discern between the comprehensive and parameterized mechanisms. When compared to the observations in the boundary layer, the P_1 and P_2 profiles are too low and C_1 and C_2 are too large. Above the boundary layer, on the other hand, all four mechanisms converge. Overall, the P_1 and P_2 profiles have larger vertical gradients than both the observations and the comprehensive schemes, so in this sense C_1 and C_2 provide a better match to the observations.

H_2SO_4 and OH Diurnal Cycles and the OH Vertical Profile Of the sulfur-bearing species measured during ACE-1, H_2SO_4 has, by far, the largest diurnal cycle because its production is intimately linked with OH. MSA also has a diurnal cycle, though it is not as large (for example, see Figure 4-13 in Chapter 4). Furthermore, OH modulates the cycles of all of the DMS-related species to a certain degree because of the initial oxidation steps in the DMS mechanism. Thus, our final analysis of the ACE-1 measurements involves a comparison between the observed and modeled diurnal profiles of H_2SO_4 and OH. These diurnal profiles are displayed on the left side in Figure 5-18 and represent composite averages over all of the ACE-1 flights. The figure also shows the vertical profiles of the observed and model-based OH concentrations averaged over the ACE-1 flights. Regarding OH, the imposed cycle in the model (using equation 5.10) matches the observations fairly well, but it has a less pronounced noontime peak. Notice that without the scaling factor of 1.5 the modeled OH profile would not match the OH observations very well. Also, the OH variations are larger for the observations than the model presumably because the latter is derived from monthly-means.

For H_2SO_4, the four modeled cases all agree reasonably well with the observed cycle, but the difference between the model-based mole fractions using the comprehensive and parameterized mechanisms is obvious. Similar to the ACE-1 boundary layer assessments, the H_2SO_4 mole fractions from C_1 and C_2 are larger than those from P_1 and P_2. Furthermore, the nighttime H_2SO_4 mole fractions using the parameterized mechanisms are extremely variable, as exhibited by the very large estimated model errors during those times. Neither the observations nor the comprehensive schemes display the same extreme variability. This implies that, putting aside their slight positive bias at night, C_1 and C_2 give a better fit to the observations. These trends also indicate that additional observations of H_2SO_4 and its variability at night may help to differentiate between the comprehensive and parameterized mechanisms.

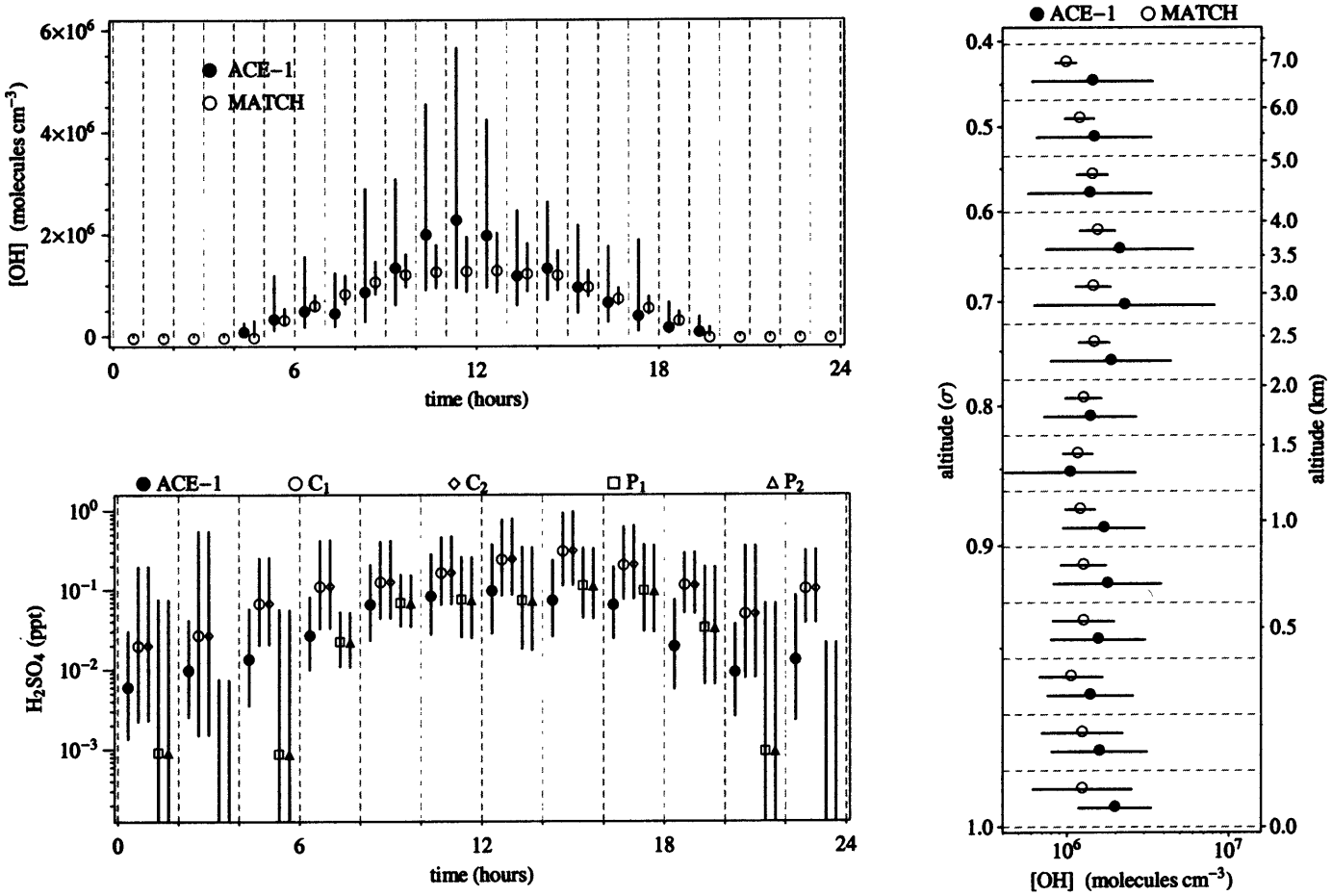

Figure 5-18: Observed and modeled diurnal cycles of H_2SO_4 mole fractions (ppt) and OH concentrations (molecules cm^{-3}) and the vertical profile of OH concentrations during ACE-1. The composite diurnal cycles are averages over all of the ACE-1 flights and are binned in 1-hour and 2-hour intervals for OH and H_2SO_4, respectively, as noted by the vertical dashed lines. The vertical profile for OH is similar to those described in Figure 5-17, but uses daytime OH concentrations selected for $0.35 \leq t \leq 0.65$, where t is the local fraction of the 24-hour day (0.5 is noon).

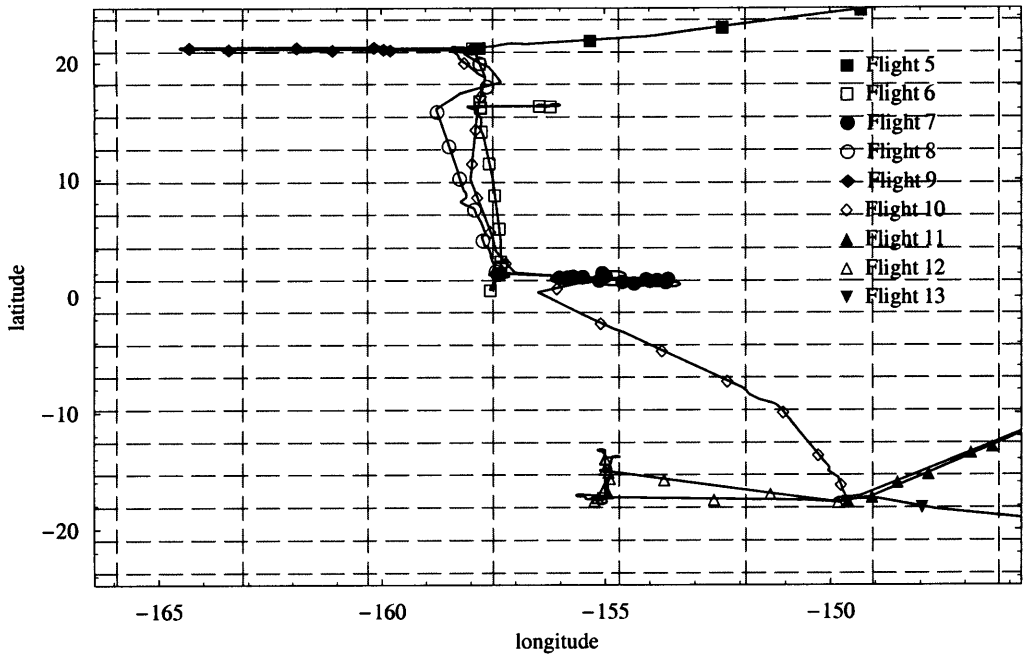

Figure 5-19: Flight tracks of the P-3B aircraft within the central-Pacific during PEM-TA. The individual flight numbers are noted by the symbols and the flights occurred between Hawaii, Christmas Island, and Tahiti. The intersections of the dashed lines show the grid points in MATCH.

Comparisons with PEM-Tropics A

The PEM-TA measurement campaign was conducted across the tropical Pacific troposphere between August and September in 1996. A detailed overview and the logistics of the PEM-TA campaign are provided by Hoell et al. (1999). In addition to characterizing the gases that contribute to the oxidizing capacity of the tropical Pacific atmosphere, the PEM-TA campaign also sought to improve upon the knowledge of the links between sulfur gases and aerosols in this region. To achieve these rather broad goals the strategy of PEM-TA was aimed at sampling a large portion of the Pacific basin through aircraft deployments that stretched laterally from western North and South America to New Zealand and Fiji. This stands in contrast to the multi-platform, regionally-focused nature of ACE-1. Because our model study is designed for the conditions of the remote marine atmosphere, only those PEM-TA observations within the central Pacific have been selected for the following model-observation comparisons. This central region is highlighted in Figures 5-10 and 5-19. Flight numbers F5 to F13 of the NASA P-3B aircraft occurred within this targeted region, and as with the ACE-1 aircraft flights, the P-

3B featured gas-phase measurements of DMS, SO_2, H_2SO_4, and MSA. Descriptions of these measurements have been reported by Thornton et al. (1999), Davis et al. (1999), and Mauldin III et al. (1999b). Also note, the following model-observation comparisons utilize 5-second merged datasets whereby all of the P-3B measurements were placed on a common scale with a time resolution of 5 seconds.

Boundary Layer The observed and modeled boundary layer mole fractions of DMS, SO_2, MSA, and H_2SO_4 aboard the P-3B during PEM-TA are displayed in Figure 5-20. Of the nine P-3B flights contained in the focal region, only 5 flights measured these species in the boundary layer. First, notice that the variabilities of the model and observations are not noticeably larger than those for ACE-1, even though the P-3B transects are longer than the C-130 flights during ACE-1. This suggests that the boundary layer conditions are as uniform across the PEM-TA focal region as across the smaller ACE-1 region.

Next, referring to the DMS mole fractions, the four model cases are nearly identical to one another and match the observations very well. The excellent model-observation agreement, however, does not confirm the accuracy of the modeled DMS surface fluxes and prescribed OH concentrations in the central Pacific, because both may be too large or too small and yet yield good agreement with observations. Although direct measurement-based assessments of the DMS fluxes during PEM-TA are not available as they were in the case during ACE-1, two model-based estimates were made for some of the P-3B flights. Using the mixed-layer gradient method, Lenschow et al. (1999) obtained a DMS flux of $6.1 \pm 1.9 \times 10^9$ molecules cm^{-2} s^{-1} over flight F7. Additionally, Davis et al. (1999) used a mass-balance approach to estimate the DMS fluxes for flights F6, F7, and F10 as 3.0 ± 1.8, 2.3 ± 1.4, and 2.1 ± 1.2 billion molecules cm^{-2} s^{-1}, respectively. Using MATCH, the daily-average DMS fluxes spatially averaged over the boundary layer portions of flights F6, F7, and F10 yield 4.7, 4.6, and 1.3 billion molecules cm^{-2} s^{-1}, respectively, which are very similar to the other estimates. Further, the near-surface averages ($\sigma > 0.95$ and $z \lesssim 500$ m) of the measured OH concentrations during F6, F7, F8, and F12 are, respectively, 1.3, 3.1, 1.9, and 3.7 million molecules cm^{-3} (Mauldin III et al., 1999a). These observed values are within a factor of two of the corresponding model-prescribed OH concentrations of 1.2, 1.6, 2.0, and 2.1 million molecules cm^{-3}. Thus, the modeled DMS mole fractions in Figure 5-20 appear to be reasonable.

Turning to the boundary layer SO_2 mole fractions in Figure 5-20, the four model cases are again similar to each other but are now three to five times lower than the observations over all of the flights. If the modeled DMS fluxes and OH concentrations are indeed reasonable as

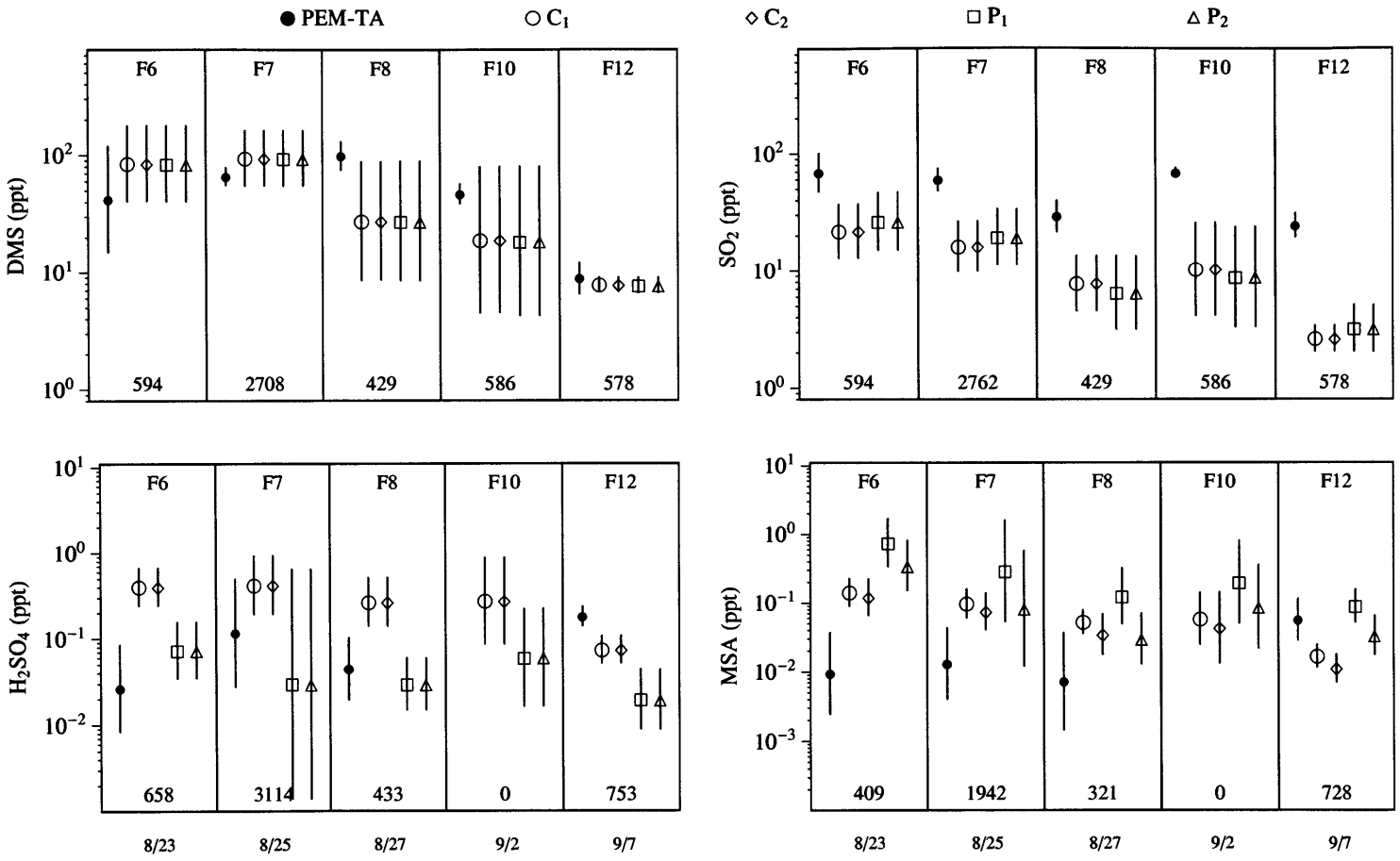

Figure 5-20: Observed and modeled boundary layer average mole fractions of DMS, SO_2, MSA, and H_2SO_4 for individual P TA flights. Refer to Figure 5-15 for additional details. Note that the large numbers of observations do not represent u measurements, but are from interpolations in the 5-second merged datasets.

proposed above, then the negative model bias for SO_2 is a result of unmodeled SO_2 sinks that are too large (for example, sea-salt scavenging and dry deposition) or a missing non-DMS source (for example, anthropogenic and volcanic SO_2) or both. It is not possible to quantitatively assess the contributions of these two factors to the relatively low SO_2 because observational characterizations of the heterogeneous loss of SO_2 were not made, and the model does not include non-DMS sources of SO_2. Thornton et al. (1999) asserted that SO_2 in the boundary layer of the central tropical Pacific is mainly created through DMS oxidation, which would then implicate excessive heterogeneous sinks of SO_2 in the model. Furthermore, Davis et al. (1999) applied a loss frequency of 1.1×10^{-5} s^{-1} in their model for the heterogeneous removal of SO_2 in the boundary layer for flight F7 near Christmas Island. The corresponding value calculated in MATCH is roughly 7×10^{-5} s^{-1}, which is the sum of a dry deposition component (1×10^{-5} s^{-1}) and a sea-salt scavenging (6×10^{-5} s^{-1}) component. To first-order, therefore, the large underestimations of the modeled boundary layer SO_2 mole fractions during PEM-TA could be due to excessive scavenging of SO_2 by sea-salt in our model. Note that heterogeneous loss of SO_2 cannot be the only factor because the much larger measured mole fractions of SO_2 than DMS during F12 points to a crucial role for atmospheric transport in that particular flight.

Finally, the model-observation comparisons of the boundary layer mole fractions of MSA and H_2SO_4 shown in Figure 5-20 are similar to the corresponding comparisons for ACE-1. That is, there are large differences among the various mechanisms, and the measurements for the individual flights often agree with the group average of the four model cases but not with any given case. For example, the observed mole fractions of H_2SO_4 on F6 are closest to the parameterized mechanisms, while on F12 they are closest to the comprehensive cases. Considering all of the flights, neither the parameterized nor comprehensive mechanisms provide a better fit to the H_2SO_4 observations. Consequently, these H_2SO_4 observations cannot distinguish between the four mechanisms. As for MSA, the measured mole fractions over all of the flights provide a slightly better fit to the comprehensive mechanisms, but again, these MSA observations do not uniquely identify a consistently better mechanism.

Vertical Profiles The observed and modeled vertical profiles of the mole fractions of DMS, SO_2, MSA, and H_2SO_4 averaged over the PEM-TA P-3B flights are shown in Figure 5-21. As in ACE-1, the modeled and measured DMS profiles track each other closely in the boundary layer but diverge in the middle troposphere presumably due to the strong model gradients there. Again, the mixing out of the boundary layer in the model appears to be too weak, which seems to be a consistent feature over oceanic grid cells in MATCH. The observed and model-based

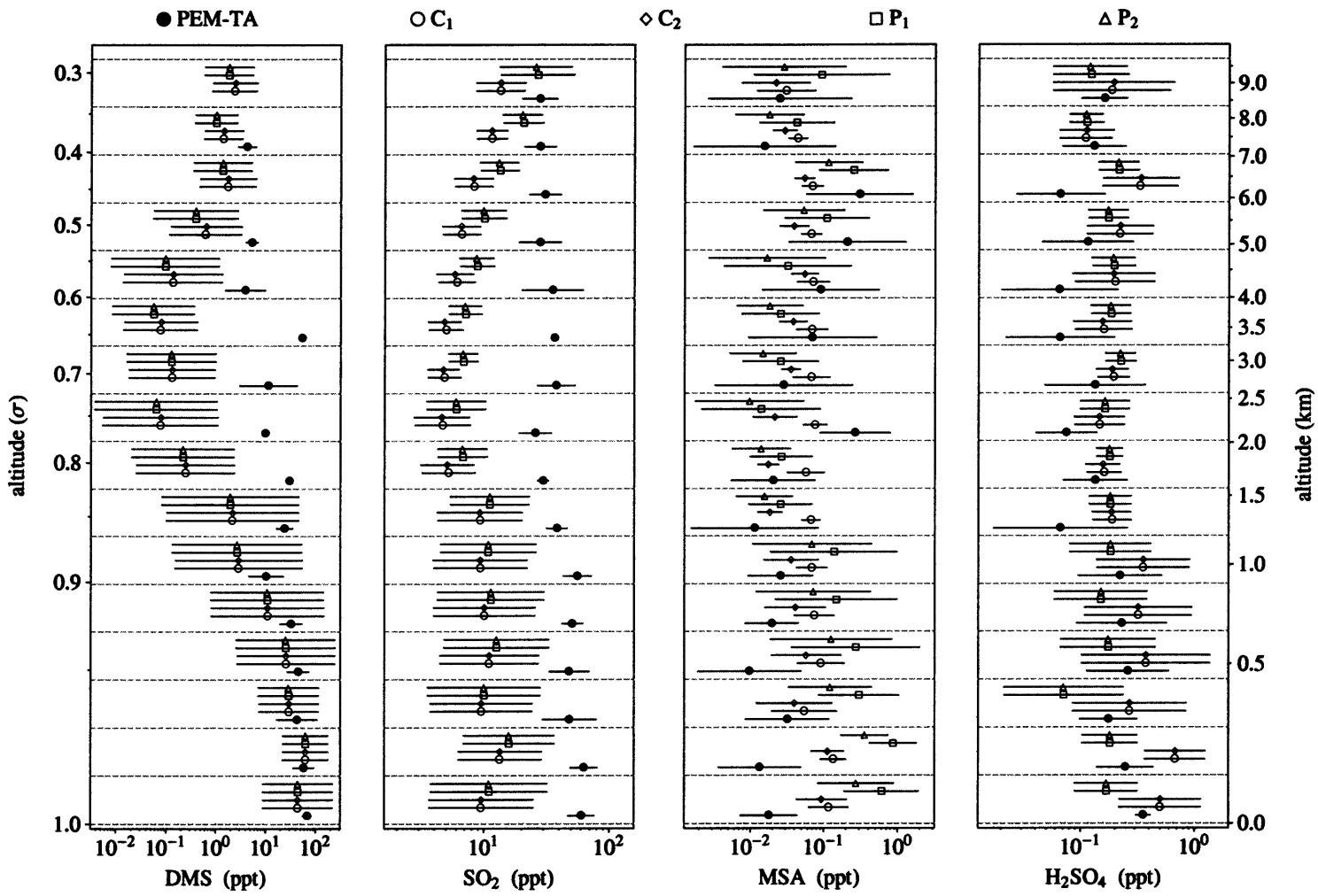

Figure 5-21: Observed and modeled vertical profiles of the mole fractions (ppt) of DMS, SO_2, MSA, and H_2SO_4 averaged over all PEM-TA P-3B flights. Refer to Figure 5-17 for additional details.

DMS profiles agree better in the upper troposphere. This improved agreement is presumably a result of the fact that OH concentrations maximize in the equatorial mid-troposphere and DMS emissions maximize in the extra-tropics.

Regarding SO_2, the four modeled profiles clearly show the same negative bias relative to observations that was described for the P-3B boundary layer averages. These model underestimations are nearly a constant factor of 5 to 6 from the surface to an altitude of about 7 km. The previous section ascribed the boundary layer underestimations to excessive sea-salt scavenging, which may shift the modeled vertical profiles to lower values if excessive numbers of sea-salt aerosols persist across the PEM-TA domain. However, Thornton et al. (1999) also note that the long-distance transport of anthropogenic and volcanic SO_2 is very important at higher altitudes in the central tropical Pacific. Thus, the vertical model underpredictions for SO_2 could be due to a combination of heterogeneous sinks that are too large in the lower troposphere and the lack of non-DMS derived SO_2 in the marine middle to upper troposphere resulting from rapid long-distance transport. This issue can be sorted out using additional runs of MATCH with altered sea-salt aerosols and volcanic and anthropogenic sources of SO_2.

Lastly, other than in the lowest layers for MSA, the collection of modeled vertical profiles for mole fractions of MSA and H_2SO_4 agree with the observations throughout the vertical column, but there are sharp differences among the individual mechanisms. For H_2SO_4, these differences are most dramatic between the comprehensive and parameterized mechanisms in the lower troposphere, where they are split by about a factor of 3. For MSA, the profiles using the parameterized mechanisms have steeper vertical gradients than the comprehensive cases because the P_1- and P_2-generated MSA mole fractions are largest and smallest in the lower and upper troposphere, respectively. In spite of these mechanistic differences, the large variabilities of the observations implies that the four mechanisms are practically indistinguishable.

H_2SO_4 and OH Diurnal Cycles and the OH Vertical Profile The measured and model-based diurnal cycles of H_2SO_4 mole fractions and OH concentrations are shown on the left side of Figure 5-22. On the right side are shown the measured and model-prescribed OH vertical concentration profiles. First, the imposed sinusoidal cycle for the model-prescribed monthly-mean OH fields captures reasonably the time and altitude variations of the OH observations. These comparisons show that the scaling factor of 1.5 again helps bring the model-based OH concentrations into better agreement with the OH observations. The reasonable agreement between the model and observations for the vertical OH profiles supports the earlier conclusion that the large model-based DMS underpredictions in the middle troposphere displayed in Figure

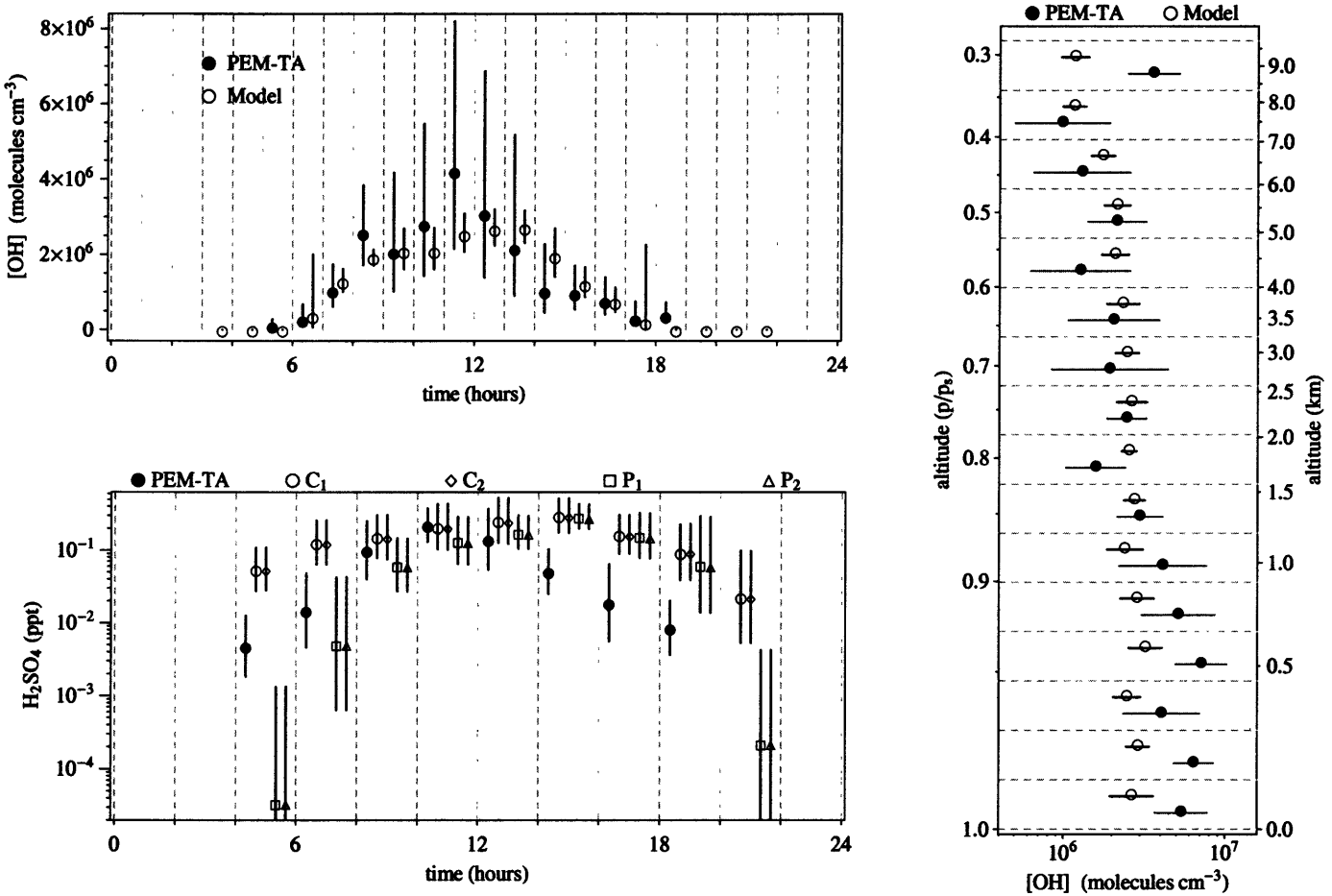

Figure 5-22: Observed and modeled diurnal cycles of H_2SO_4 mole fractions (ppt) and OH concentrations (molecules cm^{-3}) and the vertical profile of OH concentrations during during PEM-TA. Refer to Figure 5-18 for further details.

5-21 are due to inefficient mixing out of the lower model layers. Finally, the fact that the model-prescribed OH concentrations are consistent with observations in the Southern Ocean and the equatorial tropical Pacific provides additional confidence in, but not validation of, the offline OH fields on a global scale.

Regarding the H_2SO_4 diurnal cycle, the four model cases agree with each other and with the observations near mid-day. In the early morning and late afternoon, however, the parameterized mechanisms deviate very significantly from the comprehensive cases. A similar behavior among the four mechanisms was noted in our discussion of ACE-1, where the nighttime H_2SO_4 mole fractions from P_1 and P_2 were extremely variable. Together, the similarities between the ACE-1 and PEM-TA diurnal cycles for H_2SO_4 bolster the proposal from this study that nighttime observations of sulfuric acid are useful for distinguishing between the comprehensive and parameterized mechanisms and that the C_1 and C_2 cases tend to better match the available observations because they do not exhibit the same exaggerated variability.

Model and Observations RMSRs

Though detailed, the previous model-observation comparisons do not give a clear, quantitative sense of which mechanisms provide the best fits overall. For this, the four mechanisms are quantitatively compared to the individual platforms during ACE-1 and PEM-TA using the following root-mean-square residuals (RMSR)

$$\log(\text{RMSR}) = \sqrt{\frac{1}{n}\sum_{i=1}^{n}\left(\log\frac{x_{m,i}}{x_{o,i}}\right)^2} \tag{5.19}$$

where n is the number of observations, and x_o and x_m are the observed and interpolated-mean model mole fractions, respectively. The anti-logarithm of equation 5.19 indicates by what factor the model and observations agree. Recall that in the previous comparisons the observed meteorological data were used to define the model interpolation points. To make direct point-by-point comparisons with the observations here, however, the model is interpolated to the space-time points of the actual measured mole fractions. Note that mis-match model errors are not included in this formulation and that only the lower tropospheric ($z \lesssim 1.5$ km) observations are used for the C-130 and P-3B aircraft comparisons. Equation 5.19 is evaluated for each of the platforms during ACE-1 and PEM-TA and the results are displayed in Table 5.5.

For DMS the RMSR factors range between 1.8 to 4.0, with the lowest values, and hence best

Table 5.5: RMSR Factors Between MATCH and the ACE-1 and PEM-TA Observations in the Lower Troposphere

Species	Mechanism	ACE-1				PEM-TA
		Discoverer	Cape Grim	Macquarie Is.	C-130	P-3B
DMS	C_1	1.8	3.0	2.7	3.0	3.9
	C_2	1.8	3.0	2.7	3.0	3.8
	P_1	1.8	3.0	2.4	2.9	4.0
	P_2	1.8	3.0	2.4	2.9	4.0
SO_2	C_1	3.6	–	–	3.0	4.5
	C_2	3.6	–	–	3.0	4.5
	P_1	3.5	–	–	2.9	4.1
	P_2	3.5	–	–	2.9	4.1
MSA	C_1	–	–	–	8.9	9.3
	C_2	–	–	–	5.8	8.0
	P_1	–	–	–	30.	26.
	P_2	–	–	–	17.	13.
H_2SO_4	C_1	–	–	–	10.	6.8
	C_2	–	–	–	10.	6.9
	P_1	–	–	–	18.	4.9
	P_2	–	–	–	19.	4.9

Lower tropospheric measurements defined by $\sigma > 0.846$ ($\sim$ 1.5 km) are used to calculate RMSRs for the ACE-1/C-130 and PEM-TA/P-3B aircraft.

agreement, occurring for the isolated surface measurements from the *Discoverer* and Macquarie Island. Although there are some slight differences between the parameterized and comprehensive mechanisms, these differences are small and the four mechanisms perform equally well. The RMSRs are larger for SO_2 than DMS, with factors ranging between 2.9 to 4.5. The relatively worse agreement for SO_2 is caused by its multiple ill-constrained sinks (dry deposition, sea-salt scavenging, and photochemical loss). Also, the MATCH runs only simulate the DMS-based sources of SO_2, yet the observations may include anthropogenic and volcanic sources of SO_2. Again, the four model cases are very similar for SO_2 with no single mechanism significantly outperforming the others.

The RMSR factors for MSA are the largest overall among the four species, where they cover a range of 5.8 to 30. These large model-observation differences highlight the difficulty inherent in modeling short-lived oxidized sulfur-containing species using crude representations of aerosols and concentrations of oxidants. In contrast to the RMSRs for DMS and SO_2,

the MSA factors indicate that the comprehensive mechanisms significantly outperform the parameterized schemes. The parameterized schemes have factors greater than 10 for ACE-1 and PEM-TA, while the comprehensive mechanisms agree to within an order of magnitude. Of the two comprehensive cases, the C_2 mechanism does best overall and is within a factor of six of the ACE-1 measurements. It is also interesting to note that the two schemes that include MSA production paths involving DMSO as a precursor (C_2 and P_2) have lower RMSR factors than their counterparts (C_1 and P_1). This is an indication that DMSO is linked to MSA, and that models of the DMS cycle should resolve the chemical and physical sources and sinks of DMSO.

Finally, the RMSR factors for H_2SO_4 are smaller than those for MSA, where they range between 4.9 and 19. Unlike MSA, the factors for H_2SO_4 do not show a clear distinction among the four mechanism cases. In comparing to the ACE-1 data, the two comprehensive schemes provide a better fit to the H_2SO_4 observations. However, the opposite is true for the PEM-TA comparison. On this basis therefore, neither set of mechanisms is consistently better. Recall that throughout the lower troposphere the C_1 and C_2 mechanisms systematically predict higher levels of H_2SO_4 than the P_1 and P_2 schemes because the former include an SO_2-independent sulfuric acid production path not present in the latter. Relative to the four model cases, the ACE-1 and PEM-TA observations fall in-between the high and low values from the comprehensive and parameterized schemes, respectively. Thus, to determine which set of mechanisms does better will require additional model-observation comparisons using better constraints for the model-based aerosol scavenging.

5.4 Summary and Conclusions

A global 3-D chemical transport model of the atmospheric DMS cycle has been assembled using, for the first time, a realistic representation of the complex gas-phase oxidation of DMS. While previous global sulfur models oxidized DMS to SO_2 and sulfate using just 4 to 5 reactions, this model uses a comprehensive DMS mechanism containing roughly 50 DMS-related reactions that resolve many temperature- and pressure-dependencies. Moreover, this model explicitly calculates the scavenging rates (albeit approximately) onto background aerosols, which allows the model to track separately the concentrations of MSA and H_2SO_4 in the gas-phase. Other model features include explicit, wind-forced DMS surface fluxes and wet and dry deposition. The model was integrated from September 1995 to October 1996 using NCEP reanalysis winds with a horizontal resolution of $2.8° \times 2.8°$ and 28 vertical σ-pressure levels.

Four model cases are considered, two using parameterized DMS oxidation mechanisms and two comprehensive schemes taken from Lucas and Prinn (2002). The gas-phase distributions of DMS, SO_2, MSA, and H_2SO_4 are compared between these four cases as a measure of the sensitivity to the type of mechanism. The four cases predict nearly identical levels of DMS throughout the atmosphere because the four mechanisms use similar reactions and rate constants to describe the oxidation of DMS through the OH-addition and H-abstraction paths. A global annual DMS burden of 43 to 46 Tg S yr^{-1} is calculated for the four model cases. Regarding SO_2, the four model cases agree primarily to within a factor of 1.5 in the lower troposphere. But in the upper troposphere, the parameterized mechanisms predict three times more SO_2 than the comprehensive versions. These large mechanistic differences for SO_2 are caused by the fixed branching yields used in the parameterized mechanisms.

Larger mechanistic differences occur between the four model cases for the gas-phase distributions of MSA and H_2SO_4. Relative to the comprehensive mechanisms, the parameterized chemistry runs predict roughly 25-times less MSA in the upper troposphere and 10-times less H_2SO_4 in the lower troposphere. These extreme MSA differences are related to the fact that MSA production directly and indirectly involves OH in the parameterized and comprehensive mechanisms, respectively. The extreme mechanistic differences for H_2SO_4 in the lower troposphere are caused by the presence of an SO_2-independent sulfuric acid pathway in the comprehensive mechanisms. Though these sensitivity studies do not identify the type of mechanism that best matches the observations, measurements of SO_2 and MSA in the upper troposphere and H_2SO_4 in the lower troposphere may distinguish between the comprehensive and parameterized cases under well-constrained conditions. Further, the largest differences among the mechanisms for SO_2, MSA, and H_2SO_4 are even larger than the factor of two uncertainty prescribed to uncertain DMS emissions. Thus, the uncertainties associated with gas-phase DMS oxidation are just as large as the other sources of uncertainty in global models of DMS chemistry.

The four model cases are also compared with gas-phase observations of DMS, SO_2, MSA, and H_2SO_4 collected during the ACE-1 and PEM-TA campaigns. In the remote marine boundary layer the four model cases agree with the DMS observations by about a factor of two in terms of the RMSR. This level of agreement for DMS is reasonable in light of the climatologically-based DMS emissions and monthly-mean OH concentrations used in the model. Also, when considering the coarse horizontal resolution of the model, and hence the large mis-match errors, the majority of the DMS observations statistically agree with the four model cases. For SO_2 the model-observation agreement is somewhat poorer, where according to the RMSR, the four

model cases agree with the observations to within a factor of 2.9 to 4.5. The model cases have better agreement with SO_2 in the Southern Ocean than in the tropical Pacific, where the former better represents the clean marine atmosphere. This indicates that anthropogenic SO_2 not present in the model may account for these larger RMSR factors. Also, the four model cases agree with boundary layer observations of SO_2 during ACE-1 to within a factor of 2 to 3 when known continentally-influenced air parcels are identified and ignored.

Regarding gas-phase H_2SO_4 and MSA, the group of four mechanism cases agree statistically with the majority of the observations during ACE-1 and PEM-TA. However, there are large differences between the mechanism cases such that not a single case agrees with all of the observations. For H_2SO_4, the comprehensive and parameterized mechanisms tend to over- and under-estimate the mole fractions relative to the boundary layer observations, respectively. The H_2SO_4 produced using the simplified chemistry, however, is more variable than both the comprehensive cases and the observations, especially at high solar zenith angles (i.e., early morning and late evening). In terms the RMSR factors for H_2SO_4, neither the comprehensive nor parameterized schemes are consistently better, which suggests that better constraints (e.g., background aerosol distributions) are required before using these observations to differentiate between the chemical schemes. As for MSA, the average vertical profiles during ACE-1 and PEM-TA tend to match the comprehensive cases somewhat better because the vertical MSA gradients produced using the parameterized chemistry are slightly too large. Moreover, the RMSR factors for MSA, although quite large, do indicate that the comprehensive chemistry schemes fit the observations better than the simplified schemes.

Finally, the vertical profiles of the gas-phase measurements of H_2SO_4 during ACE-1 and PEM-TA fall in-between the modeled vertical profiles using the comprehensive and parameterized mechanisms. Thus, the collection of four model runs agree statistically with the H_2SO_4 observations from the surface to an altitude of 7 to 9 km. This consistency suggests that the modeled distributions of gas-phase sulfuric acid can be used to provide a first-order picture of the nucleation rates of new H_2SO_4-H_2O particles in the atmosphere. These nucleation rates are estimated using a parameterized version of binary nucleation theory, along with NCEP observations of temperature and humidity and the modeled sulfuric acid distributions. This analysis finds that the nucleation rates are maximized in the upper tropical troposphere. Further, none of the sulfuric acid distributions from the four model cases is sufficiently large enough to induce the nucleation of significant amounts of new particles in the lower atmosphere. Thus, in contrast to other studies, DMS oxidation does not appear to contribute to new particle production

in the remote marine boundary layer.

Chapter 6

Conclusions

6.1 Summary and Major Findings

DMS oxidation chemistry was analyzed in this thesis across a range of scales in time and space using three atmospheric models of varying complexity. The major conclusions from each of these studies are summarized below.

6.1.1 Sensitivities and Uncertainties in the Remote Marine Boundary Layer

The sensitivities and uncertainties of the products of dimethylsulfide (DMS) oxidation to 56 uncertain parameters were calculated using a diurnally-varying box model of the DMS cycle in the remote marine boundary layer (RMBL). The oxidation of DMS uses a comprehensive mechanism that includes newly proposed routes for the production of gas-phase methanesulfonic acid (Lucas and Prinn, 2002). Non-photochemical processes such as heterogeneous removal and RMBL mixing are parameterized and simulated. The direct integration and probabilistic collocation methods were used to compute the following quantities:

- diurnal cycles of the first-order local concentration sensitivities at the mean values of the parameters
- probabilistic concentration sensitivities that account for uncertainties in the parameters
- second- and third-order local concentration sensitivities
- probability density functions (PDFs) of the concentrations of the sulfur-containing species

- the first three moments of the concentration PDFs (mean, variance, skewness)
- contributions of uncertain parameters to uncertain concentrations
- uncertainties in the concentrations over a wide temperature range

At the mean values of the model parameters, the parametric sensitivity analysis found the oxidized DMS products to be most sensitive to the DMS+OH abstraction and addition reaction rate constants and the parameters for heterogeneous removal, DMS emissions, and mixing into/out of the RMBL. At 1-σ below the mean parameters the probabilistic sensitivities are radically different such that many gas-phase reaction rate constants have an increased influence on the DMS-related concentrations. These variations in the sensitivities to changes in the uncertain parameters are comparable to the diurnal changes in the sensitivities at the parameter means. Significant second- and third-order sensitivities were also found, which highlight some important non-linear dependencies and parameter interactions. A final, major conclusion from this sensitivity analysis is that the concentrations of DMS and SO_2 are sensitive to very few parameters, most of which are non-photochemical. The concentrations of MSA and H_2SO_4, on the other hand, are sensitive to many photochemical and non-photochemical parameters.

On the basis of the uncertainty analysis at 290 K, the uncertainties for the important DMS-related concentrations range between factors of 1.7 and 5. Although the uncertain DMS emission rate and heterogeneous removal parameters are large contributors to these uncertainties, many gas-phase reactions also contribute significantly. Moreover, non-linearities between the reaction rate constants and parameters for heterogeneous loss, DMS emissions, and RMBL mixing cause skewed PDFs for many of the species. These non-linearities account for 2 to 25% of the total uncertainty in the DMS-related concentrations. A final, major conclusion from this uncertainty analysis is that uncertainties in the concentrations of DMS and SO_2 are caused by very few uncertain parameters. Many uncertain parameters, however, induce uncertainty in MSA and H_2SO_4. Also, the uncertainty in DMS emissions is the dominant source of uncertainty only in the concentration of DMS, not the other species.

The concentration uncertainties were also computed over a temperature range of 250 to 310 K and found to vary non-linearly with temperature. Over the full temperature range, the uncertainties for concentrations of DMS, SO_2, and MSIA change very little (constant factors of about 2); the concentration uncertainties of DMSO, MSEA, MSA, and H_2SO_4 vary by factors of 2 to 4; and the $DMSO_2$ concentration uncertainty changes from a factor of 2 to 7.

6.1.2 Mechanistic Studies in an Observationally-Constrained Atmospheric Column

A one-dimensional model of dimethylsulfide (DMS) oxidation chemistry and simultaneous observations from Flight 24 of the First Aerosol Characterization Experiment are used to test the oxidation of DMS by OH and the gas-phase production of SO_2, H_2SO_4, and methanesulfonic acid (MSA) in the remote marine atmosphere. The model includes a comprehensive chemical mechanism (55 sulfur reactions, 28 sulfur species), vertical mixing, scavenging by background aerosols, and surface losses and emissions. Model parameter uncertainties have been estimated and are used to compute probability distribution functions of observable model outputs using a Monte Carlo method. Seven mechanistic scenarios are considered, which include a *baseline* case incorporating our best current knowledge, and six cases that test novel MSA production reactions involving a newly proposed MSA isomer ($CH_3S(OH)OO$) and the oxidation of methanesulfenic (MSEA) and methanesulfinic (MSIA) acids.

The results show that for each of the seven scenarios, the modeled DMS and SO_2 concentrations agree statistically with the Flight 24 observations. For MSA, however, the observations are a factor of 10^4 to 10^5 larger than the baseline mean model predictions and lie three to four orders of magnitude outside of the 1-σ model uncertainty range. Statistical agreement between the boundary layer MSA observations and the model is achieved only for the mechanism scenarios that invoke new MSA production pathways, with the best agreement occurring when MSA is produced from the oxidation of MSIA or through a path involving the DMS-OH addition adduct and MSA isomer. Above the boundary layer the best agreement for MSA occurs when MSA production involves precursors such as DMSO and MSIA that are efficiently removed in the boundary layer. This finding strongly suggests that DMSO and MSIA are involved in MSA production.

For H_2SO_4, this study finds that even though the majority of the observations lie within the 1-σ model uncertainty range, the baseline scenario systematically underproduces H_2SO_4 in the boundary layer. These systematic differences are removed when the production of SO_3 is enhanced through a pathway that is independent of SO_2. This provides evidence for an efficient H_2SO_4 production pathway that does not involve SO_2 as a precursor.

Sensitivity studies are also presented, the results of which suggest observables that are most effective at distinguishing between our seven DMS mechanistic scenarios. These studies indicate that boundary layer observations of H_2SO_4 and MSA, and measurements of the vertical profiles of MSIA and MSA may help to discern between the various mechanisms.

6.1.3 Three-Dimensional Global Studies of the DMS Cycle

The atmospheric oxidation cycle of dimethylsulfide (DMS) is simulated using the global three-dimensional Model of Atmospheric Transport and Chemistry (MATCH). Four model cases are run in MATCH corresponding to four mechanisms (2 comprehensive, 2 parameterized) that describe the oxidation of DMS and production of gas-phase sulfur dioxide (SO_2), sulfuric acid (H_2SO_4), and methanesulfonic acid (CH_3SO_3H, MSA). The comprehensive mechanisms oxidize DMS to a multitude of gas-phase end-products using approximately 50 DMS-related reactions that include many known temperature- and pressure-dependencies (Lucas and Prinn, 2002). The two parameterized mechanisms are taken from recent global sulfur models and use 4 to 5 reactions to describe the DMS oxidation sequence.

Other model features include wind-forced DMS surface emissions, wet and dry deposition, and the scavenging of sulfur gases by background aerosols. The four DMS mechanisms are integrated from September 1995 to October 1996 using reanalysis fields from the National Center for Environmental Prediction. The four model cases are compared with each other to quantify the sensitivities of important DMS-related species to the type of mechanism. The four model cases are also compared with *gas-phase* measurements of DMS, SO_2, MSA, and H_2SO_4 collected during the First Aerosol Characterization Experiment (ACE-1) and Pacific Exploratory Mission-Tropics A (PEM-TA) campaigns.

In comparing the four model cases with each other, DMS is found to be insensitive between the comprehensive and parameterized mechanisms. In terms of annual-zonal profiles the four mechanisms yield DMS levels within 20% of each other. SO_2 is moderately sensitive to the type of mechanism, whereby SO_2 mole fractions from the parameterized schemes are 2 to 3 times larger in the surface polar regions and upper troposphere. These differences arise from the lack of important temperature-dependent SO_2-precursor reactions in the parameterized cases. MSA and H_2SO_4 are extremely sensitive to the different mechanisms, with the parameterized and comprehensive schemes diverging by more than an order of magnitude at the high-latitude surface and in the upper troposphere. These comparisons clearly show that the uncertainties associated with the DMS mechanism can be more important than the typical factor of 2 uncertainty ascribed to the ill-constrained emissions of DMS.

Relative to the campaign measurements, the root-mean-square residuals (RMSR) between the model cases and observations are factors of 1.8 to 4.0 for DMS during ACE-1 and PEM-TA, with the best agreement occurring at remote surface locations. For SO_2 the RMSR factors range between 2.9 to 4.5 and show no significant differences between the four mechanisms. For MSA

and H_2SO_4 the RMSR factors fall between 4.9 and 30, with significant mechanistic differences occurring only for MSA. For MSA, the comprehensive schemes have lower RMSR factors, and hence provide a better fit to the gas-phase observations of MSA.

The generally good agreement between the measured and group of 4 modeled vertical mole fraction profiles of gas-phase H_2SO_4 allows the sulfuric acid distributions to be used to quantify the rates of nucleation of new H_2SO_4-H_2O particles in the atmosphere. This analysis shows that the production of sulfuric acid particles occurs primarily in the upper tropical troposphere where the temperature is most conducive to nucleation. Moreover, none of the H_2SO_4 distributions produced from the four mechanism cases leads to appreciable particle production in the lower atmosphere. Thus, DMS oxidation does not appear to be a source of new particles in the remote marine boundary layer.

6.2 Future Directions

Although many aspects of the seven active questions stated in Section 1.2.1 in Chapter 1 have been directly answered in this thesis, the process of answering these questions has opened up many new and exciting questions related to the atmospheric DMS cycle. Additionally, the model-based approach used throughout this thesis is based on certain underlying model assumptions that may not always be valid. Thus, this section points out some of these new questions and the further model refinements that will lead to a better understanding of the atmospheric DMS cycle.

The diurnally-varying box model of DMS chemistry in the RMBL described in Chapter 3 is an ideal tool for exploring the large multi-dimensional parameter space of the DMS cycle. Yet, many simplifications were made in this study. For instance, other than temperature and the concentrations of important oxidants, the background conditions were fixed throughout the simulations. Also, clear-sky conditions were assumed. A future direction, then, is to apply this model to other sets of conditions to determine the changes to the key sensitivities and uncertainties. One important set of conditions is for a cloudy marine boundary layer, which would strongly influence many of the soluble sulfur-containing species. Another possibility is to use greater NO_x concentrations typical in coastal surface regions. Also, certain model features could be made more realistic, such as including time-variations in the boundary layer height and mixing coefficient. Another improvement would be to separate the generic heterogeneous removal parameter into dry deposition and aerosol scavenging components so that the sensitivities to these unique processes can be ascertained.

The one-dimensional DMS chemistry and mixing model is simple enough so that it is easily constrained, yet complex enough to provide model output that can be compared with actual atmospheric data. This study answered many important questions related to MSA, but it also led to new questions about the DMS mechanism. One very important question left open involves the production of gas-phase sulfuric acid through a path that does not involve SO_2. This question was first posed and qualitatively assessed by Bandy et al. (1992). Although this 1-D study provides some quantitative evidence for the existence of an efficient SO_2-independent sulfuric acid production branch, the model errors are unfortunately too large to answer this question conclusively. By reducing the model uncertainties in the production of H_2SO_4 using the information from Chapter 3, the SO_2-independent path can then be definitively ruled for or against. Also, the 1-D study showed that the baseline mechanism is statistically insufficient for producing MSA. This led to the exciting exploration of new MSA production paths. However, using these new paths, the 1-D model was still unable to reproduce an important MSA feature that may be related to MSIA and/or other MSA-precursors. Therefore, returning to the 1-D model and attempting to reproduce this MSA-feature may shed more light on the nature of MSA production.

The three-dimensional global DMS study is the first to utilize a comprehensive DMS mechanism. This 3-D study answers many important questions related to the large-scale distributions of oxidized DMS products and the uncertainties inherent in using parameterized DMS chemistry in global models. However, the comparison of the 3-D model results with gas-phase observations from the ACE-1 and PEM-TA campaigns exposed many model features that require further improvement. Four important improvements are described here. First, the model-based aerosols used to compute aerosol scavenging rates are currently represented by the crude GADS climatological fields, which are available biannually and only at the surface. Because aerosol scavenging is a dominant sink throughout the atmosphere for many of the oxidized sulfur-bearing compounds, the GADS aerosols should be replaced. A promising candidate is a new set of aerosol fields assimilated using MATCH, which would provide a consistent and observationally-based aerosol sink for the oxidized DMS products. Second, diurnal chemistry has a large impact on the cycles of the DMS species, yet monthly-mean concentrations of HO_x, O_3, and NO_x are used to drive the DMS chemistry. Higher time-resolution oxidants can now be obtained from the same source (MATCH-MPIC) that provided the monthly-mean concentrations. Third, the 3-D model systematically underestimates SO_2 in the central tropical Pacific relative to observations. This underprediction can be better assessed by including anthropogenic and volcanic sources of

SO_2. Fourth, many of the model-observations comparisons are limited by the large estimated spatial mis-match errors in the model. These mis-match errors can be reduced by using a higher spatial-resolution, which, in turn, may also allow for better differentiation between the various mechanism cases compared to the observations.

Acknowledgements

Above all, I must first thank my advisor and mentor Ron Prinn for his unwavering support throughout my graduate research at MIT. Ron gave me enough freedom to discover my own scientific interests, enough time to pursue these interests at a fundamental level, and enough guidance to reach critical conclusions. In addition, Ron taught me two major lessons that I will carry with me for the rest of my scientific career. First, as a scientific modeler Ron taught me the importance of emphasizing the 'science' over the 'model'. It is all too easy to lose sight of the important scientific issues when faced with 1000's of lines of FORTRAN code! Second, Ron taught me the importance of using observations to ground model simulations in reality. The envelope of science is pushed forward by merging observational data from the field and laboratory with computer models of our theoretical understandings.

Many other people who played a role in the production of this thesis deserve my gratitude. Among these include my additional thesis committee members –Mario Molina, Alan Plumb, and Greg McRae– who found time in their busy schedules to review my thesis. A special thanks also goes out to Chien Wang, who opened my eyes to the atmospheric chemistry of DMS and helped ease my transition into the world of atmospheric modeling. This thesis is also infinitely better due to my discussions with Yu-Han Chen, Jin Huang, and Donnan Steele. They were always there to bounce ideas off of. And thanks again to Yu-Han for reminding me that the finish line was not far off when I was in the final stretch. I cannot forget to thank other former and current Prinn group members for their encouragement, the Prinn group support staff for their never-ending help, Phil Rasch and co-workers for help with MATCH, Mark Lawrence and co-workers for access to the results from MATCH-MPIC, and all of the researchers that collected the data during ACE-1 and PEM-TA that is used in this thesis.

The greatest pleasure in completing this thesis lies in being able to share it with someone who cherishes it as much as I do. Thank you SoYoung for your continuous devotion and for standing by me through thick and thin. Every word on every page is for you.

This thesis work was supported financially by a variety of sources, including a fellowship from the MIT Joint Program on the Science and Policy of Global Change, NSF grant ATM-9610145, and the PAOC Houghton Fund.

References

Andreae, M., Crutzen, P., 1997. Atmospheric aerosols: Biogeochemical sources and role in atmospheric chemistry. Science 276, 1052–1058.

Atkinson, R., Baulch, D. L., Cox, R. A., Hampson, R., Kerr, J. A., Rossi, M. J., Troe, J., 1997. Evaluated kinetic and photochemical data for atmospheric chemistry: Supplement VI. J. Phys. Chem. Ref. Data 26, 1329–1499.

Bandy, A. R., Scott, D. L., Blomquist, B. W., Chen, S. M., Thorton, D. C., 1992. Low yields of SO_2 from dimethyl sulfide oxidation in the marine boundary layer. Geophys. Res. Lett. 19, 1125–1127.

Bandy, A. R., Thorton, D. C., Blomquist, B. W., Chen, S., Wade, T. P., Ianni, J. C., Mitchell, G. M., Nadler, W., 1996. Chemistry of dimethyl sulfide in the Equatorial Pacific atmosphere. Geophys. Res. Lett. 23, 741–744.

Bardouki, H., Barcellos da Rosa, M., Mihalopoulos, N., Palm, W., Zetzsch, C., 2002. Kinetics and mechanism of the oxidation of dimethylsulfoxide (DMSO) and methanesulfinate (MSI^-) by OH radicals in aqueous medium. Atmos. Environ. 36, 4627–4634.

Barnes, I., Becker, K. H., Patroescu, I., 1996. FTIR product study of the OH initiated oxidation of dimethyl sulphide: Observation of carbonyl sulphide and dimethyl sulphoxide. Atmos. Environ. 30, 1805–1814.

Barone, S. B., Turnipseed, A. A., Ravishankara, A. R., 1996. Reaction of OH with dimethyl sulfide (DMS). 1. Equilibrium constant for OH + DMS reaction and the kinetics of the OH·DMS + O_2 reaction. J. Phys. Chem. 100, 14,694–14,702.

Barth, M., Rasch, P. J., Kiehl, J. T., Benkovitz, C. M., Schwartz, S. E., 2000. Sulfur chemistry in the National Center for Atmospheric Research Community Climate Model: Description, evaluation, features, and sensitivity to aqueous chemistry. J. Geophys. Res. 105, 1387–1415.

Bates, T. S., Huebert, B., Gras, J., Griffiths, F., Durkee, P., 1998a. The international global atmospheric chemistry (IGAC) project's first aerosol characterization experiment (ACE-1): Overview. J. Geophys. Res. 103, 16297–16318.

Bates, T. S., Kapustin, V. N., Quinn, P. K., Covert, D. S., Coffman, D. J., Mari, C., Durkee, P. A., De Bruyn, W. J., Saltzman, E. S., 1998b. Processes controlling the distribution of aerosol particles in the lower marine boundary layer during the First Aerosol Characterization Experiment (ACE 1). J. Geophys. Res. 103, 16,369–16,383.

Bates, T. S., Lamb, B. K., Guenther, A., Dignon, J., Stoiber, R. E., 1992. Sulfur emissions to the atmosphere from natural sources. J. Atmos. Chem. 14, 315–337.

Baumgardner, D., Clarke, A., 1998. Changes in aerosol properties with relative humidity in the remote southern hemisphere marine boundary layer. J. Geophys. Res. 103, 16,525–16,534.

Benkovitz, C. M., Berkowitz, C. M., Easter, R. C., Nemesure, S., Wagener, R., Schwartz, S. E., 1994. Sulfate over the North Atlantic and adjacent continental regions: Evaluation for October and November 1986 using a three-dimensional model driven by observation-derived meteorology. J. Geophys. Res. 99, 20725–20756.

Berresheim, H., Wine, P. H., Davis, D. D., 1995. Sulfur in the atmosphere. In: Singh, H. B. (Ed.), Composition, Chemistry, and Climate of the Atmosphere. Van Nostrand Reinhold, New York, pp. 251–307.

Brechtel, F., Kreidenweis, S., Swan, H., 1998. Air mass characteristics, aerosol particle number concentrations, and number size distributions at Macquarie Island during the First Aerosol Characterization Experiment (ACE 1). J. Geophys. Res. 103, 16,351–16,367.

Cainey, J., Harvey, M., 2002. Dimethylsulfide, a limited contributor to new particle formation in the clean marine boundary layer. Geo. Phys. Lett. 29, 2001GL014439.

Calbó, J., Pan, W., Webster, M., Prinn, R., McRae, G., 1998. Parameterization of urban subgrid scale processes in global atmospheric chemistry models. J. Geophys. Res. 103, 3437–3452.

Campolongo, F., Saltelli, A., Jensen, N. R., Wilson, J., Hjorth, J., 1999. The role of multiphase chemistry in the oxidation of dimethylsulphide (DMS). A latitude dependent study. J. Atmos. Chem. 32, 327–356.

Capaldo, K. P., Pandis, S. N., 1997. Dimethylsulfide chemistry in the remote marine atmosphere: Evaluation and sensitivity analysis of available mechanisms. J. Geophys. Res. 102, 23,251–23,267.

Charlson, R., Lovelock, J., Andreae, M., Warren, S., 1987. Oceanic phytoplankton, atmospheric sulphur, cloud albedo, and climate. Nature 326, 655–661.

Charlson, R., Schwartz, S., Hales, J., Cess, R., Coakley Jr., J., Hansen, J., Hofmann, D., 1992. Climate forcing by anthropogenic aerosols. Science 225, 423–430.

Chen, G., Davis, D. D., Kasibhatla, P., Bandy, A. R., Thornton, D. C., Huebert, B. J., Clarke, A. D., Blomquist, B. W., 2000. A study of DMS oxidation in the tropics: Comparison of Christmas Island field observations of DMS, SO_2, and DMSO with model simulations. J. Atmos. Chem. 37, 137–160.

Chen, Y.-H., 2003. Surface flux estimation of atmospheric methane and carbon dioxide using a 3-D chemical transport model. Ph.D. thesis, Massachusetts Institute of Technology, Cambridge, MA, USA.

Chin, M., Jacob, D. J., Gardner, G. M., Foreman-Fowler, M. S., Spiro, P. A., Savoie, D. L., 1996. A global three-dimensional model of tropospheric sulfate. J. Geophys. Res. 101, 18,667–18,690.

Clarke, A. D., Varner, J. L., Eisele, F., Mauldin, R. L., Tanner, D., Litchy, M., 1998. Particle production in the remote marine atmosphere: Cloud outflow and subsidence during ACE 1. J. Geophys. Res. 103, 16,397–16,409.

Clarke, J. H. R., Woodward, L. A., 1966. Raman spectrophotometric determination of the degrees of dissociation of methanesulphonic acid in aqueous solution at 25°C. T. Faraday Soc. 62, 2226–2233.

Colarco, P. R., Toon, O. B., Torres, O., Rasch, P. J., 2002. Determining the UV imaginary index of refraction of saharan dust particles from total ozone mapping spectrometer data using a three-dimensional model of dust transport. J. Geophys. Res. 107 (D16), 10.1029/2001JD000903.

Collins, W. D., Rasch, P. J., Eaton, B. E., Khattatov, B. V., Lamarque, J., Zender, C. S., 2001. Simulating aerosols using a chemical transport model with assimilation of satellite aerosol retrievals: Methodology for INDOEX. J. Geophys. Res. 106 (D7), 7313–7336.

Cowling, E. B., 1982. Acid precipitation in historical perspective. Environ. Sci. Technol. 16, 110–123.

Davis, D., Chen, G., Bandy, A., Thornton, D., Eisele, F., Mauldin, L., Tanner, D., Lenschow, D., Fuelberg, H., Huebert, B., Heath, J., Clarke, A., Blake, D., 1999. Dimethyl sulfide oxidation in the equatorial Pacific: Comparison of model simulations with field observations for DMS, SO_2, H_2SO_4(g), MSA(g), MS, and NSS. J. Geophys. Res. 104, 5765–5784.

De Bruyn, W. J., Bates, T. S., Cainey, J. M., Saltzman, E. S., 1998. Shipboard measurements of dimethyl sulfide and SO_2 southwest of Tasmania during the First Aerosol Characterization Experiment (ACE 1). J. Geophys. Res. 103, 16,703–16,711.

De Bruyn, W. J., Shorter, J. A., Davidovits, P., Worsnop, D. R., Zahniser, M. S., Kolb, C. E., 1994. Uptake of gas phase sulfur species methanesulfonic acid, dimethylsulfoxide, and dimethyl sulfone by aqueous surfaces. J. Geophys. Res. 99, 16,927–16,932.

De Bruyn, W. J., Swartz, E., Hu, J. H., Shorter, J. A., Davidovits, P., Worsnop, D. R., Zahniser, M. S., Kolb, C. E., 1995. Henry's law solubilities and Śetchenow coefficients for biogenic reduced sulfur species obtained from gas-liquid uptake measurements. J. Geophys. Res. 100D, 7245–7251.

DeMore, W., Sander, S., Golden, D., Hampson, R., Howard, C., Ravishankara, A., Kolb, C., Molina, M., Jan. 1997. Chemical Kinetics and Photochemical Data for Use in Stratospheric Modeling. Tech. Rep. Evaluation No. 12, Jet Propulsion Laboratory, NASA, Pasadena, CA.

Dickinson, R. P., Gelinas, R. J., 1976. Sensitivity analysis of ordinary differential equation systems - A direct method. J. Comp. Phys. 21, 123–143.

Dunker, A. M., 1984. The decoupled direct method for calculating sensitivity coefficients in chemical kinetics. J. Chem. Phys. 81, 2385–2393.

Easter, R. C., Peters, L. K., 1994. Binary homogeneous nucleation: Temperature and relative humidity fluctuations, nonlinearity, and aspects of new particle production in the atmosphere. J. Appl. Meterol. 33, 775–784.

Eisele, F. L., Tanner, D. J., 1993. Measurement of the gas phase concentration of H_2SO_4 and methane sulfonic acid and estimates of H_2SO_4 production and loss in the atmosphere. J. Geophys. Res. 98, 9001–9010.

Falbe-Hansen, F., Sørensen, S., Jensen, N. R., Pedersen, T., Hjorth, J., 2000. Atmospheric gas-phase reactions of dimethylsulphoxide and dimethylsulphone with OH and NO_3 radicals, Cl atoms, and ozone. Atmos. Environ. 34, 1543–1551.

Fuchs, N. A., Sutugin, A. G., 1971. Topics in Current Aerosol Research (Part 2). Pergamon, New York, Ch. Highly Dispersed Aerosols, pp. 1–200.

Gabric, A. J., Ayers, G., Murray, C. N., Parslow, J., 1996. Use of remote sensing and mathematical modeling to predict the flux of dimethylsulfide to the atmosphere in the southern ocean. Adv. Space Res. 18, 117–128.

Gao, D., Stockwell, W. R., Milford, J. B., 1995. First-order sensitivity and uncertainty analysis for a regional-scale gas-phase chemical mechanism. J. Geophys. Res. 100, 23,153–23,166.

Griffiths, F. B., Bates, T. S., Quinn, P. K., Clementson, L. A., Parslow, J. S., 1999. Oceanographic context of the First Aerosol Characterization Experiment (ACE 1): A physical, chemical, and biological overview. J. Geophys. Res. 104, 21649–21671.

Hainsworth, A. H. W., Dick, A. L., Gras, J. L., 1998. Climatic context of the First Aerosol Characterization Experiment (ACE 1): A meteorological and chemical overview. J. Geophys. Res. 103, 16,319–16,340.

Hatakeyama, S., Akimoto, H., 1983. Reactions of OH radicals with methanethiol, dimethyl sulfide, and dimethyl disulfide in air. J. Phys. Chem. 87, 2387–2395.

Hauglustaine, D. A., Granier, C., Brasseur, G. P., Mégie, G., 1994. The importance of atmospheric chemistry in the calculation of radiative forcing on the climate system. J. Geophys. Res. 99, 1173–1186.

Hertel, O., Berkowicz, R., Christensen, J., Hov, Ø., 1993. Test of two numerical schemes for use in atmospheric transport-chemistry models. Atmos. Environ. 27A, 2591–2611.

Hertel, O., Christensen, J., Hov, Ø., 1994. Modelling of the end products of the chemical decomposition of DMS in the marine boundary layer. Atmos. Environ. 28, 2431–2449.

Hindmarsh, A., Radhakrishnan, K., Dec. 1993. Description and use of LSODE, the Livermore Solver for Ordinary Differential Equations. Tech. Rep. UCRL-ID-113855, Lawrence Livermore National Laboratory, Livermore, CA.

Hoell, J. M., Davis, D. D., Jacob, D. J., Rodgers, M. O., Newell, R. E., Fuelberg, H. E., McNeal, R. J., Raper, J. L., Bendura, R. J., 1999. Pacific Exploratory Mission in the tropical pacific: PEM-Tropics A, August-September, 1996. J. Geophys. Res. 104, 5567–5583.

Holtslag, A. A. M., Boville, B. A., 1993. Local versus nonlocal boundary-layer diffusion in a global climate model. J. Climate 6, 1825–1842.

Hynes, A., Wine, P., 1996. The atmospheric chemistry of dimethylsulfoxide (DMSO) kinetics and mechanism of the OH + DMSO reaction. J. Atmos. Chem. 24, 23–37.

Hynes, A. J., Wine, P. H., Semmes, D. H., 1986. Kinetics and mechanism of OH reactions with organic sulfides. J. Phys. Chem. 90, 4148–4156.

Jacobson, M. Z., 1999. Fundamentals of Atmospheric Modeling. Cambridge Univ. Press, Cambridge, U. K.

Jaenicke, R., 1993. Tropospheric Aerosols, in *Aerosol-Cloud-Climate Interactions,* Edited by P. V. Hobbs. Academic Press, Ch. 1, pp. 1–31.

Jones, G. B., Curran, M. A. J., Swan, H. B., Greene, R. M., Griffiths, F. B., Clementson, L. A., 1998. Influence of different water masses and biological activity on dimethylsulphide and dimethylsulphonioprionate in the subantarctic zone of the Southern Ocean during ACE 1. J. Geophys. Res. 103, 16691–16701.

Jones, P. W., 1999. First- and second-order conservative remapping schemes for grids in spherical coordinates. Monthly Weather Review 127, 2204–2210.

Kalnay, E., Kanamitsu, M., Kistler, R., Collins, W., Deaven, D., Gandin, L., Iredell, M., Saha, S., White, G., Woollen, J., Zhu, Y., Chelliah, M., Ebisuzaki, W., Higgins, W., Janowiak, J., Mo, K., Ropelewski, C., Wang, J., Leetmaa, A., Reynolds, R., Jenne, R., Joseph, D., 1996. The NCEP/NCAR 40-year reanalysis project. Bull. of the Amer. Met. Soc. 77, 437–471.

Keller, M., Bellows, W., Guillard, R., 1989. Dimethylsulfide production in marine phytoplankton. In: Saltzman, E., Cooper, W. (Eds.), Biogenic Sulfur in the Environment. American Chemical Society, Washington, D.C., pp. 167–182.

Kettle, A. J., Andreae, M. O., 2000. Flux of dimethylsulfide from the oceans: A comparison of updated data sets and flux models. J. Geophys. Res. 105, 26,793–26,808.

Kettle, A. J., Andreae, M. O., Amouroux, D., Andreae, T. W., Bates, T. S., Berresheim, H., Bingemer, H., Boniforti, R., Curran, M. A. J., DiTullio, G. R., Helas, G., Jones, G. B., Keller, M. D., Kiene, R. P., Leck, C., Levasseur, M., Malin, G., Maspero, M., Matrai, P., McTaggart, A. R., Mihalopoulos, N., Nguyen, B. C., Novo, A., Putaud, J. P., Rapsomanikis, S., Roberts, G., Schebeske, G., Sharma, S., Simó, R., Staubes, R., Turner, S., Uher, G., 1999. A global database of sea surface dimethylsulfide (DMS) measurements and a procedure to predict sea surface DMS as a function of latitude, longitude and month. Global Biogeochem. Cycles 13, 399–444.

Koepke, P., Hess, M., Schult, I., Shettle, E., 1997. Global Aerosol Data Set. Tech. Rep. 243, Max-Planck-Institut für Meteorologie, Hamburg.

Koga, S., Tanaka, H., 1993. Numerical study of the oxidation process of dimethylsulfide in the marine atmosphere. J. Atmos. Chem. 17, 201–228.

Kreidenweis, S. M., Seinfeld, J. H., 1988. Nucleation of sulfuric acid-water and methanesulfonic acid-water solution particles: Implications for the atmospheric chemistry of organosulfur species. Atmos. Environ. 22, 283–296.

Kukui, A., Bossoutrot, V., Laverdet, G., LeBras, G., 2000. Mechanism of the reaction of CH_3SO with NO_2 in relation to atmospheric oxidation of dimethyl sulfide: experimental and theoretical study. J. Phys. Chem. 104, 935–946.

Kulmala, M., Kerminen, V., Laaksonen, A., 1995. Simulations on the effect of sulfuric acid formation on atmospheric aerosol concentrations. Atmos. Environ. 29, 377–382.

Kulmala, M., Laaksonen, A., Pirjola, L., 1998. Parameterizations for sulfuric acid/water nucleation rates. J. Geophys. Res. 103, 8301–8307.

Langner, J., Rodhe, H., 1991. A global three-dimensional model of the tropospheric sulfur cycle. J. Atmos. Chem. 13, 225–263.

Lawrence, M. G., Crutzen, P. J., Rasch, P. J., Eaton, B. E., Mahowald, N. M., 1999. A model for studies of tropospheric photochemistry: Description, global distributions, and evaluation. J. Geophys. Res. 104 (D21), 26245–26277.

Legrand, M., Hammer, C., DeAngelis, M., Savarino, J., Delmas, R., Clausen, H., Johnsen, S. J., 1997. Sulfur-containing species (methanesulfonate and SO_4) over the last climatic cycle in the Greenland Ice Core Project (central Greenland) ice core. J. Geophys. Res. 102, 26663–26679.

Leis, J. R., Kramer, M. A., 1988a. Algorithm 658: ODESSA - an ordinary differential equation solver with explicit simultaneous sensitivity analysis. ACM Trans. Math. Software 14, 61–67.

Leis, J. R., Kramer, M. A., 1988b. The simultaneous solution and sensitivity analysis of systems described by ordinary differential equations. ACM Trans. Math. Software 14, 45–60.

Lenschow, D. H., Paluch, I. R., Bandy, A. R., Thornton, D. C., Blake, D. R., Simpson, I., 1999. Use of a mixed-layer model to estimate dimethylsulfide flux and application to other trace gas fluxes. J. Geophys. Res. 104, 16275–16295.

Liss, P. S., Merlivat, L., 1986. Air-sea gas exchange rates: Introduction and synthesis, in The Role of Air-Sea Exchange in Geochemical Cycling, edited by P. Buat-Ménard and D. Reidel, pages 113-127. Norwell, Mass.

Lovejoy, E. R., Hanson, D. R., Huey, L. G., 1996. Kinetics and products of the gas-phase reaction of SO_3 with water. J. Phys. Chem. 100, 19,911–19,916.

Lovelock, J., Maggs, R., Rasmussen, R., 1972. Atmospheric dimethylsulfide and the natural sulfur cycle. Nature 237, 452–453.

Lucas, D. D., Prinn, R. G., 2002. Mechanistic studies of dimethylsulfide oxidation products using an observationally constrained model. J. Geophys. Res. 107(D14), 10.1029/2001JD000843.

Mahowald, N., Prinn, R., Rasch, R., 1997a. Deducing CCl_3F emissions using an inverse method and chemical transport models with assimilated winds. J. Geophys. Res. 102, 28,153–28,168.

Mahowald, N., Rasch, P., Eaton, B., Whittlestone, S., Prinn, R., 1997b. Transport of ^{222}radon to the remote troposphere using the Model of Atmospheric Transport and Chemistry and assimilated winds from ECMWF and the National Center for Environmental Prediction/NCAR. J. Geophys. Res. 102, 28139–28151.

Mari, C., Suhre, K., Rosset, R., Bates, T. S., Huebert, B. J., Bandy, A. R., Thorton, D. C., Businger, S., 1999. One-dimensional modeling of sulfur species during the First Aerosol Characterization Experiment (ACE 1) Lagrangian B. J. Geophys. Res. 104, 21,733–21,749.

Marti, J. J., Jefferson, A., Cai, X. P., Richert, C., H., M. P., Eisele, F., 1997. H_2SO_4 vapor pressure of sulfuric acid and ammonium sulfate solutions. J. Geophys. Res. 102, 3725–3735.

Mauldin III, R. L., Frost, G. J., Chen, G., Tanner, D. J., Prévôt, A. S. H., Davis, D. D., Eisele, F. L., 1998. OH measurements during the First Aerosol Characterization Experiment (ACE 1): Observations and model comparisons. J. Geophys. Res. 103, 16,731–16,736.

Mauldin III, R. L., Tanner, D. J., Eisele, F. L., 1999a. Measurement of OH during PEM-Tropics A. J. Geophys. Res. 104, 5817–5827.

Mauldin III, R. L., Tanner, D. J., Heath, J. A., Huebert, B., Eisele, F. L., 1999b. Observations of H_2SO_4 and MSA during PEM-Tropics A. J. Geophys. Res. 104, 5801–5816.

Mayer, M., Wang, C., Webster, M., Prinn, R. G., 2000. Linking local air pollution to global chemistry and climate. J. Geophys. Res. 105, 22869–22896.

Pan, W., Tatang, M., McRae, G., Prinn, R., 1997. Uncertainty analysis of direct radiative forcing by anthropogenic sulfate aerosols. J. Geophys. Res. 102, 21,915–21,924.

Pan, W., Tatang, M., McRae, G., Prinn, R., 1998. Uncertainty analysis of indirect radiative forcing by anthropogenic sulfate aerosols. J. Geophys. Res. 103, 3815–3824.

Pandis, S. N., Russell, L. M., Seinfeld, J. H., 1994. The relationship between DMS flux and CCN concentration in remote marine regions. J. Geophys. Res. 99, 16,945–16,957.

Pandis, S. N., Seinfeld, J. H., 1989. Sensitivity analysis of a chemical mechanism for aqueous-phase atmospheric chemistry. J. Geophys. Res. 94, 1105–1126.

Patroescu, I. V., Barnes, I., Becker, K. H., Mihaloposlos, N., 1999. FT-IR product study of the OH-initiated oxidation of DMS in the presence of NO_x. Atmos. Environ. 33, 25–35.

Pham, M., Müller, J., Brasseur, G., Granier, C., Mégie, G., 1995. A three dimensional study of the tropospheric sulfur cycle. J. Geophys. Res. 100, 26,061–26,092.

Pirjola, L., Kulmala, M., 1998. Modelling the formation of H_2SO_4-H_2O particles in rural, urban, and marine conditions. Atmos. Res. 46, 321–347.

Pöschl, U., Canagaratna, M., Jayne, J. T., Molina, L. T., Worsnop, D. R., Kolb, C. E., Molina, M. J., 1998. Mass accommodation coefficient of H_2SO_4 vapor on aqueous sulfuric acid surfaces and gaseous diffusion coefficient of H_2SO_4 in N_2/H_2O. J. Phys. Chem. 102, 10082–10089.

Press, W. H., Teukolsky, S., Vetterling, W., Flannery, B., 1992. Numerical Recipes in Fortran 77, 2nd Edition. Vol. one. Cambridge University Press.

Putaud, J. P., Mihalopoulos, N., Nguyen, B. C., Campin, J. M., Belviso, S., 1992. Seasonal variations of atmospheric sulfur dioxide and dimethylsulfide concentrations at Amsterdam Island in the Southern Indian Ocean. J. Atmos. Chem. 15, 117–131.

Raes, F., 1995. Entrainment of free tropospheric aerosols as a regulating mechanism for cloud condensation nuclei in the remote marine boundary layer. J. Geophys. Res. 100, 2893–2903.

Raes, F., Van Dingenen, R., 1992. Simulations of condensation and cloud condensation nuclei from biogenic SO_2 in the remote marine boundary layer. J. Geophys. Res. 97, 12,901–12,912.

Ramanathan, V., Crutzen, P. J., Kiehl, J. T., Rosenfeld, D., 2001. Aerosols, climate, and the hydrological cycle. Science 294, 2119–2124.

Ramaswamy, V., Boucher, O., Haigh, J., Hauglustaine, D., Haywood, J., Myhre, G., Nakajima, T., Shi, G., Solomon, S., Betts, R., Charlson, R., Chuang, C., Daniel, J., Del Genio, A., Van Dorland, R., Feichter, J., Fuglestvedt, J., de F. Forster, P., Ghan, S., Jones, A., Kiehl, J., Koch, D., Land, C., Lean, J., Lohmann, U., Minschwaner, K., Penner, J., Roberts, D., Rodhe, H., Roelofs, G., Rotstayn, L., Schneider, T., Schumann, U., Schwartz, S., Schwarzkopf, M., Shine, K., Smith, S., Stevenson, D., Stordal, F., Tegen, I., Zhang, Y., 2001. Radiative forcing of climate change. In: Climate Chage 2001: The Scientific Basis. Cambridge Univ. Press, pp. 349–416.

Rasch, P., Mahowald, N., Eaton, B., 1997. Representations of transport, convection, and the hydrologic cycle in chemical transport models: Implications for the modeling of short-lived and soluble species. J. Geophys. Res. 102, 28,127–28,138.

Rasch, P. J., Collins, W. D., Eaton, B. E., 2001. Understanding the indian ocean experiment (INDOEX) aerosol distributions with an aerosol assimilation. J. Geophys. Res. 106 (D7), 7337–7355.

Ray, A., Vassalli, I., Laverdet, G., LeBras, G., 1996. Kinetics of the thermal decomposition of the CH_3SO_2 radical and its reaction with NO_2 at 1 Torr and 298 K. J. Phys. Chem. 100, 8895–8900.

Restelli, G., Angeletti, G. (Eds.), 1993. Dimethylsulphide: Oceans, Atmosphere, and Climate. Kluwer, Dordrecht, Netherlands.

Russell, L. M., Lenschow, D. H., Laursen, K. K., Krummel, P. B., Siems, S. T., Bandy, A. R., Thorton, D. C., Bates, T. S., 1998. Bidirectional mixing in an ACE 1 marine boundary layer overlain by a second turbulent layer. J. Geophys. Res. 103, 16,411–16,432.

Russell, L. M., Pandis, S. N., Seinfeld, J. H., 1994. Aerosol production and growth in the marine boundary layer. J. Geophys. Res. 99, 20,989–21,003.

Saltelli, A., 1999. Sensitivity analysis: Could better methods be used? J. Geophys. Res. 104, 3789–3793.

Saltelli, A., Hjorth, J., 1995. Uncertainty and sensitivity analyses of OH-initiated dimethyl sulphide (DMS) oxidation kinetics. J. Atmos. Chem. 21, 187–221.

Saltzman, E. S., Whung, P. Y., Mayewski, P. A., 1997. Methanesulfonate in the Greenland Ice Sheet Project 2 ice core. J. Geophys. Res. 102, 26649–26657.

Sander, R., 1997. Henry's law constants available on the web. EUROTRAC newsletter 18, 24–25.

Sandu, A., Verwer, J., Blom, J., Spee, E., Carmichael, G., Potra, F., 1997a. Benchmarking stiff ODE solvers for atmospheric chemistry problems - II. Rosenbrock solvers. Atmos. Environ. 31, 3459–3472.

Sandu, A., Verwer, J., Van Loon, M., Carmichael, G., Potra, F., Dabdub, D., Seinfeld, J., 1997b. Benchmarking stiff ODE solvers for atmospheric chemistry problems - I. Implicit vs explicit. Atmos. Environ. 31, 3151–3166.

Sehmel, G. A., 1980. Particle and gas deposition, a review. Atmos. Environ. 14, 983–1011.

Seinfeld, J., Pandis, S., 1998. Atmospheric Chemistry and Physics, From Air Pollution to Climate Change. Wiley-Interscience, New York.

Shaw, G., 1983. Bio-controlled thermostasis involving the sulfur cycle. Climatic Change 5, 297–303.

Shea, D. J., Trenberth, K. E., Reynolds, R. W., 1990. A global monthly sea surface temperature climatology. Tech. Rep. NCAR Technical Note TN-435-STR, National Center for Atmospheric Research.

Shon, Z., Davis, D., Chen, G., Grodzinsky, G., Bandy, A., Thorton, D., Sandholm, S., Bradshaw, J., Stickel, R., Chameides, W., Kok, G., Russell, L., Mauldin, L., Tanner, D., Eisele, F., 2001. Evaluation of the DMS flux and its conversion to SO_2 over the southern ocean. Atmos. Environ. 35, 159–172.

Sørensen, S., Falbe-Hansen, H., Mangoni, M., Hjorth, J., Jensen, N., 1996. Observation of DMSO and $CH_3S(O)OH$ from the gas phase reaction between DMS and OH. J. Atmos. Chem. 24, 299–315.

Spiro, P., Jacob, D. J., Logan, J. A., 1992. Global inventory of sulfur emissions with $1° \times 1°$ resolution. J. Geophys. Res. 97, 6023–6036.

Suhre, K., Mari, C., Bates, T. S., Johnson, J. E., Rosset, R., Wang, Q., Bandy, A. R., Blake, D. R., Businger, S., Eisele, F. L., Huebert, B. J., Kok, G. L., Mauldin III, R. L., Prévot, A. S. H., Schillawski, R. D., Tanner, D. J., Thorton, D. C., 1998. Physico-chemical modeling of the First Aerosol Characterization Experiment (ACE 1) Lagrangian B 1. A moving column approach. J. Geophys. Res. 103, 16,433–16,455.

Sundra, W., Kieber, D. J., Kiene, R. P., Huntsman, S., 2002. An antioxidant function for DMSP and DMS in marine algae. Nature 418, 317–320.

Tatang, M., Pan, W., Prinn, R., McRae, G., 1997. An efficient method for parametric uncertainty analysis of numerical geophysical models. J. Geophys. Res. 102, 21,925–21,932.

Thompson, A. M., Stewart, R. W., 1991. Effect of chemical kinetics uncertainties on calculated constituents in a tropospheric photochemical model. J. Geophys. Res. 96, 13,089–13,108.

Thornton, D. C., Bandy, A. R., Blomquist, B. W., Driedger, A. R., Wade, T. P., 1999. Sulfur dioxide distribution over the Pacific Ocean 1991-1996. J. Geophys. Res. 104, 5845–5854.

Turányi, T., 1990. Sensitivity analysis of complex kinetic systems. Tools and applications. J. Math. Chem. 5, 203–248.

Turnipseed, A. A., Barone, S. B., Ravishankara, A. R., 1992. Observation of CH_3S addition to O_2 in the gas-phase. J. Phys. Chem. 96, 7502–7505.

Turnipseed, A. A., Barone, S. B., Ravishankara, A. R., 1993. Reactions of CH_3S and CH_3SOO with O_3, NO_2, and NO. J. Phys. Chem. 97, 5926–5934.

Turnipseed, A. A., Barone, S. B., Ravishankara, A. R., 1996. Reaction of OH with dimethyl sulfide, 2. Products and mechanisms. J. Phys. Chem. 100, 14,703–14,713.

Turnipseed, A. A., Ravishankara, A. R., 1993. The atmospheric oxidation of dimethyl sulfide: Elementary steps in a complex mechanism. In: Restelli, G., Angeletti, G. (Eds.), Dimethylsulphide: Oceans, Atmospheres, and Climate. Kluwer, Dordrecht, pp. 185–195.

Twomey, S. A., 1974. Pollution and the planetary albedo. Atmos. Environ. 8, 1251–1256.

Urbanski, S. B., Stickel, R. E., Wine, P. H., 1998. Mechanistic and kinetic study of the gas-phase reaction of hydroxyl radical with dimethyl sulfoxide. J. Phys. Chem. 102, 10,522–10,529.

Urbanski, S. P., Wine, P. H., 1999. Chemistry of gas phase organic sulfur-centered radicals. In: Alfassi, Z. B. (Ed.), S-Centered Radicals. Wiley, Chichester, pp. 97–140.

Van Dingenen, R., Raes, F., 1993. Ternary nucleation of methane sulfonic acid, sulphuric acid, and water vapor. J. Aerosol. Sci. 24, 1–17.

Vehkamäki, H., Kulmala, M., Napari, I., Lehtinen, K. E., Timmreck, C., Noppel, M., Laaksonen, A., 2002. An improved parameterization for sulfuric acid-water nucleation rates for tropospheric and stratospheric conditions. J. Geophys. Res. D22.

Verheggen, B., Mozurkewich, M., 2002. Determination of nucleation and growth rates from observations of a SO_2 induced atmospheric nucleation event. J. Geophys. Res. 107(D11), 10.1029/2001JD000683.

Viisanen, Y., Kulmala, M., Laaksonen, A., 1997. Experiments on gas-liquid nucleation of sulfuric acid and water. J. Phys. Chem. 107, 920–926.

von Glasow, R., Sander, R., Bott, A., Crutzen, P. J., 2002. Modeling halogen chemistry in the marine boudary layer 2. Interactions with sulfur and the cloud-covered MBL. J. Geophys. Res. 107, doi:10.1029/2001JD000943.

von Kuhlmann, R., 2001. Tropospheric photochemistry of ozone, its precursors and the hydroxyl radical: A 3D-modeling study considering non-methane hydrocarbons. Ph.D. thesis, University of Mainz, Germany.

Wagner, J., Andrews, E., Larson, S. M., 1996. Sorption of vapor phase octanoic acid onto deliquescent salt particles. J. Geophys. Res. 101, 19,533–19,540.

Wang, L., Zhang, J., 2001. Addition complexes of dimethyl sulfide (DMS) and OH radical and their reactions with O_2 by ab initio and density functional theory. J. Mol. Struct. 543, 167–175.

Wang, L., Zhang, J., 2002a. Ab initio calculation on thermochemistry of CH_3SO_xH ($x = 1-3$) and H_2SO_y ($y = 2, 3$). J. Mol. Struct. 581, 129–138.

Wang, L., Zhang, J., 2002b. Ab initio study of reaction of dimethyl sulfoxide (DMSO) with OH radical. Chem. Phys. Lett. 356, 490–496.

Wang, Q., Lenschow, D. H., Pan, L., Schillawski, R. D., Kok, G. L., Prèvot, A. S. H., Laursen, K., Russell, L. M., Bandy, A. R., Thorton, D. C., Suhre, K., 1999a. Characteristics of the marine boundary layers during two Lagrangian periods 2. Turbulence structure. J. Geophys. Res. 104, 21,767–21,784.

Wang, Q., Suhre, K., P., K., Siems, S., Pan, L., Bates, T. S., Johnson, J. E., Lenschow, D. H., Hubert, B. J., Kok, G. L., Schillawski, R. D., H., P. A. S., Businger, S., 1999b. Characteristics of marine boundary layers during two Lagrangian measurement periods 1. General conditions and mean characteristics. J. Geophys. Res. 104, 21,751–21,765.

Wanninkhof, R., 1992. Relationship between wind speed and gas exchange over the ocean. J. Geophys. Res. 97, 7373–7382.

Wesely, M. L., 1989. Parameterizations of surface resistance to gaseous dry deposition in regional-scale, numerical models. Atmos. Environ. 23, 1293–1304.

Whittlestone, S., Gras, J. L., Siems, S. T., 1998. Surface air mass origins during the First Aerosol Characterization Experiment (ACE 1). J. Geophys. Res. 103, 16,341–16,350.

Whung, P. Y., Saltzman, E. S., Spencer, M. J., Mayewski, P. A., Gundestrup, N., 1994. Two-hundred-year record of biogenic sulfur in a south Greenland ice core. J. Geophys. Res. 99, 1147–1156.

Wilson, J., Cuvelier, C., Raes, F., 2001. A modeling study of global mixed aerosol fields. J. Geophys. Res. 106, 34081–34108.

World Health Organization, 2000. Guidelines for Air Quality. WHO, Geneva.

Yin, F., Grosjean, D., Flagan, R., Seinfeld, J., 1990a. Photooxidation of dimethyl sulfide and dimethyl disulfide. II: Mechanism evaluation. J. Atmos. Chem. 11, 365–399.

Yin, F., Grosjean, D., Seinfeld, J., 1990b. Photooxidation of dimethyl sulfide and dimethyl disulfide. I. Mechanism development. J. Atmos. Chem. 11, 309–364.

Yoon, Y. J., Brimblecombe, P., 2002. Modelling the contribution of sea salt and dimethyl sulfide derived aerosol to marine CCN. Atmos. Chem. Phys. 2, 17–30.

Zhang, X. J., Zhang, N., Schuchmann, H. P., von Sonntag, C., 1994. Pulse-radiolysis of 2-Mercaptoethanol in oxygenated aqueous-solution - Generation and reactions of the thiylperoxyl radical. J. Phys. Chem. 98, 6541–6547.